A STUDY ON MODELLING OF SINGLE LAYER ACSR CONDUCTORS

By

FANG LIU, M. Sc. (Electrical)

Xi'an Jiaotong University, Shaanxi, P. R. China, 1997

A Thesis

Submitted to the School of Graduate Studies

in Partial Fulfilment of the Requirements

for the Degree

Doctor of Philosophy

McMaster University

Your file Votre référence
ISBN: 978-0-494-28221-2
Our file Notre référence
ISBN: 978-0-494-28221-2

A STUDY ON MODELLING OF SINGLE LAYER ACSR CONDUCTORS

DOCTOR OF PHILOSOPHY MCMASTER UNIVERSITY

(Electrical & Computer Engineering) Hamilton, Ontario

TITLE: A Study on Modelling of Single Layer ACSR Conductors

AUTHOR: Fang Liu

M. Sc. (Electrical)

Xi'an Jiaotong University, Shaanxi, P. R. China, 1997

SUPERVISOR: Professor Raymond D. Findlay

NUMBER OF PAGES: xiii, 199

ABSTRACT

In this thesis, an Integrated Model, a physical experimental model, and an artificial neural network model have been developed and investigated to study and predict the operational behaviors of single layer aluminum conductor steel reinforced (ACSR) conductors, used extensively in rural electrification.

The Integrated Model, comprising a mechanical model, an electromagnetic model, a heat transfer thermal model, and a radial conduction model, is an original work to enable the simultaneous prediction of all aspects of the behavior of single layer overhead ACSR conductors at various conditions. Using this Integrated Model, we investigate the effects of lay length, ambient temperature, supply frequency, and other environmental parameters such as time of exposure, air gap thickness, and span length, on the operational behaviors of single layer ACSR conductors.

The comprehensive physical experiment has been designed and performed on three different types of single layer ACSR conductors to measure their thermal and electromagnetic properties under various mechanical conditions. The results compare favorably with the model results over the life of the conductors.

This thesis has developed the artificial neural network model which is trained by the Levenberg-Marquardt optimization algorithm and validated by system identification and statistical criteria. Many modeling techniques are involved: pre-processing and post-processing of datasets; division of training, testing, and forecasting sub-dataset; improvement of the convergence rate and weight updating; neural network topology selection; adaptive parameters optimization; etc. Hourly load demands in Ontario, Canada, have been successfully predicted through an implementation of this artificial neural network model.

Mechanical properties of single layer ACSR conductors are discussed and predicted with the Integrated Model and the neural network model. The analyses of the mechanical properties include their interactive relationship, variation with long time duration, and variation with Ontario daily demands after conductor long service of time.

The design, selection, and improvement of ACSR conductors require intensive understanding of their characteristics. The Integrated Model and the neural network model are powerful tools to design new single layer conductors and to improve existing conductors for their appropriate operating conditions.

ACKNOWLEDGEMENTS

First, and foremost I would like to thank my supervisor, Professor Dr. Raymond D. Findlay for his excellent advice, patience, understanding, and support through the course of this research. Dr. Findlay is wonderful in counseling and excellent in guidance. His dealings with me are always thoughtful and purposeful. Besides the continuous inspiration I derived from him, the opportunity given by Dr. Findlay to be involved in this research is thankfully acknowledged.

I want to thank my committee members: Professors Barna Szabados and Natalia Nikolova for their valuable suggestions and always being available to discuss my work during my Ph.D. studies. Thanks to Professors Tim Davidson and James Reilly for their participation as committee members during my comprehensive examination. The comments and questions in the examination forced me to understand even better some of the issues in academia.

I would also like to thank the faculty and staff members from the Power Research Laboratory. Special thanks to all my friends and colleagues at McMaster University for their support and comments.

I am grateful to my spouse Qiang Song for his belief in me, patience, and support.

I am grateful to my parents for encouraging my endless studies.

TABLE OF CONTENTS

LIST OF TABLES

LIST OF FIGURES

CHAPTER 1
INTRODUCTION

1.1 Background Information

With increased industrial development, more and more energy needs to be transferred through transmission grids. The increases of load affect the transmission capacity of the existing lines. There is little room for increased corridor expansion in many areas. Consequently, there is a need for increased ability to determine appropriate current limits on the existing lines. The system stability and reliability are affected by the load. To ensure system stability and reliability, it is necessary to study limitations to safe operating conditions on the existing lines or proposed new lines. This research investigates ways to study the operation of some types of transmission conductor.

Bare overhead lines are the most economical means to transport energy from generating plants to distribution stations. At transmission level voltages, the capital costs of an underground power cable are usually several times those of an overhead line of equal capacity. In heavily populated urban areas, underground cable systems are mostly preferred. ACSR, Aluminum Conductor Steel Reinforced, is a popular choice of conductors in overhead transmission and distribution lines because of its excellent conductivity and strength-to-weight ratio. The design, selection, and improvement of the conductors require intensive understanding of their characteristics: load capacity, thermal properties, current loading, thermal loading, creep, sag, strength, and metal fatigue. Especially, the load capacity influences the stability, losses, efficiency, and reliability of the system.

ACSR, with the steel core sustaining the tension due to the weight of the conductor between supports, and the aluminum layer carrying most of the current, is popularly used in North America as transmission and distribution conductor. Most of the overhead lines in North America are short lines. Current-carrying capacity of short lines is limited by the maximum conductor temperature, the sag, the loss of tensile strength of nonferrous part of the conductor due to annealing. In the case of a long transmission line, the maximum current is mostly dependent on system stability, voltage drop, and power losses.

One classification of ACSR conductors is according to the number of aluminum layers. If there is only one aluminum layer stranding over the steel core, this conductor is called single layer ACSR. If two or three or more aluminum layers are used, the layers strand concentrically around the steel core with alternate left hand and right hand directions. The conductor is called two-layer ACSR, or three-layer ACSR, or multi-layer ACSR, respectively. Figure 1.1 shows a typical structure of a single layer ACSR conductor. It has a steel king wire in the center and six aluminum strands helically surrounding it. Depending on the application, the steel core may have one or more steel layers surrounded by six or more helically wound aluminum strands.

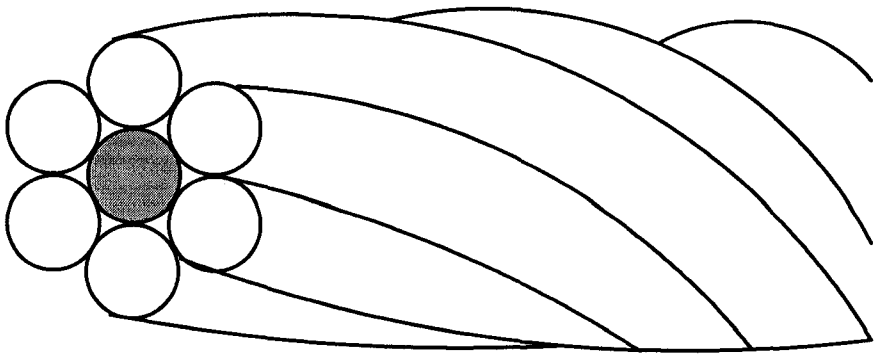

Figure 1.1 Structure of a single layer ACSR conductor

1.2 Previous Work

Lewis and Tuttle [1] performed early investigations of the resistance and reactance of ACSR conductors. In their research, a question was raised from theoretical and practical aspects that single layer ACSR conductors should be treated differently from all other multi-layer ACSR conductors. The companion paper, written by Matsch and Lewis [2], confirmed that:

> "The resistance and reactance of single layer ACSR must inherently be subject to some variation from sample to sample and in the same sample for different conditions of temperature and stress."

A Task Force Group, led by Douglass and Kirkpatrick [3], evaluated possible methods of calculating ac/dc resistance ratio for ACSR conductors. They investigated the value of increases in ac resistance and noted that the apparent maximum occurs with single layer ACSR conductors. They commented that "the usefulness of analytical models is questionable" because the error between analytical value and experimental value reaches as high as "6.6% for single layer ACSR conductors".

Over the years, four determinate models have been developed to analyze various aspects of ACSR: the mechanical model, the electromagnetic model, the radial temperature conduction model, and the steady-state thermal model. The operational behaviors cannot be accurately predicted with separate models due to lack of interrelations among mechanical, electromagnetic, thermal radial conduction, and steady-state thermal characteristics, especially at high temperatures with large current.

Filipovic-Gledja and her coauthors [4, 5] developed a Unified Model for three-layer ACSR, which combined the behaviors of mechanical, electromagnetic, and thermal together.

1.3 Problem Description

A comprehensive and accurate model needs to be established to predict the operational behaviors of single layer ACSR conductors from electromagnetic, mechanical, and steady-state thermal viewpoints.

The economic choice of conductors is significantly influenced by the conductor resistance which affects both the voltage drop and the energy loss along the line. It is important for the designer to have a reasonably good assessment of the actual resistance at the operating frequency. The accurate ac resistance prediction of ACSR becomes necessary and of practical importance.

For ACSR conductors, ac resistance has higher value than dc resistance because of skin effect, transformer effect, proximity effect, and steel core losses. The current in the spiraling aluminum strands in ACSR creates an axial field which coincides with the direction of the steel core, leading to a strong transformer-like coupling between the currents injecting in the aluminum layer. The longitudinal flux causes hysteresis and eddy currents in the steel core and the redistribution of the currents in aluminum layers. In multi-layer ACSR, the currents wound alternatively right and left handed around the steel core, and their resulting magnetic field contributions tend to cancel. For the even-layer ACSR, the cancellation of the magnetic field proves that there is almost no significant longitudinal flux in the steel core. For odd-layer ACSR, the cancellation is partial, and there is some longitudinal flux in the steel core. For single layer ACSR, no cancellation occurs because there is only one aluminum layer in the conductor. The longitudinal flux is greatly increased because of the steel core, and produces a significant increase in ac resistance and ac reactance of the conductor. The strong electromagnetic field affects other operational behaviors such as capacity, transmission loss, conductor temperature, and some mechanical properties for single layer conductors.

Usually, three-layer ACSR has two steel layers while single layer ACSR may have only one steel layer or just a king wire that carries the tension. Both aluminum and steel wires of single layer ACSR experience more tensile strength than those of three-layer ACSR. Mechanical properties of ACSR such as sag and loss of tensile strength of aluminum wires are greatly affected by the variation of stress in the aluminum wires.

The development of the Integrated Model is based on the Unified Model which was designed initially for three-layer ACSR. Due to the strong magnetic field in the steel core and large stress in aluminum wires, the Integrated Model is different from the Unified Model. An experimental model has also been designed and conducted on single layer ACSR conductors. The results from the Integrated Model are compared and discussed with those from the experiment over the life of the conductors.

1.4 Major Contributions

Major contributions in this research include the development of the Integrated Model, the design and performance of an experimental model, the development of an artificial neural network model, prediction of Ontario daily load variations, discussion and prediction of the mechanical properties of single layer ACSR conductors.

- **The Development of the Integrated Model**

The Integrated Model comprises an electromagnetic model, a mechanical model, a heat transfer thermal model, and a radial conduction model. The contribution to the

Integrated Model utilizes the four individual models which have been developed further to adapt to single layer ACSR conductors. Successful combination of the developed models into this Integrated Model is also a contribution in this research.

In the electromagnetic model, the classical algorithm [6] was not good enough to express the electromagnetic properties for single layer ACSR conductors because it did not consider eddy current loss in the aluminum layer. The additional loss caused by the eddy current is identified in the aluminum layer and investigated through the solution of a partial differential equation [7]. The calculation takes consideration of the helical lay length, temperature variation, magnetic characteristics, and frequency variation at power frequencies, etc.

For the mechanical model, this research analyzes the interactions among the horizontal tension, tensile strength, strain, stress, and sag for single layer ACSR conductors. The elongation of the conductor, caused by creep, cold work during stranding, conductor temperature, and the material characteristics are discussed. The stress decreases and sag increases with an increase of current resulting from the variation of elongation. The criteria and algorithm in the mechanical model are changed correspondingly to accommodate situations for single layer conductors experiencing large stress in aluminum wires. The birdcaging phenomenon is also considered for single layer ACSR conductors.

The radial conduction model and thermal model involving layers are modified to adapt to single layer ACSR as well. The Integrated Model can be used to predict the operational behavior of single layer ACSR conductors at various conditions. To simulate indoor conductors, both natural convection and buoyancy effects should be taken into consideration within the Integrated Model. Surface roughness caused by the conductor helical strands is also necessarily considered at the same time.

- **The Design and Performance of Physical Experimental Model**

A comprehensive physical experiment has been designed and performed in this research on three types of single layer ACSR conductors coded as Guinea, Penguin, and Raven. Electromagnetic and thermal properties of aluminum and steel are measured under various mechanical conditions. A birdcaged cable was involved to check how the steel properties vary after birdcaging. The measured relative permeability of the steel core was compared with that of three-layer ACSR [8]. Experimental resistivity of an aluminum wire was measured through a carefully designed dc experiment and compared with the standard book value [9]. As many as possible technical procedures and strategies were used in this experiment to ensure experimental results were valid and within good precision.

Barrett, Nigol, Fehervari, and Findlay [6] conducted experiments on ACSR to measure its electromagnetic properties. The single layer ACSR they used, with 19 steel wires, was from a three-layer conductor with two aluminum layers removed. Rong [10] performed physical experiments on a complete single layer conductor, but only on Guinea conductor, with naturally decreased tension as an increase of conductor current.

- **The Development of Artificial Neural Network Model and Load Forecasting**

This research has resulted in the development of an artificial neural network model, which is trained by Levenberg-Marquardt optimization algorithm. The non-linear functional mapping in the neural network was achieved using sigmoidal activation functions. System identification and statistical techniques have been discussed and exploited as well to build and validate this neural network model. Many modeling techniques are involved in this research such as pre-processing and post-processing of the dataset; division of training, testing, and forecasting sub-dataset; improvement of the convergence rate and weight updating; neural network topology selection; adaptive parameters optimization; etc.

Hourly load demands in Ontario have been successfully forecasted through an implementation of this artificial neural network model. Accurate and reliable load forecasting is necessary to ameliorate energy management.

- **The Discussion and Prediction of Mechanical Properties of Single Layer ACSR**

With combination of the Integrated Model and the neural network model, the mechanical properties were analyzed and predicted and the contributions focus on

- The relationship among mechanical properties including strain, stress, horizontal tension, sag, loss of tensile strength of the aluminum layer due to annealing, etc.
- The variation of mechanical properties with the time of duration from year 1 to year 50
- The variation of mechanical properties with actual daily demands in Ontario after conductor 55 years service life
- Prediction of mechanical properties with actual daily loads after conductor 55 years duration

1.5 Thesis Outline

The outline of this thesis is as follows.

The second chapter describes the development of the Integrated Model. In the context of this thesis, it plays a key role since the subsequent chapters are all related to this Integrated Model. Four individual models: the electromagnetic model, the mechanical model, the heat transfer thermal model, and the radial conduction model are sketched in detail in this chapter.

The third chapter focuses on the physical experimental model. Apparatus used in this experiment are depicted such as steel testing frame, single layer conductors, probes, instruments to measure voltage and current, thermocouples, and Data Logger to measure temperature, etc. The procedure and practical skills for the experiment are also involved. The measurement of aluminum resistivity with dc source is given in this chapter as well as experimental data processing and error analysis. Some experimental results with error bound analysis are shown at the end of this chapter.

Since the experiment is designed to compare and validate the Integrated Model, some results from the experiment and from the simulation are compared and discussed in the fourth chapter. The comparison includes ac resistance, ac/dc resistance ratio, ac reactance, current density in the aluminum layer, and complex relative permeability in the steel core. This chapter draws a conclusion that the Integrated Model is reasonably acceptable. Then, thermal and mechanical properties can be obtained from the Integrated Model for single layer ACSR conductors. Thermal properties include resistive heating, convective cooling, and radiative cooling. Mechanical properties include stress of the aluminum layer, horizontal tension, sag, and the loss of tensile strength of the aluminum layer.

Chapter 5 deals with the investigation of the Integrated Model. The investigations include effects of lay length, ambient temperature, supply frequency, conductor exposure time, air gap thickness, and span length, etc. These analyses focus on conductor electrical properties and mechanical properties. The Integrated Model suitable for single layer ACSR allows a designer or manufacturer to analyze conductors in advance before improvements are attempted.

In Chapter 6 a sensitivity analysis is performed on such input parameters as lay length of the aluminum layer, wire diameter of an aluminum strand, resistivity of aluminum, resistivity of steel, permeability, frequency, and surface layer temperature. AC resistance, ac reactance, convection heat loss, and radiation heat loss are chosen as the output parameters. The sensitivity level of these parameters is summarized in this chapter.

Chapter 7 introduces the modeling procedure for an artificial neural network and its implementation. System identification and statistical techniques are involved to build and validate this model and the Levenberg-Marquardt algorithm is used to train this model. Hourly load demands in Ontario are successfully forecasted through an implementation of this neural network model.

Mechanical properties of single layer ACSR are discussed and predicted in Chapter 8 on a sample conductor "Guinea". Both the Integrated Model and the neural network model are used to analyze and forecast the creep strain and sag under various conditions. The significance to predict the creep strain of ACSR conductors lies in power system safety because power failure might be avoided with limitation of the creep strain, especially in stormy weather.

Conclusions are drawn in Chapter 9 for the Integrated Model, the physical experimental model, the neural network model, their investigations, and implementations. Directions and suggestions for further research are also given in this chapter.

CHAPTER 2
INTEGRATED MODEL

2.1 Overview

Chapter 2 introduces the development of the Integrated Model and its components. Information provided in this chapter lays the foundation to understand analytical procedures for single layer ACSR conductors for their electromagnetic, mechanical, thermal, and radial conduction characteristics. This chapter is a key point in this research and the following chapters are more or less related to the Integrated Model: its validation, its investigation, its sensitivity analysis, and its applications.

As described in Chapter 1, the Integrated Model, which is for single layer ACSR conductors, is based on the Unified Model developed by Filipovic-Gledja [4, 5]. The difference between the Unified Model and the Integrated Model roots in separate models and will be described in this chapter.

Zhang [8] measured the complex relative magnetic permeability of the steel core of a three-layer ACSR as a function of magnetic field strength, tensile stress, and conductor temperature. Zhang's experimental permeability data is necessary and a great support to accurately analyze ACSR conductors in model simulation. The Unified Model was initially programmed in Matlab language and Xue [11] improved this model in C/C++ language by significantly reducing execution time and by combining Zhang's experimental findings in it. Brocilo [12] modified the Unified Model by developing a multi-section lines algorithm for sag calculation, adding more accurate results for the complex permeability through a spline method, and improving the thermal radial temperature model. The Unified Model and its successive improvement and modification are mainly for three layer ACSR conductors.

Figure 2.1 shows that the Integrated Model comprises four separate models together for single layer ACSR conductors: the mechanical model, the electromagnetic model, the heat transfer thermal model, and the radial conduction model. The inputs for the Integrated Model consist of all inputs of the four models. Some output variables of one model are the input variables of some other models. In the Integrated Model, the coupling variables which meet the requirements of both the mutual dependencies between two models and each individual model must be computed in Figure 2.1. In order to combine the four experimentally verified models into the Integrated Model, each of them has been developed further to adapt to single layer ACSR conductors.

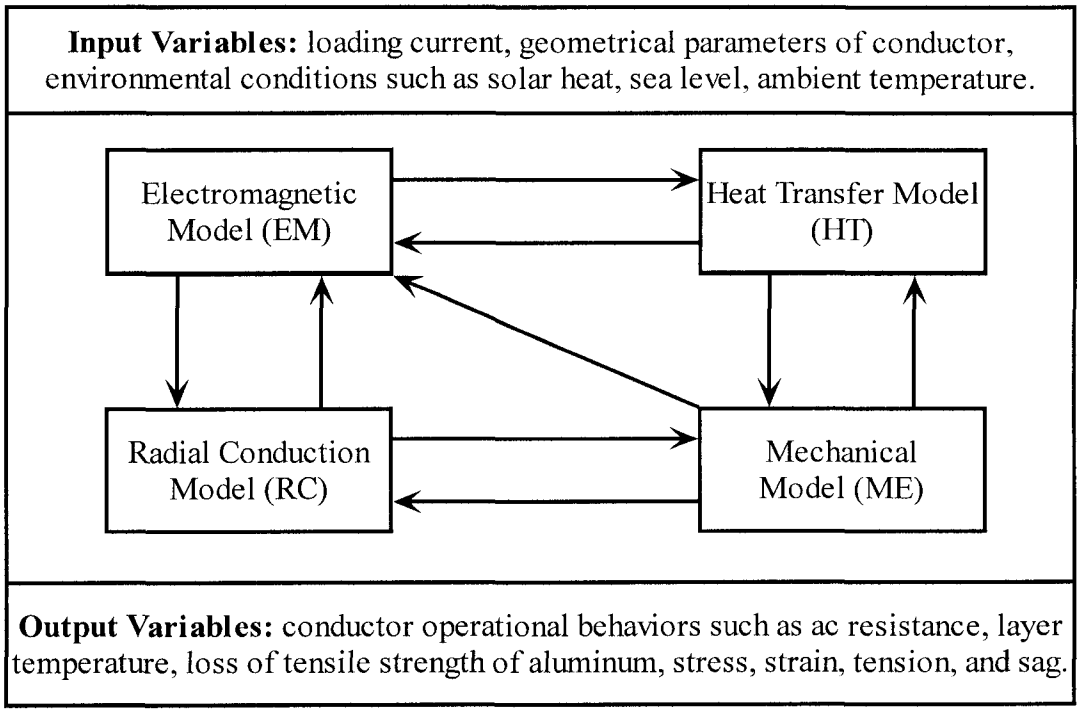

Figure 2.1 Integrated Model for single layer ACSR conductors

Both deterministic and probabilistic algorithms are used in conjunction with the Integrated Model. With the probability-based algorithm, conductor loading and thermal history can be applied to obtain operational behaviors of single layer ACSR. Accurate calculation of mechanical properties such as strain and sag is greatly related to the load history. Probabilistic algorithm also makes it possible in the Integrated Model the statistical distribution of the actual temperatures of the conductor over exposure period based on the statistical variation of atmospheric parameters.

An interactive and friendly interface of the Integrated Model has been developed in this research and it is very convenient and helpful for the designer and manufacturer to use.

2.2 Mechanical Model

The maximum load capacity of ACSR is greatly determined by its electromagnetic, mechanical, and thermal characteristics. The purpose of ampacity ratings is to ensure the lines operating within designed sags, to estimate the loss of tensile strength of aluminum, and to limit the elevated temperature creep of conductors. The mechanical properties of ACSR have been studied from practical and theoretical aspects for over fifty years [6, 13-17].

The basic principle and formulae to describe the mechanical properties is the same in the Unified Model and in the Integrated Model because of the nature of ACSR conductors. Since stress is a significant factor in single layer ACSR conductors, which

also experience larger stress than those in three-layer ACSR, some criteria and algorithms in the mechanical model are greatly modified from the Unified Model to the Integrated Model.

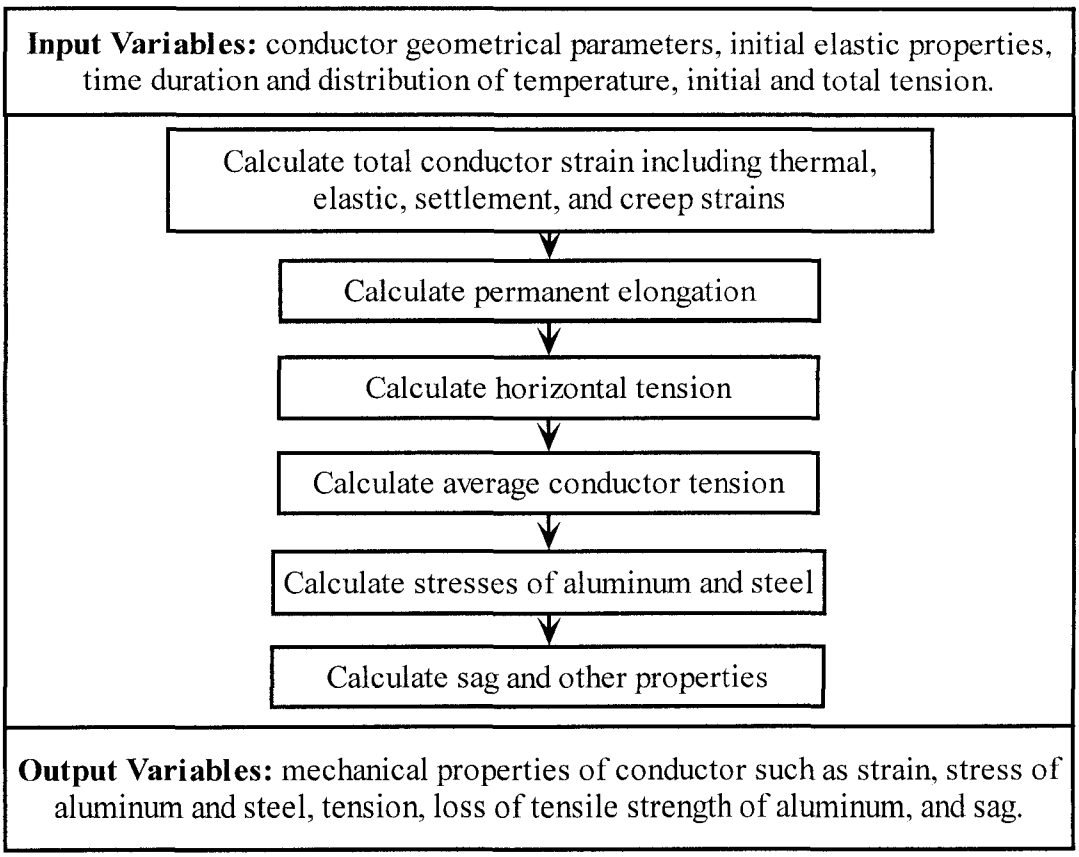

Figure 2.2 Mechanical model embedded in the Integrated Model

The input variables, output variables and flowchart of the mechanical model embedded in the Integrated Model are shown in Figure 2.2. The temperatures of aluminum and steel come out of the radial conduction model and work as input for the mechanical model. From layer temperatures and load history, the total strain of the steel and aluminum can be derived. Elongation of the conductor can be calculated with the strain. Then, the horizontal tension and average tension can be obtained from the elongation data. Finally, the sag results from the tension calculation in the mechanical model. Since the parameters of the different models affect each other, an iterative calculation needs to be exploited to obtain the steady state operational characteristics of single layer ACSR in the Integrated Model.

In detailed calculation, the following equations are involved:
The strain is the summation of the four [14] as listed in Figure 2.2:
Total Strain = Thermal Strain + Elastic Strain + Settling Strain + Creep Strain

The thermal elongation strains for steel DT_{st} and for aluminum DT_{al} are functions of the temperature of steel T_{st} and aluminum T_{al}, respectively, and described by the combination of a linear and a quadratic term for each: [14]

$$DT_{st} = \left[11.3(T_{st} - 20) + 0.008\left(T_{st}^{\,2} - 400\right)\right] \times 10^{-6} \quad \text{m/m} \tag{2.1}$$

$$DT_{al} = \left[22.8(T_{al} - 20) + 0.009\left(T_{al}^{\,2} - 400\right)\right] \times 10^{-6} \quad \text{m/m} \tag{2.2}$$

The stress-strain curves of the conductor vary with the increasing load and duration time. The elastic moduli of the steel and aluminum are obtained from the "final" curves of stress-strain curves for each conductor. Barrett [15] chooses the elastic moduli to represent the steel and aluminum components of ACSR for optimization purposes given by:

$E_{st} = 190000$ MPa

$E_{al} = 55000$ MPa

The elastic strain is obtained by the axial stress over the modulus.

Barrett [15] also gives the common initial one hour stress-strain curves for steel and aluminum:

$$ST_{st} = 5.75 \times 10^{-6} \sigma_{st} + 9.7 \times 10^{-22} \sigma_{st}^{\,6} \quad \text{m/m} \tag{2.3}$$

$$ST_{al} = 3.1 \times 10^{-5} \sigma_{al} + 2.5 \times 10^{-16} \sigma_{al}^{\,6} \quad \text{m/m} \tag{2.4}$$

where σ_{st} and σ_{al} are the steel and aluminum axial stresses in MPa.

The creep strain CRP is the plastic deformation of the wire materials under a given stress. The creep is the consequence of the change of the internal molecular structure of the material when it is exposed to a mechanical tension over time. Barrett *et al* [14, 15] gives creep strains to the 1350-H19 aluminum and to the "160-grade" steel as follows:

$$CRP_{st} = 7.0 \times 10^{-18} e^{0.02(T_{st}-20)} \sigma_{st}^{\,4.7} t^{0.13} \quad \text{m/m} \tag{2.5}$$

$$CRP_{al} = 9.0 \times 10^{-6} e^{0.03(T_{al}-20)} \sigma_{al}^{\,1.3} t^{0.2} \quad \text{m/m} \tag{2.6}$$

where t is the time in years.

Using the stress in the steel core as the reference parameter, the sags of ACSR conductors can be calculated by the following set of equations provided by Nigol and Barrett [16].

The average conductor tension P is given by:

$$P = A_{st}\sigma_{st} + A_{al}\sigma_{al} \quad \text{N} \tag{2.7}$$

where A_{st} and A_{al} are the steel and aluminum cross-sectional areas in m^2.

Similarly, the horizontal tension H can be obtained from the average tension:

$$H = P\left[1 - \frac{1}{3}\left(\frac{BW}{P}\right)^2\right] \quad \text{N} \tag{2.8}$$

Where B is half of the span in m; W is the conductor weight per unit length in N/m.

The conductor length L can be obtained as the following in m:

$$L = 2\frac{H}{W}\sinh\left(\frac{BW}{H}\right) \quad \text{m} \tag{2.9}$$

$$L = L_0(1 + strain) \quad \text{m} \tag{2.10}$$

where L_0 is the unstressed conductor length at room temperature in m.
The sag D in m:

$$D = \frac{H}{W}\left[\cosh\left(\frac{BH}{W}\right) - 1\right] \quad \text{m} \tag{2.11}$$

Birdcaging phenomenon should be mentioned because it occurs on single layer ACSR frequently. The aluminum and steel have different thermal expansion coefficient and the aluminum experiences compressive load when its elongation is longer than that of steel since they are clapped together in ACSR. The aluminum wires will move radially away from the steel wires to accommodate excess stress at some elevated temperature which is "birdcaging temperature". Birdcaging results in extra sag increase. Nigol and Barrett [16] showed aluminum wires can support 6 MPa to 12 MPa compressive stresses. They measured stress-strain curve on ACSR conductor and 3.43 m of excess residual sag was produced by 70 % RTS loading in 300 m span. Among the excess sag, 1.86 m was from unavoidable elastic elongation of steel; 0.28 m was due to 6 MPa aluminum compressive stress; and 1.29 m was due to permanent elongation of the steel core. Single layer conductors have the thinnest steel core and they are vulnerable of compressive stresses and to birdcaging.

Besides compressive load, loss of tensile strength is another result from conductor elongation. The strength of a material from an engineering standpoint can be stated as the maximum stress that can be applied safely in use without inducing failure. During the drawing process the ACSR conductors are made, the wires are severely deformed through cold work and energy is stored in the form of defects. Plastic deformation is caused by the stored energy and the strained structures recover and return to their unstrained condition through two ways: resoftening and recrystallization [18]. Both of these mechanisms depend on the use of thermal energy to relieve the lattice distortion or release the energy stored in the structure by the working operation. Resoftening is a recovery process in which thermal energy is used to permit the stored strain energy to diffuse out of the structure. During resoftening process, the recovery is a function of time and temperature. In recrystallization, a strained portion of the crystal nucleates a new and unstrained site, generally at the points of highest stress. In the recovery process, the hardness and tensile strength decrease due to annealing.

The calculation of the loss of tensile strength is embedded in the mechanical model. The steel wires in ACSR conductors do not lose strength by annealing at temperature up to 250 °C. The loss of tensile strength W of aluminum is given: [19]

$$W = W_a\{1 - \exp[-\exp(A' + (B'/T^*)\ln t + C'/T^* + D'\ln(R/80))]\} \quad \% \tag{2.12}$$

where T^* is the absolute temperature in K; t is the time duration in hours; W_a is the percentage loss of the strength in the fully-annealed state, for aluminum, W_a = 56 %; A', B', C', and D' are constants related to conductor material; R is percentage reduction in cross-sectional area during wire drawing.

2.3 Electromagnetic Model

Electromagnetic properties, especially ac resistance, of ACSR conductors have been studied for many years as stated in Chapter 1. One of the main objectives in this research is to predict electromagnetic properties as accurately as possible for single layer ACSR conductors.

In the Integrated Model, the input variables of the electromagnetic model are the geometrical parameter, the electrical and magnetic properties of the conductor, the total current, and the layer temperature. The output variables of the electromagnetic model are the complex layer currents, the resistive or Joule heating, the ac resistance, and ac reactance.

AC resistance has higher value than dc resistance in ACSR because of the spiraling effect, skin effect, proximity effect, transformer effect, and steel core losses. For solid conductors, skin effect and proximity effect are considered in ac resistance based on dc resistance. For stranded conductors, the spiraling of the strands introduces inductive effects in addition to the skin and proximity effects. For ACSR conductors, steel core losses are added based on the spiraling effect, skin effect, and proximity effect. The ac resistance of ACSR conductors is traditionally based on the assumption that the conductor is a hollow solid tube with the inner diameter equal to the diameter of the steel core. The dc resistance at the temperature of the conductor is then corrected for the skin and proximity effect. For single layer ACSR conductors, ac resistance is usually obtained from tables and curves that show test results at various load currents [9].

As will be seen, eddy current loss is appreciable in the increase of ac resistance over dc resistance for single layer ACSR conductors. The Unified Model considers current redistribution caused by transformer effect and hysteresis loss, without any consideration of eddy current loss. The Integrated Model involves eddy current loss, hysteresis loss, skin effect, spiralling effect, and transformer effect to predict ac resistance of single layer ACSR conductors. The electromagnetic models in the Unified Model and in the Integrated Model are different.

Since all considerations of ac resistance are based on dc resistance, dc resistance of ACSR conductors is discussed in the first place.

- **DC Resistance of ACSR Conductors**

The dc resistance, R can be expressed by [9, 20]:

$$R = \rho(T)\frac{L}{A} \quad \Omega \tag{2.13}$$

where A is the cross-sectional area of the conductor in m^2; L is the length in m; ρ is the dc resistivity at temperature, T in Ω·m.

It is customary to find the conductor resistance from a known resistance at a standard temperature of 20 °C. Over a moderate temperature range (0 °C to 120 °C) the resistance of a conductor increases linearly with increase of temperature, and can be calculated by

$$R = R_{20^\circ C}[1+\alpha(T-T_{20^\circ C})] \quad \Omega \tag{2.14}$$

where $R_{20°C}$ is the resistance at temperature 20 °C; and α is the temperature coefficient of resistance at 20 °C.

Morgan [21] proved the linearity of the variation with temperature of the dc resistance of ACSR. In stranded ACSR conductors, conductances of the aluminum layers and of the steel layers should be calculated separately as the following [22].

The conductance of the steel core is

$$\frac{1}{R_{st}} = \frac{\pi d_{st}^{\,2}}{4\rho_{st}}\left(1+\sum_{1}^{m}\frac{6m}{K_{stm}}\right) \quad \text{S} \tag{2.15}$$

and $K_{stm} = \sqrt{1+\left(\frac{\pi d_{st}}{l_m}\right)^2}$

in which d_{st} is the diameter of the steel core in m; ρ_{st} is the resistivity of steel in Ω·m; K_{stm} is the length factor of the wire in layer m, and l_m is the lay length of wires in layer m.

The conductance of each layer m of the aluminum wires is

$$\frac{1}{R_{alm}} = \frac{\pi d_{al}^{\,2} n_{alm}}{4\rho_{al} K_{alm}} \quad \text{S} \tag{2.16}$$

and $K_{alm} = \sqrt{1+\left(\frac{\pi d_{al}}{l_m}\right)^2}$

in which d_{al} is the diameter of an aluminum wire in m; ρ_{al} is the resistivity of aluminum in Ω·m; n_{alm} is the number of wires in layer m, and K_{alm} is the length factor for the m^{th} layer of aluminum.

The total dc resistance R of the conductor can be found from

$$\frac{1}{R} = \frac{1}{R_{st}} + \sum_{1}^{m}\frac{1}{R_{alm}} \quad \text{S} \tag{2.17}$$

- **Additional Resistance Caused by the Eddy Current in ACSR**

Due to the geometrical structure of ACSR, there is circular flux and longitudinal flux in the steel core. The longitudinal flux causes hysteresis and eddy current losses in the steel core and current redistribution in the aluminum layer. Findlay and his coauthors [6, 7] contributed the investigation of the losses caused by the steel core.

Findlay and Jones [7] presented the circuit lumped parameter model to calculate the additional resistance caused by the eddy current in the steel core. A magnetic circuit model for single layer ACSR is shown in Figure 2.3 (a). The conductor is assumed to consist of a loop, which is a partially dotted line and excited by a primary source of magnetomotive force, F_0 associated with the field due to the spiraling aluminum layer. F_1 is the magnetomotive force associated with the eddy current in the steel core. Since the induced current in the steel core must be opposite to the magnetic field, the

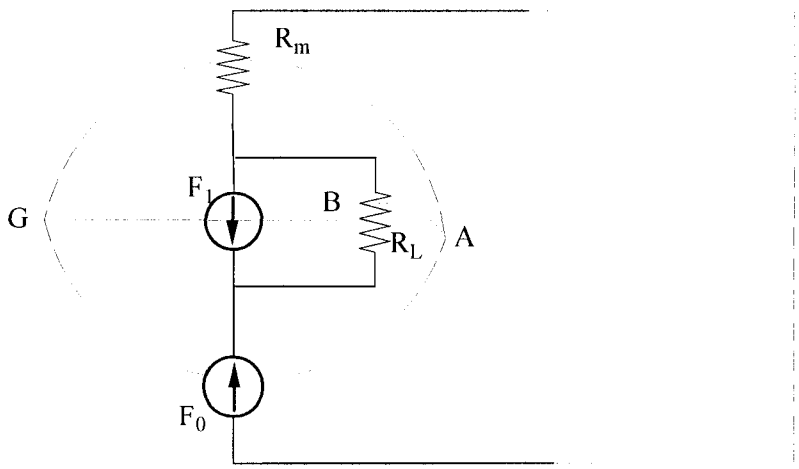

(a) A model for a single layer ACSR magnetic circuit

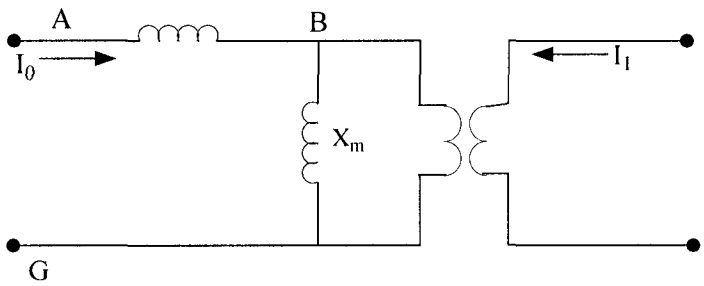

(b) Electrical dual for model of (a)

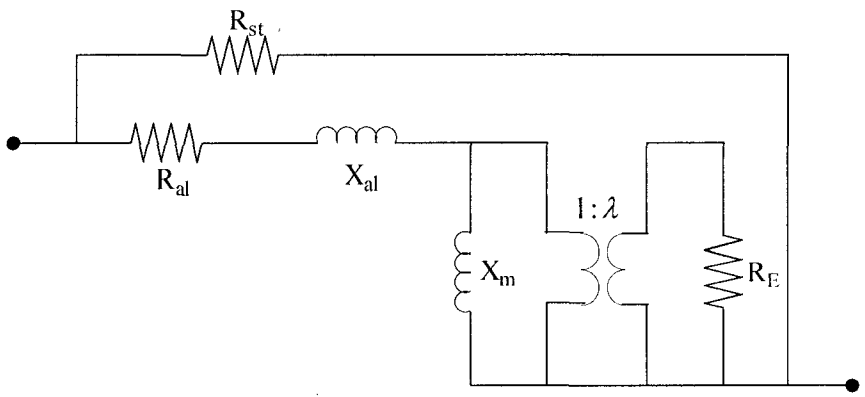

(c) Complete lumped parameter model for single layer ACSR conductor

Figure 2.3 Lumped parameter algorithm for single layer ACSR [7]

magnetomotive force, F_1 is oppositely directed to that of the aluminum layer. R_m is the reluctance in the steel core magnetic circuit. R_L is the reluctance associated with the leakage flux in the air gap between the aluminum layer and the steel core. In Figure 2.3 (b), the reference nodes such as A, B, and G are used to obtain the equivalent electric circuit by taking the electrical paths through the magnetic circuit elements. An ideal transformer element is included in the electrical equivalent. Figure 2.3 (c) shows the

complete lumped parameter model for single layer ACSR conductors. Besides ac resistance of the aluminum and steel strands, the core loss is identified to the aluminum layer through the transformer.

The ac resistance of the aluminum layer R_{al} in Figure 2.3 (c) can be calculated based on its resistivity:

$$R_{al} = \frac{\lambda_h}{\lambda_{al}} \cdot \frac{\rho_{al}}{A_{al}} \quad \Omega/\mathrm{m}$$

where λ_h is the helical lay length of the aluminum layer in m; λ_{al} is the straight lay length of the aluminum layer in m. Similarly, the steel core ac resistance R_{st} is calculated as

$$R_{st} = \frac{\rho_{st}}{A_{st}} \quad \Omega/\mathrm{m} \tag{2.18}$$

If a single layer ACSR conductor is assumed to be a very long cylinder of solid conducting material, its field equation satisfies

$$\nabla^2 H = \sigma\mu \frac{\partial H}{\partial t} \tag{2.19}$$

where σ is the conductivity of the material in S/m and μ is the permeability in H/m.
The above equation is obtained by reducing Maxwell's equations to a quasi-linear approach and ignoring the displacement current. Assuming μ is a single-valued function of H which varies only in the radial direction, and in a homogeneous, isotropic, and linear medium, the partial differential equation can be converted in cylindrical coordinates as

$$\frac{1}{r}\frac{\partial}{\partial r}\left(r\frac{\partial H_z}{\partial r}\right) = \mu\sigma\frac{\partial H_z}{\partial t} \tag{2.20}$$

If the harmonics are separable and the fundamental component is substantially greater than the losses due to other components, the equation can be simplified in phasor form, approximately, as:

$$\frac{1}{r}\frac{\partial}{\partial r}\left(r\frac{\partial H_z}{\partial r}\right) = j\omega\mu\sigma H_z \tag{2.21}$$

The equation results in a solution [23]

$$H_z(r) = H_m \frac{ber(kr) + jbei(kr)}{ber(ka) + jbei(ka)} \quad \mathrm{A/m} \tag{2.22}$$

where H_m is the magnitude of the field strength in A/m at conductor radius a; k is a function of frequency ω, conductivity σ, and permeability μ of the material, the factor $k = \sqrt{\omega\mu\sigma}$; *ber* and *bei* are Kelvin functions of zero order obtained from modified Bessel functions.

The current density can be obtained from:

$$J(kr) = kH_m \frac{ber'(kr) + jbei'(kr)}{ber(ka) + jbei(ka)} \quad \mathrm{A/m^2} \tag{2.23}$$

where *ber'* and *bei'* are the first derivative of the Kelvin function.

The power dissipation is shown as follows [7]

$$P = \frac{2\sqrt{2}}{\delta}\pi a \rho_{st} H_m^{\,2} \frac{ber(ka)ber'(ka)+bei(ka)bei'(ka)}{ber^2(ka)+bei^2(ka)} \quad \text{W} \tag{2.24}$$

where δ is the penetration depth in m.

The additional component of resistance can be obtained by separating the resistive component from the power dissipation: [7]

$$R_{eddy} = \frac{2\pi ka}{\lambda_{al}^{\,2}} \rho_{st} \frac{ber(ka)ber'(ka)+bei(ka)bei'(ka)}{ber^2(ka)+bei^2(ka)} \quad \Omega/\text{m} \tag{2.25}$$

R_{eddy} reflects the additional resistive component in Figure 2.3 (c).

- **Modified Classical Electromagnetic Algorithm**

Figure 2.4 shows the classical electromagnetic model for single layer ACSR conductors. This model was presented by Barrett, Nigol, Fehervari, and Findlay [6] in 1986. This model, like Morgan's [24], considered the resistance in each layer including the steel core, inductances caused by longitudinal flux and inductances caused by circular flux. The longitudinal inductance of the steel core is too small to significantly alter the current distribution in the aluminum layer and can be ignored in Figure 2.4.

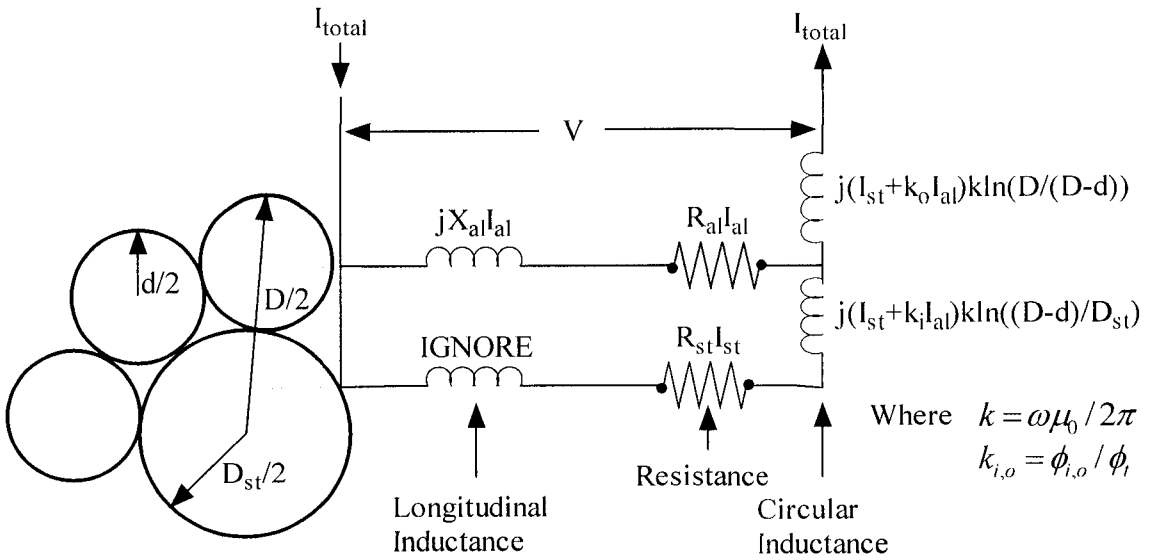

Figure 2.4 Classical electromagnetic model for single layer ACSR [6]

The magnetic field strength can be calculated from the current in the aluminum strands and the lay length. The resultant longitudinal flux is

$$\Psi = \mu_0 \left[\mu_r A_{st} + \frac{\pi}{4}(D-d_{al})^2 - A_{st} \right] \cdot \frac{I_{al}}{\lambda_{al}} \quad \text{Wb} \tag{2.26}$$

where μ_r is the relative permeability in the steel core (unitless); μ_0 is the permeability in free space ($\mu_0 = 4\pi * 10^{-7}$ H/m); D is the diameter of the complete conductor in m.

The self reactance of the aluminum layer X_{al} is given by

$$X_{al} = \frac{\omega\mu_0\left[\mu_r A_{st} + \left(\pi(D-d_{al})^2/4 - A_{st}\right)\right]}{\lambda_{al}^{\ 2}} \quad \Omega \tag{2.27}$$

where ω is the angular frequency in rad/s. The complex relative permeability μ_r used here makes self reactance partially resistive. Through the use of complex relative permeability, part of the core losses is included in this classical electromagnetic model. The complex relative permeability is a nonlinear function of temperature, tensile stress, and magnetic field strength. The experimental complex permeability data conducted by Morgan, Zhang, and Findlay [8, 25] are a great support to both the Unified Model and the Integrated Model.

Considering the skin effect, the circular flux distributes as

$$\Psi_{inner} = \frac{\mu_0(I_{st} + k_i I_{al})}{2\pi} \ln\frac{D-d_{al}}{D_{st}} \quad \text{Wb} \tag{2.28}$$

$$\Psi_{outer} = \frac{\mu_0(I_{st} + k_o I_{al})}{2\pi} \ln\frac{D}{D-d_{al}} \quad \text{Wb} \tag{2.29}$$

This classical electromagnetic model works fine for three-layer ACSR and double layer ACSR. Barrett et al. [6] state that this model has been developed and verified for single, two, and three layer conductors. They also state that current redistribution was found to be far more important in determining the ac/dc resistance ratio than hysteresis losses in the steel core, except in single layer conductors. According to their experiments, the measured ac/dc resistance ratio for three layer ACSR "Grackle" is less than 1.08 at 1700 A (the maximum current rating). The model predicts ac/dc resistance ratio 1.078 at 1608 A. This prediction is accurate by the comparison with the experimental value. For three layer ACSR, current redistribution accounts for 6.0 % among the 7.6 % increase of ac resistance over dc resistance while magnetic core loss only for 1.8 % [6]. Loss caused by current redistribution is far more significant than the steel core losses for three layer conductors. As will be seen in this research, steel core losses are far more important than the loss caused by current redistribution for single layer conductors.

The single layer conductor in [6] was formed by removing the outer two layers of Grackle conductor. The ac/dc resistance ratio for this single layer ACSR is only 1.25 at 400 A. There is no saturation between 100A and 500A because of 19 steel wires in their single layer ACSR. As will be seen, experiments on popularly used single layer ACSR, "Guinea", "Penguin", and "Raven" conducted by the author show that ac/dc resistance ratio is as high as 1.99 around 280 A for Guinea at its saturation point, 1.68 at 330 A for Penguin, and 1.48 at 210 A for Raven. From ac/dc resistance ratio we can estimate that this classical model underestimated ac resistance for single layer ACSR conductors. Core losses caused by the eddy current have to be considered in this classical electromagnetic model for single layer ACSR conductors. The modification in Figure 2.4 lies in that core losses are identified in the aluminum layer by applying the lumped parameter algorithm analysis.

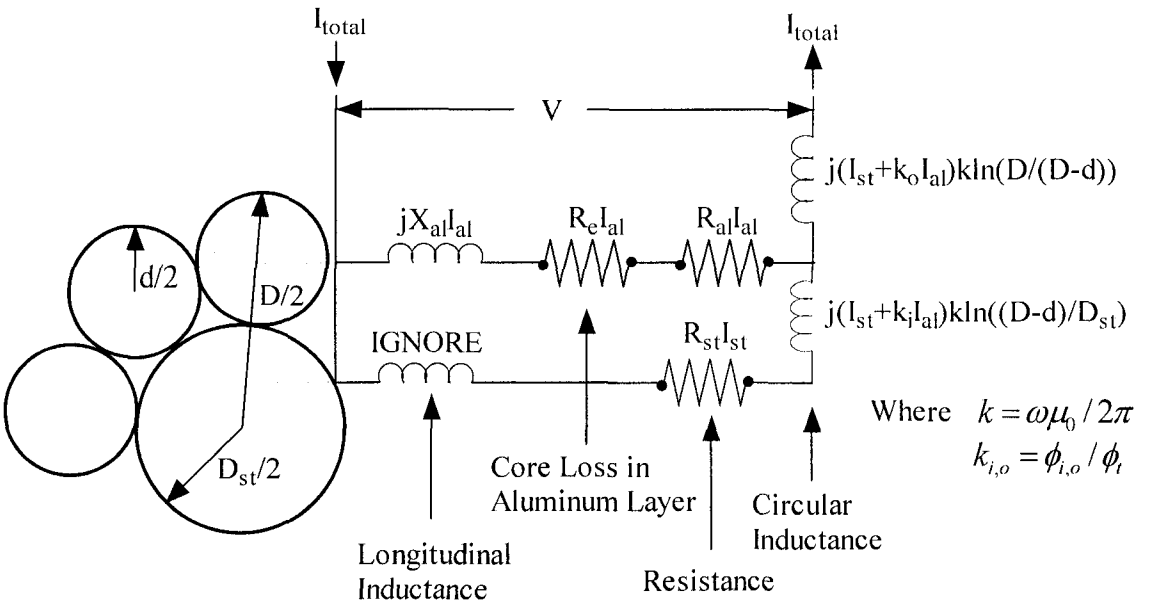

Figure 2.5 Modified classical electromagnetic model for single layer ACSR

From a simplistic viewpoint, since the voltage drop in the aluminum layer and the steel layer are the same, we can develop two equations according to Kirchhoff's voltage law. However, there are three unknowns, hence, we need another equation. The third equation is formed as the sum of the layer currents to be equal to the total current. For an approximate solution, we solve these three equations to get three complex values: current in the steel core, current in the aluminum layer, and the total voltage drop. The ac resistance and the ac reactance of conductors are the real part and imaginary part of the division of the total voltage drop and the total current, respectively. This model can be used as the stating power for iterations in the Integrated Model to obtain the steady-state operational properties of single layer ACSR conductors.

The factors k_i and k_o in the flux calculation in Figures 2.4 and 2.5 are the ratio of the magnetic flux inside the mean diameter of the aluminum wire to the total magnetic flux. They can be calculated according to the area and diameter of the aluminum wires. By applying the method of Barrett et al [6], for single layer ACSR conductors, we have 20.51 % of the layer current contributes to the inner flux of the layer, and 79.49 % contributes to the outer layer.

2.4 Heat Transfer Thermal Model

The heat transfer thermal model plays an important role in the Integrated Model and it calculates the steady-state temperature at the surface of the conductor. The steady state thermal rating is defined in IEEE standard 738 [26] as the constant electrical current that would yield the maximum allowable conductor temperature for specified weather conditions and conductor characteristics under the assumption that the conductor is in thermal equilibrium (steady state). The ampacity rating of ACSR is confined within its

thermal rating. Also in this IEEE standard, the maximum allowable conductor temperature is defined as the maximum temperature limit to minimize losses of strength, sag, line losses, or a combination of the above. Following the IEEE standard, the heat transfer model connects very tightly with the electromagnetic model and the mechanical model as shown in Figure 2.1.

Both the Integrated Model and the Unified Model are based upon steady-state heat balance equation and are developed for various environmental conditions. The Integrated Model contributes to simulate conductors in the laboratory while the Unified Model does not have this function. To simulate indoor conductors, buoyancy effect and lay angle of the conductor have to be taken into consideration.

In the Integrated Model, the input variables of the heat transfer thermal model are the geometrical parameter, total current, ac resistance and atmospheric variables, such as wind speed and its direction, the intensity of solar radiation. The output variables are heat gains, heat losses, and the surface temperature of the conductor.

Heat transfer thermal model is based on heat balance equation [22, 27]

$$P_{ele} + P_{solar} + k_{ion}P_{ion} = P_{con} + P_{rc} + P_{eva} \tag{2.30}$$

where P_{ele} is the electric resistive or Joule heating in W/m; P_{solar} is the solar heating in W/m; P_{ion} is the ionization or corona heating in W/m, k_{ion} is a heat diffusion factor; P_{con} is the convection heat loss in W/m; P_{rc} is the radiation heat loss in W/m; P_{eva} is the evaporation heat loss in W/m. The hear transfer by ionization and evaporation seldom occurs, so we usually consider

$$P_{ele} + P_{soalr} = P_{con} + P_{rc} \tag{2.31}$$

The resistive heating is calculated as $P_{ele}=I_{tot}^2 R_{ac}$, where R_{ac} is ac resistance in Ω/m corresponding to the actual surface temperature of the conductor with the total current I_{tot} in A.

2.4.1 Solar Heating

The solar heating calculation in the Integrated Model is the same as that in the Unified Model according the conductor, the Sun and the position between them. For isotropic diffuse sky radiation, the total solar heat gain received per unit length of the conductor is given by [27]

$$P_{solar} = \alpha_S D\left[I_B\left(\sin\eta + \frac{\pi}{2} F \sin H_S \cos^2\frac{\zeta}{2}\right) + \frac{\pi}{2}\cos^2\frac{\zeta}{2} I_d(1+F)\right] \quad \text{W/m} \tag{2.32}$$

where α_S is the absorptivity of the conductor surface for short wave radiation; D is the overall diameter in Figure 2.4; I_B is the intensity of the direct solar beam on a surface normal to the beam in W/m^2; η is the angle between the solar beam and the axis of the conductor in degree; F is albedo of the ground; H_S is the solar altitude in degree; ζ is the inclination to the horizontal; I_d is the intensity of the diffuse sky radiation in W/m^2.

The calculation of angle η and solar altitude H_S needs some specific environmental conditions such as geographical latitude, declination of the Sun which depends on the hour and the day of the year, the intensity of the direct solar beam above

sea level at some atmosphere, the intensity of diffuse radiation which is a function of various albedos.

When the Integrated Model is used to simulate indoor conductors, the solar heating is confined within a very small value, for example, 0.05 W/m.

2.4.2 Convective Cooling

The calculation of convective cooling is different from the Integrated Model and from the Unified Model because of augments selection which is based on geometrical parameters of ACSR.

For the fluid adjacent to the hot surface of the conductor, its density decreases, and the hot fluid rises. The convective heat transfer occurs. If there is no wind, the fluid flows upwards directly and the heat is lost by the natural convection. The natural convective flow is vertically downloads if the conductor is cooler than the fluid. When the wind blows, the fluid is carried away and the forced convection takes place. The total or mixed convection, which actually occurs in practice, occurs due to both natural and forced convection. The method for calculation of mixed convection, used in the Integrated Model, combines both natural and buoyancy effects as nominally forced convection procedures to determine the Nusselt number in this research.

The convective heat loss is given by [22, 27]

$$P_{con} = \pi Nu \lambda_f (T_{sur} - T_{amb}) \quad \text{W/m} \tag{2.33}$$

where Nu is the unitless Nusselt number; T_{sur} and T_{amb} are temperatures of the conductor surface and the ambient in °C.

Film temperature T_f is the temperature of the fluid at the surface of the conductor

$$T_f = 0.5(T_{sur} + T_{amb}) \quad ^\circ\text{C} \tag{2.34}$$

The thermal conductivity λ_f of the air at the surface of the conductor, for the temperature up to 100 °C is [20, 26]

$$\lambda_f = 2.42 \times 10^{-2} + 7.2 \times 10^{-5} T_f \quad \text{W/mK} \tag{2.35}$$

The calculation of the Nusselt number differs for natural and forced convection. The Nusselt number depends on the kinematic viscosity of the air which changes with the height above sea level. For temperatures up to 100 °C, the kinematic viscosity v_0 of air at sea level is given by

$$v_0 = 1.32 \times 10^{-5} + 9.5 \times 10^{-8} T_f \quad \text{m}^2/\text{s} \tag{2.36}$$

The kinematic viscosity v_H at the altitude H in m is

$$v_H = v_0 (1 - 6.5 \times 10^{-3} H / 288.16)^{-5.2561} \quad \text{m}^2/\text{s} \tag{2.37}$$

- **Natural Convection**

In the natural convection, the Grashof number Gr, the Prandtl number Pr, and their product, known as a Rayleigh number Gr.Pr are used to obtain the Nusselt number. All of these numbers are unitless. The Nusselt number for an isothermal horizontal cylinder in the range $10^{-10} \le Gr.\text{Pr} \le 10^{10}$ is found from [22]

$$Nu = A(Gr.\Pr)^m \tag{2.38}$$

where the coefficients A and m are given in Table 2.1.

Table 2.1 Constants for Nusselt number in natural convection [22]

Range of Gr.Pr (0.7≤Pr≤5)			
From	**To**	**A**	**m**
10^{-10}	10^{-4}	0.675	0.058
10^{-4}	10^{-1}	0.889	0.088
10^{-1}	10^{2}	1.02	0.148
10^{2}	10^{4}	0.850	0.188
10^{4}	10^{7}	0.480	0.250
10^{7}	10^{12}	0.125	0.333

The Grashof number for the conductor with diameter D is calculated from [27]

$$Gr = D^3 g(T_{sur} - T_{amb})/(T_f + 273)v_H^{\ 2} \tag{2.39}$$

where g is the acceleration due to gravity in m/s^2.

For moderate temperatures up to 100 °C, the Prandtl number is approximated by [22, 27]

$$\Pr = 0.715 - 2.5\times10^{-4} T_f \tag{2.40}$$

The Nusselt number for a conductor inclined at angle ζ (deg) to the horizontal is obtained by multiplying the Nusselt number by the factor $(\cos\zeta)^{1-3m}$, except for $\zeta \to 90^\circ$ [27].

- **Forced Convection**

The Nusselt number for a wind with velocity U, blowing normal to the axis of the stranded conductor, is given by [22]

$$Nu = 1.1C\,\mathrm{Re}^n \tag{2.41}$$

where Re is the Reynolds number [22]

$$\mathrm{Re} = UD/v_H \tag{2.42}$$

C and n are coefficients depends on Re. The values of C and n are given in Table 2.2.

Table 2.2 Constants for Reynolds number in forced convection [22]

Reynolds number, Re			
From	**To**	**C**	**n**
1×10^{-4}	4×10^{-3}	0.437	0.0895
4×10^{-3}	9×10^{-2}	0.565	0.136
9×10^{-2}	1	0.800	0.280
1	35	0.795	0.384
35	5×10^{3}	0.583	0.471
5×10^{3}	5×10^{4}	0.148	0.633
5×10^{4}	2×10^{5}	0.0208	0.814

The roughness of surface affects the convective heating in many ways. According to his experimental data, Morgan [22] states that the overall heat transfer from the stranded conductors is approximately 10 % higher than that from a smooth cylinder. The factor 1.1 in the above equation allows for this.

The angle of attack of the wind with respect to the conductor axis is not a constant. It fluctuates about a mean value ψ_{mean} in degree with standard deviation $\sigma\psi$ which depends on the terrain. The fluctuation in the wind results in an effective mean angle of attack ψ^*, higher than the following [22]

$$\psi^* = \frac{1}{\sqrt{2\pi}}\left[2(\sigma\psi)e^{-\frac{\psi_{mean}^2}{2(\sigma\psi)^2}} + \sqrt{2\pi}|\psi_{mean}|erf\left(\frac{|\psi_{mean}|}{\sqrt{2}(\sigma\psi)}\right)\right] \quad \text{deg} \qquad (2.43)$$

- **Mixed Convection**

When neither the natural convection nor the forced convection are negligible compared to one another, they are combined in a mixed convection. The Nusselt number for mixed convection is obtained from the effective Reynolds number Re_{eff}, the vectorial sum of Reynolds numbers for the natural and forced flows.

Table 2.3 Limiting constants for mixed convection [22]

Gr.Pr		Re			C_l		
From	**To**	**From**	**To**	**n/m**	**α =0°**	**α=90°**	**α=180°**
10^{-10}	10^{-2}	10^{-4}	4×10^{-3}	1.54	$.30\times10^{-3}$	$.69\times10^{-4}$	1.69×10^{-4}
		4×10^{-3}	9×10^{-2}	2.34	0.477	0.0629	8.28×10^{-3}
		9×10^{-2}	1	4.83	8.04×10^{4}	221	0.607
10^{-2}	10^{2}	4×10^{-3}	9×10^{-2}	0.919	0.0571	0.0258	0.0117
		9×10^{-2}	1	1.89	6.38	0.633	0.0628
		1	35	2.59	47.4	1.33	0.0370
10^{2}	10^{4}	9×10^{-2}	1	1.49	12.2	1.99	0.322
		1	35	2.04	59.4	3.55	0.212
		35	5×10^{3}	2.51	49.4	1.21	0.0296
10^{4}	10^{7}	1	35	1.54	232	27.9	3.35
		35	5×10^{3}	1.88	202	12.4	0.762
		5×10^{3}	5×10^{4}	2.53	7.70	0.125	2.02×10^{-3}
10^{7}	10^{12}	35	5×10^{3}	1.41	3330	411	50.6
		5×10^{3}	5×10^{4}	1.90	288	13.0	0.590
		5×10^{4}	2×10^{5}	2.44	5.91	0.0813	1.12×10^{-3}

The boundary between pure natural convection and mixed convection is stated in [22]. The limiting Grashof number Gr_{lim} is defined as that value of the Grashof number at which the total effective Nusselt number, Nu_{eff}, is 100δ% greater than the Nusselt number

corresponding to pure natural convection, Nu_N. The margin of 100 δ is usually taken to be 5 %.

$$Gr_{lim}=C_l \mathrm{Re}^{n/m} \quad (2.44)$$

Coefficients "*n/m* and C_l" are selected from Table 2.3.

Reynolds number is defined as a nondimensional number equal to air velocity times conductor diameter divided by kinematic viscosity [26]. Air velocity includes the wind velocity.

Re can be considered as a measure of the ratio of inertia to viscous forces over the cylinder [28]. When Re << 1, the inertia forces are negligible compared with the viscous forces, and the flow is potential in nature, i.e., streamlines move over the surface, leaving it at the rear stagnation point. When the stream velocity increases and the vorticity in the flow near the cylinder increases until Re ≈ 6 [29], the flow separates from the rear surface under the adverse pressure gradient. A pair of symmetrical vortices might be formed at the rear of the cylinder, and these vortices grow until they become unstable at Re ≈ 90 and develop into a system of alternating vortices, known as Karman vortex street in Figure 2.6. At high Reynolds numbers, the wake becomes irregular, and eventually the wake becomes turbulent [22].

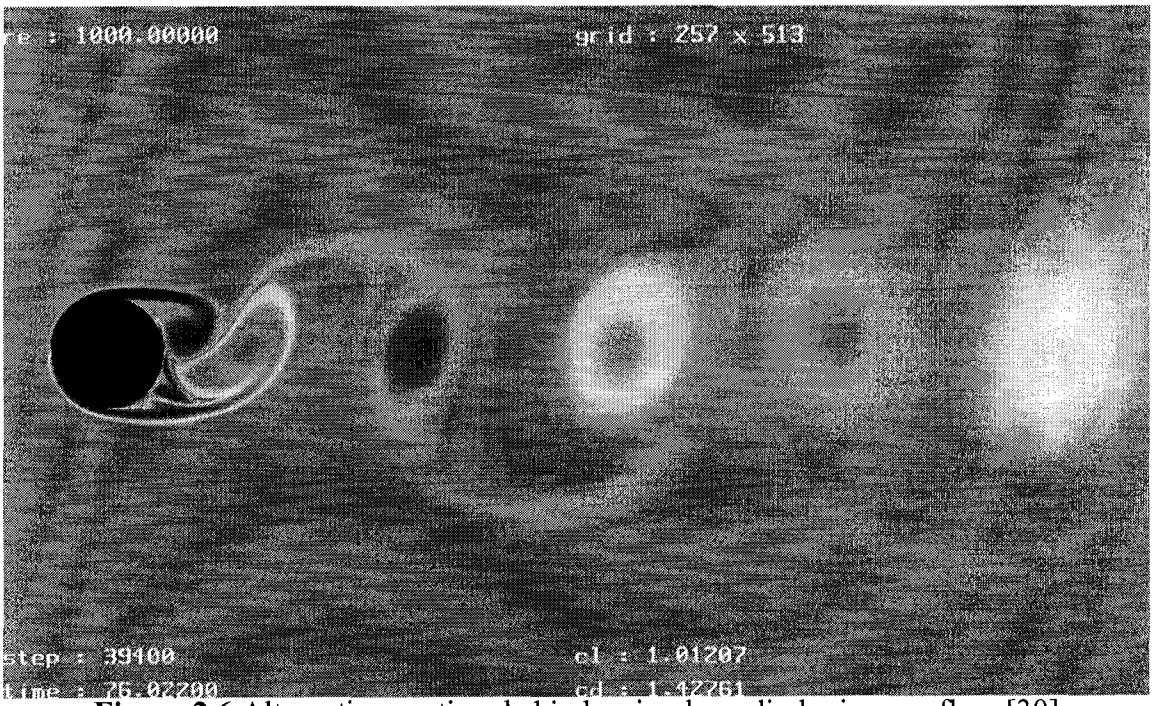

Figure 2.6 Alternating vortices behind a circular cylinder in crossflow [30]

Sometimes buoyancy effects have to be considered with nominally forced convection with large Reynolds number. The natural convective flow, acting upwards for the heated cylinders, increases the heat transfer and the increase is greater when the Grashof number becomes higher [31]. The natural convection and buoyancy effects consist of mixed convection in the Integrated Model.

Hatton et al. [32] did experiments in air flowing upwards, downwards, and in crossflow with cylinders which have diameters of 0.1, 8.13, and 12.58 mm. By equating the work done by the buoyancy force on a fluid element with the gain in kinetic energy, they derived the relationship for the equivalent Reynolds number,

$$\mathrm{Re}_{eq} = \sqrt{2Gr} \tag{2.45}$$

Using this equivalent Reynolds number for natural convection, and adding vectorially the natural and forced flow Reynolds numbers, we can obtain the effective Reynolds number for the mixed flow derived by Morgan [22] who followed Hatton [32]:

$$\mathrm{Re}_{eff} = \sqrt{(\mathrm{Re}_{eq} + \mathrm{Re}\cos\alpha)^2 + (\mathrm{Re}\sin\alpha)^2} \tag{2.46}$$

where α is the angle between the natural convection and buoyancy force. The total heat transfer is by using Re_{eff} in place of Re in Table 2.2.

Table 2.4 lists the calculation of Grashof number for Guinea, Penguin, and Raven conductors under the 100 °C surface conductor temperature and 20 °C ambient temperature. "A" and "m" are selected from Table 2.1. "n/m and C_1" are selected from Table 2.3. The limiting Grashof number for $\alpha = 90°$ is calculated in the Table 2.4 and it is the harmonic mean of the limiting Grashof numbers for $\alpha = 0°$ and $\alpha = 180°$.

Table 2.4 Calculation of the boundary between pure natural convection and mixed convection

	Gr_N	Pr	GrPr	A	m	Re_{eq}	k	n/m	C_1			Gr_{lim}
									0°	90°	180°	
Guinea	20661	0.7	14463	0.48	0.25	203.28	0.548	1.88	202	12.4	0.762	270790
Penguin	19294	0.7	13506	0.48	0.25	196.44	0.548	1.88	202	12.4	0.762	253910
Raven	6816.2	0.7	4771.3	0.85	0.188	116.76	1.93	2.51	49.4	1.21	0.0296	186930

By comparing the numbers in the Table 2.4, we can see that pure natural convection is not enough to simulate convective cooling for indoor single layer conductors. Hence we consider the mixed convection which includes the effect of spiraling on the direction of cool out.

The angle between the natural and forced convection is 90° in the Integrated Model designed for outdoor single layer ACSR conductors. The direction of natural convection is upward because of the density of the hot fluid. The outside wind direction is assumed in cross-flow or horizontal to the axis of the conductor. That is why the angle between them is 90°.

It is not the case for indoor conductors. For indoor conductors, the natural convection is still upward. Since no wind flows indoors, the nominally forced convection caused by buoyancy force is upward. Because of the lay angle of wires in the conductor, the angle between the two kinds of convection is not 90° and it should be the lay angle of the wire.

Figure 2.7 gives us some clue of the direction of the buoyancy force working on indoor conductors. The hot air at the bottom of the conductor rises upward. Its direction changes when it comes across the side surface of the conductor because of the roughness of the aluminum strands as shown in Figure 2.7. The angle between the buoyancy force

and natural convection can be calculated from the lay angle of the aluminum layer in the conductor.

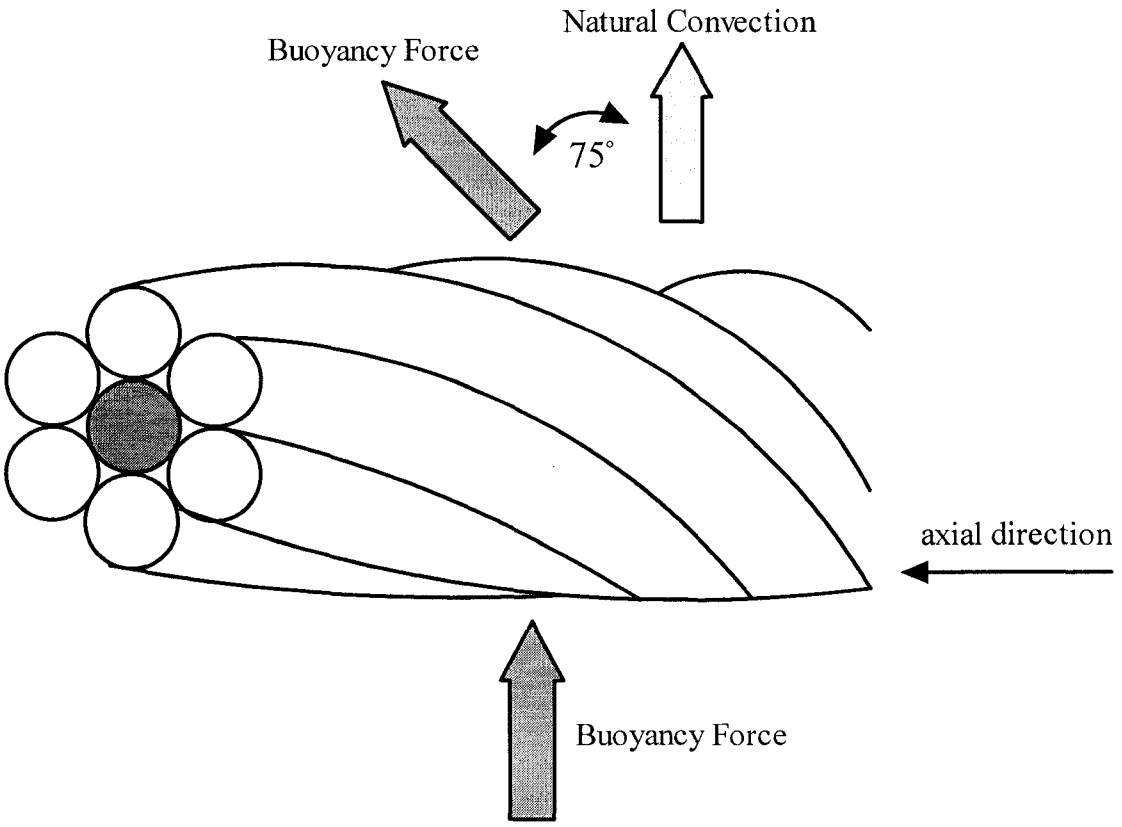

Figure 2.7 Angle between buoyancy force cooling and natural convective cooling for indoor single layer ACSR conductors

Figure 2.8 shows the lay angle γ of the aluminum layer for single layer ACSR conductors in degree; λ is the lay length of the aluminum layer in m; D is the mean diameter of the complete conductor in m.

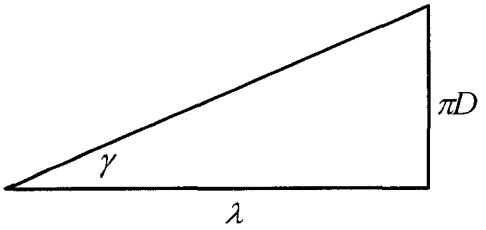

Figure 2.8 Lay angle of the aluminum layer

From Figure 2.8, we know that $\gamma = tg^{-1}\frac{\pi D}{\lambda}$. The calculation of the lay angle for Guinea, Penguin, and Raven conductors is listed in Table 2.5. The lay angle of wires for

single layer ACSR conductors is approximately 15°, and the angle between the natural convection and buoyancy force is almost $\alpha = 90° - 15° = 75°$, as shown in Figure 2.7.

Table 2.5 Calculation of the lay angle for single layer ACSR conductors

Conductor Code	Lay Length λ (cm)	Diameter D (cm)	Lay Angle γ (deg)
Guinea	17.6	1.46	14.7°
Penguin	18.6	1.43	13.6°
Raven	12.8	1.01	14.0°

2.4.3 Radiative Cooling

The radiative heat cooling P_{rc} is calculated from [22, 27], the same in the Integrated Model and in the Unified Model

$$P_{rc} = \pi D \sigma_B \varepsilon_S [(T_{sur} + 273)^4 - 0.5(T_{gr} + 273)^4 - 0.5(T_{sky} + 273)^4] \quad \text{W/m} \qquad (2.47)$$

where T_{gr} and T_{sky} in °C are ground and sky temperatures; σ_B is the Stefan-Boltzman constant (σ_B = 5.66997*10^{-8} W/m^{2}K^4); ε_S is the emissivity of the conductor, which depends on the type of metal and increases with aging and oxidation.

Since the radiative heat loss for a typical conductor does not exceed 30 % [27] of the total heat loss, the ground and sky temperatures may be approximately equated to the ambient air temperature T_{amb} in °C, and the radiative heat loss becomes

$$P_{rc} = \pi D \sigma_B \varepsilon_S [(T_{sur} + 273)^4 - (T_{amb} + 273)^4] \quad \text{W/m} \qquad (2.48)$$

2.5 Radial Conduction Model

For ACSR conductors, most of the heat is transferred by conduction through the metal to metal contacts, through the very thin air gaps and through the triangular or rectangular air voids between the layers. Radiation and convection heat transfer within the conductor can be neglected in the radial conduction model. The temperature difference between layers depends on the number of contacts and the area of each contact. Experiment [33] shows that the radial temperature difference increases with all increasing number of layers of wires, and decreases with increasing axial tension and radial pressure.

The radial conduction model calculates the radial temperature distribution within stranded conductors. The flowchart shown in Figure 2.9 is used in the Integrated Model. Both the Integrated Model and the Unified Model are using the same principle including formulas and algorithms developed by Morgan and Findlay [33]. The difference of the radial conduction model in the Unified Model and in the Integrated Model lies in the implementations which are related to the geometrical structures of ACSR conductors.

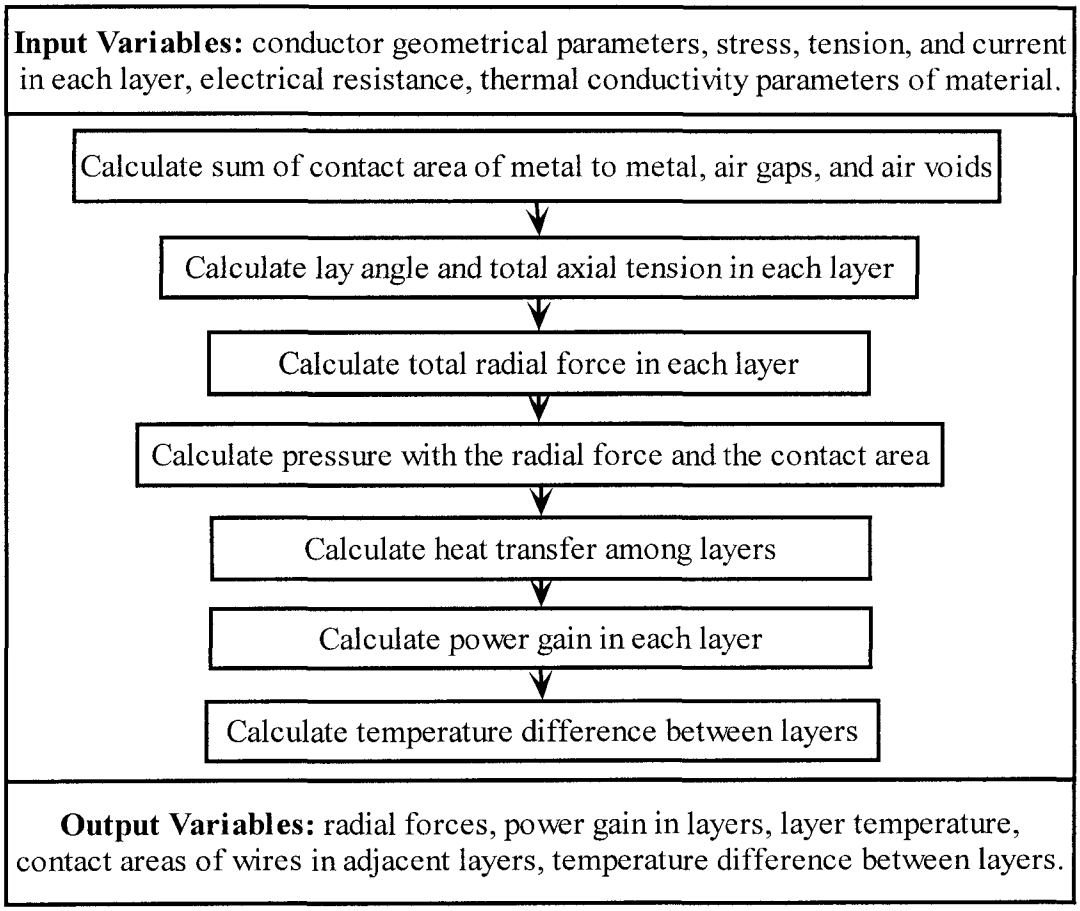

Figure 2.9 Radial conduction model embedded in the Integrated Model

If the king wire is denoted with zero, succeeding layers with numbers growing from 1, the difference between temperatures of layers n and n+1 denoted by subscript n(n+1) was given by Morgan and Findlay [33]

$$T_n - T_{n+1} = \sum_{i=0}^{n} P_i / \sum (hA)_{n(n+1)} \quad ^\circ\text{C} \tag{2.49}$$

where $\sum_{i=0}^{n} P_i$ (W/m) is the total power gain per unit of length of the conductor up to the layer and including the layer n; $\sum (hA)_{n(n+1)}$ (W/°C) is the sum of the products of the heat transfer coefficients due to the conduction h (W/m^{2}K) and contact area A (m^2) between layers n and n+1.

$$\sum (hA)_{n(n+1)} = \sum (h_m A_m)_{n(n+1)} + \sum (h_g A_g)_{n(n+1)} + \sum (h_v A_v)_{n(n+1)} \quad \text{W/°C} \tag{2.50}$$

Subscripts m, g, and v denote metal to metal contacts, air gaps and air voids respectively.

Morgan and Findlay [33] also gave the calculation of the conductive heat transfer coefficients h_m, h_g, and h_v, respectively as the following.

The conductive heat transfer coefficient for metal-metal contacts may be approximated as:

$$h_m = \frac{1.13 k_{hm} \tan\theta}{\sigma}\left[\frac{p_q}{H}\right]^{0.94} \quad \text{W/m}^2\text{K} \tag{2.51}$$

where σ in meter is the root-mean- square height of the asperities; $tan\theta$ is the mean slope of the asperities, and H in Pa is the microhardness of the softer material. The harmonic mean of the bulk thermal conductivities k_1 and k_2 of two metals in contact is given by

$$k_{hm} = 2k_1k_2/(k_1 + k_2) \quad \text{W/mK} \tag{2.52}$$

The conductive heat transfer coefficient for the air gaps between asperities is found from

$$h_g = k_g / \delta_g \quad \text{W/m}^2\text{K} \tag{2.53}$$

where k_g in W/mK is the air thermal conductivity, and δ_g in m is the effective length of the gap. For ACSR conductor, δ_g is approximately 1μm.

Similarly, the conductive heat transfer coefficient for the air voids is found from

$$h_v = k_g / \delta_v \quad \text{W/m}^2\text{K} \tag{2.54}$$

Applying hydraulic diameter, i.e., 4 (area/perimeter) of the void, for the triangular voids, the effective length of the void is given by

$$\delta_v = \left[\frac{2\sqrt{3}}{\pi} - 1\right] d = 0.1027d \quad \text{m} \tag{2.55}$$

and for the rectangular void it is given by

$$\delta_v = \left(\frac{4}{\pi} - 1\right) d = 0.2732d \quad \text{m} \tag{2.56}$$

The calculation of the radial temperature gradient is given by Morgan and Findlay [33] as the following.

The sum of the area of true metallic contacts A_m and the area of the air gaps A_g is equal to the product of the number of contacts q between wires in layers n and n+1 and apparent total area A_q of each contact.

$$A_{mn(n+1)} + A_{gn(n+1)} = q_{n(n+1)} A_{qn(n+1)} \quad \text{m}^2 \tag{2.57}$$

$$A_{vn(n+1)} = \pi d(2n+1) - q_{n(n+1)} A_{qn(n+1)} \quad \text{m}^2 \tag{2.58}$$

The total radial temperature difference for a conductor with N layers is given by

$$T_0 - T_N = \sum_{n=0}^{N-1} (T_n - T_{n+1}) \quad ^\circ\text{C} \tag{2.59}$$

The number of contacts between wires with diameter d in layers n and n+1 with lay lengths λ_n and λ_{n+1} is obtained by

$$q_{n(n+1)} = m_n^2 \left[\frac{1}{\lambda_n} + \frac{1}{\lambda_{n+1}}\right] \tag{2.60}$$

where m_n is the number of wires in layer n, and for the king wire we assume $1/\lambda_0 = 0$.

For the total axial tension T' in a conductor with N layers, the tension in layer n is given by

$$T_n' = 6nT' \cos^2 \beta_n \left[1 + \sum_{n=1}^{N} 6n \cos^3 \beta_n \right]^{-1} \quad \text{N} \tag{2.61}$$

where β_n in degree is the angle of lay of wires in layer n, and

$$\cos \beta_n = \lambda_n \left[\lambda_n^{\,2} + (\pi nd)^2 \right]^{-1/2} \tag{2.62}$$

The total radial force F_{rn} in layer n is calculated by

$$F_{rn} = T_n' \sin^2 \beta_n / nd \quad \text{N} \tag{2.63}$$

The total radial force on the wires in layer n F_{rn}' is obtained as the sum of the radial forces of all layers above the layer n

$$F_{rn}' = \sum_{i=n+1}^{N} F_{rn} \quad \text{N} \tag{2.64}$$

The radial force per contact F_{rqn} is then

$$F_{rqn} = F_{rn}' / q_{n(n+1)} \quad \text{N} \tag{2.65}$$

and the apparent area of each contact

$$A_{qn(n+1)} = F_{rqn} / f_y \quad \text{m}^2 \tag{2.66}$$

where f_y in Pa is the compressive yield stress which depends on the type of wire material. The mean pressure over apparent area p_q is found from

$$p_q = F_{rqn} / A_{qn(n+1)} \quad \text{Pa} \tag{2.67}$$

If the mean pressure over the actual total contact area $A_{tn(n+1)}$ during plastic deformation, is assumed to be equal to H, then we have

$$\frac{p_q}{H} = \frac{A_{tn(n+1)}}{A_{qn(n+1)}} \tag{2.68}$$

The ratio of the actual contact area to the apparent total contact area is found from

$$A_{tn(n+1)} / A_{qn(n+1)} = (1/2) erf[Y / \sqrt{2}\sigma] \tag{2.69}$$

where Y in m is the separation distance between the mean lines of the two surfaces in contact.

CHAPTER 3
EXPERIMENTAL MODEL

3.1 Introduction

The previous chapter introduced the development of the Integrated Model. In this chapter we describe the design and performance of a comprehensive experimental model to validate the Integrated Model. The physical experiment was conducted on three single layer ACSR conductors: Guinea with 7 steel wires and 12 aluminum wires, Penguin with a king steel wire and 6 aluminum wires, and Raven with a king wire and 6 aluminum wires. Electromagnetic properties of aluminum and steel were measured at fixed tension levels. Aluminum resistivity was also measured through a carefully designed dc experiment on a single aluminum wire removed from Penguin conductor.

Test conductors and apparatus are introduced in this chapter as well as some measuring strategies and data processing. Testing errors and their propagation are discussed and analyzed. Some experimental results such as ac resistance and the current density in the aluminum layer are given at the end of this chapter with their corresponding error bounds.

The experiment conducted by Barrett et al. [6] was on Grackle with 19 steel wires and 54 aluminum wires. By removing two aluminum layers, a "single layer conductor" with 19 steel wires was obtained. The popularly used single layer ACSR has a king wire with or without a steel layer. Compared with the practical single layer conductors, the single layer conductor used in [6] can carry stronger tension and larger current while current, tension, and sag are dominant factors to influence the operational behaviors and the remaining life of ACSR.

Rong [10] performed a physical experiment on a complete single layer ACSR Guinea, not involving ACSR which has only a single steel wire. In Rong's experiment, the tension was not kept constant during the current range. In other words, the tension was naturally decreasing with an increase of current and temperature.

3.2 Apparatus

Below, a brief summary is provided detailing the equipments used in this experiment. The apparatus include a test frame, test conductors, test probes, and measuring instruments.

Test conductors include typical types of single layer ACSR as mentioned in the beginning of this chapter. Before ACSR are used as overhead transmission and distribution conductors, they usually experience pre-tensioning procedure to stand tough conditions in practice. The pre-tensioning force, conductor temperature, and time duration depend on conductor types and individual geometrical configurations. During the stranding process the wires are left loose enough so that they tighten together and deform when force is applied. The conductor deforms permanently when subjected to tension over a period of time.

3.2.1 Description of Test Setup

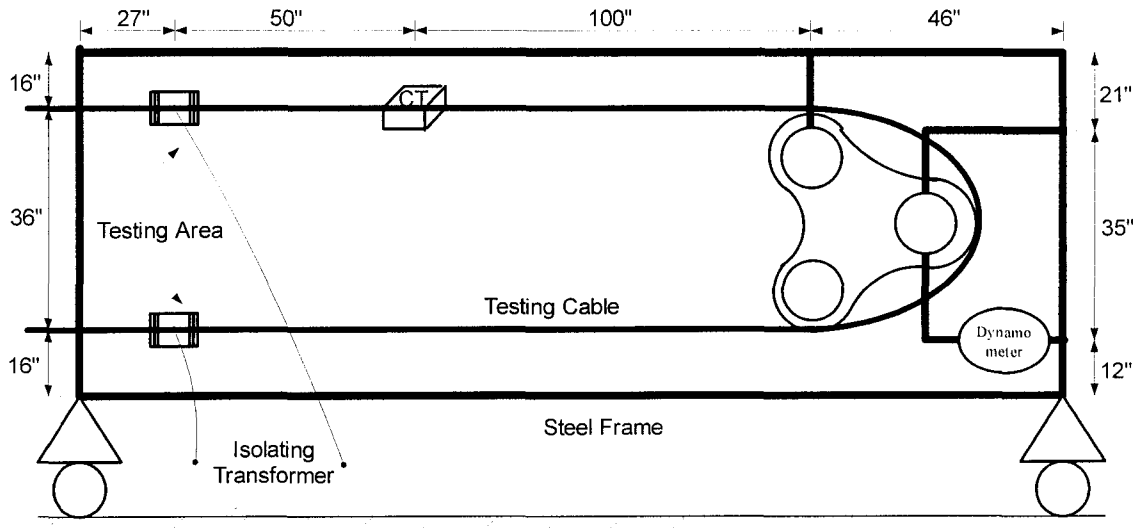

Figure 3.1 The structure of experiment frame

A specialized testing frame was built to enable the required physical experiments (shown in Figure 3.1). To test the influence of the frame, measurements were taken using an ac fluxmeter showing that the maximum deviation from the mean at 5 cm from the conductor axis was less than 4 %. We concluded that the frame had minimal effects on the cable operation [34]. The test conductor was installed on the frame with necessary insulators between the connection parts.

The dynamometer in Figure 3.1 was made in W. C. Dillon Incorporation. The capacity is 44482 N and the division is 444.82 N. The dynamometer is designated to show the axial tension of the test conductor. Since the permeability is a function of conductor temperature and tension, the tension of the conductor was kept constant in the experiment to decrease its effect on the permeability. The tension of the conductor decreases naturally with an increase of the conductor current resulting in increased temperature. During the measurement, tension was added to compensate for this decrease. The tension can be added either through the tension bar on the lower part of the left side or through the dynamometer structure on the right side. To least affect the record of the dynamometer, tension was added from the left tension bar in the experiment.

An isolating transformer was used between the power and the test conductor. Current was injected from the isolating transformer to the conductor through two connectors made of aluminum. The testing area was between the two connectors shown in Figure 3.1.

Two current transformers (CT) were used to measure the current. One was used in the primary side of the isolating transformer and the other was used to hang on the test conductor. The test conductor went through the hole of the CT and without touching the CT.

3.2.2 Test Conductors

Cross-sectional areas of the test conductors are shown in Figure 3.2: A white circle indicates an aluminum wire and a gray circle indicates a steel wire. All the wires of Guinea conductor have the same diameter of 0.292 cm, 0.477 cm of Penguin and 0.337 cm of Raven. The voids between the layers and among the wires are different as shown in Figure 3.2: some of them are in triangular type; some of them are similar to rectangular type; some of them resemble the combination of triangle and rectangle. As the wires spiral and rotate, the voids deform and rotate as well. The heat of the conductor is transferred through metal-to-metal contacts, air gaps, and voids.

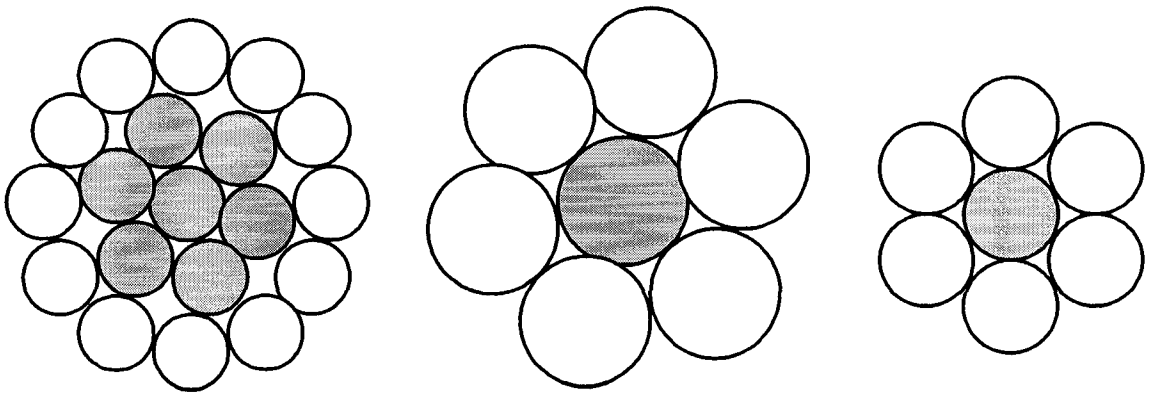

(a) Guinea (b) Penguin (c) Raven

Figure 3.2 Cross-sectional areas of Guinea, Penguin, and Raven, respectively

The detailed information from the Aluminum Handbook [9] on the physical and electrical properties of the three conductors is given in Tables 3.1 and 3.2, respectively. Table 3.3 gives the possible maximum current for Guinea, Penguin, and Raven, respectively. The current ranges of the conductors can be chosen according to Table 3.3.

Table 3.1 Physical properties of Guinea, Penguin, and Raven, respectively [9]

Code Word	Size (Kcmil)	Size (cm^2)	Diameter (cm)		Complete Diameter (cm)	Steel Core Diameter (cm)	Rated Strength (kips)
			Alum.	Steel			
Guinea	159	0.806	12 x 0.292354	7 x 0.292354	1.46304	0.877062	16.0
Penguin	211.6 (4/0)	1.072	6x 0.477012	1x 0.477012	1.43002	0.477012	8.35
Raven	105.6 (1/0)	0.535	6x 0.337058	1x 0.337058	1.01092	0.337058	4.38

Table 3.2 Electrical properties of Guinea, Penguin, and Raven, respectively [9]

Size and Stranding		Resistance				Inductive Reactance			Capa. Xac
kc mil	Wire	DC (Ω/km) 20° C	AC – 60 Hz (Ω/km)			30.48cm Equivalent Spacing 60 Hz (Ω/km)			30.48cm Eq. Spa. – 60 Hz (MΩ.km)
			25° C	50° C	75° C	25° C	50° C	75° C	
159	12/7	0.3326	0.343	0.4679	0.5425	0.3212	0.3666	0.3902	0.1782
4/0	6/1	0.2609	0.2697	0.3498	0.3797	0.3163	0.3436	0.3455	0.1819
1/0	6/1	0.5226	0.5356	0.6468	0.709	0.3411	0.3734	0.3815	0.0756

Table 3.3 Ampacity versus temperature rise (in still air) [9]

Code Word	$\Delta T = 10°C$	$\Delta T = 30°C$	$\Delta T = 60°C$	75°C Current	Maximum Current
Guinea	104	182	262	330 A	390 A
Penguin	130	218	320	390 A	470 A
Raven				255 A	300 A

3.2.3 Test Probes

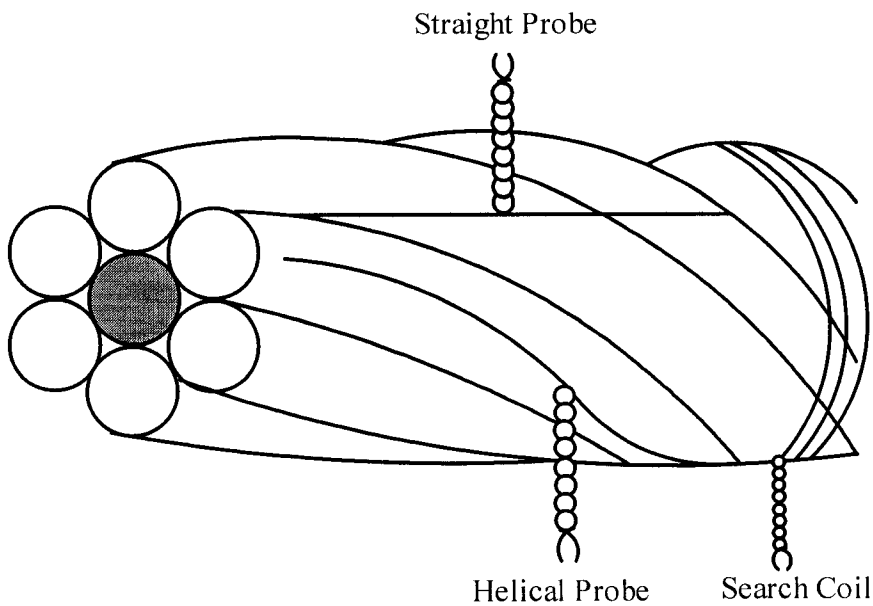

Figure 3.3 Arrangement of three kinds of probes

Three kinds of probes (shown in Figure 3.3), made of AWG #24 insulated copper wire, were used in this experiment [6]. Straight probes were used to measure ac resistance and ac reactance of the test conductors. Helical probes were used to ascertain the surface current density in the aluminum layer. Search coils were used to obtain the complex

permeability of the steel core. Each probe was placed as tightly as possible on the conductor surfaces. Thermal tape was used to secure the probes in place. In theory the probes do not have to lie on the conductor surface because any extra loop area enclosed by the probe would result in an induced voltage which is 90° out of phase with the total current. However, in practice, the extra flux could be affected by ferrous and conductive objects near the conductor, causing changes in the measured value of conductor resistances [35].

Both straight probes and helical probes were mounted on the outer surface of the test conductor. The probes, with the exception of the two extreme ends, were insulated electrically from the conductor. Two contacts for each probe were made by drilling small holes approximately half-way to the radial center of the same aluminum wire, and securing the ends of the probe wire in the holes with a small aluminum wedge to enhance good contact and to keep the possible error at a minimum..

Burke and Alden [36] have demonstrated the proportional relationship between the helical probe output voltage and the current density. The proof in [36] is shown briefly as the following:

Figure 3.4 is used to demonstrate the relationship between probe output voltage and current density in a general case. In Figure 3.4, *EF* and *BC* represent the two portions of the filament, *GF* and *AB* the leads, and *CDE* any fixed but arbitrary path in the conductor. Points *G* and *A* are placed in a field free region so that the potential difference V_{GA} is uniquely defined.

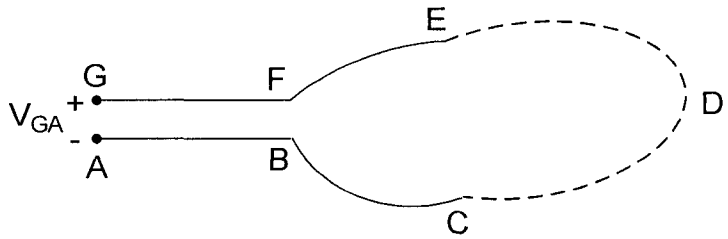

Figure 3.4 Arbitrary filament of current density probe [36]

Applying KVL in the loop ABCDEFGA:

$$V_{GA} + \int_{ADG} \rho J \cdot dl = \oint E \cdot dl \qquad (3.1)$$

where ρ is resistivity in $\Omega \cdot m$; J is current density in A/m^2; l is integral line in m, and E is electric field intensity in V/m.

If the current drawn by the measuring instrument is assumed to be negligible compared with the current in conductor *CDE*, the current density will be zero everywhere in the paths *ABC* and *GFE*. We can write

$$\int_{ADG} \rho J \cdot dl = \int_{CDE} \rho J \cdot dl . \qquad (3.2)$$

GF and *AB* are twisted tightly so that they experience exactly the same velocity and electromagnetic fields. Point *E* and *C* are electrically connected to the conductor with solder. Terminals *G* and *A* are in a field free region. We have the following formula

$$V_{GA} = \int_{EF} \rho J \cdot dl + \int_{BC} \rho J \cdot dl \tag{3.3}$$

which is the integral of the ρJ product along the length of the probe filament in the adjacent conducting medium. In this case

$$V_{GA} = \rho J \cdot l \tag{3.4}$$

where l is the length of the probe. The direction of J is the same as that of l.

The terminal voltage is proportional to the product of ρJ and l. The following considerations are noted in [36]: 1) Current waveform is preserved. This is important in our situation where the single layer ACSR conductor is nonlinear; e.g., surface probes on magnetic materials. 2) The signal is independent of frequency. This allows the measurement of current distributions for low frequency periodic wave shapes. 3) The signal is proportional to the resistivity of the conductor at the probe location. Since at steady state the temperature is close to being homogeneous, it is not necessary to correct for temperature variations.

The above analysis of the general case was incomplete because the magnetic flux through the surface bounded by *BCDEFB* was ignored. Findlay and Riaz [34] modified the relationship to:

$$V = \int_{p} \rho J \cdot dl + \frac{\partial \phi}{\partial t} \tag{3.5}$$

where the second term may arise due to the influence of external fields. Since the loop formed by the helical probe and the conductor is too small to allow a significant amount of magnetic flux, only the first term of the above equation contributes to the measured voltage.

In this experiment, Burke and Alden's probe was modified to encompass several integral number of lay segments of the outer conductor, mounted along the spiraling aluminum wire shown in Figure 3.3 in order to measure the voltage accurately and without distortion from either the steel frame or the conductor ends. In order to obtain adequate resolution of the helical probe, the diameter of the probe filament must be small compared to the penetration depth, which is a function of frequency, resistivity, and permeability. The diameter of the applicable AWG #24 wire, 0.5 mm, is small compared to the penetration depth 6.599 mm, satisfying the criterion.

One problem remains: the probes may disturb the current distribution in the test conductor. Measurements for the longitudinal magnetic flux had stabilized within approximately 30 cm of the ends of the test cable [6]. In this physical experiment, all current and voltage probes were approximately 178 cm from the ends so the probes would not affect the current distribution. As we will see in the result comparison, matched experimental results and simulation results indicate that the sample is long enough for the current to redistribute from wherever its distribution in the clamps to the distributions measured at the centers of the clamps.

Every effort was taken to ensure the measurement valid and within good precision. All probe leads were shielded and twisted tightly to the conductor to avoid stray pick-up. The leads connected to high-impedance voltmeters and gain phase meters were also shielded and twisted. Two sets of probes were used to make the experimental

data valid. Each set of probes includes a straight probe, a helical probe, and search coils. Each curve measured from the experiment was done several times and the characteristic curves were consistent.

The probe and the test conductor are made of two different metals which have a tendency to oscillate when injected ac current. To reduce this uncertainty, mechanical clips were used to fix the mounted probes and Fiberoid Fish paper was used between the mechanical clip and the test conductor as an insulator.

3.2.4 Measuring Instruments

Some measuring instruments were used in this experiment: PFA Telfon insulated T-type 24 AWG thermocouples, a Fluke 2240C data logger, HP 3575A gain-phase meters, German-made BBC M2110 multi-meters, and HP 3435A multi-meters. Details of these instruments are shown in Appendix A.

3.2.5 Temperature Measurement

Temperature measurement plays a key role in this physical experiment. PFA Telfon insulated T-type 24 AWG thermocouples were used both externally and internally to monitor temperatures. The true surface temperature will be disturbed by the attachment of thermocouples. Careful installation can make disturbances as small as reasonably possible. Drilling straight, small-diameter holes becomes significantly important.

A thermocouple normally covers a wide range of temperatures, and its output is reasonably linear over portions of that range. The exposed or bare bead of thermocouple with fast response can be made small to facilitate precise measurement of temperature at a point. The analyses by Quant and Fink [37], Green and Hunt [38] showed that in order to obtain a rapid response with a small, steady-state error, it is necessary to use a small junction bead with good surface contact, small diameter wires, and good insulation between the wires and the surroundings. Thermocouples mounted on a surface subject to radiant heating at temperature-rise rates up to 17 °C/s were investigated by White [39]. His results showed that a separated-junction thermocouple produced the least error. The selected thermocouples in this experiment meet those requirements.

We need to attach thermocouple to the surface of the conductor to measure its surface temperature. A depression just below the surface is used to install the thermocouple. The larger the diameter of the depression, the greater will be the disturbance in temperature distribution within the body, because of the existence of the depression and of the thermocouple installation. The best diameter is that which will just accommodate the installation. The success of drilling depression depends on three factors: the drill used, the drilling machine, and the skill of the operator.

American-made high-speed steel twist drill in standard size 0.159 cm in diameter was chosen in the experiment, since they can be operated at twice the RPM of carbon steel and can withstand temperatures up to 1000 °F. The lips are formed in the sharpening process to the desired angle. At the very tip the spiral point is formed, which has less of a tendency to wobble at the start than the chisel point.

A hand-drill machine with adjustable drilling speed was used with a spindle that moved up and down easily, and was arranged to allow delicate fingertip control. Since there is always a critical speed at which an unsupported drill vibrates laterally [39], a skill was used as follows. In the experiment, the drill projected from the chuck by an amount only slightly greater than the depth of the hole to raise speed as high as possible and also to minimize the flexing of the drill with the consequent tendency to drift or run out. Thus, when the drill was cutting, the unsupported length between the chuck and the entrance to the hole did not exceed 5 drill diameters. As the depth of the hole increased, the drill was made to project more and more from the chuck to correspond to the increased depth of the hole.

During the experiment, the operator attempted to apply just sufficient pressure to make the drill "cut". Excess pressure or excess force may result in a crooked, bell-mouthed hole even though the drill might not break. The smaller the drill, the lighter is the permissible pressure. Guinea has an aluminum layer, a steel layer, and a king wire. The hole drilled in the surface of the king wire was the most difficult one because of the outer two layers. Firstly, a hardened high-speed tool steel drill with cutting lips made of cemented carbide was used. Secondly, the drilling location was chosen on the spot which was exactly beneath the contacts both of two aluminum wires and of two steel wires. Thirdly, a hard spot or hole in the steel surface tended to deflect a drill, resulting in a crooked hole and a broken drill. Two drills were broken in this case. Finally, maximum drill speed, minimum drill pressure, and a perfectly sharp drill were used to drill this hole successfully at the surface of the king wire. The drill was withdrawn and cleaned after every 1 or 2 seconds in action. Much patience was required for the operator.

The holes drilled in this experiment to install thermocouples satisfied the requirements in [40]: (1) holes were drilled small in diameter, i.e., the diameter which just accommodates the thermocouple installation; (2) holes were drilled as straight as possible with a large ratio of depth to diameter; (3) holes were drilled in various locations to obtain the required average temperature and were just below the surface of each layer including the king wire; (4) chips of steel or aluminum were removed from the hole frequently enough to prevent pressure, and thereby friction, from developing in the space filled by the chips. The hole was cleaned before the thermocouple was installed.

Thermally conducting epoxy resin and epoxy hardener (50% each) were mixed together to work as thermal conducting glue to secure the end of the thermocouples. This process yielded good thermal conductivity and sufficient electrical insulation. Thermal conductivity measurements had been taken by Garrett and Rosenberg [41] between 2 and 300 K on composites made from an epoxy resin with powder fillers of glass spheres. They claimed "above about 10 K the conductivity of the composites is in good agreement with theory for the glass spheres". Deeper study about the thermal conductivity of the epoxy resin and metal-powder materials including steel and aluminum was performed by de Araujo and Rosenberg [42].

A lamp was also installed on top of the conductor so that the operator had the best possible vision of the mouth of the hole and the exposed portion of the drill. For the speed in drilling, it was feasible with one quick, easy motion of the fingers to withdraw

the drill its entire length for cleaning. Other procedures were implemented to minimize the error:

- The smallest possible hole was drilled to avoid perturbation errors.
- The thermocouple wires were brought away from the junction along an isotherm for at least 20 wire diameters to reduce conduction errors.
- The measuring junction was located as close to the surface as possible rather than above or below it.
- The installation of thermocouples was carefully designed so that it caused a minimum disturbance of any change in the emissivity of the surface, to avoid changes in convective or radiative heat transfer.
- The installation of thermocouples was designed to make the total response fast enough to cause negligible lag for the transients expected in service.
- Epoxy resin was used as thermal conducting glue to secure the end of the wire.
- The thermal resistance was reduced between the measuring junction and the surface conductor material in an effect to reduce it to as low a value as possible.
- The mean temperature value was averaged with several thermocouples installed in the same layer.
- The uncertainty of the thermocouples was improved by calibration, especially at low temperatures.
- The air gap was avoided for installation of thermocouples. Also, cold soldering joints were avoided in soldering the probe ends.

3.3 Measuring Strategies and Processing Data

3.3.1 Measurement with DC Source

The measurement with dc source was designed to obtain aluminum resistivity by measuring dc voltage, dc current, temperature, radius, and the length of aluminum wire. Figure 3.5 shows the circuit for aluminum resistivity measurement.

The measuring instruments are described in Appendix A.

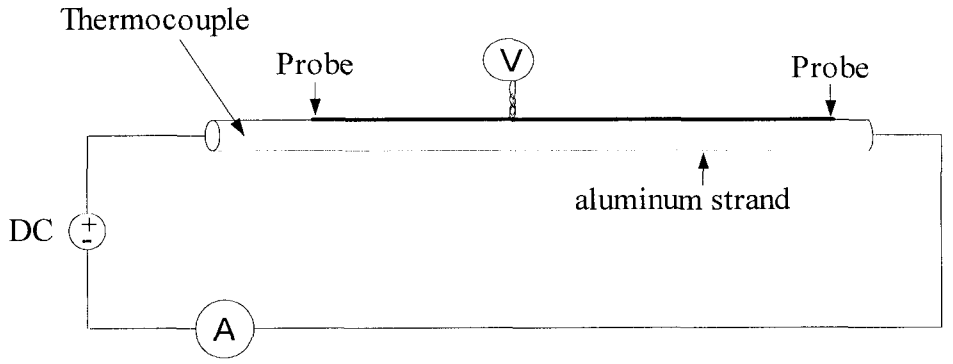

Figure 3.5 The circuit for aluminum resistivity measurement

3.3.2 Measurement with AC Source

The measurement with an ac source was designed to obtain the electromagnetic properties of Guinea, Penguin, and Raven conductors by measuring probe voltages, currents, and phasor angles between them at 60 Hz.

Measurements were made from 100 A to the maximum current shown in Table 3.3 for Guinea, Penguin, and Raven respectively at intervals of 10 A. Voltage drops of straight probes, helical probes, and search coils were recorded from 6 multimeters. The current was read from the ammeter connected to the test conductor. The angle between the probe voltage and the conductor current was recorded by the gain-phase meter. Two gain-phase meters were involved because of the two sets of probes. Temperatures were printed and displayed on the monitor of the data logger 2240C sequentially from the first channel to the last channel. Thermocouples mounted on the test conductor were connected to a board which was inserted into the data logger.

For Guinea conductor, seven thermocouples were used. One was mounted on the king wire, three on the first steel layer in different locations, and the other three on the aluminum layer. The temperature of each layer was averaged to decrease the random error. The ambient temperature was also recorded as the reference. For Penguin and Rave conductors, six thermocouples were used respectively. Three were on the king wire and the other three on the aluminum layer.

During the experiment, the temperature increased and the axial tension decreased with the increase of the conductor current. At some fixed conductor current, tension was added through the tension bar to keep as a constant value. Measurements from meters were recorded when equilibrium was reached and the temperature for all channels were printed at the same time.

Several rounds of experiments were repeated on each test conductor at different times in an effort to ensure that the measurements were valid.

3.3.3 Data Processing

- **Data Processing of the Measurement with DC Source**

Since high accuracy is required for this experiment, the probe shown in Figure 3.5 was installed and measured very carefully. The measurement included a voltage drop, V of the probe in Volts, dc current, I through the circuit in amperes, conductor temperature, T in degrees Celsius, length L and radius r of the conductor in meters.

Aluminum resistivity can be obtained through the calculation of the following:

$$R_{dc} = V/I \quad (3.6)$$

$$R_{dc} = R_{dc20°C}(1+0.00404*(T-20)) \quad (3.7)$$

$$\rho_{20°C} = R_{dc20°C}*\pi r^2/L \quad (3.8)$$

where R_{dc} in Ω means dc resistance of the conductor at temperature T °C; $R_{dc20°C}$ in Ω means dc resistance at 20 °C; 0.00404 /°C is the temperature coefficient of resistance from and at 20 °C suggested in [9]; $\rho_{20°C}$ is the aluminum resistivity at 20 °C.

After several rounds of measurements, the average of dc resistance can be obtained: $R_{dc} = 0.0025\ \Omega$.

- **Data Processing of the Measurement with AC Source**

The measurement of ac source test includes the conductor current I, the straight probe voltage V_s and θ_s which is the phase difference between V_s and I, the helical probe voltage V_h, the search coil voltage V_{sc} and angle θ_{sc}, the king wire temperature T_0, the first steel layer temperature T_1, the aluminum layer temperature T_2, the straight probe length L_s and the helical probe length L_h, the tension T_{en}, the aluminum lay length λ.

The physical properties of the conductor were also measured: the normal cross-sectional area of steel A_{st} and aluminum A_{al}, the resistivity of conductor ρ_{al} and ρ_{st}, the number of strands for steel N_{st} and aluminum N_{al}.

The resistance per unit length of the conductor was measured by the straight probe. The calculation is given by

$$R_{ac} = \frac{V_s * \cos\theta_s}{I * L_s} \quad \Omega/\mathrm{m} \tag{3.9}$$

The dc resistance is

$$R_{dc} = R_{20^\circ C}(1 + \alpha_{al}(T_2 - 20)) \quad \Omega/\mathrm{m} \tag{3.10}$$

where α_{al} is the temperature coefficient of the resistivity.

The internal reactance per unit length of the conductor is

$$X_{ac} = \frac{V_s * \sin\theta_s}{I * L_s} \quad \Omega/\mathrm{m} \tag{3.11}$$

The current density in the aluminum layer was measured by the helical probe attached to the surface of an aluminum wire. We have

$$J = \frac{V_h}{\rho_{al} * L_h} \quad \mathrm{A/m^2} \tag{3.12}$$

The spiral current, i.e., current in the aluminum layer, can be calculated from the current density

$$I_{al} = J * A_{al} \quad \mathrm{A} \tag{3.13}$$

The characteristics of the steel core were measured by the search coil probes. The axial magnetic flux in the steel core can be obtained from the voltage drop of the search coil and the turns N_{sc} of the search coil:

$$\psi = \frac{V_{sc}}{2\pi f N_{sc}} \quad \mathrm{Wb} \tag{3.14}$$

Then the flux density in the steel core is

$$B = \frac{V_{sc}}{2\pi f N_{sc} A_{st}} \quad \mathrm{Wb/m^2} \tag{3.15}$$

The magnetic field intensity is given by

$$H = \frac{I_{al}}{\lambda} \quad \text{A/m} \tag{3.16}$$

We also have the complex relative permeability

$$\mu_r = \frac{B\angle(\pi/2 - \theta_{sc})}{\mu_0 H} \quad \text{unitless} \tag{3.17}$$

the imaginary part of which implies losses in the steel.

where μ_0 is the permeability in free space and $\mu_0 = 4\pi \times 10^{-7}$ H/m.

3.4 Experiment Results

Error considerations of this experiment, ac resistance, current density in the aluminum layer, and their corresponding error bounds are shown in this section.

3.4.1 Error Considerations

All measurements, however careful and scientific, are subject to some uncertainties. As Taylor [43] stated:

> In science the word 'error' does not carry the usual connotation of 'mistake' or 'blunder'. 'Error' in a scientific measurement means the inevitable uncertainty that attends all measurements.

Errors are not mistakes. We can not avoid them no matter how experienced and careful we are by doing physical experiments. What we can do is to ensure that errors are as small as reasonably possible, and to have some reliable estimate of how large they are. Most textbooks introduce additional definitions of "error". We shall use "error" exclusively in the sense of "uncertainty", and treat the two words as being interchangeable [43].

We are interested in resistance, reactance, and current density of the test conductor. Unfortunately, we cannot obtain them in a single direct measurement. What we can do is to measure voltage, current, and the phase difference between them to calculate the quantities that we want. The calculation was shown in Section 3.3.3.

Almost all interesting measurements involve two distinct steps: direct measurement followed by calculation. When a measurement is made in these two steps, the estimation of error or uncertainties also involves two steps. First, find out uncertainties in the quantities that are measurement directly, and then find out how these uncertainties "propagate" through the calculation to produce an uncertainty in the final answer.

In our measurement of aluminum resistivity, if we assume the uncertainties in our measurement are independent and random, the propagation of errors for the calculation can be estimated as: [43]

$$\frac{\delta R_{dc20^\circ C}}{R_{dc20^\circ C}} = \sqrt{\left(\frac{\delta V}{V}\right)^2 + \left(\frac{\delta I}{I}\right)^2 + \left(\frac{\delta T}{T}\right)^2} \tag{3.18}$$

$$\frac{\delta \rho_{20^\circ C}}{\rho_{20^\circ C}} = \sqrt{\left(\frac{\delta R_{dc20^\circ C}}{R_{dc20^\circ C}}\right)^2 + \left(\frac{2\delta r}{r^2}\right)^2 + \left(\frac{\delta L}{L}\right)^2} \tag{3.19}$$

Table 3.4 Maximum error in the dc test

	Range	Accuracy	Maximum Error
δV	300 mV	0.05 %	0.15 mV
δI	20 A	0.35 %	0.07 A
δT	above 0 °C	0.75 %	1.5 °C
δL		1 mm	10^{-3} m
δr		0.01 mm	10^{-5} m

The mean value of measured resistivity is

$\rho_{20^\circ C} = 2.8028*10^{-8}$ Ω·m (3.20)

By performing error propagation analysis, we have an error bound on this measurement as:

$\delta\rho_{20^\circ C}/\rho_{20^\circ C} = 2.2$ % (3.21)

That means the aluminum resistivity is within (2.7411 ~ 2.8645)*10^{-8} Ω·m. The aluminum resistivity suggested in [9] is 2.818*10^{-8} Ω·m, just inside our experimental range.

In the measurement with ac source, we take ac resistance and current density in the aluminum layer as examples to analyze their error bounds. Similarly, applying propagation error analysis, we can estimate

$$\frac{\delta R_{ac}}{R_{ac}} = \sqrt{\left(\frac{\delta V_s}{V_s}\right)^2 + \left(\frac{\delta I}{I}\right)^2 + \left(\frac{\delta L_s}{L_s}\right)^2 + \left(\frac{\delta(\cos\theta_s)}{\cos\theta_s}\right)^2} \tag{3.22}$$

$$\frac{\delta(\cos\theta_s)}{|\cos\theta_s|} = \frac{|\sin\theta_s|}{|\cos\theta_s|}\delta\theta_s = |tg\theta_s| \cdot \delta\theta_s \tag{3.23}$$

$$\frac{\delta J}{J} = \sqrt{\left(\frac{\delta V_h}{V_h}\right)^2 + \left(\frac{\delta L_h}{L_h}\right)^2 + \left(\frac{\delta \rho_{al}}{\rho_{al}}\right)^2} \tag{3.24}$$

The curves with error bounds for ac resistance and current density for three different kinds of single layer ACSR will be shown in Section 3.4.2. The maximum error is shown in Table 3.5.

Take Guinea conductor at 390 A as an example to calculate the errorbound of the ac resistance. The measurements for Guinea conductor at 390A are: V_s = 221.7 mV, I = 390 A, L_s = 0.7031 m, and θ_s = 2.0°. With the measurements and the maximum error in Table 3.5, we can calculate the error bound for Guinea conductor at 390 A:

$$\frac{\delta R_{ac}}{R_{ac}} = \sqrt{\left(\frac{0.5}{221.7}\right)^2 + \left(\frac{25}{390}\right)^2 + \left(\frac{0.0015875}{0.7031}\right)^2 + \left(\tan 2^\circ * \frac{\pi}{60}\right)^2} = 6.42\% \qquad (3.25)$$

The calculation of reactance is similar to that of resistance. Magnetic field strength and relative permeability are dependent on the current density calculation.

Table 3.5 The maximum error in the ac measurement

Instrument	Quantity	Maximum Error with Unit
Thermocouple	Temperature	1.0°C
Fluke 2240C Data Logger	Temperature	0.5°C
HP 3575A Gain-Phase Meter	Angle	3 degrees or π/60 radius
HP 3435A Multimeter	Voltage	0.5mV
Ammeter	Current	25A
Ruler	Length	1/16 in. or 0.00159m

There are imponderable uncertainties such as mounting the probes on the test conductor and connecting probes to the measurement instruments in this physical experiment. This kind of uncertainties is not included in the above error-bound analysis. What the author did in the experiment is to keep such uncertainties as small as possible. For example: probes were placed on the surface of the test conductor very tightly; the ends of each probe were electrically connected to the leads of the measuring instruments; probes were twisted very tightly; and other techniques.

3.4.2 Results of Resistance and Current Density with Error Bound

- **AC Resistance**

Figure 3.6 shows the ac resistance and its error bound for Guinea conductor. Figure 3.7 shows the percentage of the relative ac resistance with the variation of the conductor current.

The error decreases with an increase of the current for resistance. This is because we used the maximum error to calculate the error bound. The error at lower current is exaggerated. For example, the error for HP 3435A is 0.5 mV with the range of 199.9 mV. We used 0.5 mV, the maximum error, for all our voltage measurement. When the current is low, the voltage is low and it is possible within 1.999 mV. The HP 3435A adjusts the range automatically. The error is 0.005 mV with this voltage range. When the voltage is within 19.99 mV, the error is 0.05 mV.

Actually the distribution and transmission lines are designed to transfer the maximum energy that they can carry. The potential of carrying the maximum current under some system voltage is pretty high. The analysis of error around the maximum current ratings has some practical meaning.

Figures 3.8 and 3.9 show ac resistance and the error bound, respectively, for Penguin conductor with the variation of the conductor current.

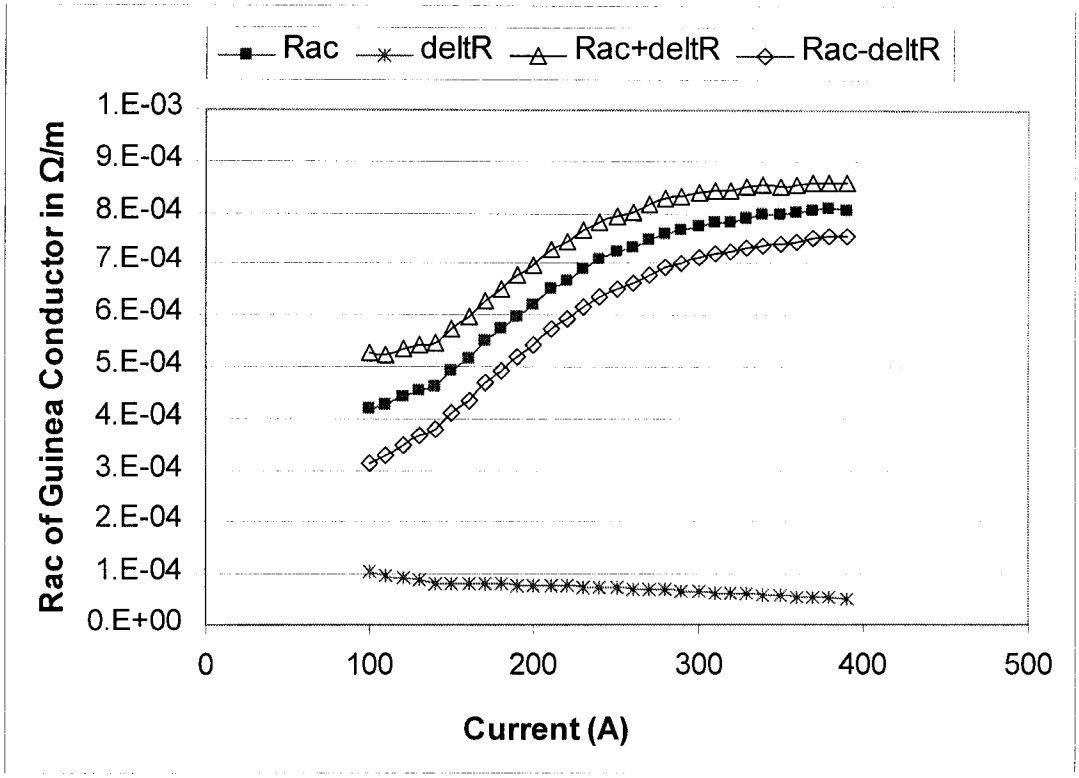

Figure 3.6 Measured ac resistance and its error bound for Guinea conductor

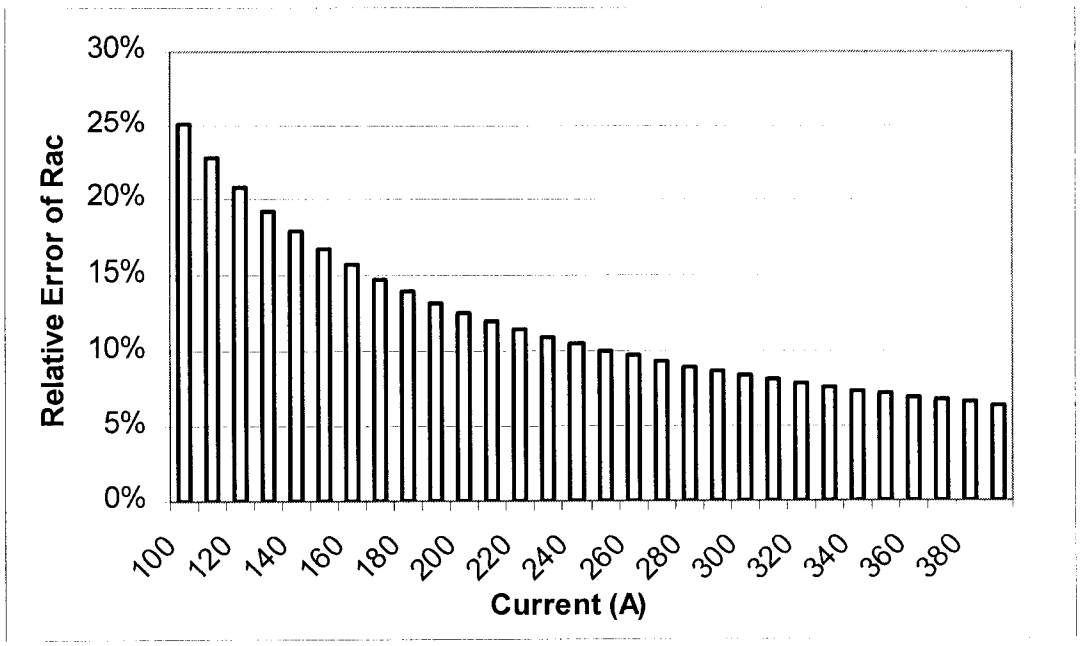

Figure 3.7 Relative error bound in percentage for Guinea conductor

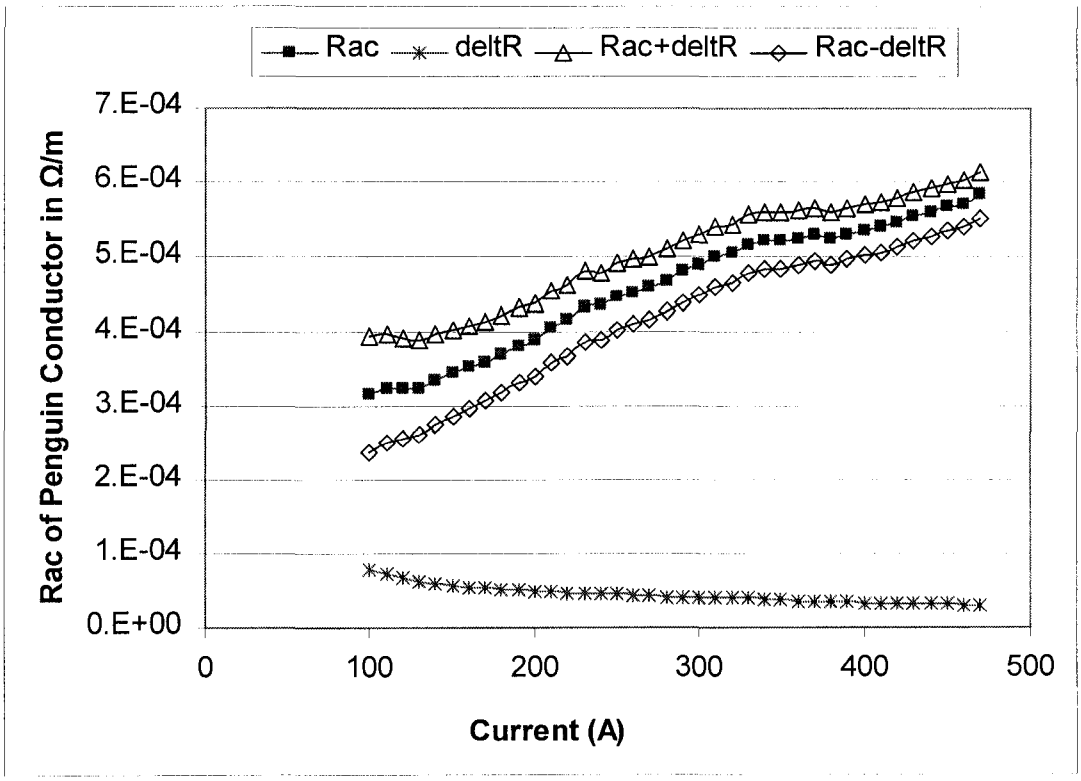

Figure 3.8 Measured ac resistance and its error bound for Penguin conductor

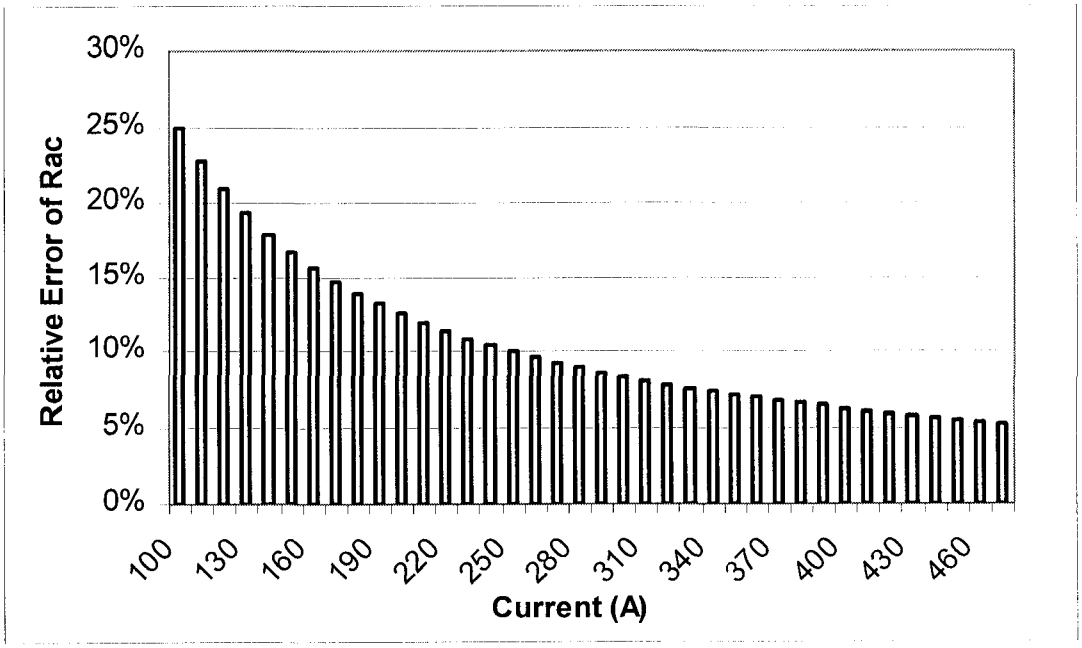

Figure 3.9 Relative error bound in percentage for Penguin conductor

AC resistance and the corresponding error bound for Raven conductor are shown in Figures 3.10 and 3.11, respectively.

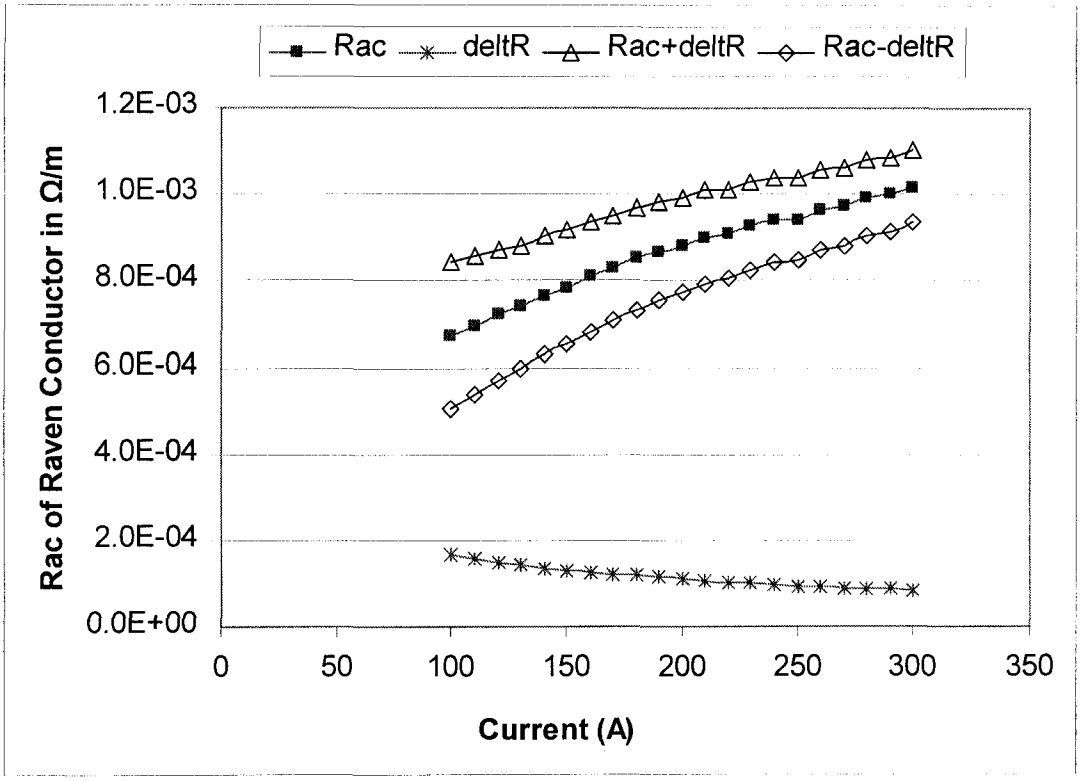

Figure 3.10 Measured ac resistance and its error bound for Raven conductor

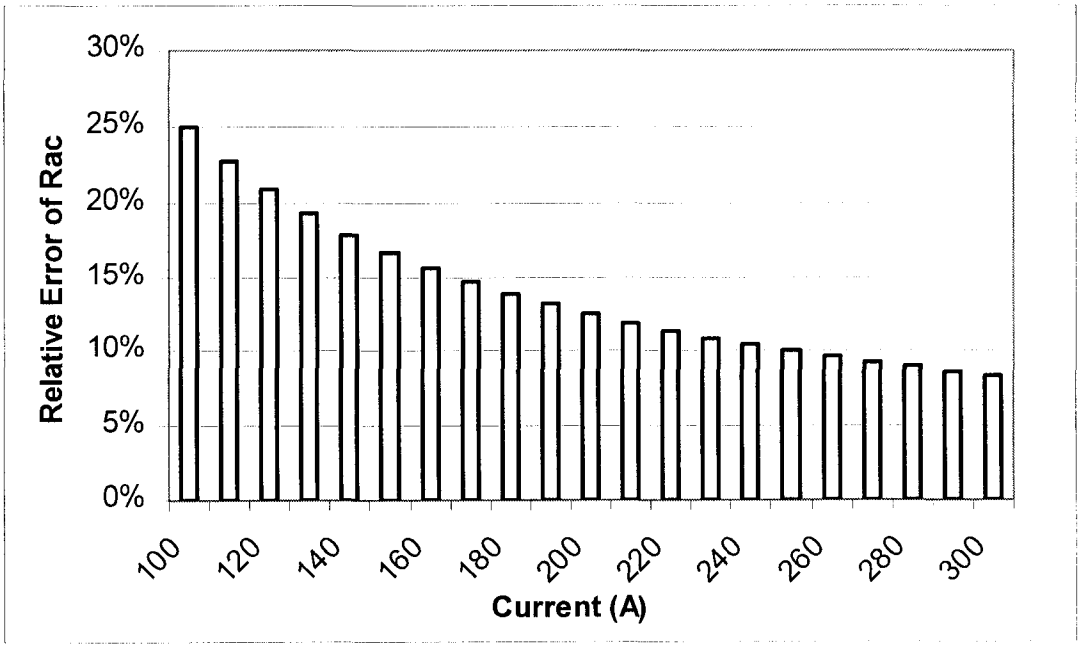

Figure 3.11 Relative error bound in percentage for Raven conductor

- **Current Density in the Aluminum Layer**

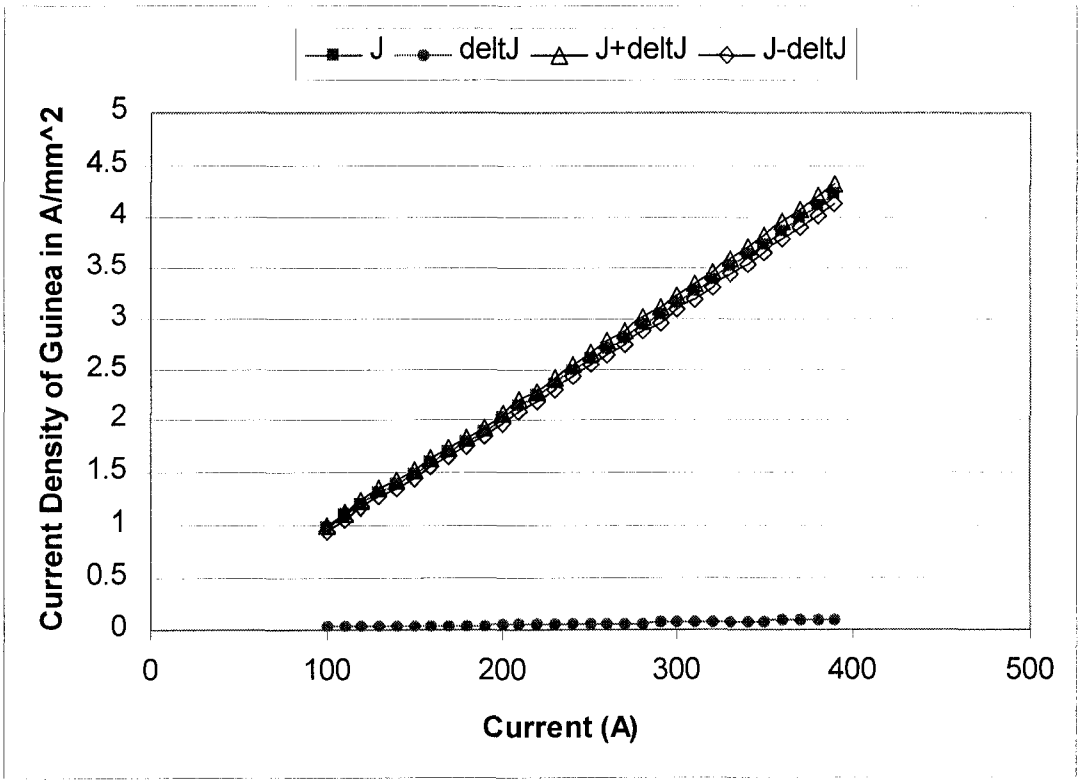

Figure 3.12 Measured current density and its error bound for Guinea conductor

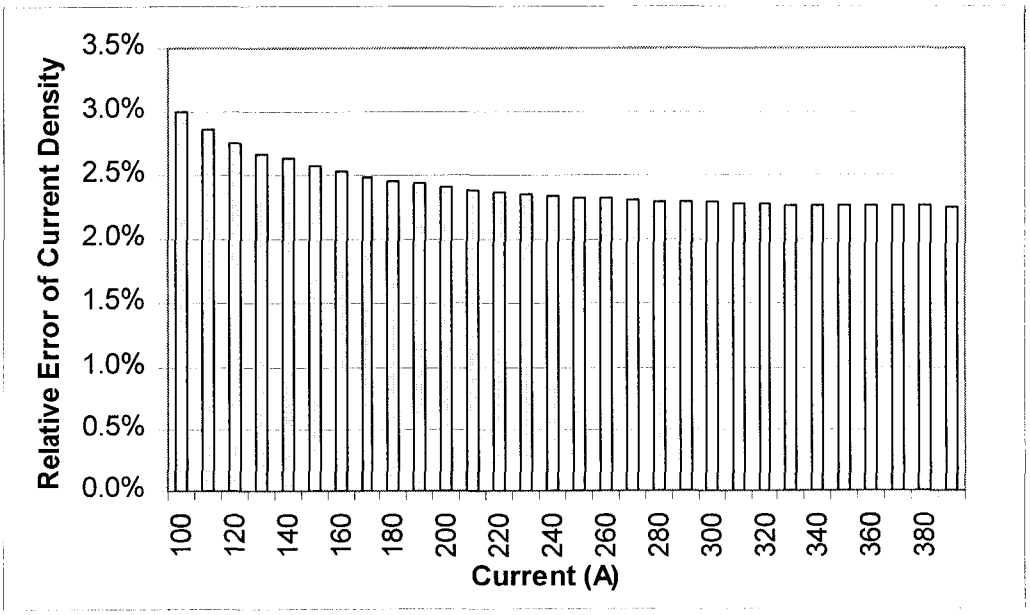

Figure 3.13 Relative error bound in percentage for Guinea conductor

The measured current density in the aluminum layer for Guinea conductor is shown in Figure 3.12 with the variation of the conductor current. The corresponding relative percentage of the error is shown in Figure 3.13 as well.

Figures 3.14 and 3.15 show the aluminum current density and the error bound for Penguin conductor and Figures 3.16 and 3.17 for Raven conductor.

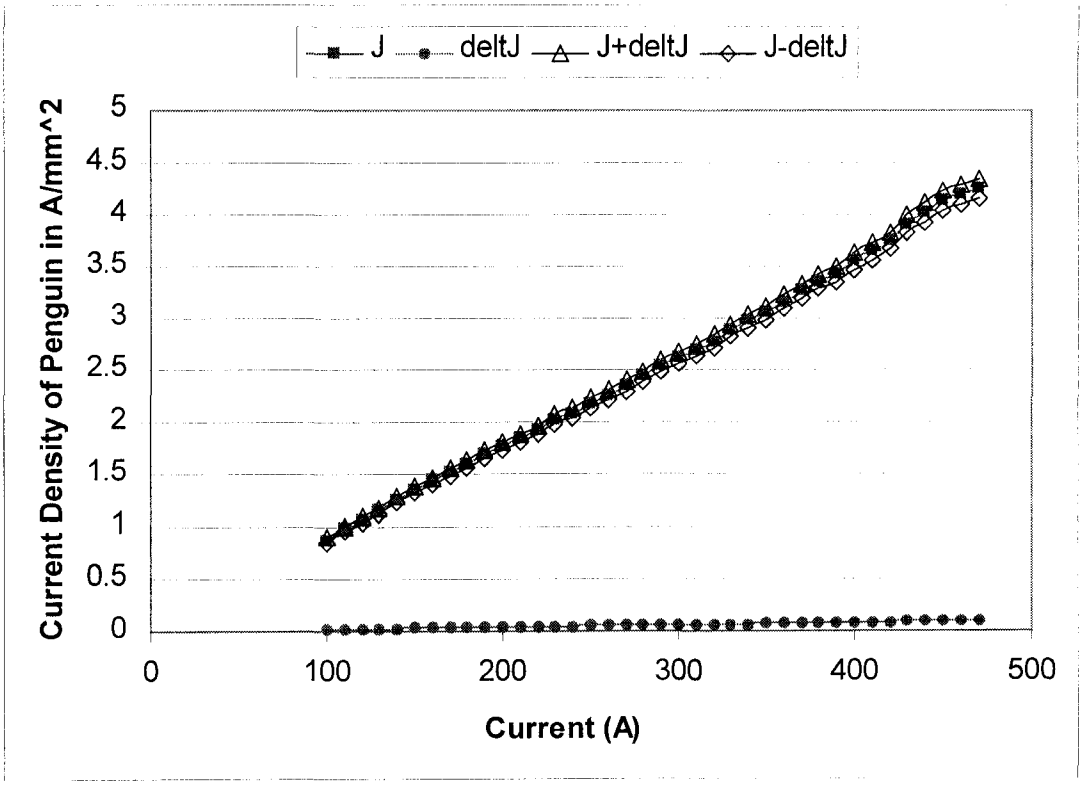

Figure 3.14 Measured current density and its error bound for Penguin conductor

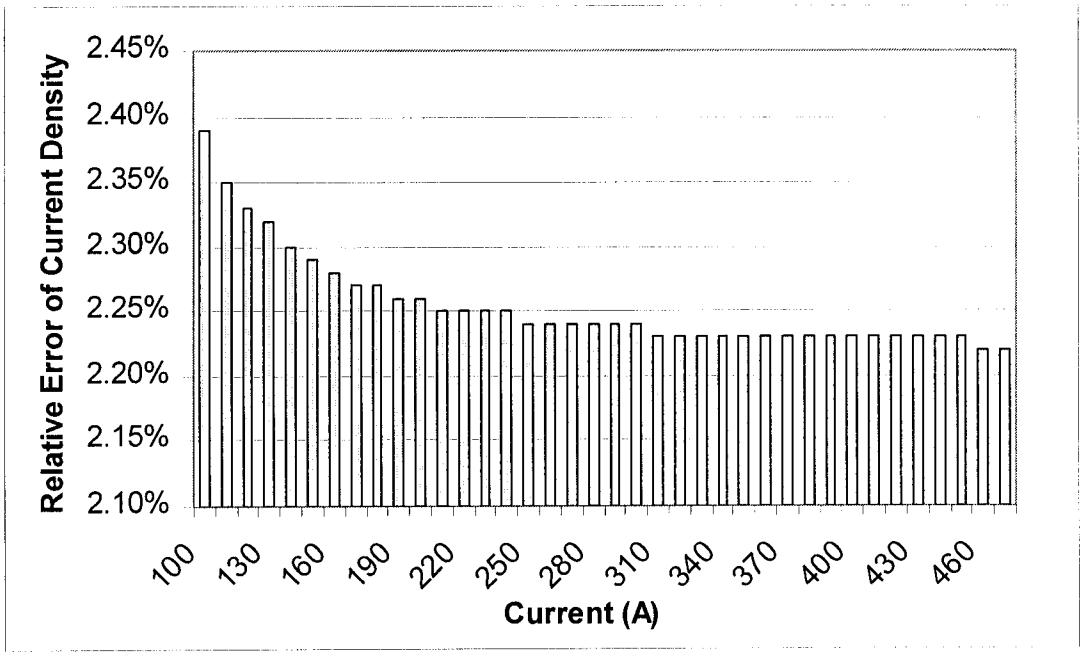

Figure 3.15 Relative error bound in percentage for Penguin conductor

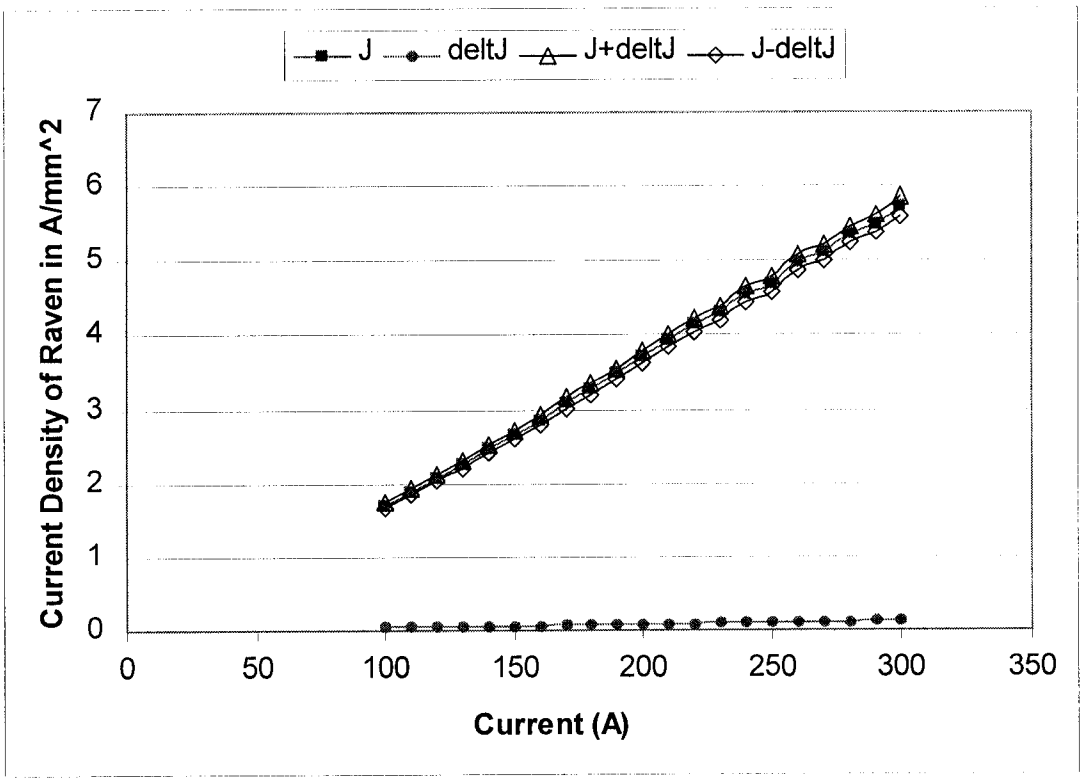

Figure 3.16 Measured current density and its error bound for Raven conductor

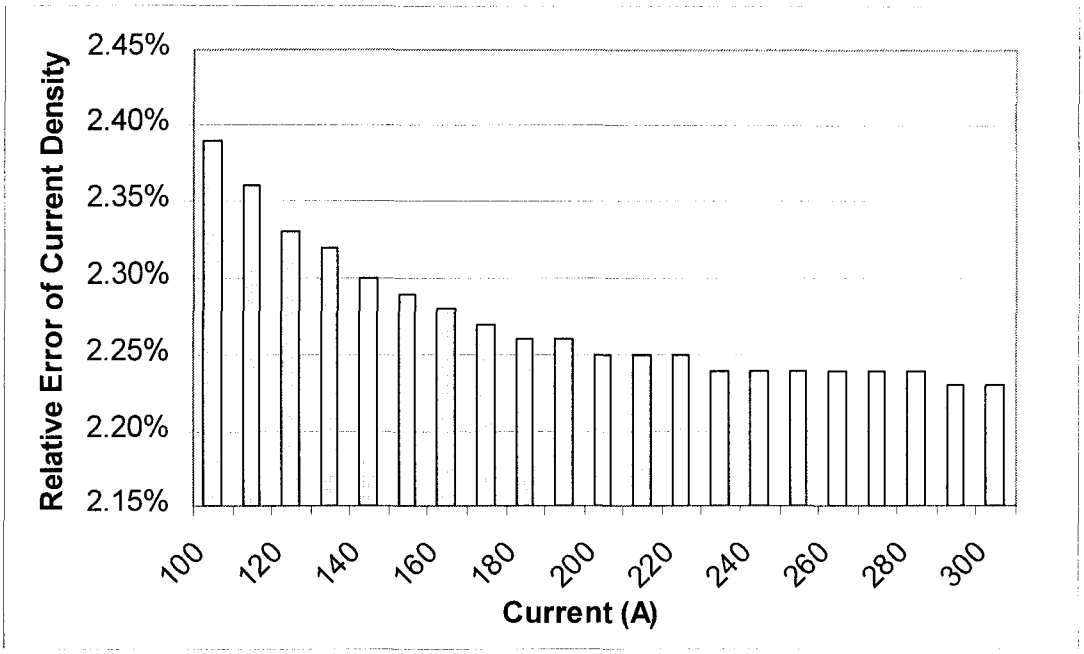

Figure 3.17 Relative error bound in percentage for Raven conductor

The error bounds are summarized in Table 3.6 as follows.

Table 3.6 Some specific values from Figure 3.6 to Figure 3.17

Conductor Code	Current (A)	ΔRac/Rac	ΔJal/Jal
Guinea	100	25.1 %	2.99 %
	200	12.5 %	2.41 %
	300	8.35 %	2.29 %
	390	6.42 %	2.25 %
Penguin	100	25.0 %	2.39 %
	200	12.5 %	2.26 %
	300	8.34 %	2.24 %
	400	6.26 %	2.23 %
	470	5.33 %	2.22 %
Raven	100	25.0 %	2.39 %
	200	12.5 %	2.25 %
	300	8.34 %	2.23 %

From Table 3.6, the error decreases with the increase of the current no matter for ac resistance or for current density in the aluminum layer. The error bound of current density is smaller than that of resistance. Part of the reason might be the uncertainty in the ammeter measurement. The maximum error of current measurement is 25 A out of 500 A range and this error is not involved in the current density calculation.

The error bound calculation of the current density is confined by the error of the measured resistivity. Under no circumstance should the error of current density be smaller than the error of measured resistivity. If the standard book value of aluminum resistivity which has error of 0.15 % in [9] is used in the calculation of the current density, the error decreases to 0.6 % for Guinea conductor at 390 A, 0.52 % for Penguin conductor at 470 A, and 0.51 % for Raven conductor at 300 A.

CHAPTER 4
RESULTS FROM THE INTEGRATED MODEL AND THE EXPERIMENTAL MODEL

4.1 Introduction

This chapter gives the results from the Integrated Model and compares them with experimental results. Experiments were conducted to establish the electrical properties of single layer ACSR conductors coded as Guinea, Penguin, and Raven. Implementations of the Integrated Model were also performed on Guinea, Penguin, and Raven as well. A comparison of the values from the Integrated Model and from the experiment intends to provide validation of the model. The comparison includes ac resistance, ac/dc resistance ratio, ac reactance, current density in the aluminum layer, and the complex relative permeability in the steel core. Both experimental and simulation values are given for the operational range of current from 100 A to the maximum current rating for each type of single layer ACSR conductors. The maximum current for Guinea is 390 A, for Penguin, 470 A, and for Raven, 300 A. Thermal and mechanical properties of single layer ACSR conductors are also given in this chapter.

4.2 AC Resistance

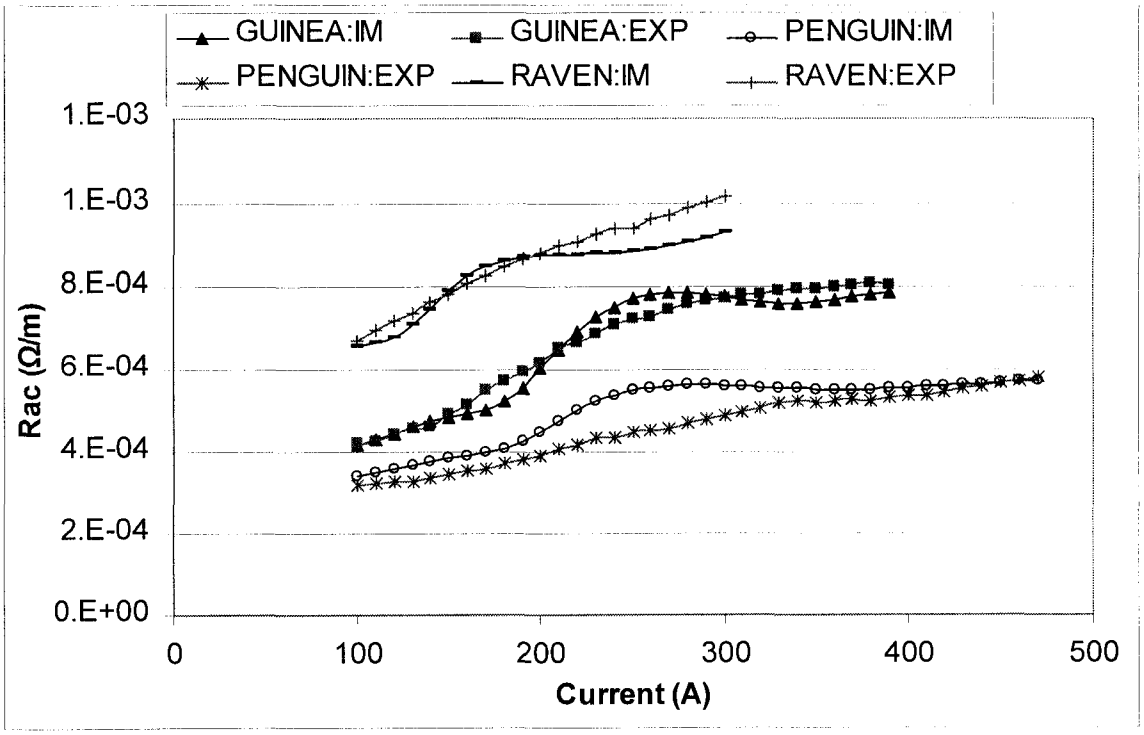

Figure 4.1 Variation of the ac resistance with the conductor current

Figure 4.1 shows the variation of ac resistance (Rac) from the Integrated Model (IM) and from the experiment (EXP) with current for Guinea, Penguin, and Raven conductors. Rac increases with an increase of the current. For Guinea, the prediction of Rac from the Integrated Model matches very well with the experimental data. The Integrated Model predicts Rac well for Penguin, especially with the current lower than 200 A and higher than 330 A. Prediction is in very good agreement with experimental values around the maximum current ratings. For Raven, the Integrated Model predicts Rac well with the current less than 210 A.

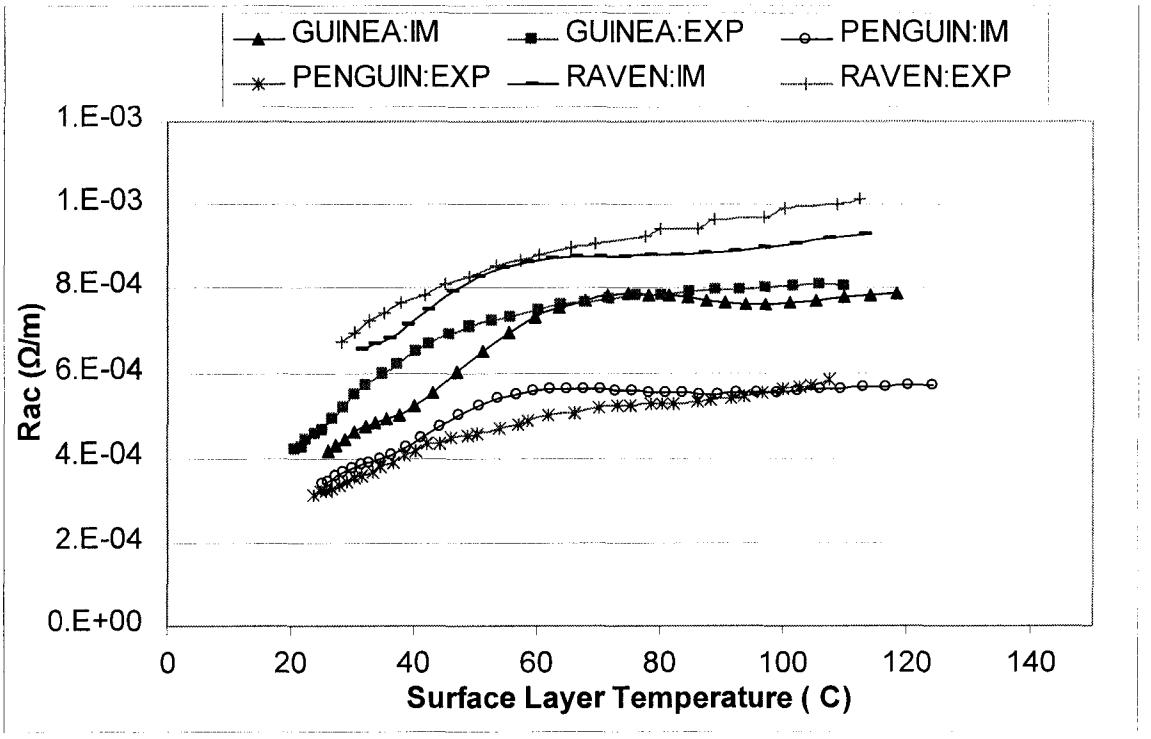

Figure 4.2 Variation of the ac resistance with the conductor surface layer temperature

Figure 4.2 shows how the ac resistance increases with an increase of the surface layer temperature of the conductor. The temperature prediction of the Integrated Model for Guinea conductor at its maximum current is 8 °C higher than the corresponding experimental value. The temperature difference from the Integrated Model and from the experiment for Raven conductor at its maximum current rating is less than 1 °C. At Penguin's maximum current rating, the temperature from simulation is 16 °C higher than its experimental value.

The simulation curves in Figures 4.1 and 4.2 clearly show saturation of conductors. The saturation current ratings for Guinea and Penguin is from 200 A to 320 A and for Raven is from 150 A to 210 A. The experimental curves of Guinea and Raven also show saturation current ratings which are not clear in Figure 4.1 but very clear in Figure 4.7. The experimental curve of Penguin does not reach saturation and we conjecture that the birdcaging in the test conductor greatly affects the steel core

properties. The temperature difference from the model and from the experiment is large in saturation current ratings. The difference is larger than 10 °C for Guinea, and the maximum (15 °C) occurs at 250 A, 260 A. The difference is around 5 °C for Raven from 150 A to 210 A. In the case of Penguin, the maximum difference occurs at 470 A and the difference does not mean anything because no saturation reached in the experiment. The temperature difference is from 5 °C to 11 °C for Penguin at the current intervals 200 A – 320 A. The Integrated Model is not accurate to present the saturation simulation.

The difference of ac resistance and surface layer temperature of the conductors between the Integrated Model and the experiment partly results from the parameters selection in simulation and environmental conditions in the experiment. For example, to simulate conductors indoors, the solar heating in the Integrated Model is reduced to a very small number (0.05 J).

Table 4.1 lists some of the surface layer temperatures from Figure 4.2 for three types of conductors at some fixed current ratings.

Table 4.1 Temperature of the surface layer from IM and EXP

I(A)	T_{Guinea} (°C)		$T_{Penguin}$ (°C)		T_{Raven} (°C)	
	IM	EXP	IM	EXP	IM	EXP
100	26	20.7	25.1	23.7	31.4	28.3
150	33.7	26.6	31.4	29.1	46.5	41.8
200	46.8	37.1	41.2	36.8	66.3	60.4
250	67.7	52.8	56.6	46.2	87.2	86.1
300	84.5	71.8	70.2	58.6	113.3	112.4
350	101.2	93.1	83.5	75.1		
390	118.6	110	95.6	86.2		
440			113	100		
470			124.1	107.6		

Figure 4.3 shows the variation of relative difference of ac resistance with the various currents for Guinea conductor. The relative difference of ac resistance is defined as

$$Relative\ \ Difference\ \ of\ \ Rac\ = \frac{|Rac(EXP) - Rac(IM)|}{Rac(EXP)}\ \ p.u. \qquad (4.1)$$

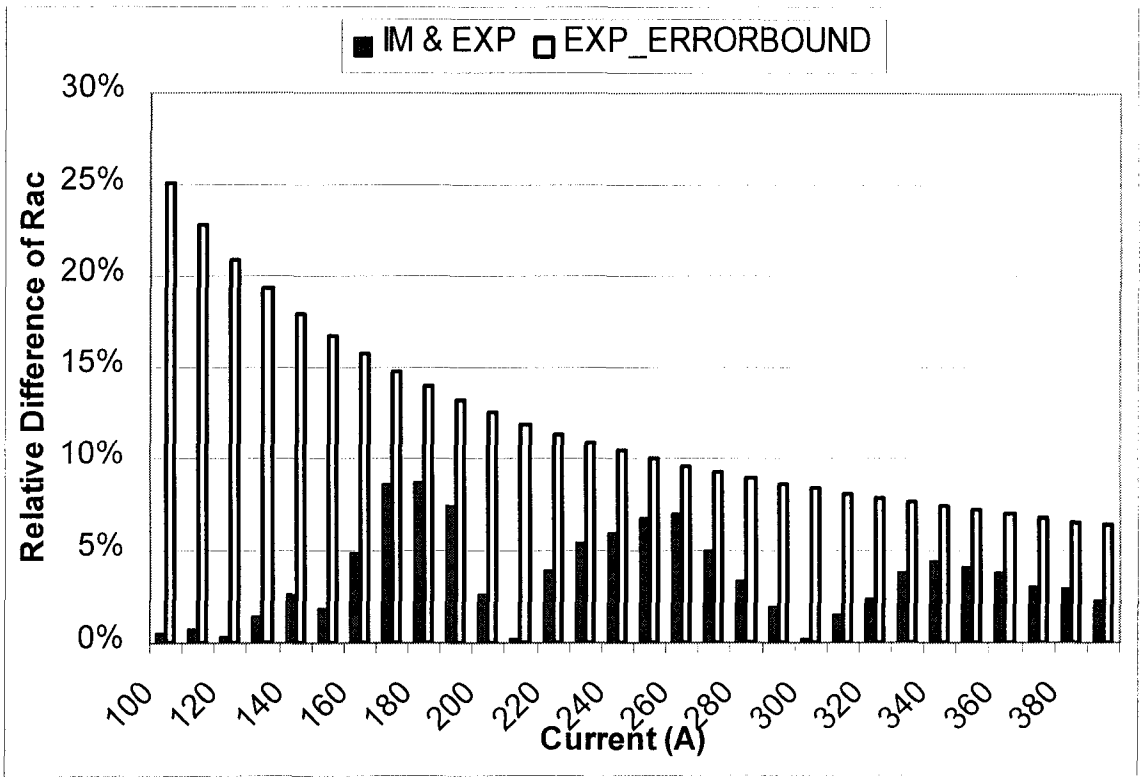

Figure 4.3 Variation of the relative difference of Rac with the current for Guinea

"*EXP_ERRORBOUND*" in Figure 4.3 comes from the error analysis of the physical experiment in Section 3.4. The experimental values are valid within the error bound:

$$Rac(EXP)*(1-Errorbound) \le Rac(EXP) \le Rac(EXP)*(1+Errorbound)$$

From Figure 4.3 we can see that the prediction of ac resistance from the Integrated Model is within the experimental error bound during all operational current ranges. The difference is within 5 % with the current larger than 270 A. At the maximum current rating 390 A, the difference of Rac between the Integrated Model and the experiment is 2.29 %. The Integrated Model works very well for Guinea conductor especially at its maximum current rating.

The peaks in Figure 4.3 are corresponding to the difference of Rac curves in Figure 4.1. The Integrated Model is sensitive to the saturation of conductors. It overestimates Rac at 250 A, 260A while it underestimates Rac at 180 A and 350 A. Variations of Rac prediction, from underestimation to overestimation before saturation and from overestimation to underestimation after saturation, result in the peaks shown in Figure 4.3.

Figure 4.4 shows how the relative difference of Rac for Penguin conductor varies with the current. From Figures 4.1 and 4.4 we can see that the Integrated Model overestimates Rac within the current range from 200 A to 320 A (saturation). The difference is even larger than the corresponding error bound. At high current from 430 A

to 470 A, the Integrated Model predicts Rac very close to the experimental values with the difference less than 2 %.

The saying "overestimation" of the model is based on the experimental value of Penguin conductor. The test Penguin cable is a birdcaged one and we do not know how significant an effect the birdcaging has on the measurement of ac resistance. The experimental resistance ratio curve for Penguin in Figure 4.7 indicates no saturation. Saturation is definitely related to the steel core of ACSR conductor. From Rac simulation curves in Figure 4.1, we can see that the Integrated Model works consistently for three types of single layer ACSR conductors.

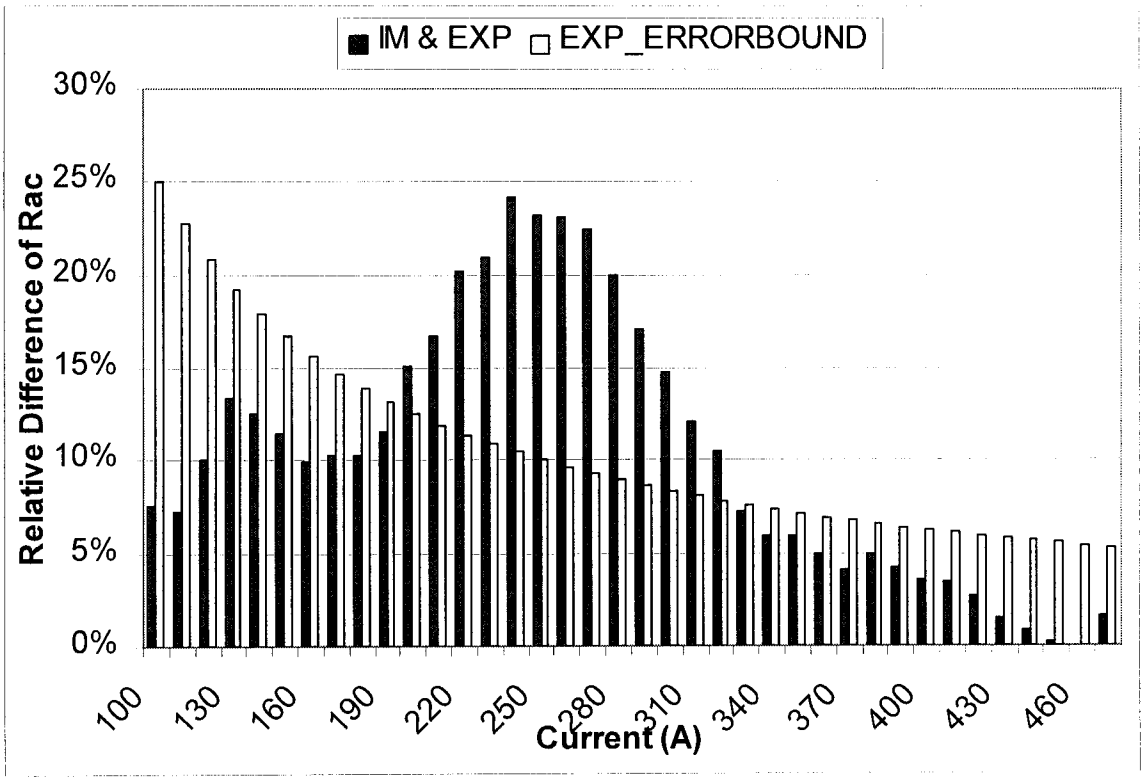

Figure 4.4 Variation of the relative difference of Rac with the current for Penguin

The relative difference of Rac for Raven conductor with different currents is given in Figure 4.5. The Integrated Model works well for Raven conductor based on the experimental work. The relative difference is less than 5 % when the current is less than 230 A. All the difference is within the error bound.

The Integrated Model incorporates the eddy current loss in the aluminum layer, rather than the steel core itself. The axial field flux in the steel core due to the spiraling current is considered as the main reason to cause the eddy current and hysteresis which give extra power losses. This axial field flux is stronger in single layer ACSR than that in the multi-layer ACSR. Figure 4.6 shows the increase of ac resistance over dc resistance caused by the eddy current in the steel core in percentage for three types of conductors.

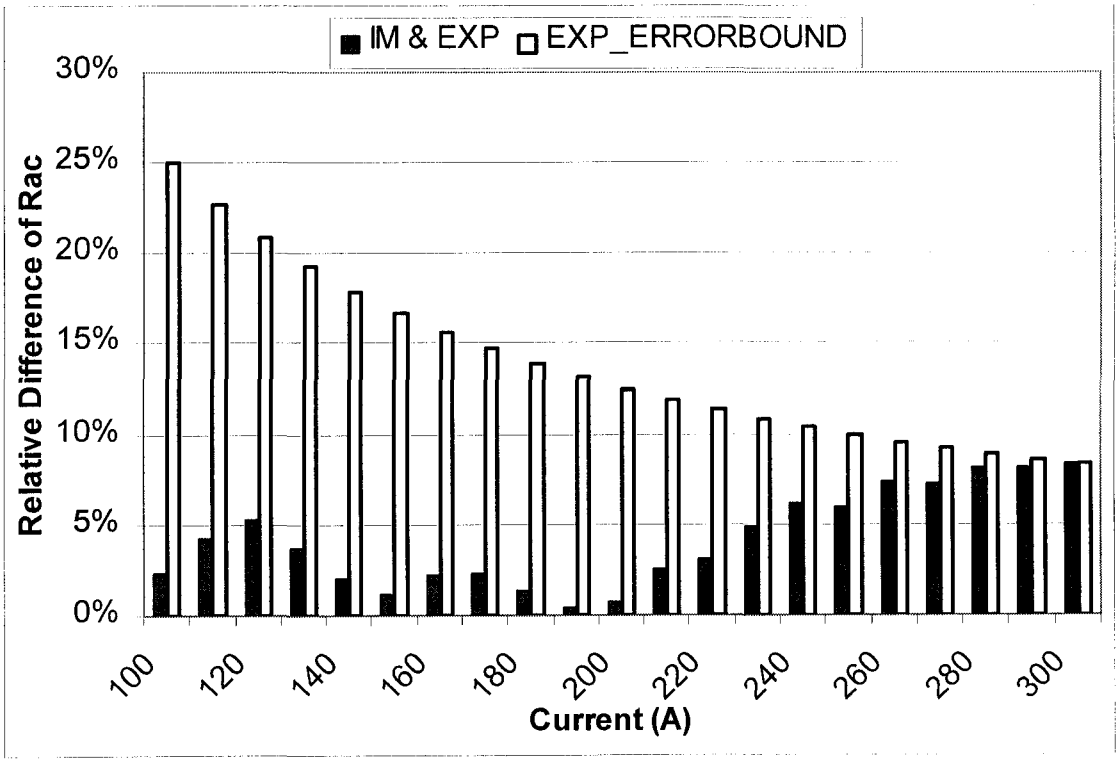

Figure 4.5 Variation of the relative difference of Rac with the current for Raven

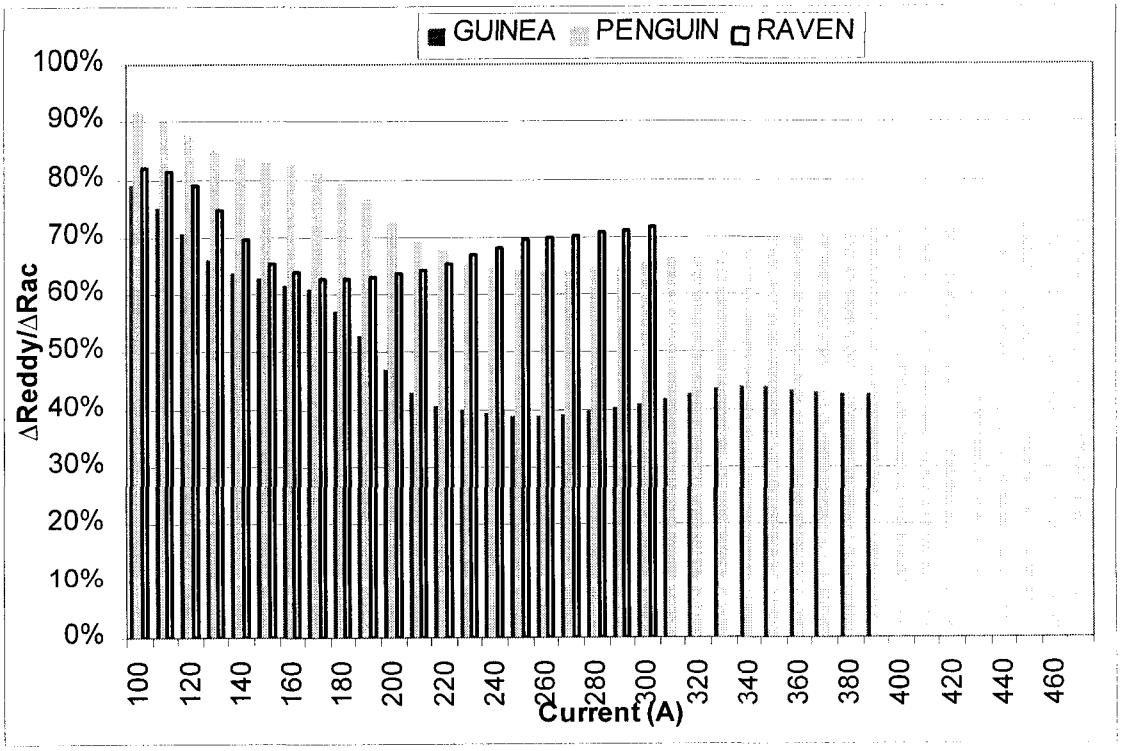

Figure 4.6 Contribution of loss caused by the eddy current in Rac for three conductors

For Guinea conductor, the percentage is 78.9 % at 100 A and 42.8 % at 390 A. For Penguin and Raven, the percentage is over 80 % at 100 A and around 70 % at their maximum current ratings.

The increase of Rac over Rdc is caused by the eddy current, hysteresis, and the current redistribution in the aluminum layer for single layer ACSR conductors. The current redistribution involves the skin effect and the transformer effect. At lower current ratings, the effect of the current redistribution is not strong, and the loss caused by the eddy current is significant. With the current increasing, the percentage of the current redistribution loss increases as well. The loss caused by hysteresis is bigger in saturation than that in other current ratings. At saturation, Guinea, Penguin: 200 A – 320 A, Raven: 150 A – 210 A, the percentage contributed by the eddy current loss decreases. The importance of the current redistribution loss and hysteresis loss results in curve shapes in Figure 4.6.

The decrease of the percentage for Guinea is larger than that for Penguin and Raven. This phenomenon occurs because of the conductor structure. Since the wires are stranded and spiraled, not all the current follows the spiraling aluminum strands. Some of the current is carried in the steel core, called leakage current. The leakage current is 13 % in Guinea steel core and 4 % in Penguin and Raven king wire. The direction of the leakage current is opposite to that of the eddy current and they tend to cancel [7]. That is the reason why the eddy current loss is near half in Guinea while over 70% in Penguin and Raven at their maximum current ratings.

To make use of the transmission capacity, ACSR conductors usually work around their maximum current ratings. From this perspective, the Integrated Model can predict the operational behaviors for single layer ACSR conductors.

4.3 AC to DC Resistance Ratio

At the same current rating, the higher the ac to dc resistance ratio, the larger the resistive heating loss generated. The variation of the ac/dc resistance ratio with the conductor current for Guinea, Penguin, and Raven, are shown in Figure 4.7, respectively.

The ratio of Rac/Rdc increases with an increase of the current until the core reaches saturation. The ratio is 1.95 from the Integrated Model and 1.97 from the experiment for Guinea at 250 A and 260 A. The experiment also shows that for Penguin, Rac/Rdc is 1.7 at 340 A and for Raven, 1.48 at 200 A. After saturation, the ratio decreases while the conductor current still increases. This phenomenon is obvious for both experiment and simulation curves in Figure 4.7.

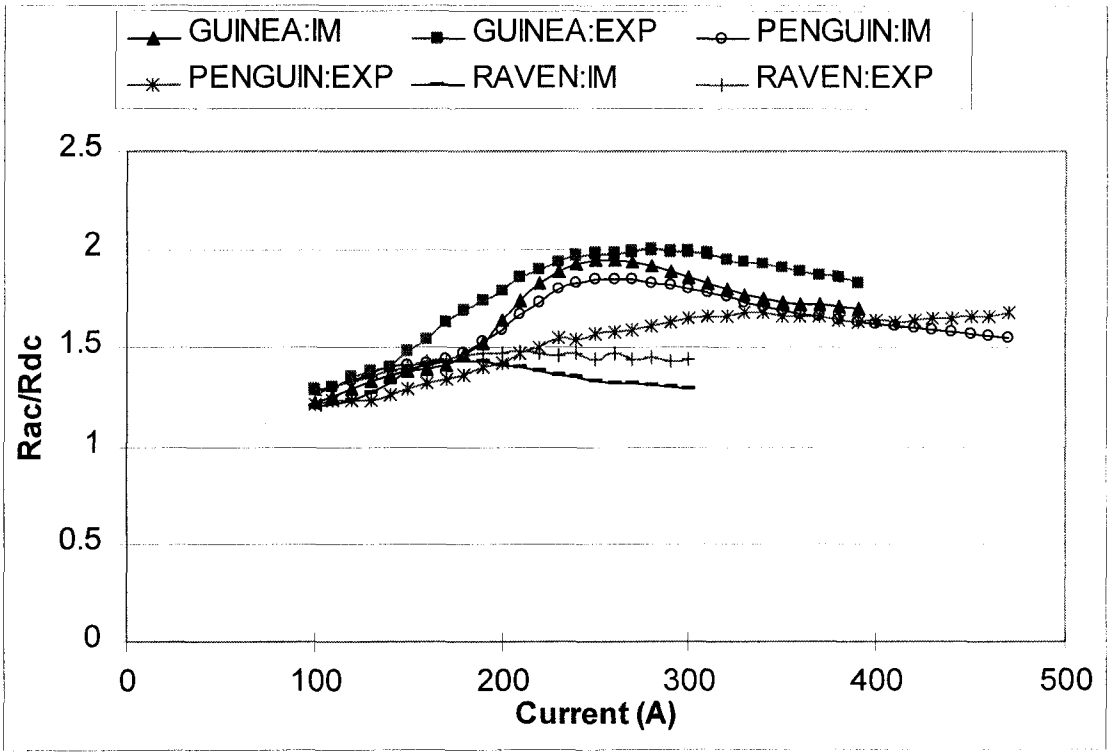

Figure 4.7 Variation of the ac/dc resistance ratio with the conductor current

In Figures 4.1, 4.2, and 4.7, the variation of ac resistance with the current is not monotonically increasing when the current is higher than 240 A on the experimental curve of Raven conductor at high current ratings. The aluminum layer is slightly expanded for Raven conductor at the current range from 240 A to 300 A and the surface layer temperature is higher than 80 °C. Compressive loading of aluminum wires causes the radial displacement of the aluminum layer. The elongation of aluminum is larger than that of steel so the aluminum experiences a compressive load. At some elevated temperature after the aluminum wires expand and become unstressed, they begin to move radially away from the steel core to accommodate the excess thermal elongation. In the extreme, birdcaging occurs.

Guinea conductor has the highest ac/dc resistance ratio among the three. The increasing part in ac resistance is almost 100 % larger than its dc resistance because the ac/dc resistance ratio is almost 2 in Figure 4.7. The leakage current of Guinea conductor is as much as 13 % which increases the additional resistance. Similarly, Rac for Penguin conductor is 70 % higher than its Rdc and for Raven, 50 % higher. The number means the power losses in single layer ACSR conductors are appreciable.

Experiments conducted by Barrett et al. [6] showed that the ratio of Rac/Rdc for Grackle is 1.078 at 1608 A. Grackle has two steel layers and a king wire, total 19 steel wires. Its ac/dc resistance ratio is much smaller than that for single layer ACSR. From this, we can see the longitudinal flux and the eddy current loss is greater in single layer ACSR conductors than from either two layer or three layer aluminum conductors.

Experiments in [6] also showed that the measured Rac/Rdc for two layer ACSR is 1.006. From the ratio we can estimate there is almost no longitudinal flux in the steel core in double layer ACSR conductors.

4.4 AC Reactance

The variation of ac reactance with an increase of conductor current is shown in Figure 4.8 for Guinea, Penguin, and Raven, respectively. The internal reactance is larger with higher current. The ac reactance is caused by the magnetic flux in ACSR conductors. The correspondence of reactance curves from the experiment and from the Integrated Model for Guinea is better than that for either Penguin or Raven.

We can see from Figure 4.8 that the steel core greatly affects the reactance calculation. Guinea conductor has seven steel wires and the magnitude of its reactance reaches 10^{-4} Ω/m. Penguin and Raven conductors, each have only one steel wire and their reactance is limited within 10^{-5} Ω/m.

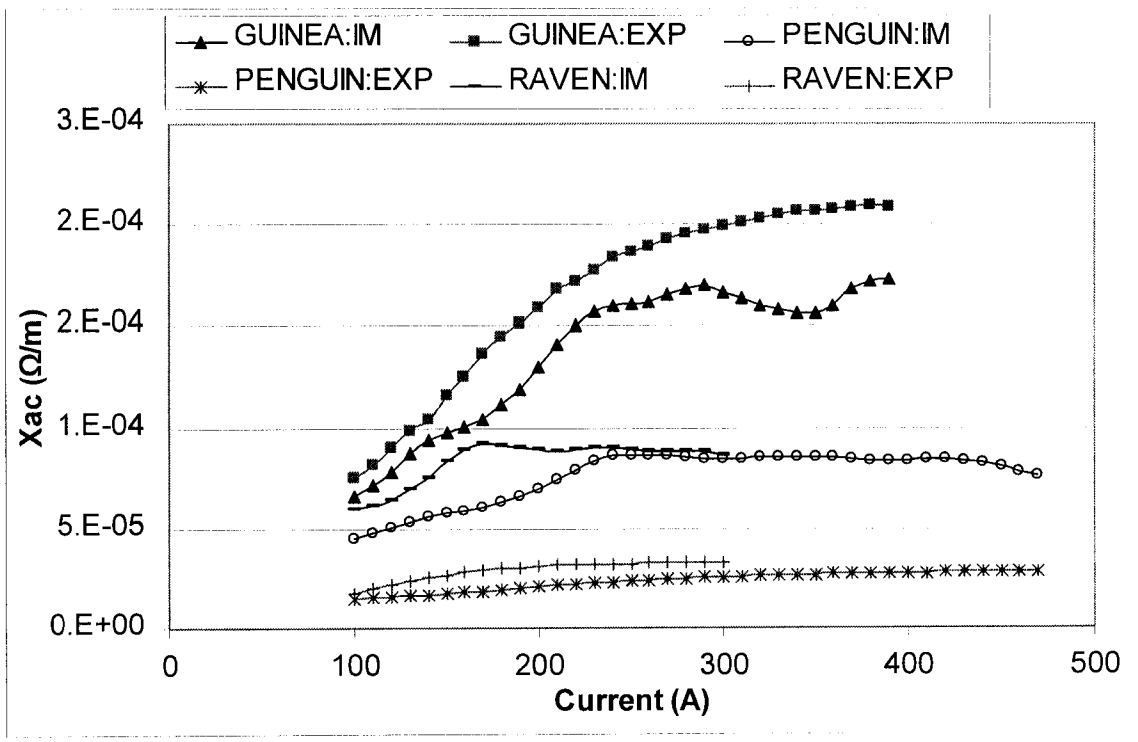

Figure 4.8 Variation of the ac reactance with the conductor current

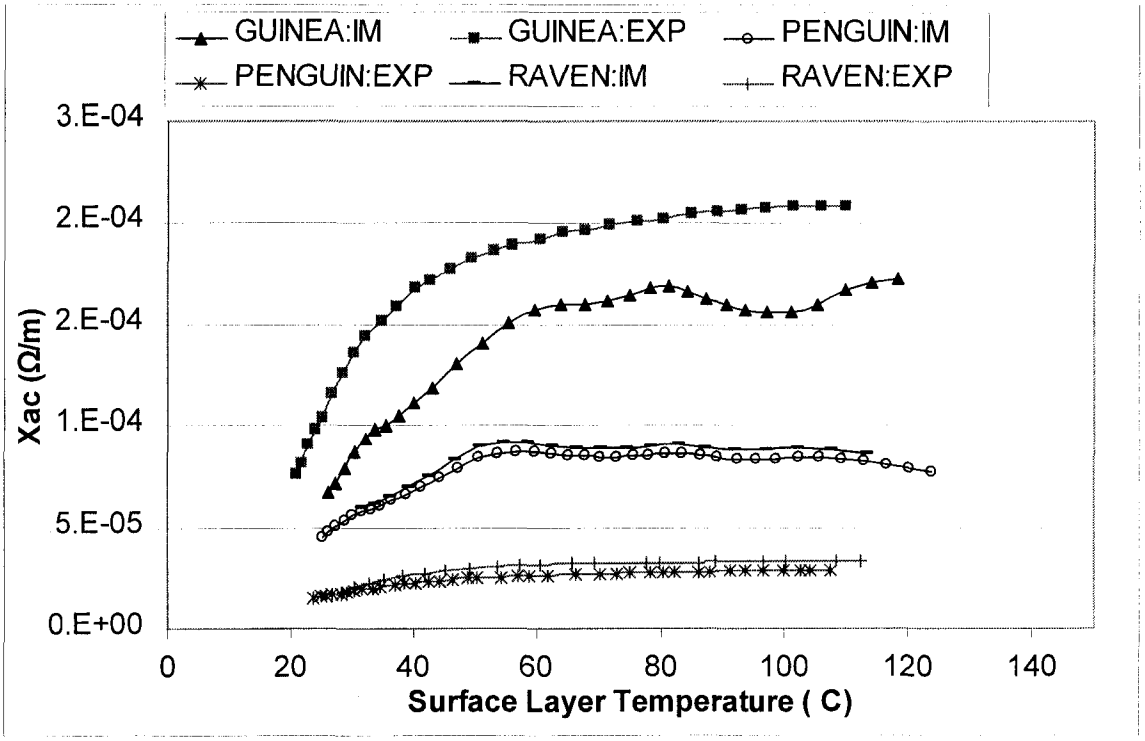

Figure 4.9 Variation of the ac reactance with the surface temperature of the conductor

Figure 4.9 shows the variation of ac reactance with the conductor surface layer temperature for Guinea, Penguin, and Raven, respectively. The variation of ac reactance with the surface layer temperature is similar to that with the conductor current shown in Figure 4.8.

4.5 Current Density in the Aluminum Layer

Figure 4.10 shows the variation of the surface current density in the aluminum layer with the current. The current density in the aluminum layer increases linearly with an increase of the conductor current. In the aluminum layer, the skin effect and the transformer effect tend to cancel each other and the current density in the outer part is a little larger than that in the inner part.

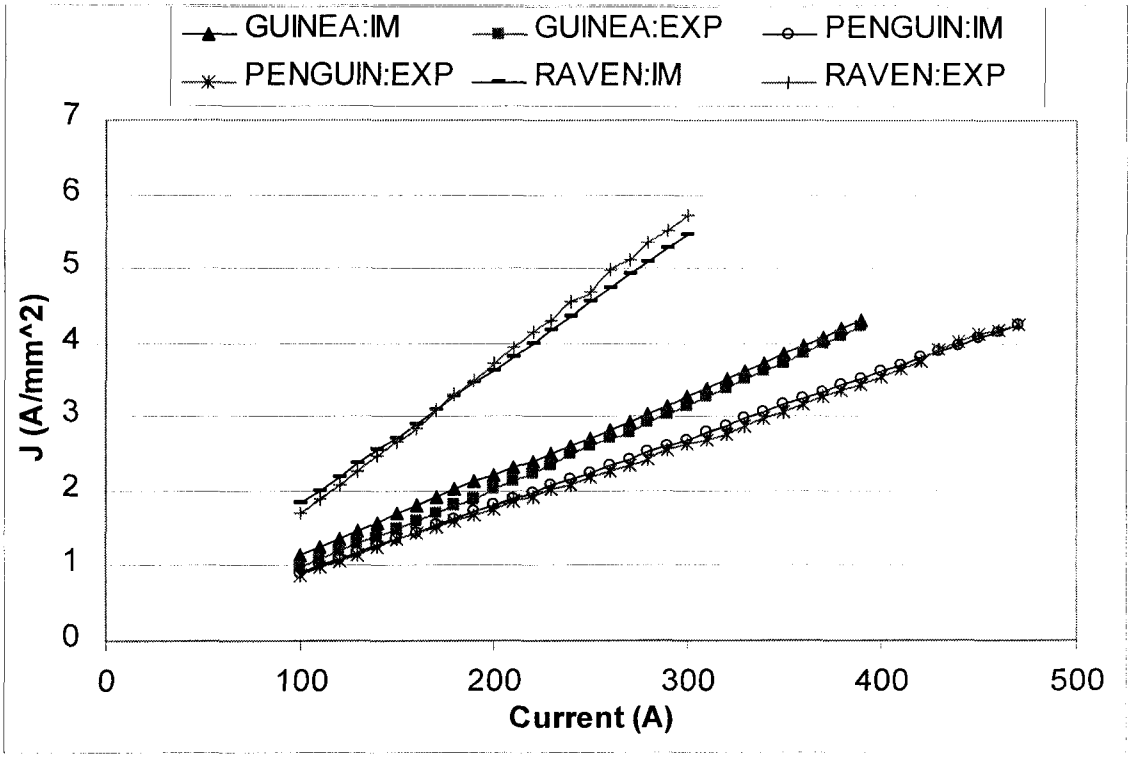

Figure 4.10 Variation of the aluminum current density with the conductor current

From Figure 4.10, we can find the prediction of the current density from the Integrated Model agrees very well with the experimental values for Guinea and Penguin conductors. For Raven conductor, the prediction is good at low current ratings. At high current (higher than 240 A), there is a discrepancy between the prediction from the Integrated Model and the corresponding experimental values. The prediction of the current density at 300 A in the aluminum layer from the Integrated Model is 5.46 A/mm^2 while the experiment shows 5.72 A/mm^2. We conjecture that birdcaging might be part of the reason for the discrepancy. The birdcaging did occur in the physical experiment when the current was larger than 240 A.

The geometrical parameters affect the distribution of the total current in single layer ACSR conductors. We can approximate the layer current based on the current density in the aluminum strands. For Guinea conductor at 390 A, 87 % of the total current is carried in the aluminum layer, while 13 % of the total current is in the steel core. For Penguin at 470 A and Raven at 300 A, 96 % of the total current is carried in the aluminum layer and 4 % in the steel core. For three layer ACSR conductors, the leakage current through the steel core is only about 2 % [4].

4.6 Complex Relative Permeability

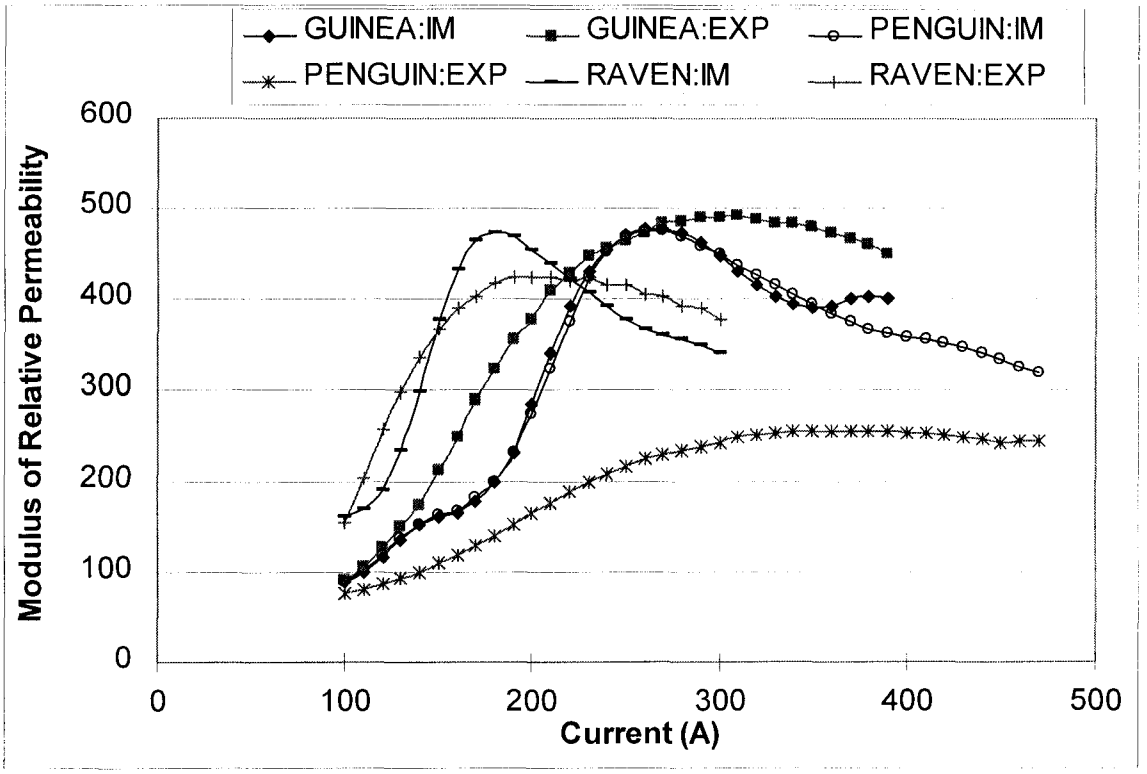

Figure 4.11 Variation of the relative permeability with the conductor current

Figure 4.11 shows the variation of the relative permeability in the steel core with the current from the experiment and from the Integrated Model. In the Integrated Model, the complex relative permeability is obtained by interpolation as functions of magnetic field strength, temperature, and tension. The data in the Integrated Model is based on experiments conducted on the steel core of three layer ACSR by Morgan, Zhang, and Findlay [8, 25]. The relative permeability curves in Figure 4.11 for "EXP" are from the experiment performed by the author.

In the physical experiment, a search coil was used as a sensor for the voltage, current, and angle between them. The relative permeability in the steel core can be given based on the search coil measurements as we discussed in Chapter 3. The magnitude of the relative permeability is affected by the number and the cross-sectional area of the steel wires, and we can see this in Figure 4.11. Guinea has the largest relative permeability among the three. Penguin has a smaller permeability value than either Guinea or Raven. The birdcaged part of the Penguin conductor affects the calculation of the magnitude of the relative permeability, even though the search coil was remote from the birdcaged part. We can see how significant an effect the birdcaging has on the calculation of the steel characteristic.

The lay length is a dominant factor to analyze ACSR conductors. The relative permeability curves are shown in Figure 4.12 as a function of the magnetic field strength.

It is noted from Figure 4.12 that Guinea, Penguin, and Raven, in the Integrated Model have almost the same curves for relative permeability with a variation of the magnetic field strength. This makes sense because the variation of the relative permeability with the magnetic field strength shows the characteristics of the steel core.

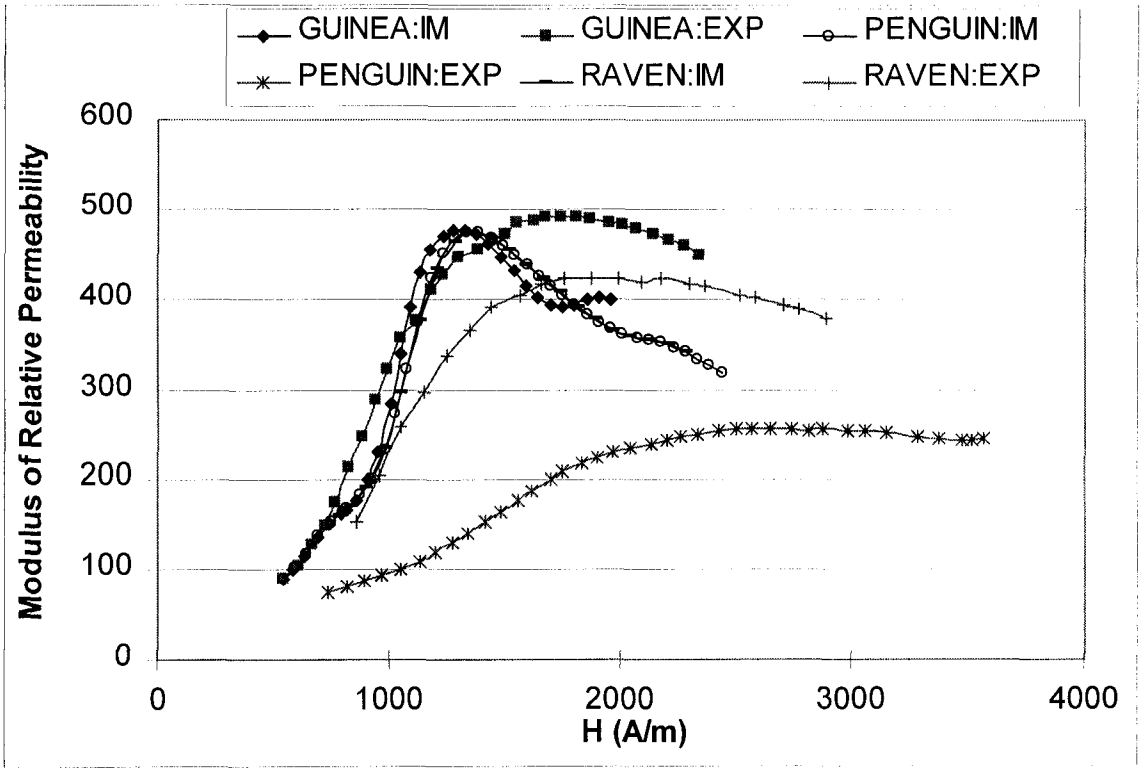

Figure 4.12 Variation of the relative permeability with the magnetic field strength

Figure 4.13 (a) and (b) show the variation of real part and imaginary part of the complex relative permeability with the magnetic field strength, respectively. The imaginary part of the complex relative permeability identifies part of the core losses in the aluminum layer and contributes to the increase of the ac resistance over dc resistance.

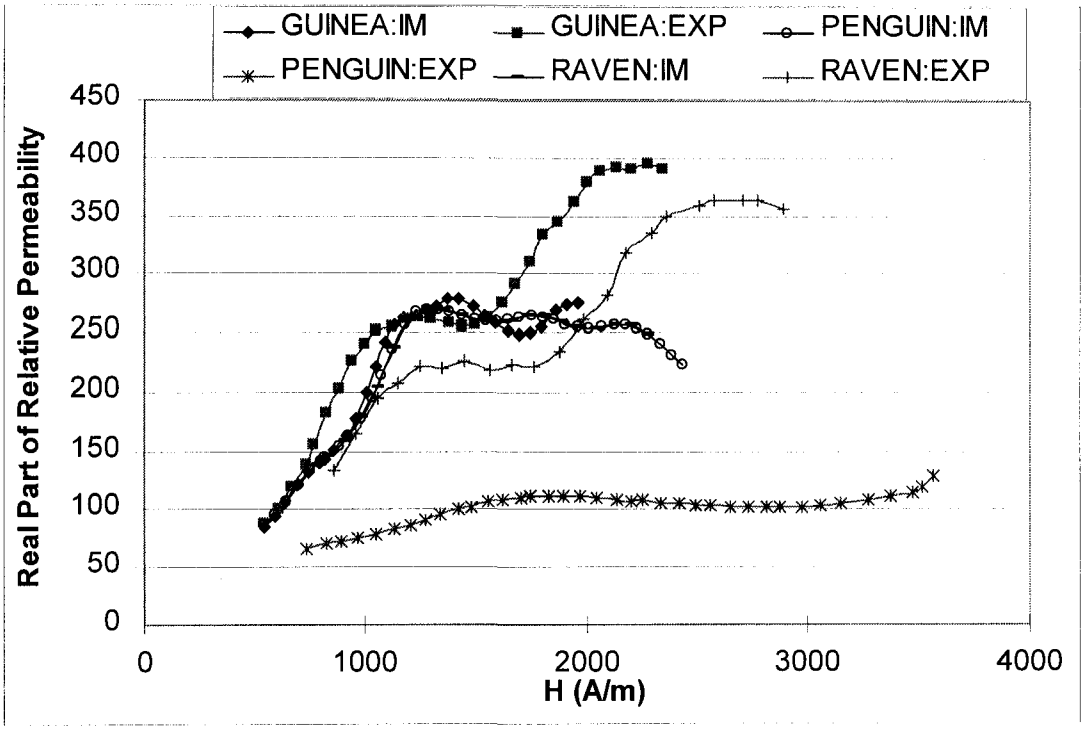

(a)

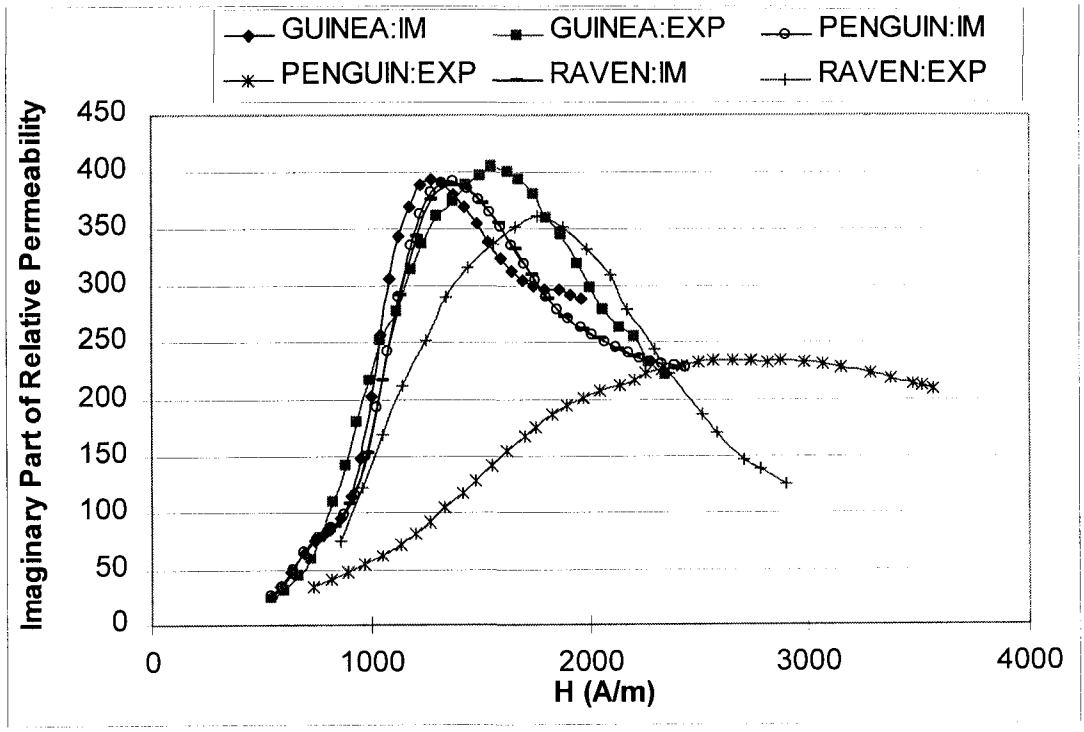

(b)

Figure 4.13 Variation of real part (a) and imaginary part (b) of the complex relative permeability with the magnetic field strength

We have compared the experimental values and the simulation values from the Integrated Model for ac resistance, ac/dc resistance ratio, ac reactance, complex relative permeability, and the current density in the aluminum layer with the current and the temperature rise. The correspondence of the curves from the experiment and from the Integrated Model is reasonably acceptable. We can conclude that the Integrated Model works for single layer ACSR conductors. Hence, we can use this Integrated Model to predict the behavior of the conductors under varying circumstances.

4.7 Thermal and Mechanical Properties of Single Layer ACSR Conductors

The development of the Integrated Model for single layer ACSR conductors is based on the steady-state heat balance equation. The Integrated Model can predict the operational behaviors of the single layer ACSR including the thermal and mechanical properties. Due to the limitation of the laboratory, the thermal and mechanical properties were not measured from the physical experiment. In this part, the thermal and mechanical properties of single layer ACSR conductors are the outputs from the Integrated Model, without any comparison with the experimental values.

- **Resistive Heating**

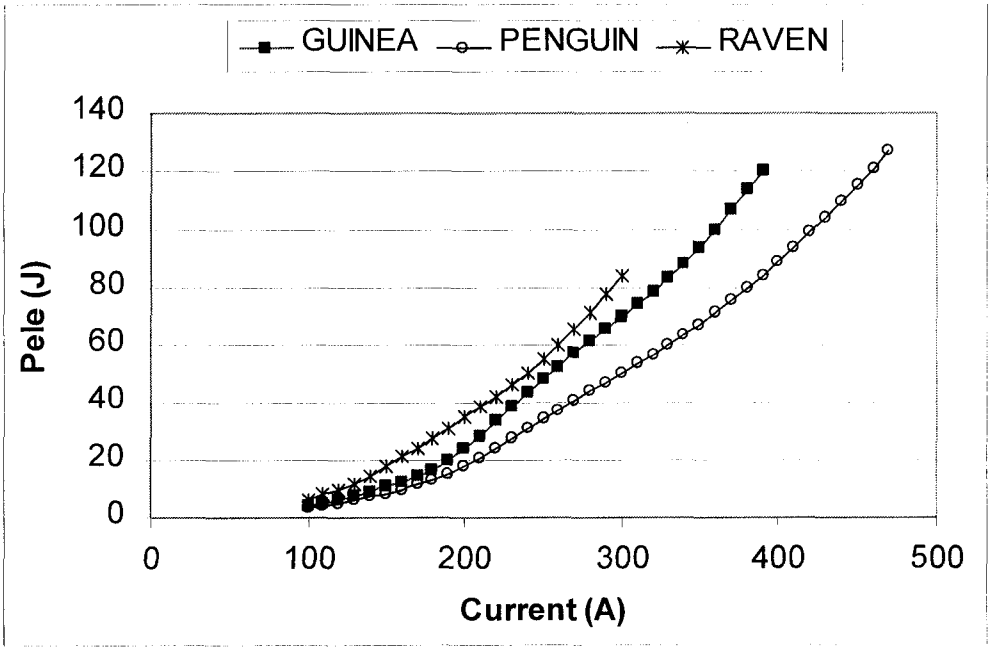

Figure 4.14 Variation of the resistive heating with conductor current

The variation of the resistive or Joule heating with the conductor current is shown in Figure 4.14. The resistive heating increases with the increase of the conductor current. The resistive heating is a function of current, resistance, and conductor temperature. We can see it from the following formula [27]:

$$P_{ele} = k_J I^2 R_0 (1 + \alpha_0 T_{av}) \quad \text{J} \tag{4.2}$$

where the factor k_J takes account of the increase of resistance due to the skin effect and the current redistribution; I is the root mean square value in A; R_0 is the resistance at 0 °C in Ω; α_0 is the temperature coefficient of resistance between 0 °C and the mean temperature of the conductor T_{av} in °C.

Let us compare the resistive heating among the three types of single layer ACSR conductors when they have the same current rating. For example, at 300 A, Raven has the largest resistive heating while Penguin has the smallest under 20 °C ambient temperature. The surface temperature of Raven conductor is 113 °C and the resistive heat is 84 J. The surface temperature of Penguin is only 70 °C and its resistive heat is 50 J. The surface temperature of Guinea is between the above two temperature values, 84 °C, and its resistive heat is 70 J. Obviously, the effect of the surface temperature of the conductor to the resistive heating is significant.

- **Convective Cooling**

The convective cooling calculated with the Integrated Model is shown in Figure 4.15 for Guinea, Penguin, and Raven conductors, respectively. The convective heat cooling increases with the increase of the conductor current. The convective cooling is dependent on the Nusselt number, the thermal conductivity of the air at the surface of the conductor, the difference between the surface conductor temperature, and the ambient temperature. Nusselt number and the thermal conductivity are a function of the conductor surface layer temperature. Raven has the highest temperature difference and the largest convective heat cooling among the three kinds of conductors if they are assumed to have the same other conditions.

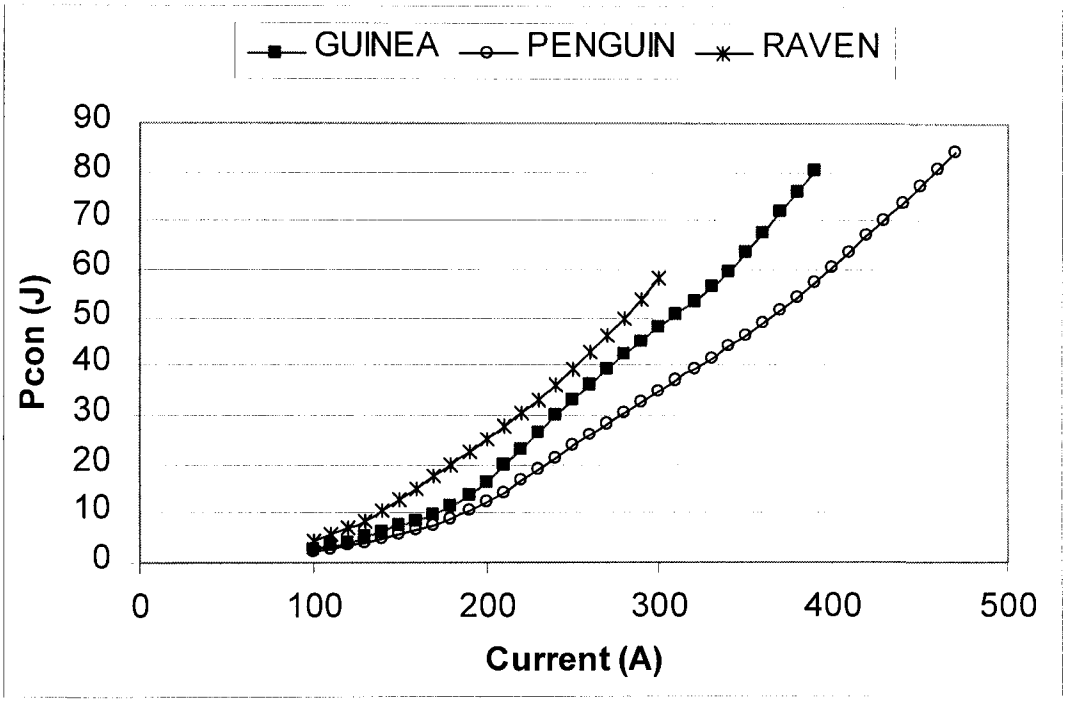

Figure 4.15 Variation of the convective cooling with the current

- **Radiative Cooling**

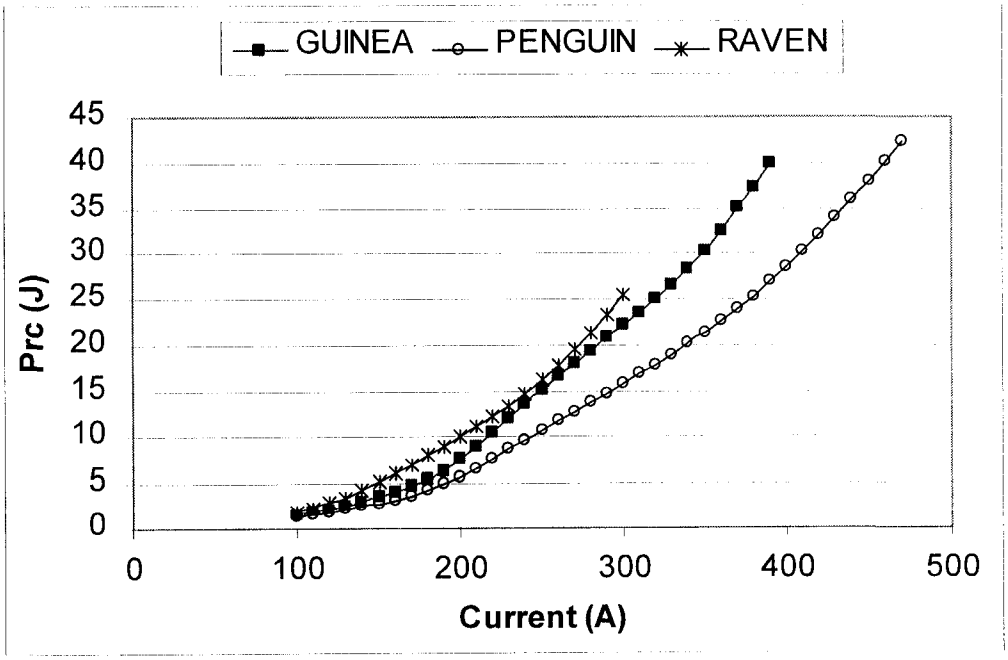

Figure 4.16 Variation of the radiative cooling with the conductor current

Figure 4.16 shows the predicted variation of the radiative cooling with the current for Guinea, Penguin, and Raven respectively. The radiative cooling increases with the increases of the current and the conductor temperature. The radiative cooling is a function of the emissivity, the diameter of the conductor, the conductor surface temperature, and the ambient temperature. Among all the parameters, the conductor temperature is the most important one. From previous explanation it is not surprising for us to see that Raven conductor has the highest rate of cooling among the three for fixed current levels.

To derive the formula to calculate the radiative heat loss, we assumed the ground and sky temperatures are equal to the ambient temperature based on "the radiative heat loss for a typical conductor does not exceed 30 % of the total heat loss" [27]. The total heat loss in the Integrated Model consists of the convective heat loss and the radiative heat loss. The convective heat loss P_{con} for Guinea conductor at 390 A is 80 J and the radiative heat loss P_{rc} is 40 J, for Penguin conductor: P_{con} = 84 J and P_{rc} = 42 J at 470 A, for Raven: P_{con} = 58 J and P_{rc} = 25 J at 300 A. The radiative heat loss is one third of the total heat loss for single layer ACSR conductors.

- **Stress of the Aluminum Layer**

The variation of the stress of the aluminum layer with the current is shown in Figure 4.17. The aluminum stress decreases with an increase of the conductor current. The variation of the stress for Raven conductor is the largest among the three. Figure 4.17 shows the variation of the aluminum stress for Guinea conductor from 100 A to 390 A is 43 MPa. When the current is larger than 360 A (temperature at 105 °C), the negative value of the aluminum stress for Guinea conductor in Figure 4.17 means that the aluminum layer experiences a compressive load which is opposite to the elongation direction. The variation of the aluminum stress for Penguin conductor is 80 MPa from 100 A to 470 A, and for Raven, 91 MPa from 100 A to 300 A.

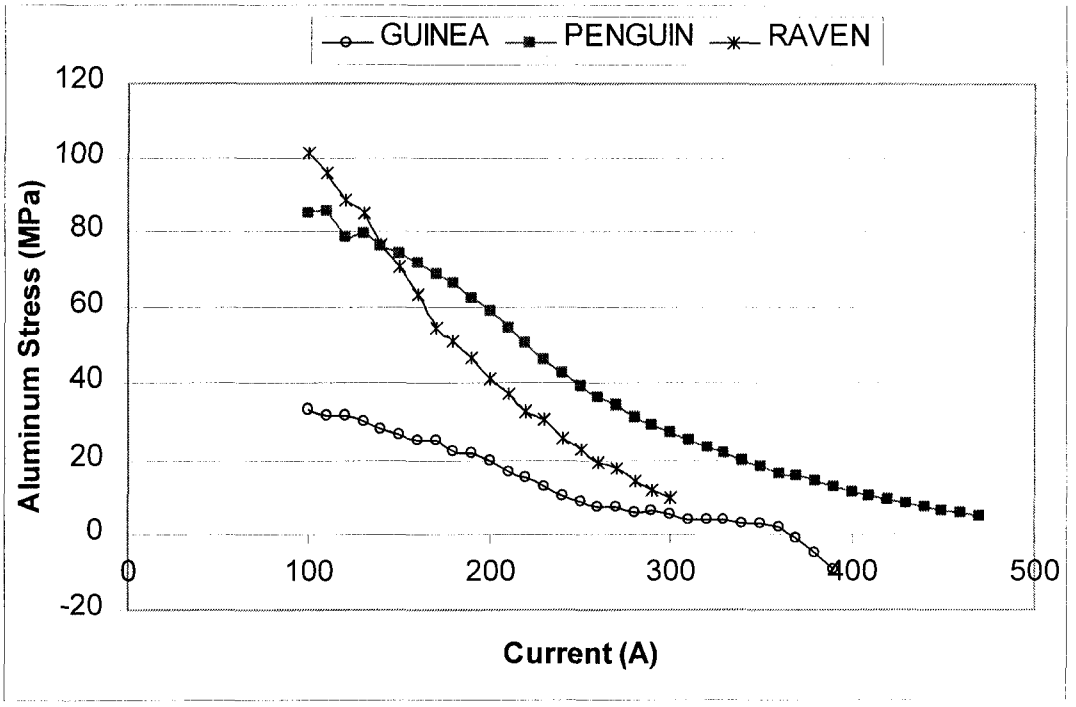

Figure 4.17 Variation of the aluminum stress with the conductor current

The steel core is supposed to carry most of the tension and stress of ACSR conductors. The aluminum layer is supposed to conduct most of the current. This is the case for three layer ACSR conductors. According to Filipovic-Gledja's work [4], the aluminum wires of Grackle experience 11 MPa at 200 A when the ambient temperature is 20 °C. The aluminum stress decreases with an increase of the conductor current. The aluminum layer of Raven conductor experiences 101 MPa at 100 A which drops to 41 MPa at 200 A. The aluminum wires of single layer ACSR experience higher stress than those of three layer ACSR.

- **Horizontal Tension**

Figure 4.18 shows the variation of the horizontal tension with the conductor current for three kinds of single layer ACSR conductors. The horizontal tension decreases with an increase of the conductor current. The horizontal tension curves are obtained when the current increases from 100 A to the maximum values and the span length keeps 400 m invariant.

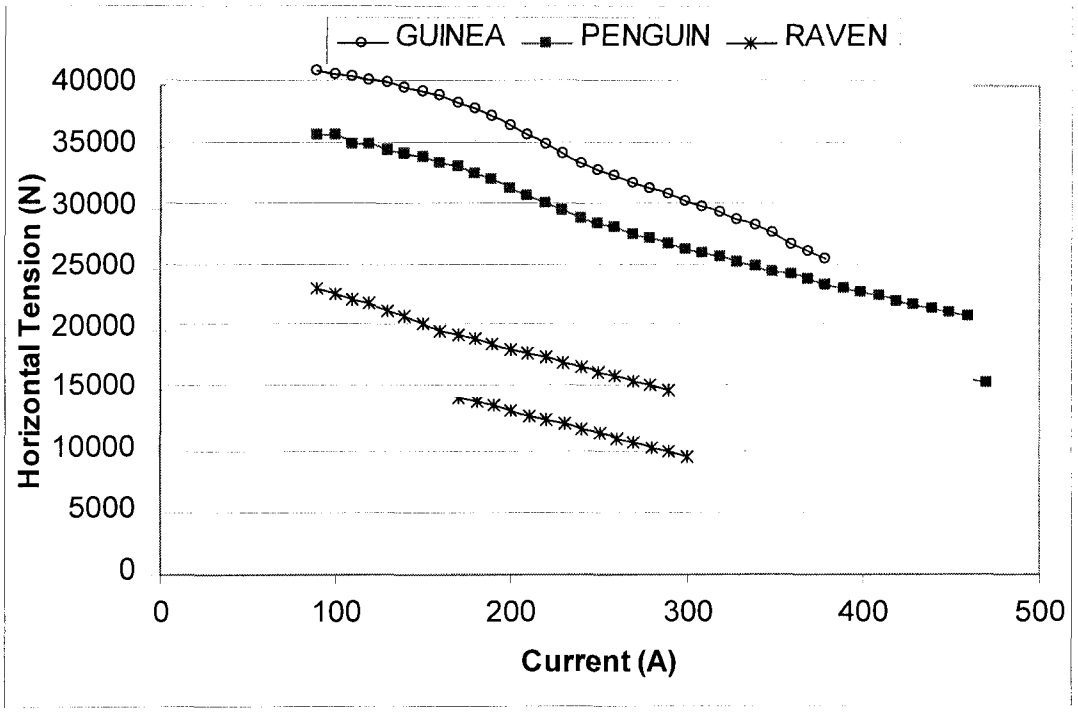

Figure 4.18 Variation of the horizontal tension with the conductor current

- **Sag**

The variation of the sag with the conductor current is shown in Figure 4.19 for Guinea, Penguin, and Raven, respectively. The sag curves are calculated under 400 m span length for three conductors. The sag increases with increasing conductor current. Take Guinea conductor as an example, the increasing rate is low when the current is smaller than 200 A. From 200 A to 360 A, the increasing rate is high. When current is larger than 360 A, the sag increases dramatically with the compressive load.

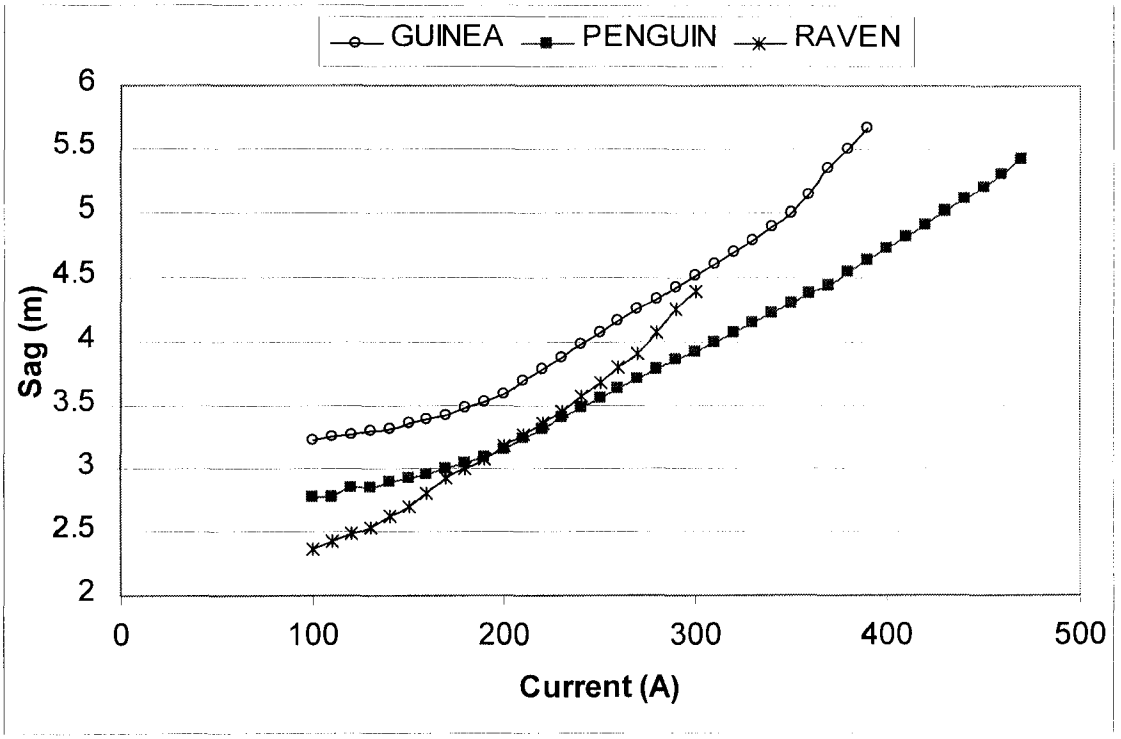

Figure 4.19 Variation of the sag with the current for three conductors

- **Loss of Tensile Strength of the Aluminum Layer**

The loss of tensile strength of the aluminum layer due to annealing increases with an increase of the current as shown in Figure 4.20. The difference of the tensile strength loss among the three conductors increases with increasing current because the temperature difference increases as well.

The loss of tensile strength of three-layer ACSR Grackle is only 20 % with 1400 A at 20 °C ambient temperature [4]. From Figure 4.20, we can see the loss of tensile strength of single layer ACSR conductors reaches over 30 % at 20 °C ambient temperature, 37 % for Penguin conductor. The aluminum wires of single layer ACSR experience higher stress and lose larger tensile strength than the aluminum wires of three layer ACSR conductors.

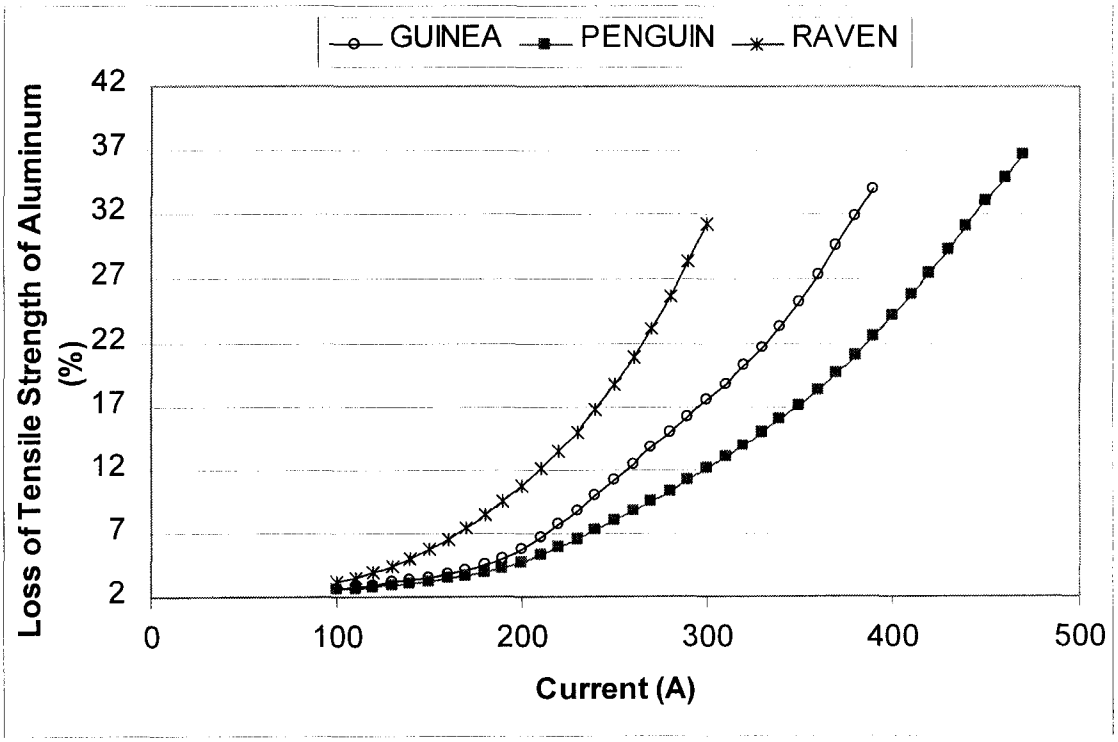

Figure 4.20 Variation of the loss of tensile strength of aluminum with the current

CHAPTER 5
INVESTIGATIONS OF THE INTEGRATED MODEL

5.1 Introduction

The previous chapter validates the Integrated Model through the comparison with the physical experimental model. This chapter considers the Integrated Model in respect of a variation of environmental conditions to investigate the operational behaviors of single layer ACSR conductors.

The advantages of the Integrated Model allow a transmission line designer or conductor manufacturer to test the existing conductor types and to analyze new conductor constructions. The Integrated Model provides information related to all aspects of single layer ACSR behaviors. Not only can it predict the variation of heat gains and heat losses, the loss of tensile strength of the aluminum layer, the horizontal tension, the aluminum stress, and the sag with the variation of conductor current, but also it can predict the effect of variation of lay length and supply frequency for single layer ACSR conductors. The Integrated Model can also be used to investigate the influence of the environment on the conductor parameters. For example, we include variation of the ambient temperature, time of exposure, additional loads, air gap thickness, and span length, etc.

This chapter describes the investigation of the Integrated Model with variation of the parameters: lay length, ambient temperature, power supply frequency, time of conductor exposure, air gap thickness inside conductor, and span length. All investigations in this chapter were performed on Guinea, Penguin, and Raven conductors with typical conditions such as 10 °C ambient temperature, 60 Hz supply frequency, 10 years time of exposure, 1 μm air gap thickness, and 400 m span length, etc. The pre-tensioning conditions are set as 50% of each RTS and lasting for an hour for three types single layer conductors.

5.2 Lay Length

Lay factor is defined as the ratio of length of lay to nominal outside diameter of aluminum layer for ACSR in ASTM standard: [20]

ACSR	Min	Preferred	Max
12/7	10	12.5	14.5
6/1	12	13	14.5

Usually, for single layer ACSR, we consider only lay factor of the aluminum layer indicated in the above table. According to the standard lay factor, we can calculate "minimum lay length", "preferred lay length", and "maximum lay length" for Guinea, Penguin, and Raven conductors, respectively. In the figures of this section, "MIN_LAY" means that the minimum lay length is used in the Integrated Model. Similarly,

"EXP_LAY" means the experimental lay length which is almost the same as the "preferred lay length". "MAX_LAY" means the maximum lay length used.

- **Effect of Current on AC Resistance and AC Reactance**

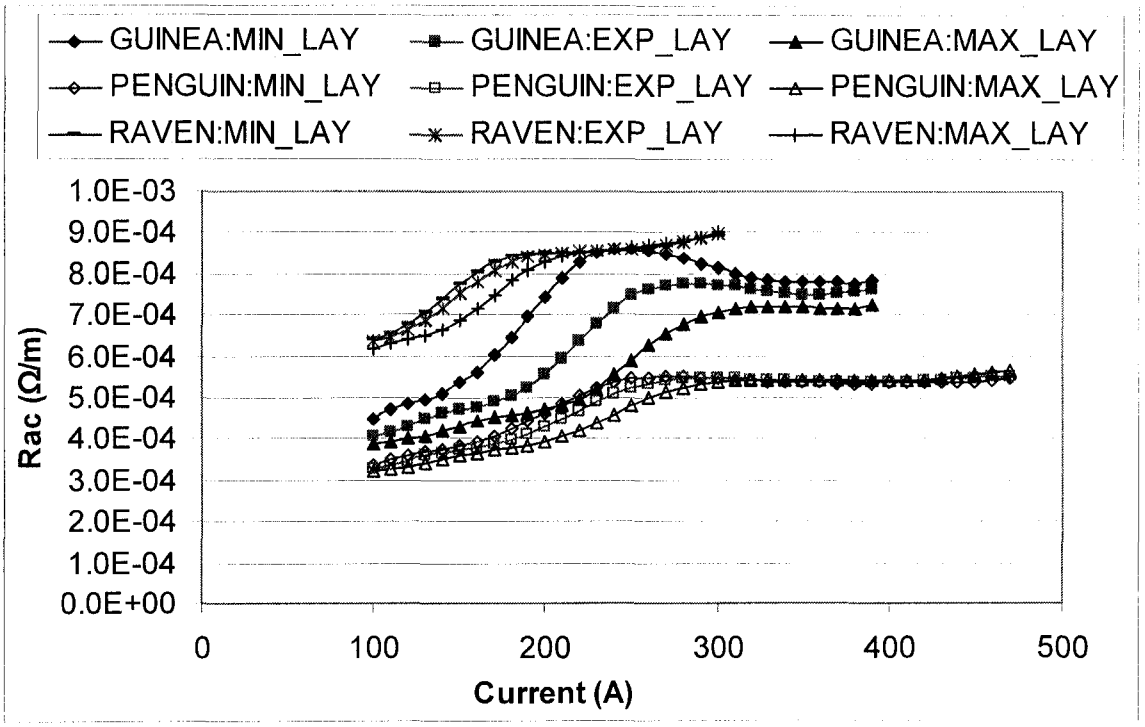

Figure 5.1 Variation of the ac resistance with the current at various lay lengths

Figure 5.1 shows the variation of the ac resistance with the conductor current for various lay lengths. From Figure 5.1 we can see that Guinea conductor is more sensitive to the variation of the lay length than Penguin and Raven conductors. For Guinea conductor, the variation of the resistance is obviously large when the conductor current ranges from 150 A to 300 A. Penguin and Raven conductors exhibit similar results, although the variation is not as obvious. The shorter the lay length, the larger the resistance is, and the lower the current at which the steel core approaches saturation. The maximum lay length results in the smallest ac resistance.

The effect of the lay length to ac resistance is easily seen from Figure 5.2. For Guinea conductor, the maximum ac/dc resistance ratio is 2.22 around 240 A when the minimum lay factor is used; the maximum ac/dc resistance ratio is 1.78 at 300 A when the maximum lay factor is used. The steel core approaches saturation of lower currents with the minimum lay length. For Penguin conductor, the maximum ac/dc resistance ratio is 1.89 at 250 A with the minimum lay length; 1.79 at 290 A with the maximum lay length. For Raven conductor, the maximum ratio is 1.45 at 180 A when the minimum lay length is used, and 1.40 at 210 A with the maximum lay length. From ac/dc resistance ratio we can predict that the power losses would be greatly reduced in the transmission

and distribution lines when the maximum lay length is exploited for single layer ACSR conductors.

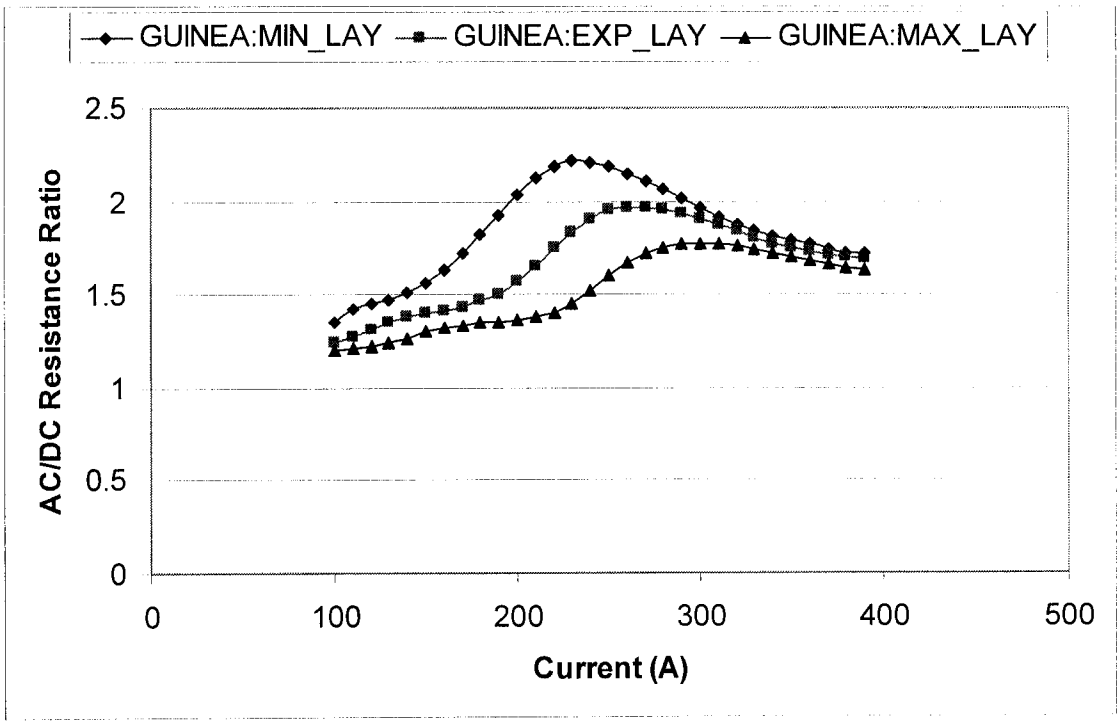

Figure 5.2 (a) Variation of the Rac/Rdc with current at various lay lengths for Guinea

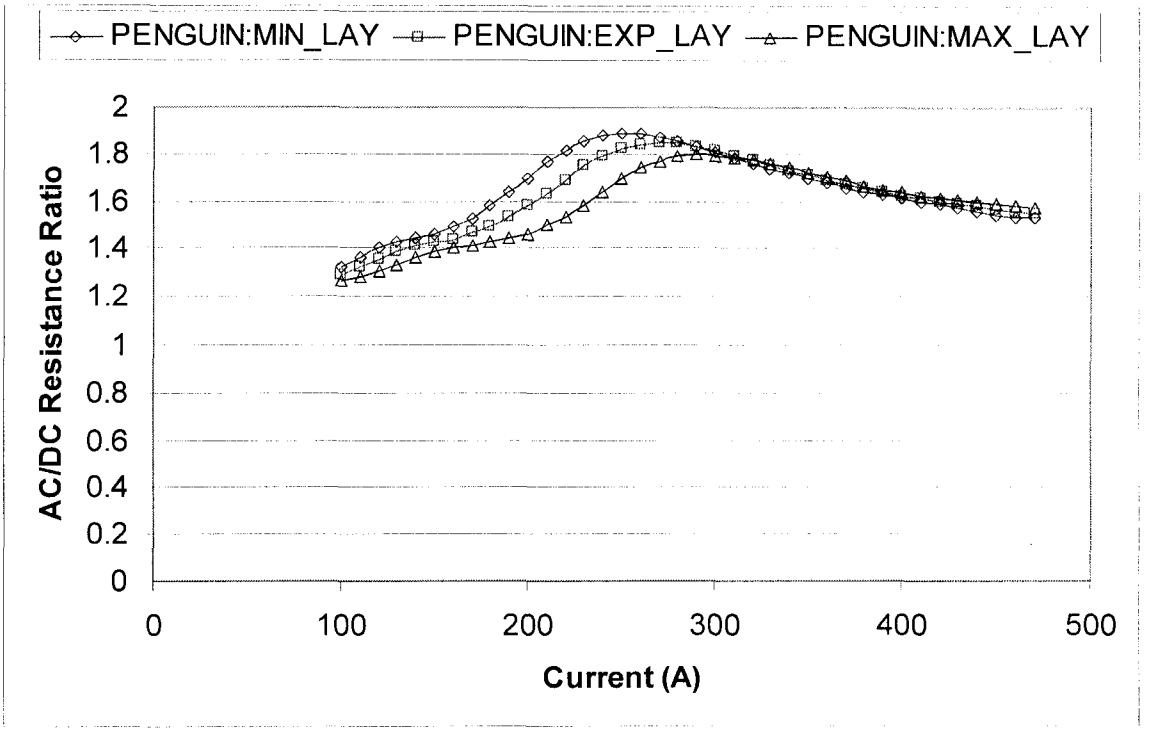

(b)

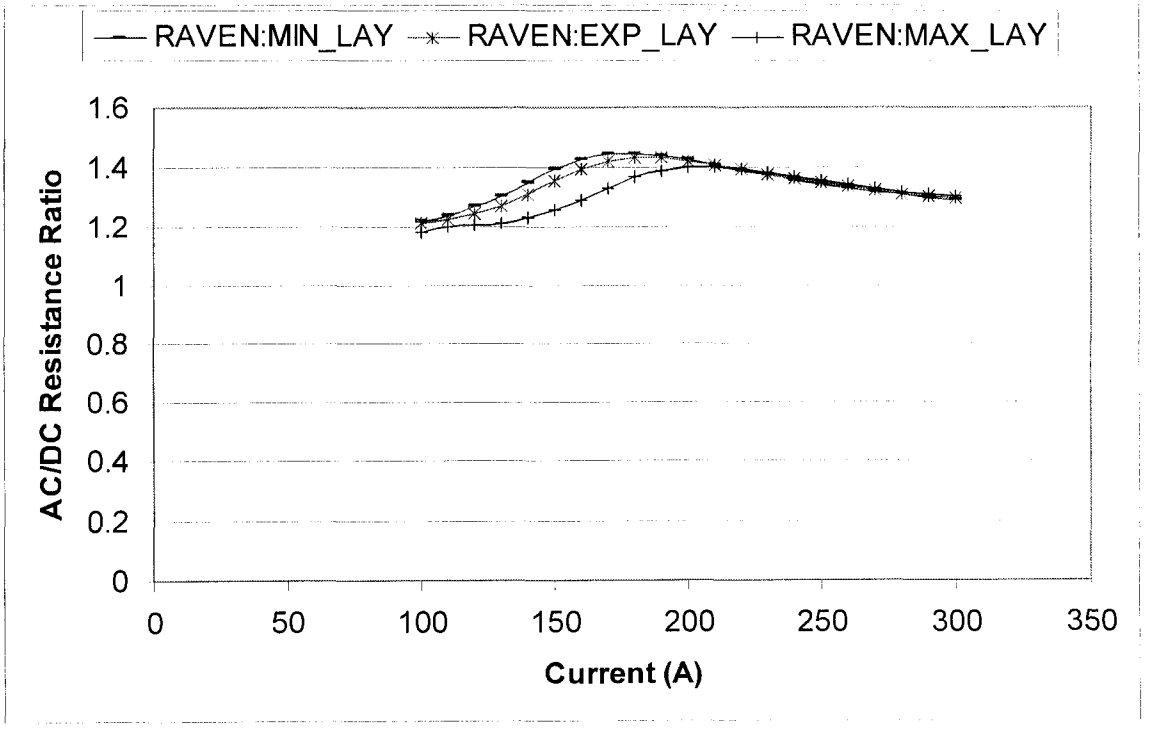

(c)

Figure 5.2 Variation of the Rac/Rdc with current at various lay lengths for (b) Penguin and (c) Raven conductors, respectively

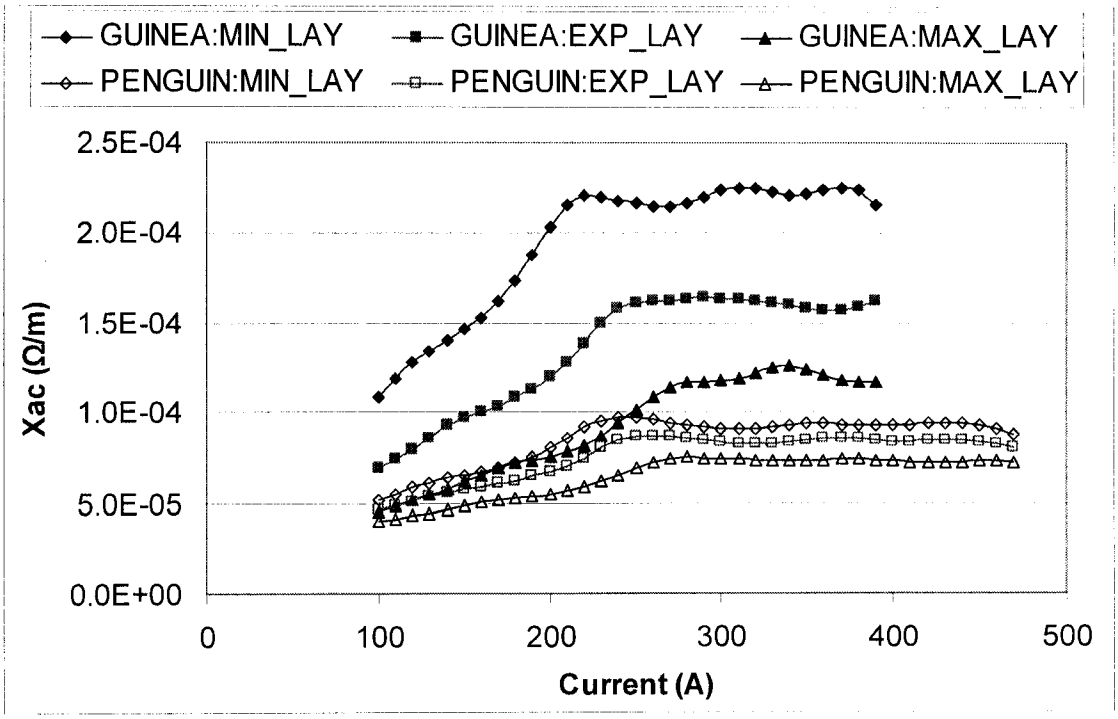

(a)

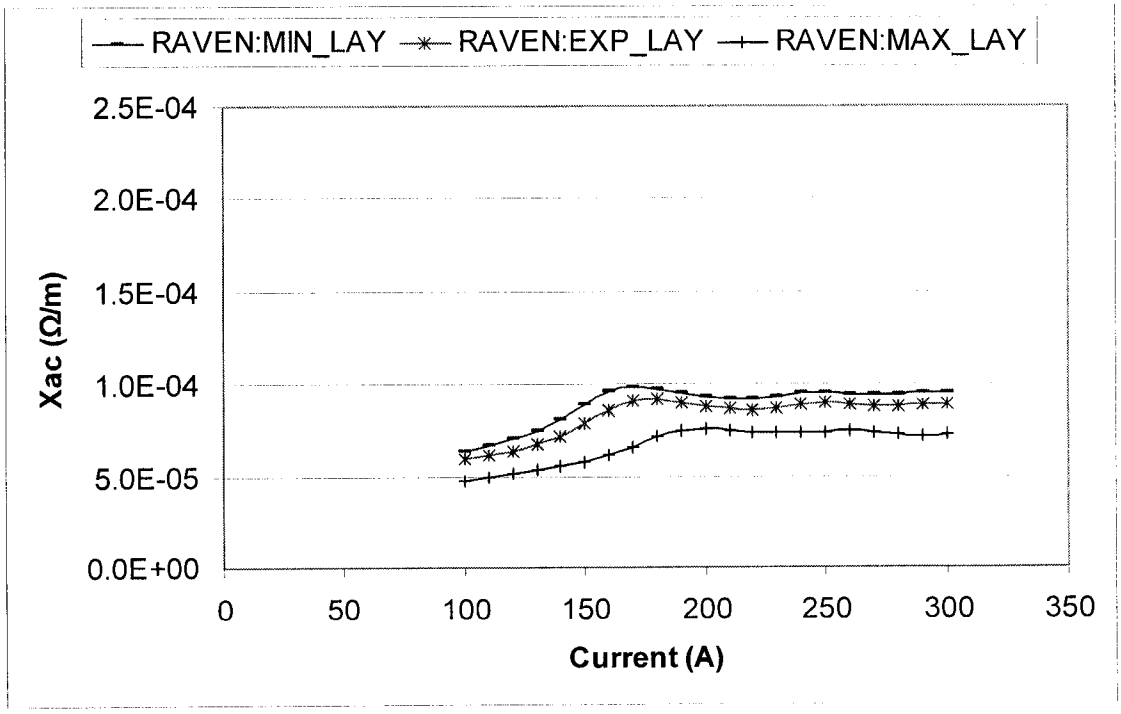

(b)

Figure 5.3 Variation of the ac reactance with current at various lay lengths for (a) Guinea and Penguin conductors, and (b) Raven conductor, respectively

The variation of ac reactance with lay length is similar to that of ac resistance (Figure 5.3). AC reactance is less when the maximum lay length is adopted. From Figure 5.3 (a) and (b), we can see that Guinea conductor is more sensitive to the difference between the minimum lay length and the maximum lay length than either Penguin or Raven. For Guinea conductor, the combination of outer steel layer wounded spiraling in the opposite direction to the aluminum layer results in a transformer effect. Consequently Guinea is more susceptible to changes in the aluminum layer lay length than those of Penguin and Raven conductors.

- **Effect on Convective and Radiative Cooling**

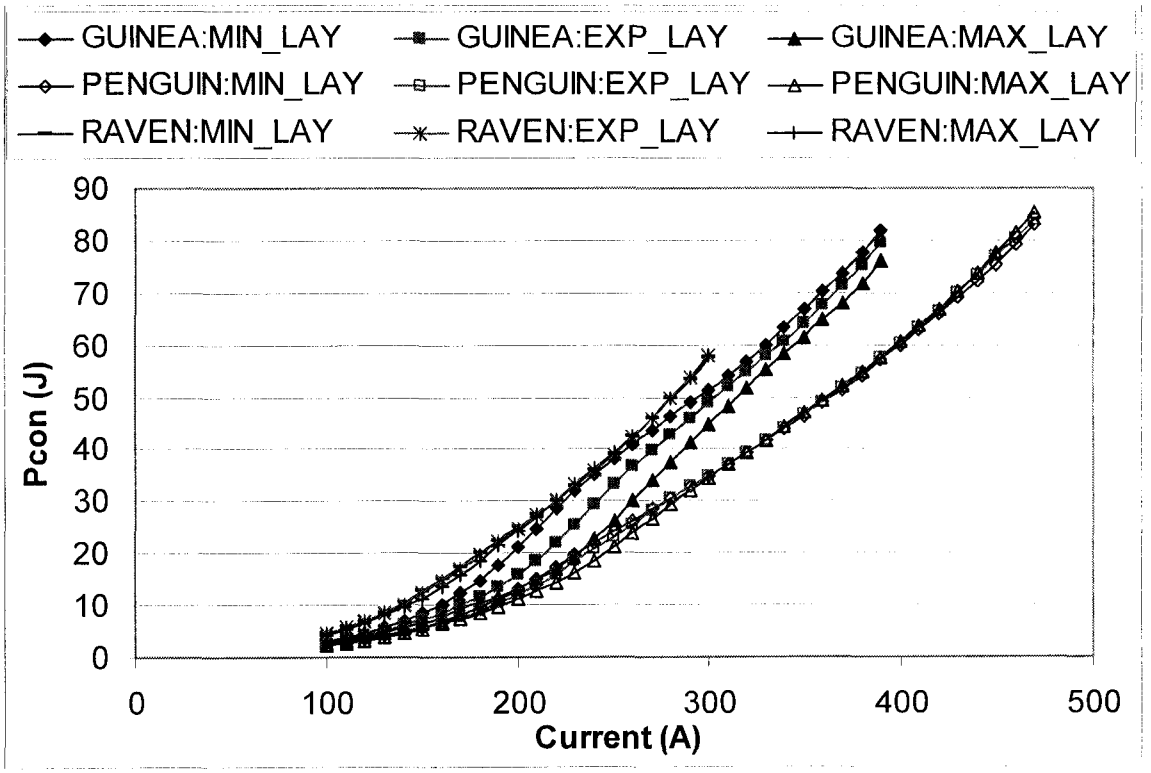

Figure 5.4 Variation of the convective cooling with the current and lay length

Figure 5.4 shows the variation of the convective cooling with current for different lay lengths of three types of single layer ACSR conductors. The convective cooling is a function of the conductor surface temperature. With the maximum lay length, the magnetic field is not as strong as with the minimum lay length. The surface temperature is thus lower with the maximum lay length than with the minimum lay length. The curves in Figure 5.4 show that the convective cooling is less with the maximum lay length than that with the minimum lay length.

The effect of lay length to the radiative cooling is shown in Figure 5.5. The convective cooling and radiative cooling of Guinea conductor are both more sensitive to

the variation of lay length than those of Penguin and Raven conductors. The radiative cooling with the maximum lay length is less than that with the minimum lay length.

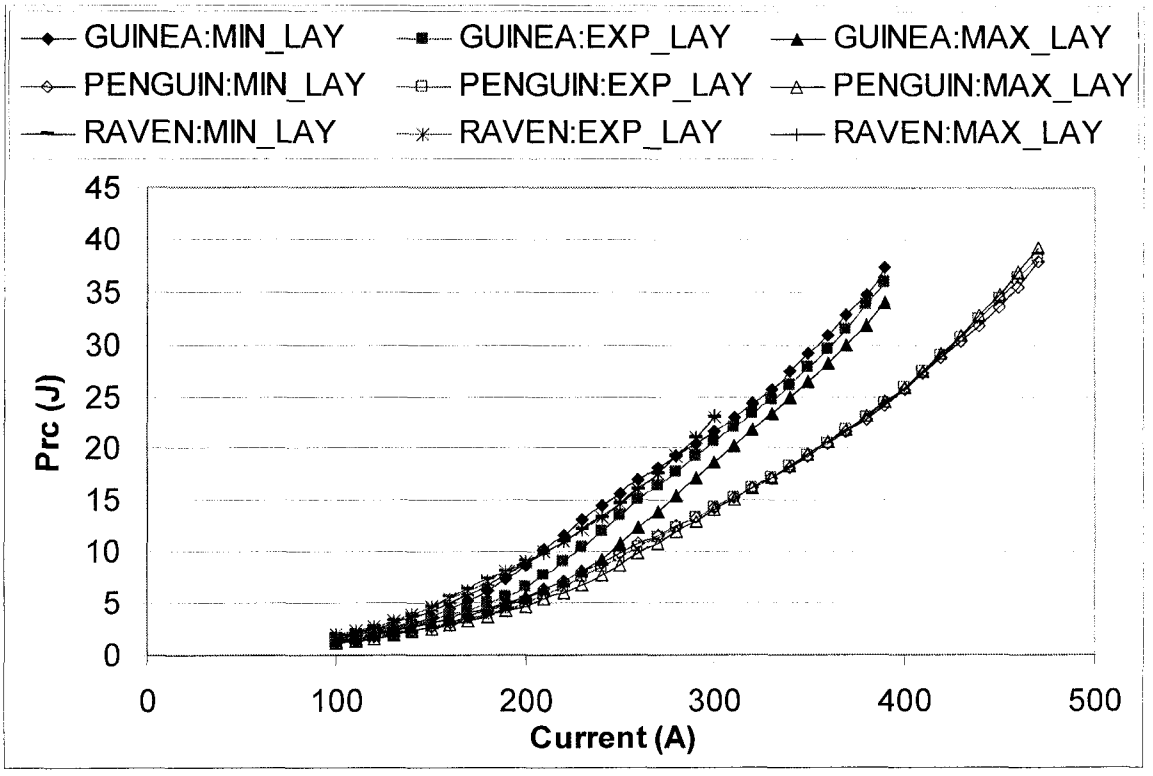

Figure 5.5 Variation of the radiative cooling with the current and lay length

- **Effect on Mechanical Properties**

As shown in Figure 5.6, the stress of the aluminum layer is not very sensitive to the variation of the lay length. For Guinea and Penguin conductors, the variation of the aluminum stress from 200 A to 300 A is more obvious than at other operating current regions. Raven conductor, which has a smaller strand diameter, is not as smooth with the minimum lay length as with the maximum lay length.

Generally speaking, the aluminum strands experience less stress with the minimum lay length than that with the maximum lay length. The total spiraling length increases per unit length when the minimum lay length is used so the corresponding stress on per unit spiraled aluminum strands decreases.

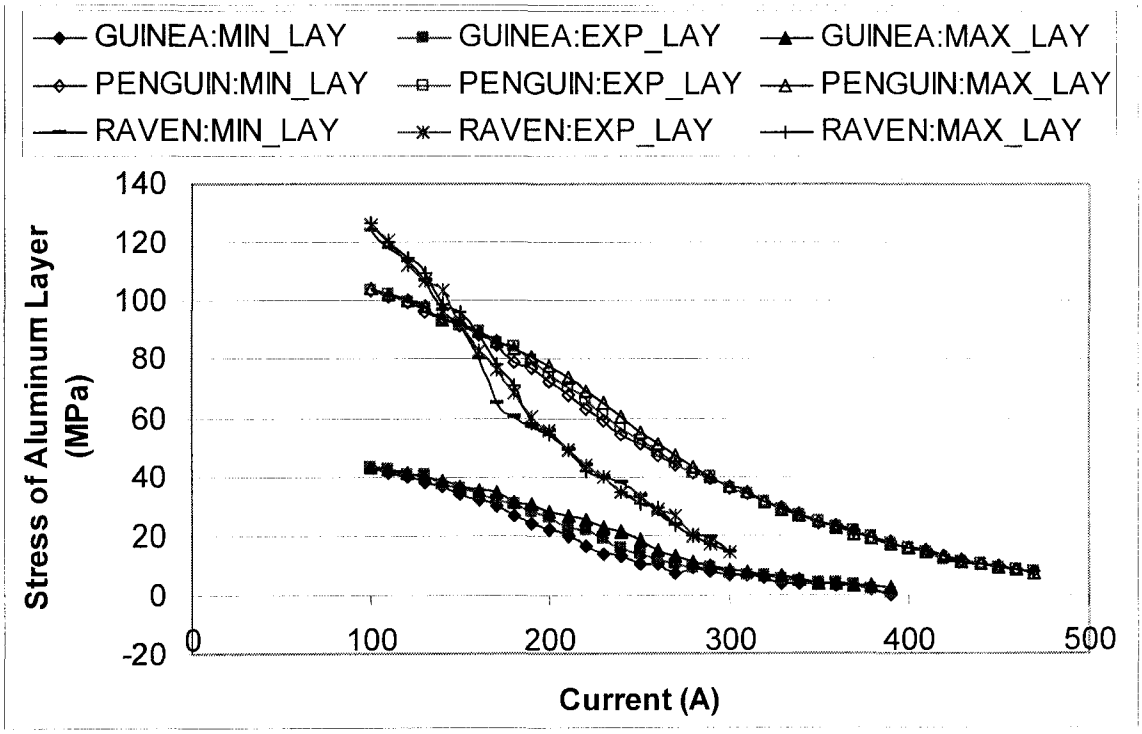

Figure 5.6 Variation of the aluminum stress with the current and lay length

The variation of the horizontal tension with the current at various lay lengths is shown in Figure 5.7. The horizontal tension of Penguin and Raven conductors is not sensitive to the change of the lay length. The horizontal tension of Guinea conductor is sensitive to the variation of the lay length when the current is between 150 A and 300 A. The minimum lay length results in smaller horizontal tension than the maximum lay length, as we can see this in Figure 5.7.

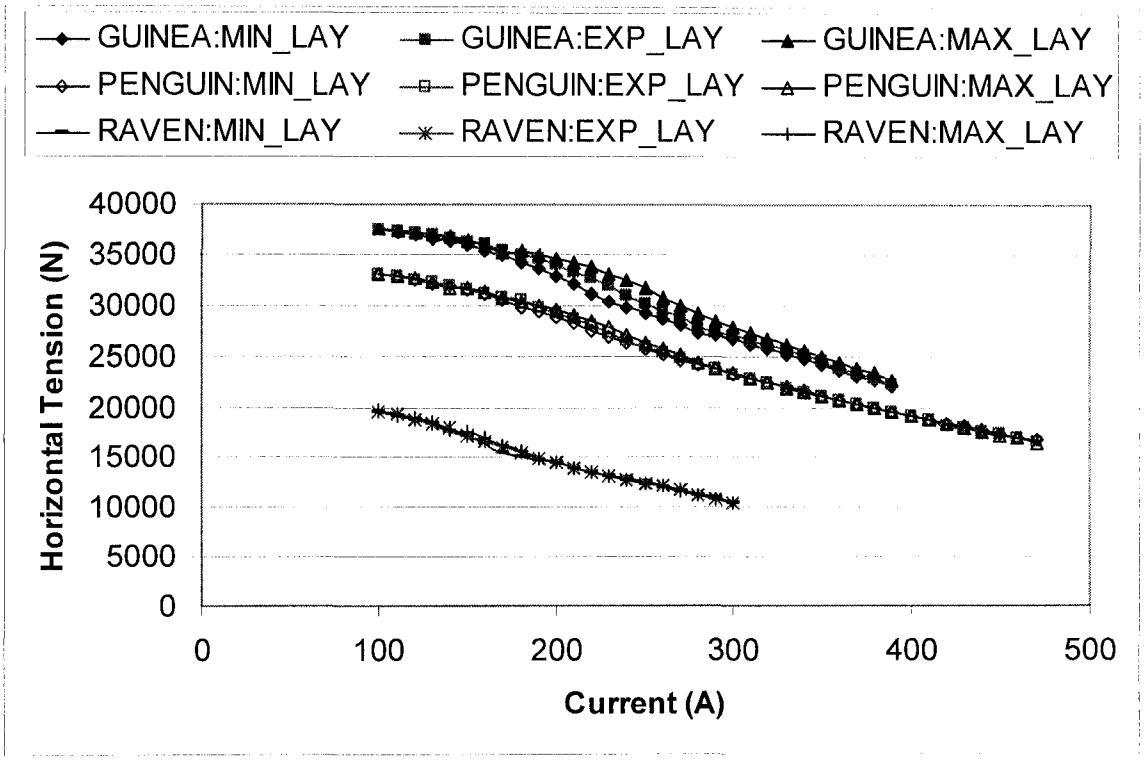

Figure 5.7 Variation of the horizontal tension with the current and lay length

The sag calculation is related to the variation of stress and horizontal tension. The variation of the sag with the current and lay length is shown in Figure 5.8. For Guinea conductor, the minimum lay length results in larger sag and higher temperature than the maximum lay length does.

The loss of tensile strength of the aluminum layer with various currents and lay lengths is shown in Figure 5.9 for Guinea, Penguin, and Raven conductors, respectively. The loss of tensile strength is a function of sustained conductor higher temperatures. The minimum lay length results in larger resistance and higher temperature, and consequently, it results in higher tensile strength loss in the aluminum strands. Taking Guinea as an example, the loss of tensile strength is 29.3 % at 390 A when the minimum lay length is used. It is 26.6 % at 390 A when the maximum lay length is used. The difference is 2.7 %.

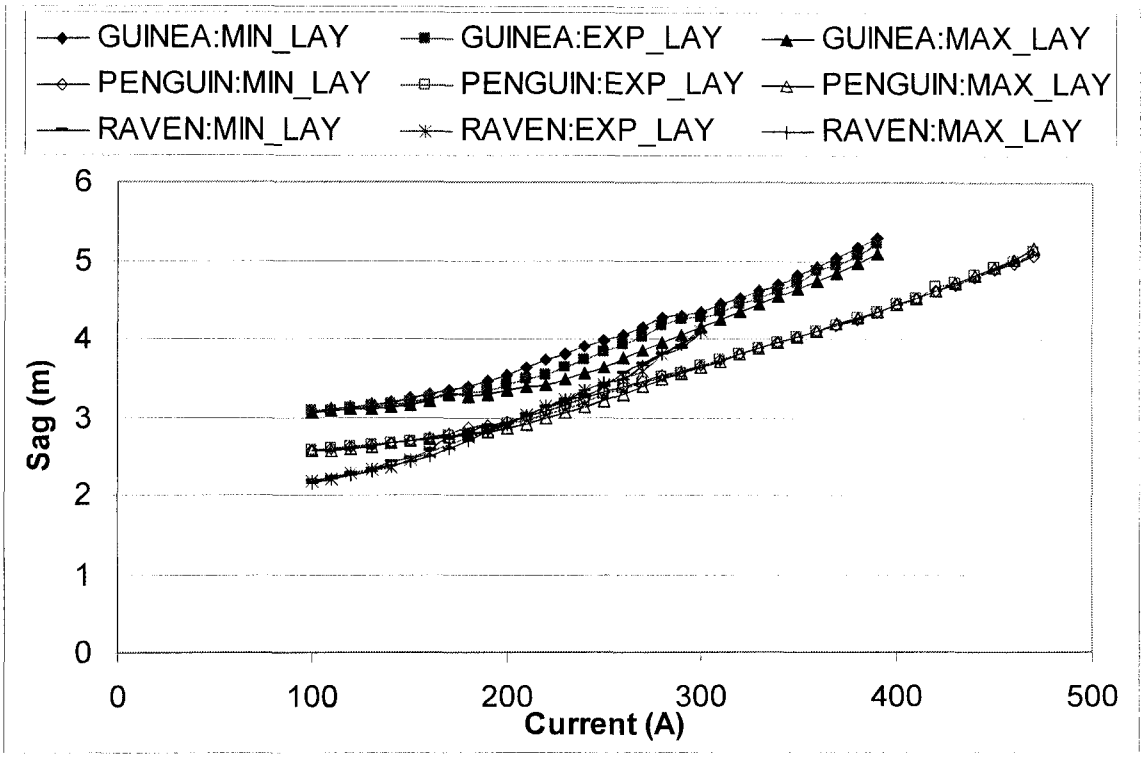

Figure 5.8 Variation of the sag with the current at various lay lengths

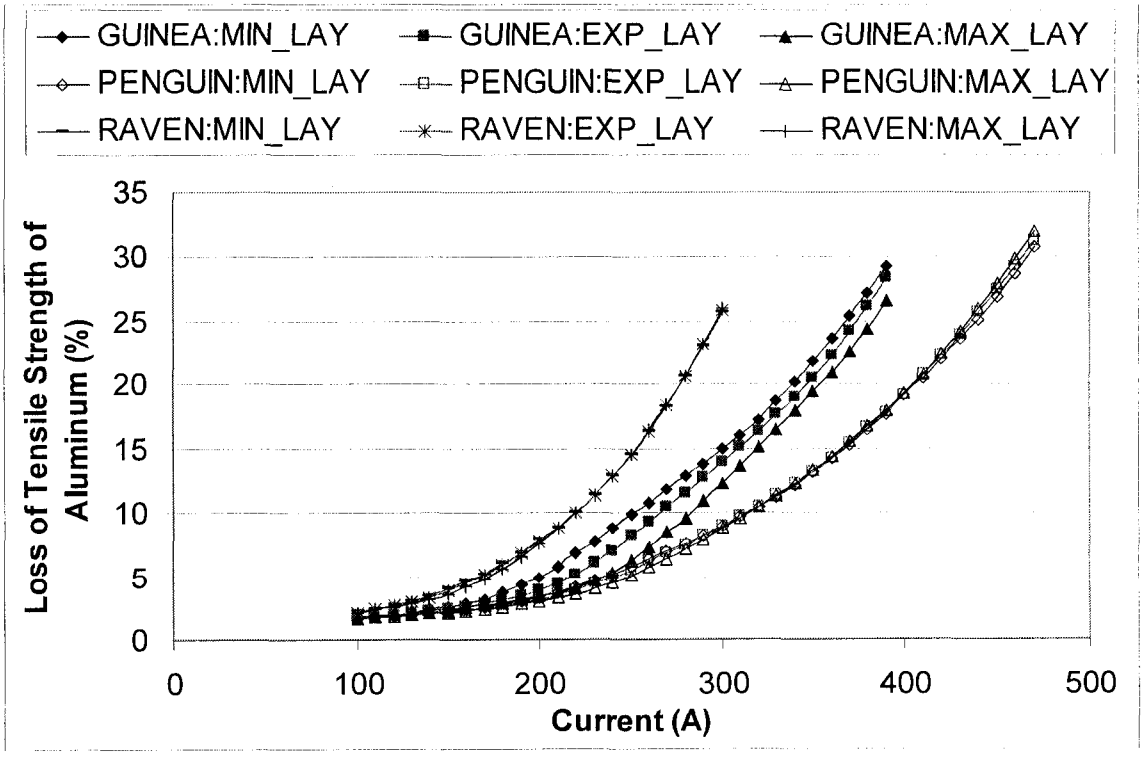

Figure 5.9 Variation of the loss of tensile strength with the current and lay length

5.3 Ambient Temperature

The ambient temperature is acceptable from a mean annual average temperature of 0 °C to 30 °C. The ambient temperature will affect the properties of the conductor. The investigation of this part shows the variation of the conductor properties when the average ambient temperature is taken as four conditions: 0 °C, 10 °C, 20 °C, and 30 °C.

All figures in this section are calculated under the same conditions such as that the experimental lay length, frequency, and time of exposure etc. are the same, and additionally that the ambient temperature varies from 0 °C to 30 °C for comparison.

- **Effect of Ambient Temperature on AC Resistance and AC Reactance**

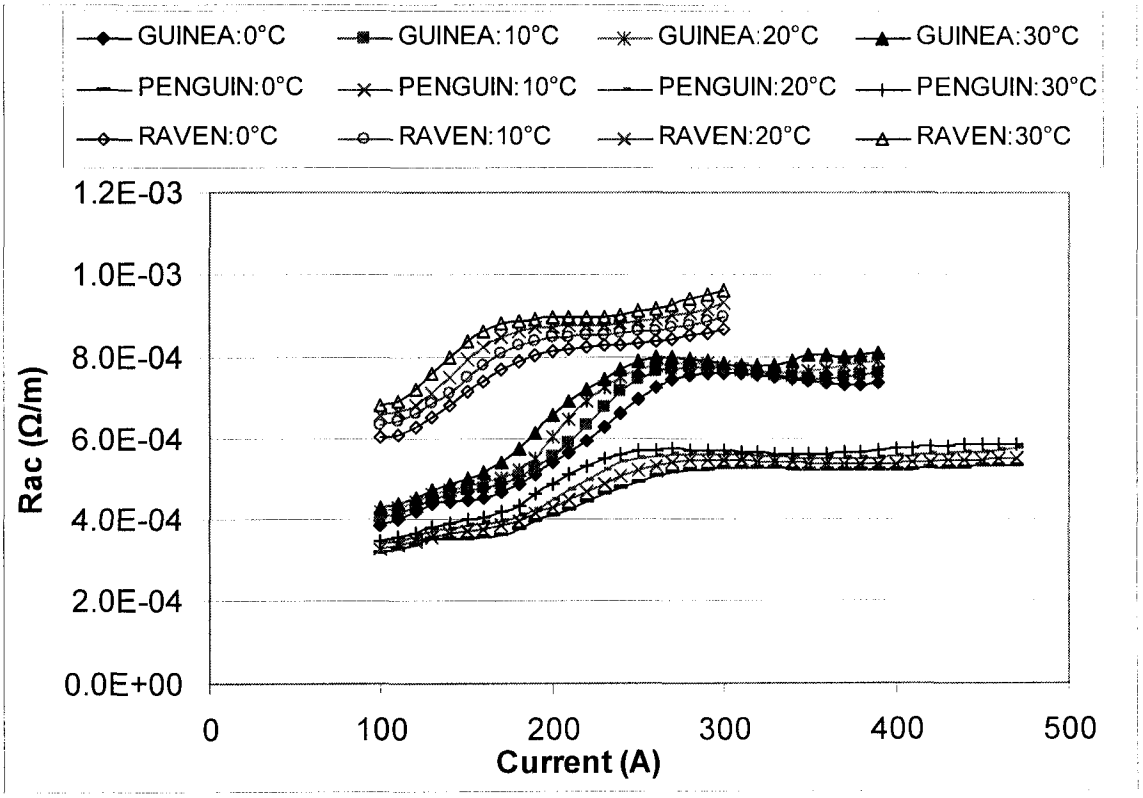

Figure 5.10 Variation of the ac resistance with the current and ambient temperature

Figure 5.10 shows the variation of the ac resistance with the current at ambient temperatures of 0 °C, 10 °C, 20 °C, and 30 °C. The ac resistance increases with increases of current and ambient temperature. For three types of single layer ACSR conductors, resistances at 0 °C ambient temperature are the smallest and the largest at 30 °C ambient temperature. For Guinea conductor, there is overlap of resistance curves from 290 A to 320 A at different ambient temperatures. At saturation, the ac resistance does not increase linearly with an increase of the ambient temperature. The same thing occurs for Penguin conductor from 310 A to 330 A.

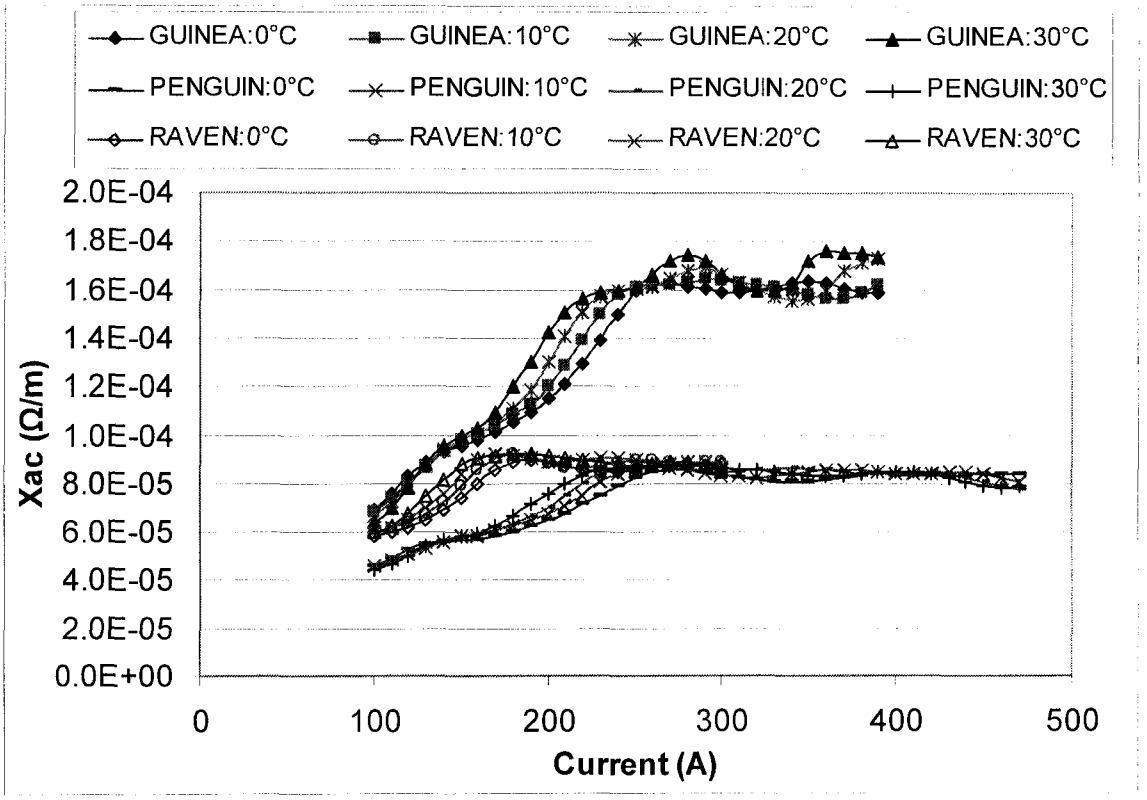

Figure 5.11 Variation of the ac reactance with the current and ambient temperature

The variation of the ac reactance with current at four ambient temperatures is shown in Figure 5.11. Generally, the lower the ambient temperature, the smaller the ac reactance is. Reactance curves are sensitive to the variation of the electromagnetic field inside the ACSR conductors. Reactive curves are not increasing monotonically when the electromagnetic field changes with ambient temperature at various currents.

Comparing the resistance curves in Figure 5.10 and the reactance curves in Figure 5.11, we can see that the resistance curves change is smoother than the reactance curves at four different ambient temperatures.

- **Effect on Convective and Radiative Cooling**

The resistive Joule heating is proportional to the resistance with constant current. The resistive heat losses increase with an increase of the ambient temperature if the same surface temperature rise of the conductor is reached.

The convective cooling does not change much with a variation of the ambient temperature, as we can see from Figure 5.12.

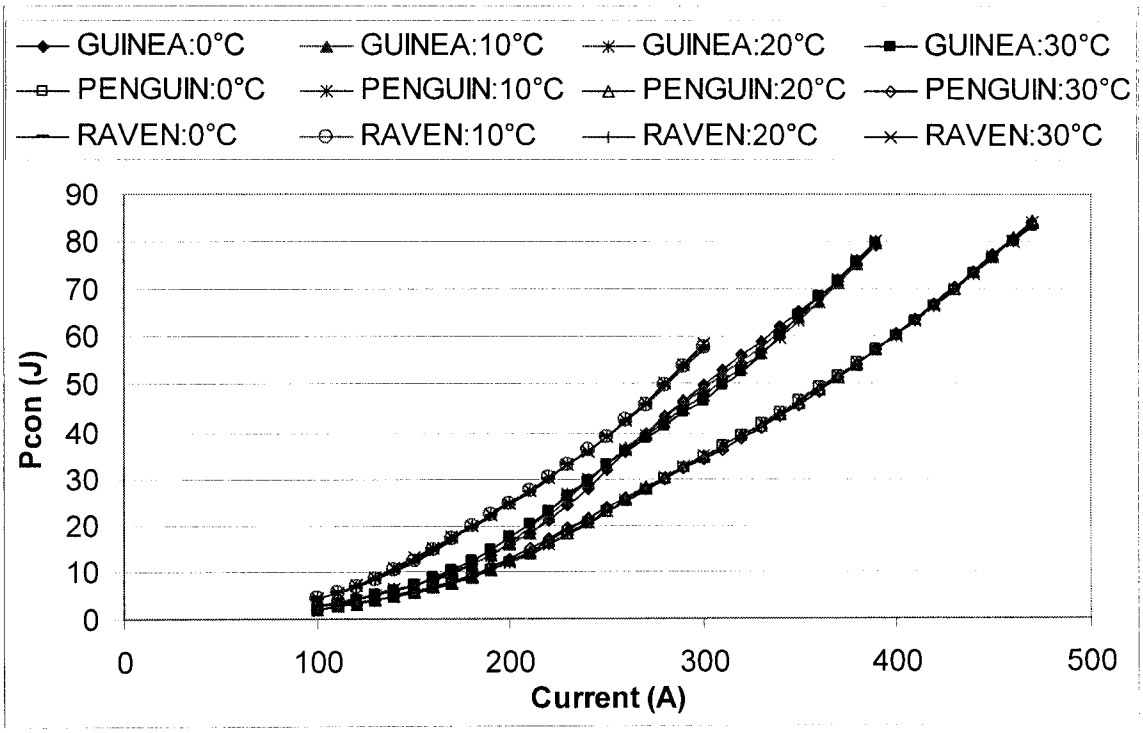

Figure 5.12 Variation of convective cooling with the current and ambient temperature

Figure 5.13 shows the variation of radiative cooling with current and ambient temperature for Guinea, Penguin, and Raven conductors. The radiative cooling increases with increases in the current and ambient temperature. The variation is more obvious than that of the convective cooling. For Guinea conductor at 390 A, the radiative cooling is 43 W/m at 30 °C ambient temperature and 32 W/m at 0 °C ambient temperature.

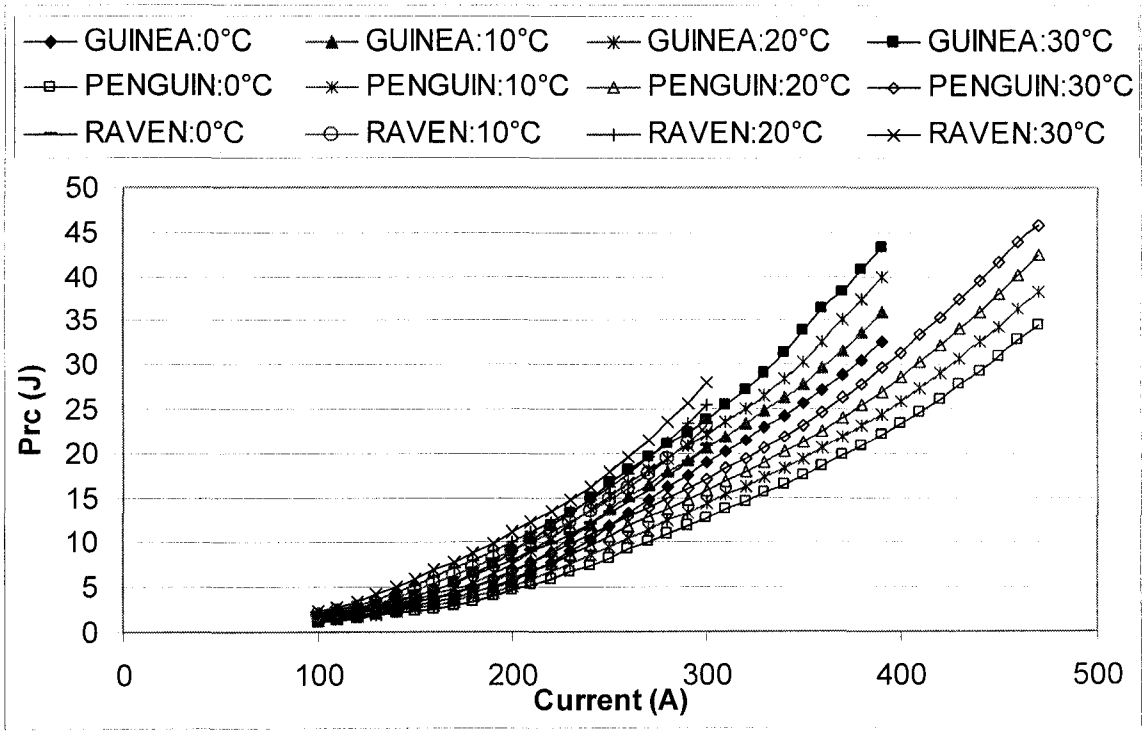

Figure 5.13 Variation of the radiative cooling with the current and ambient temperature

In the calculation of the radiative cooling, the ground and sky temperature are assumed to be equal to the ambient temperature. Rewrite the radiative cooling Eq. (2.48) as:

$$P_{rc} = \pi D \sigma_B \varepsilon_S (T_{sur} - T_{amb})(T_{sur} + T_{amb} + 556)[(T_{sur} + 273)^2 + (T_{amb} + 273)^2] \quad \text{W/m} \quad (5.1)$$

Consequently, small variations between surface temperatures and ambient temperatures cause substantive changes in radiative cooling.

- **Effect on Mechanical Properties**

The variation of the aluminum stress for Guinea and Penguin conductors with current and the ambient temperature is shown in Figure 5.14 (a), and for Raven conductor in Figure 5.14 (b). The stress of the aluminum layer decreases with increases of the current and the ambient temperature. The aluminum wires experience larger stress at 0 °C ambient temperature than at 30 °C ambient temperature for single layer ACSR conductors. It is seen from Figure 5.14 that the aluminum stress in the conductors decreases almost exponentially after 200 A. From 100 A to 200 A, the aluminum stress decreases linearly with an increase of the current.

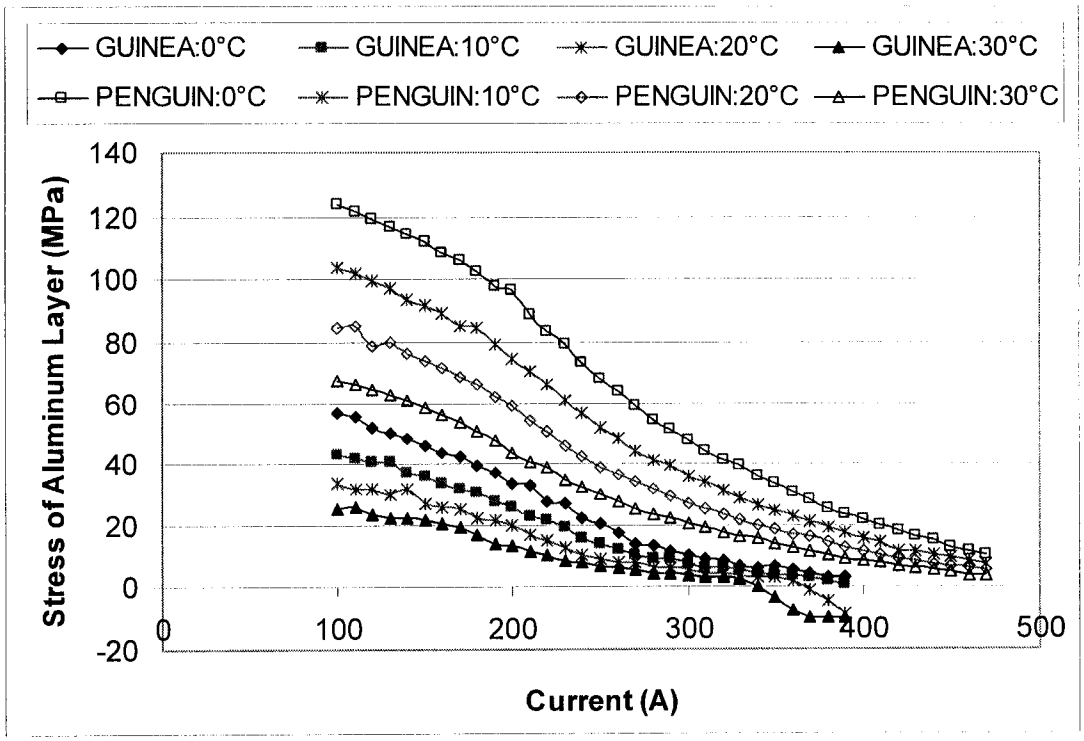

(a)

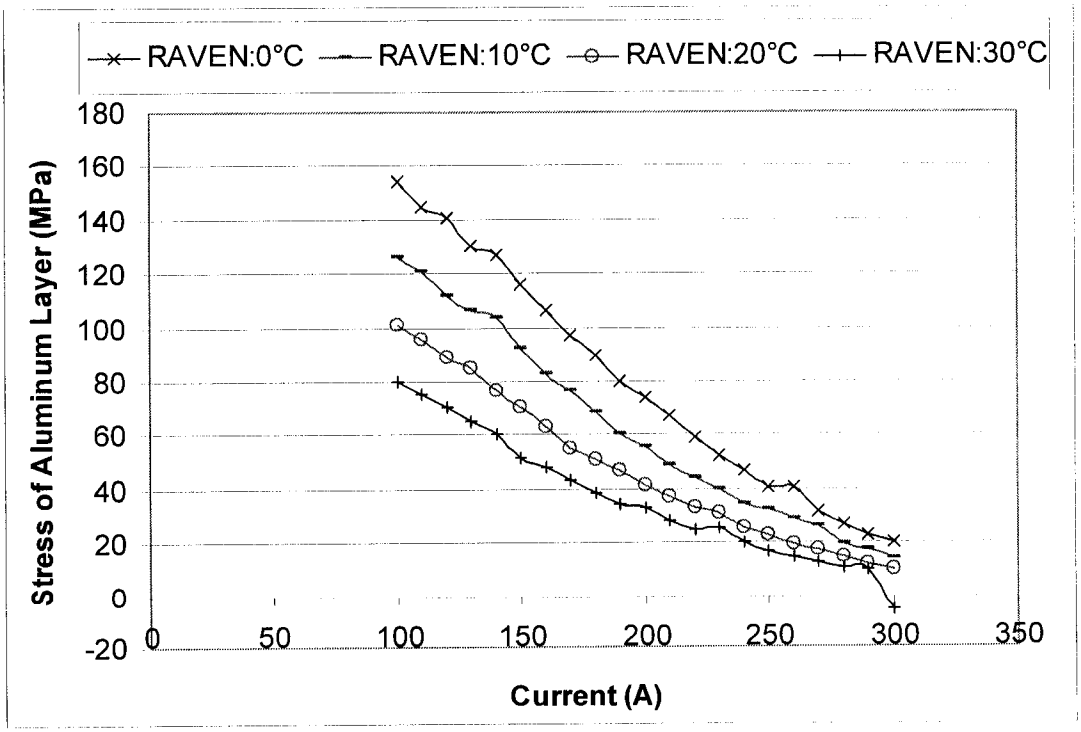

(b)

Figure 5.14 Variation of the aluminum stress with the current and ambient temperature for (a) Guinea and Penguin conductors, and (b) Raven conductor, respectively

From Figure 5.14 (a), we can see that the aluminum layer of Guinea conductor experiences a compressive load at 30°C ambient temperature when the current is higher than 340 A. At higher ambient temperatures, this conductor approaches its birdcaging temperature. The thermal rating should be paid attention for the conductor used in high ambient temperature areas.

The variation of horizontal tension with current and ambient temperature for Guinea conductor is shown in Figure 5.15 (a) and for Penguin and Raven conductors in Figure 5.15 (b), respectively. The horizontal tension decreases with increases of the current and the ambient temperature. From Figure 5.15 we can see that the horizontal tension of the conductors decreases more or less linearly, except for Penguin in which saturation effects can be noted.

The variation of the sag with the conductor current and ambient temperature is shown in Figure 5.16 (a) for Guinea conductor, Figure 5.16 (b) for Penguin conductor, and Figure 5.16 (c) for Raven conductor, respectively. The sag increases with increases of the current and the ambient temperature in all cases exponentially. The difference between 0 °C and 30 °C ambient temperatures results in one meter length difference in the sag at the maximum current ratings for single layer ACSR conductors.

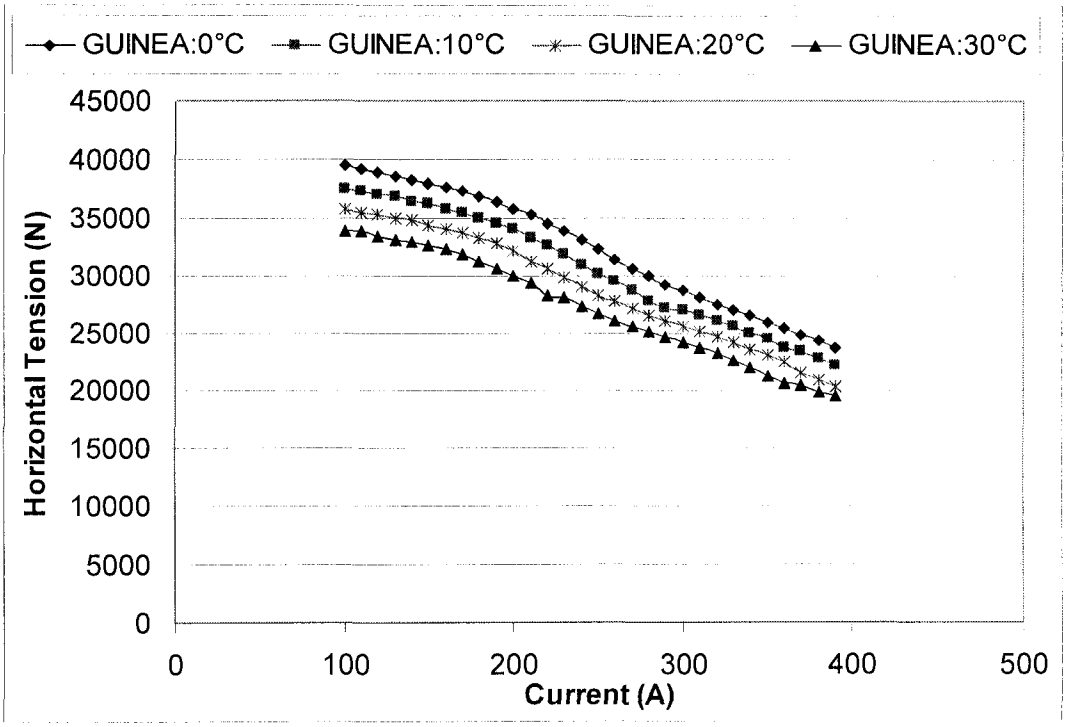

(a)

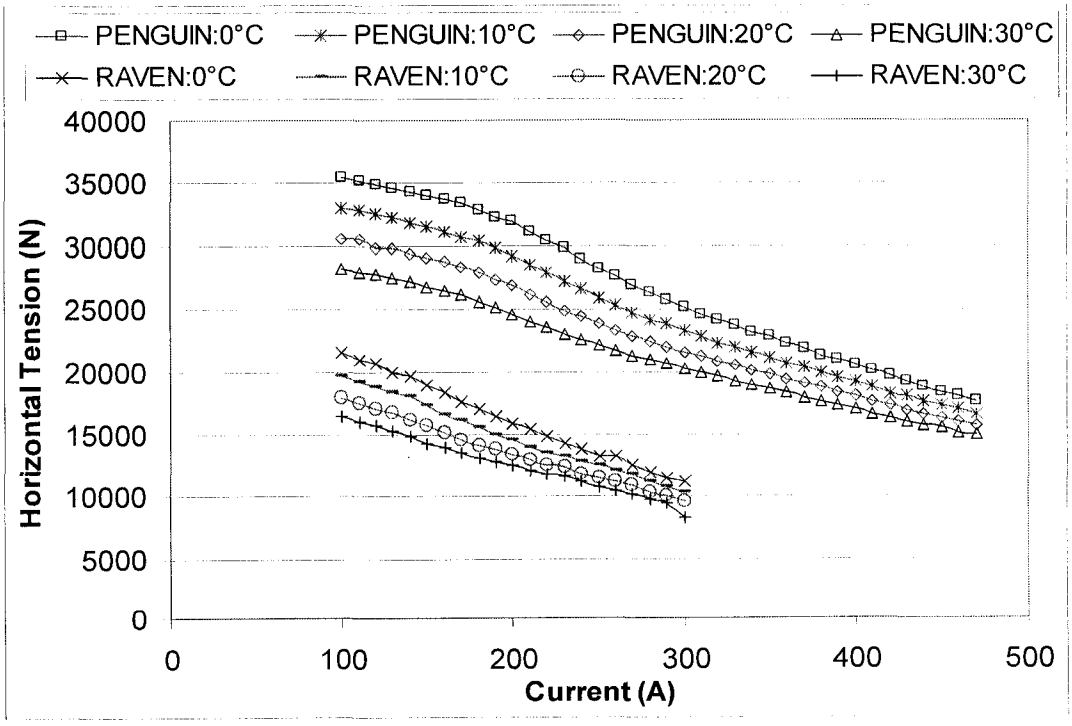

(b)

Figure 5.15 Variation of the horizontal tension with the current and ambient temperature for (a) Guinea conductor, (b) Penguin and Raven conductors, respectively

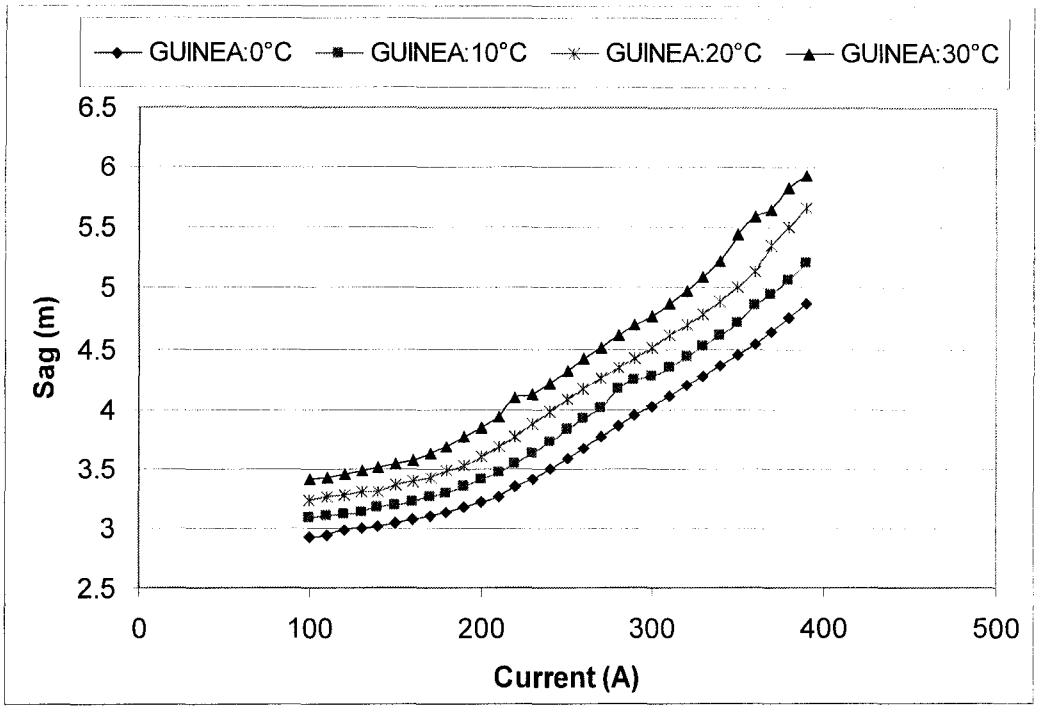

(a)

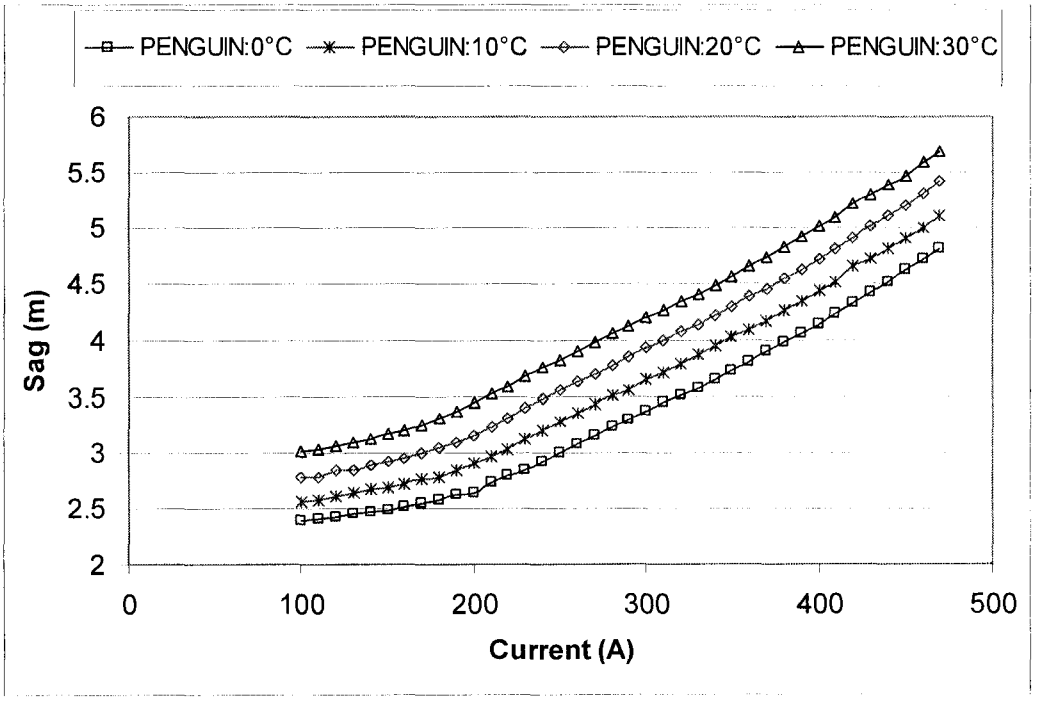

(b)

Figure 5.16 Variation of the sag with the current and ambient temperature for (a) Guinea and (b) Penguin conductors, respectively

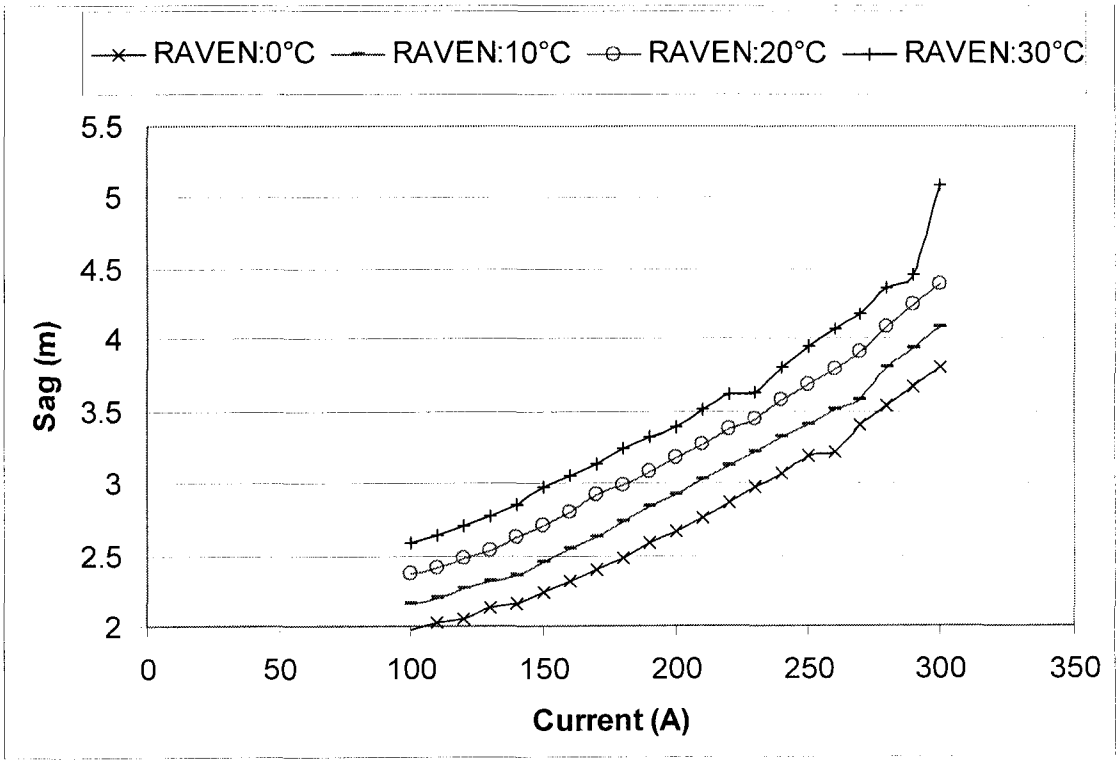

(c)

Figure 5.16 Variation of the sag with the current and ambient temperature for Raven conductor

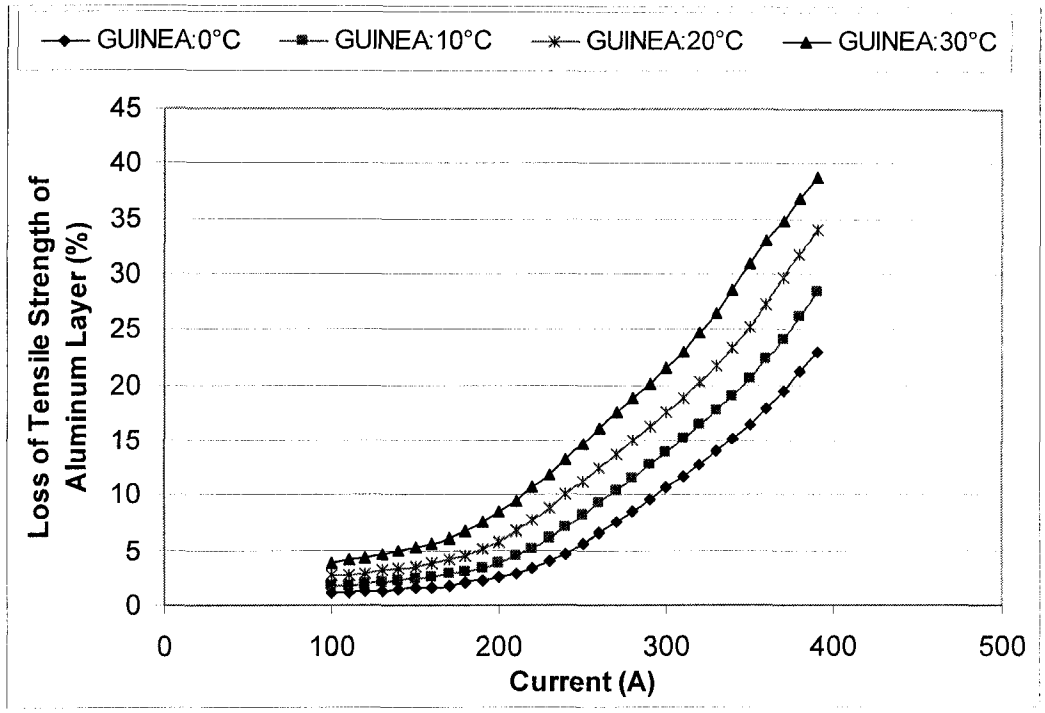

(a)

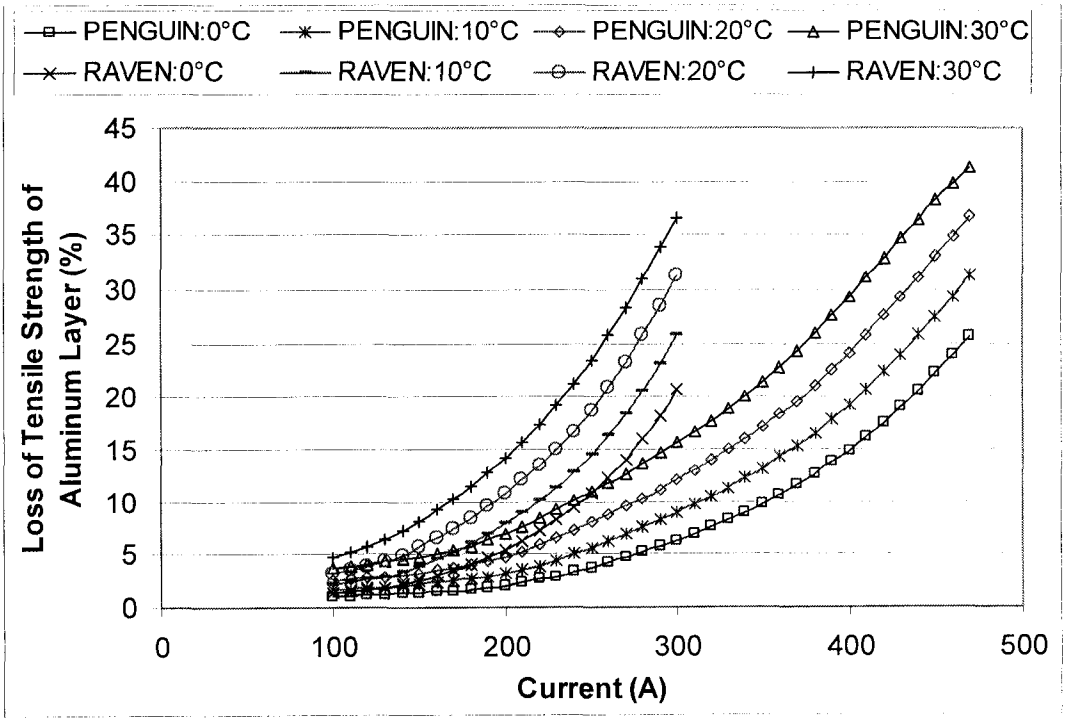

(b)

Figure 5.17 Variation of the loss of tensile strength of the aluminum layer with the current and ambient temperature for (a) Guinea (b) Penguin and Raven, respectively

The loss of tensile strength of the aluminum layer increases with increases of conductor current and ambient temperature as we see in Figure 5.17. The increasing loss of tensile strength becomes larger at higher current. Quantitative values are shown in Table 5.1 for Guinea conductor, for example.

Table 5.1 Loss of tensile strength of aluminum layer for Guinea conductor with variation of ambient temperature and conductor current

Ambient temperature (°C)	Loss of tensile strength of aluminum layer (%)	
	at 100 A	at 390 A
0 °C	1.08	23.0
10 °C	1.73	28.4
20 °C	2.64	34.0
30 °C	3.91	38.8

At 390 A, the loss of tensile strength in the aluminum layer increases about 5 % for every 10 °C increase in the ambient temperature.

The loss of tensile strength of the aluminum layer for single layer ACSR conductors is 25 % at their thermal rating under 0 °C ambient temperature, but it is 40 % under 30 °C ambient temperature. Both conductor temperature and the ambient temperature are the determinant factors to affect the loss of tensile strength of the nonferrous part of ACSR conductors.

5.4 Supply Frequency

The Integrated Model can be used to analyze the variation of resistance and other characteristics of single layer ACSR conductors with various supply frequencies. The investigation in this section shows the characteristics of Guinea, Penguin, and Raven conductors with different frequencies at 25 Hz, 40 Hz, 50 Hz, and 60 Hz, respectively.

- **Effect of Variation of Frequency on AC Resistance and AC Reactance**

The variation of ac resistance with current and frequency is shown for companies of the three types of conductors in Figure 5.18. The ac resistance increases with increases of current or frequency. The higher the frequency, the larger the resistance is. The increase becomes larger when the conductor current increases. The core losses including hysteresis and eddy current losses increase approximately with f^2 [44]. The skin effect decreases with $f^{1/2}$. The redistribution of the current due to the transformer effect depends on the self and mutual inductive reactances in a complex manner due to the longitudinal and circumferential magnetic fluxes for the various layers of the conductor.

The ac/dc resistance ratio is shown in Figure 5.19 with the conductor current and the frequency. Figure 5.19 (a) shows the highest ratio is 1.5 at 270 A and 25 Hz for Guinea conductor, and 1.97 at 260 A and 60 Hz. Figures 5.19 (b) and (c) also show the ac/dc resistance ratio for Penguin and Raven conductors increases at some fixed current when the frequency increases from 25 Hz to 60 Hz.

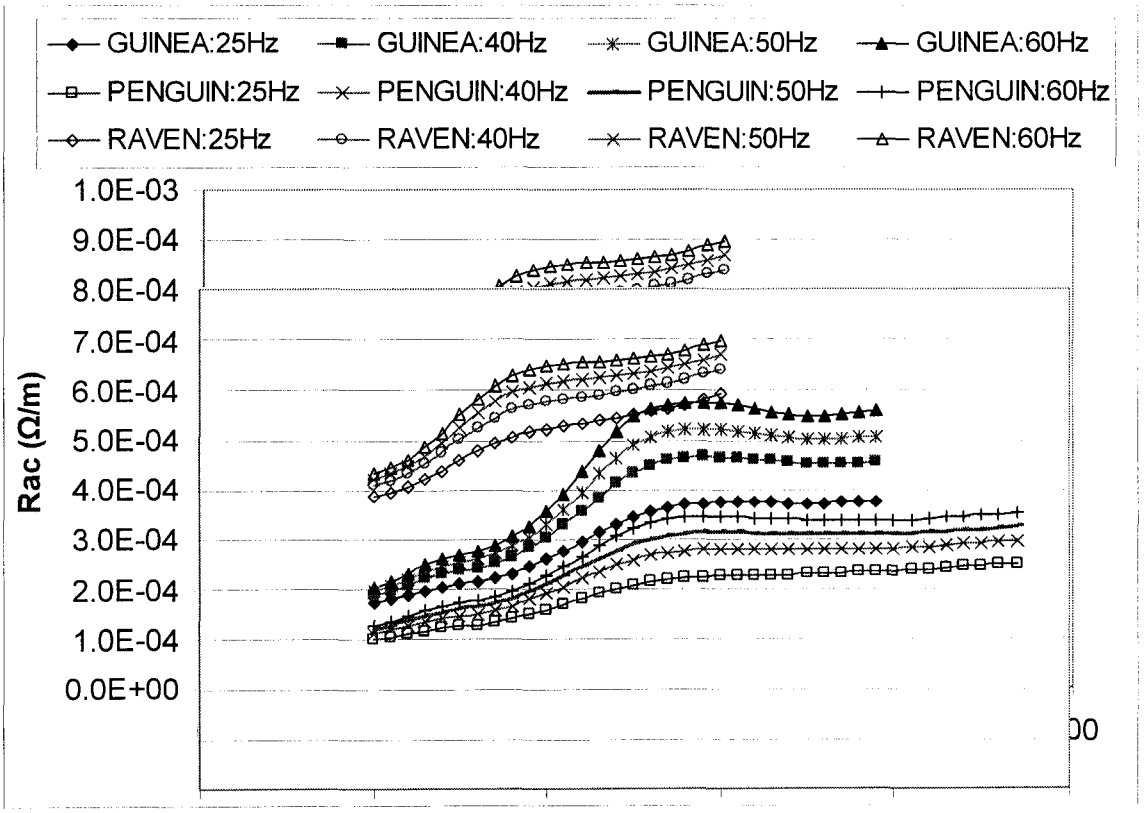

Figure 5.18 Variation of the ac resistance with the current and supply frequency

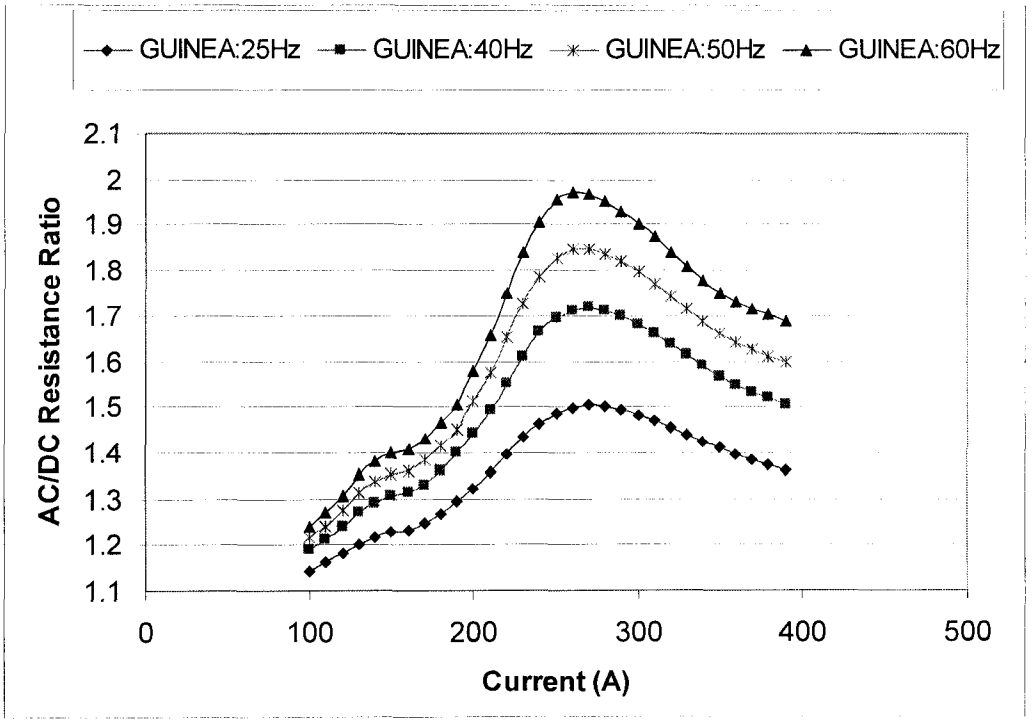

(a)

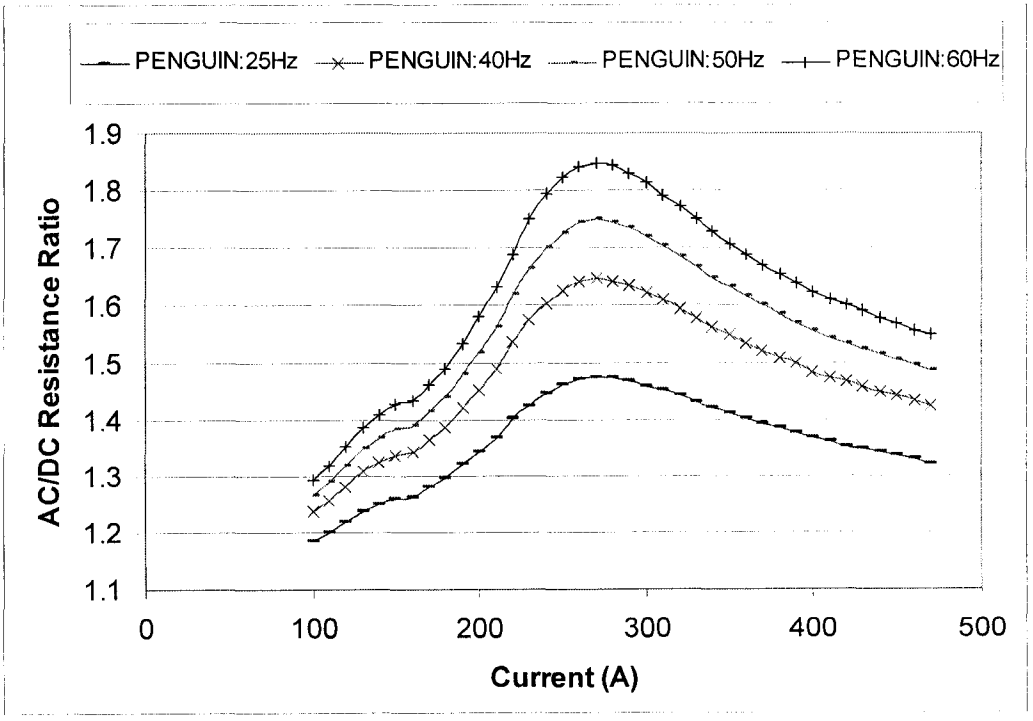

(b)

Figure 5.19 Variation of the ac/dc resistance ratio with the current and frequency for (a) Guinea and (b) Penguin conductors, respectively

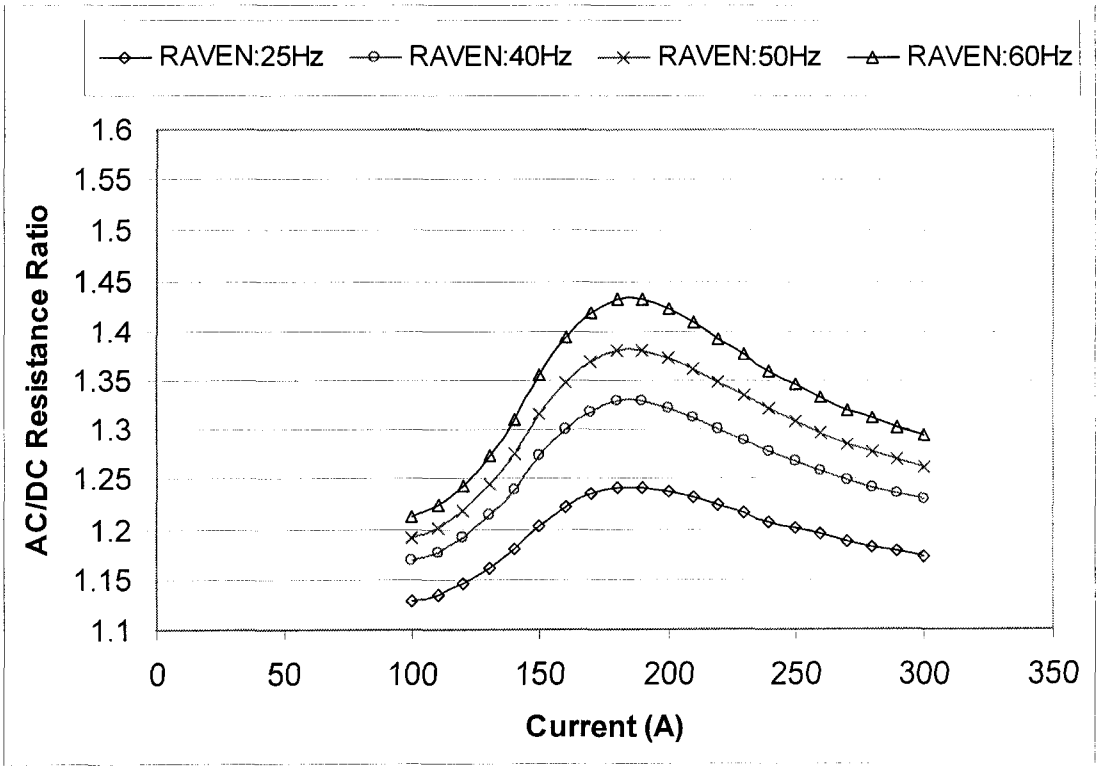

(c)

Figure 5.19 Variation of the ac/dc resistance ratio with the current and frequency for Raven conductor

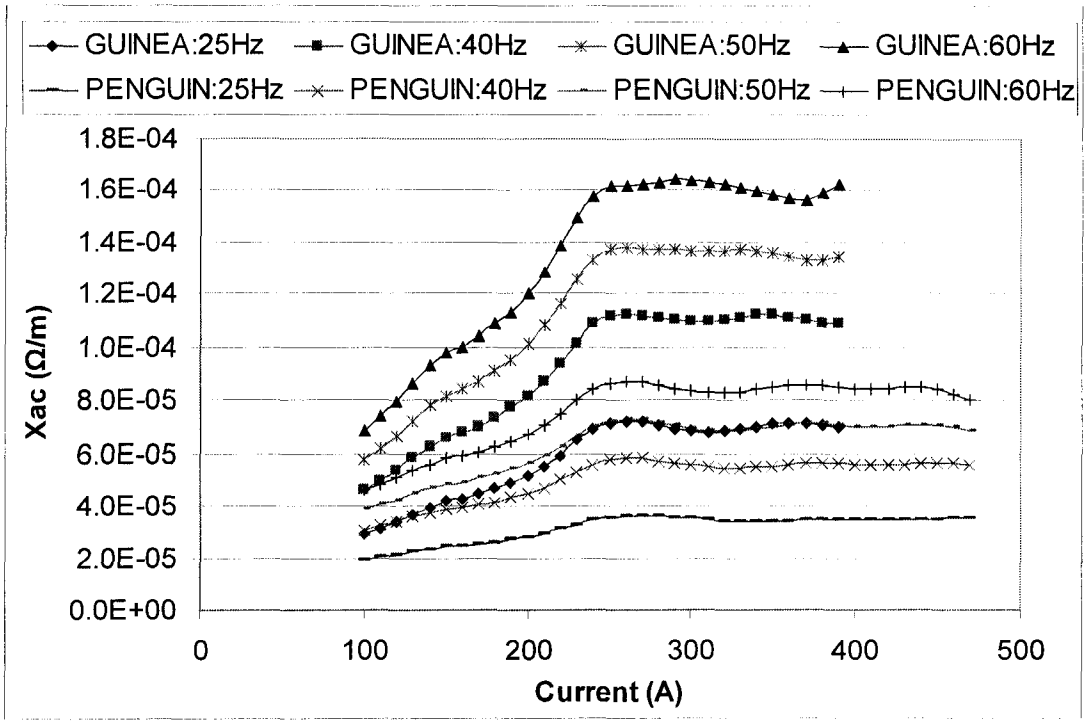

(a)

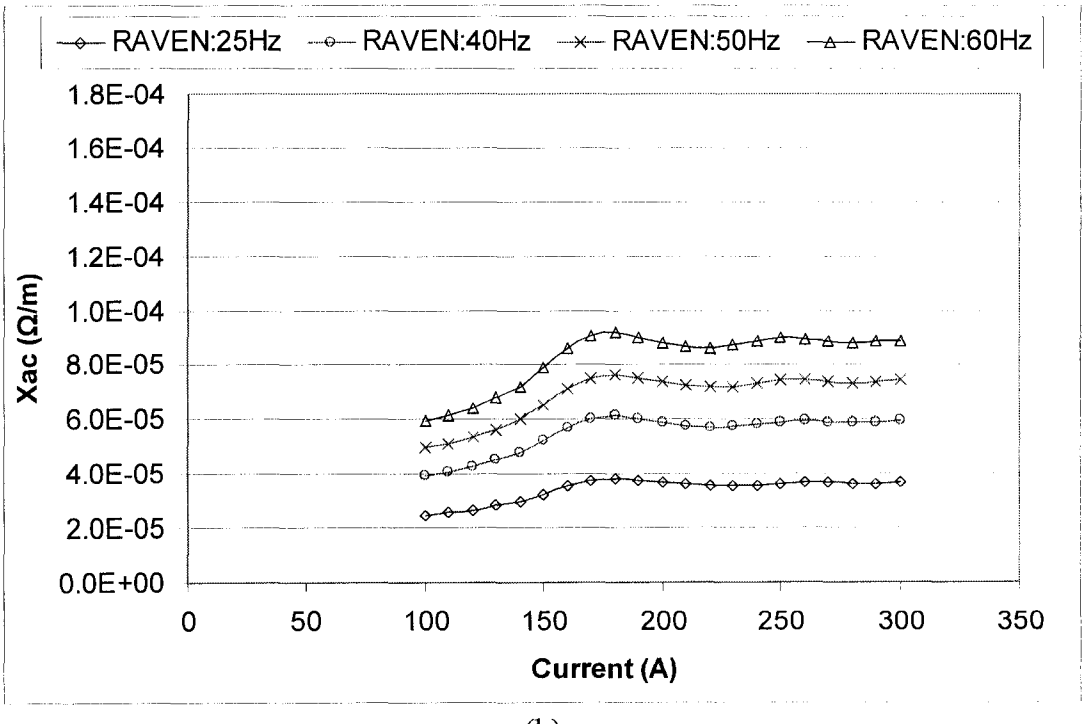

(b)

Figure 5.20 Variation of the ac reactance with the current and frequency for (a) Guinea and Penguin, (b) Raven conductors, respectively

Figure 5.20 shows the variation of the ac reactance with the current and frequency for the three single layer ACSR conductors. The ac reactance increases with increases of current and frequency. Similarly to the ac resistance curves, the increase becomes larger when the conductor current increases to saturation.

The reactances increase approximately linearly with the increasing frequency for three layer ACSR conductors [44] while they increase nonlinearly for single layer ACSR conductors because of the strong longitudinal and circumferential fluxes. The effect of increased frequency for the reactance is complex, as we can see from Figure 5.20 (a) and (b). They are different from the variation of reactance curves with frequency for three layer ACSR conductors [44]. Reactance is calculated directly from the supply frequency using the Integrated Model and the saturation area is easily seen from the resistance curves in Figure 5.18 and the reactance curves in Figure 5.20.

The variation of the resistive heating with the current is similar to the variation of the resistance with current at various frequencies. The resistive heat losses increase with an increase of the frequency.

- **Effect on Convective Cooling and Radiative Cooling**

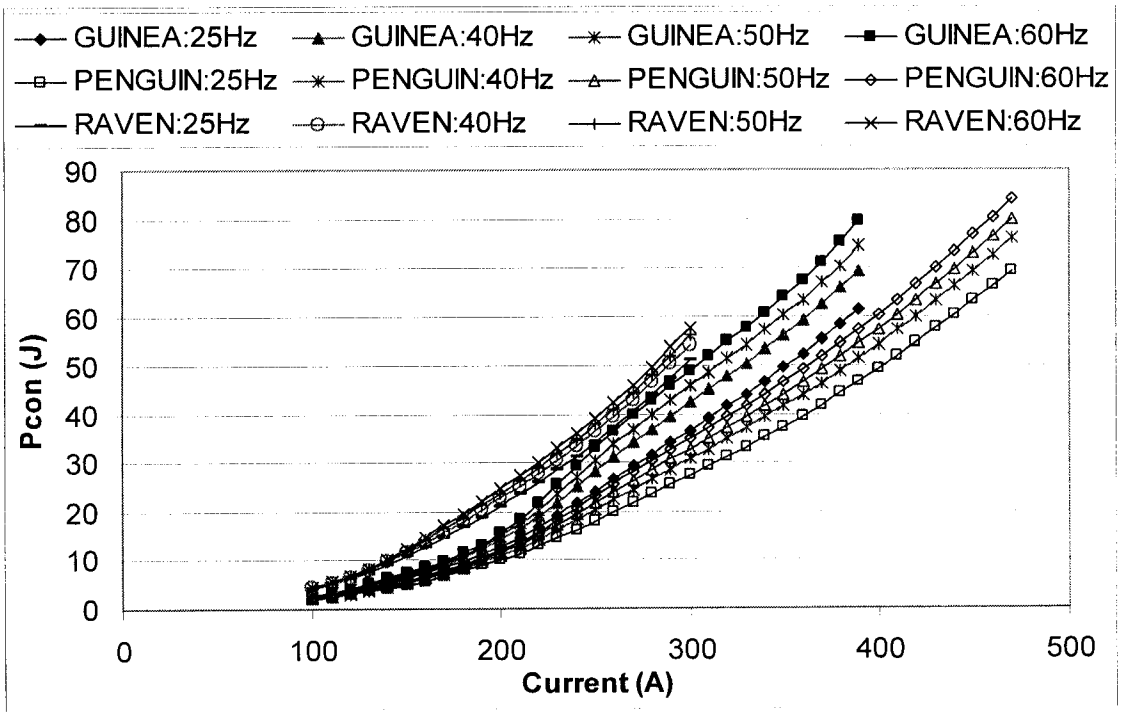

Figure 5.21 Variation of the convective cooling with the current and frequency

The variation of the convective cooling with the current and frequency is shown in Figure 5.21. The convective cooling increases with increases of current and ambient temperature. The convective cooling is a function of the conductor surface temperature,

as is the radiative cooling. The radiative cooling increases with increases of the current and ambient temperature, as is shown in Figure 5.22.

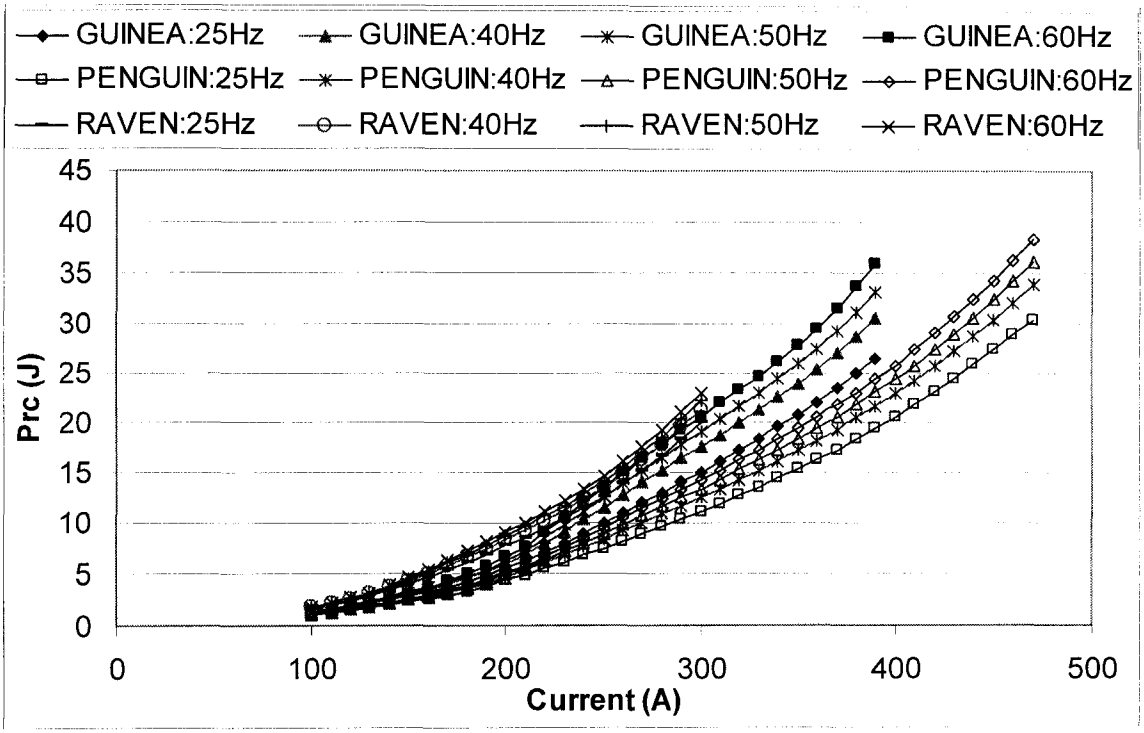

Figure 5.22 Variation of the radiative cooling with the current and frequency

- **Effect on Mechanical Properties**

The variation of the aluminum stress decreases with increases of current and frequency as shown in Figure 5.23, and it is more obvious at higher current than at lower current. The aluminum layer experiences higher stress at the lower supply frequency.

Comparing the aluminum stress for Guinea conductor and stresses for Penguin and Raven conductors, we can see that the more steel wires, the less change of stress of the aluminum layer varies from 100 A to the maximum current rating. The stress of the aluminum layer for Guinea conductor varies from 43 MPa to 2 MPa when the conductor current changes from 100 A to 390 A. For Penguin and Raven conductors, the stress of the aluminum layer decreases from over 100 MPa at 100 A to less than 10 MPa at their maximum current ratings.

Figure 5.24 shows that the horizontal tension decreases with increases of current and frequency for the three types of single layer ACSR conductors. At 25 Hz, the horizontal tension decreases almost linearly with an increase of the conductor current. At 60 Hz, the tension decreases but it is no longer linear, especially when the current is larger than 200 A.

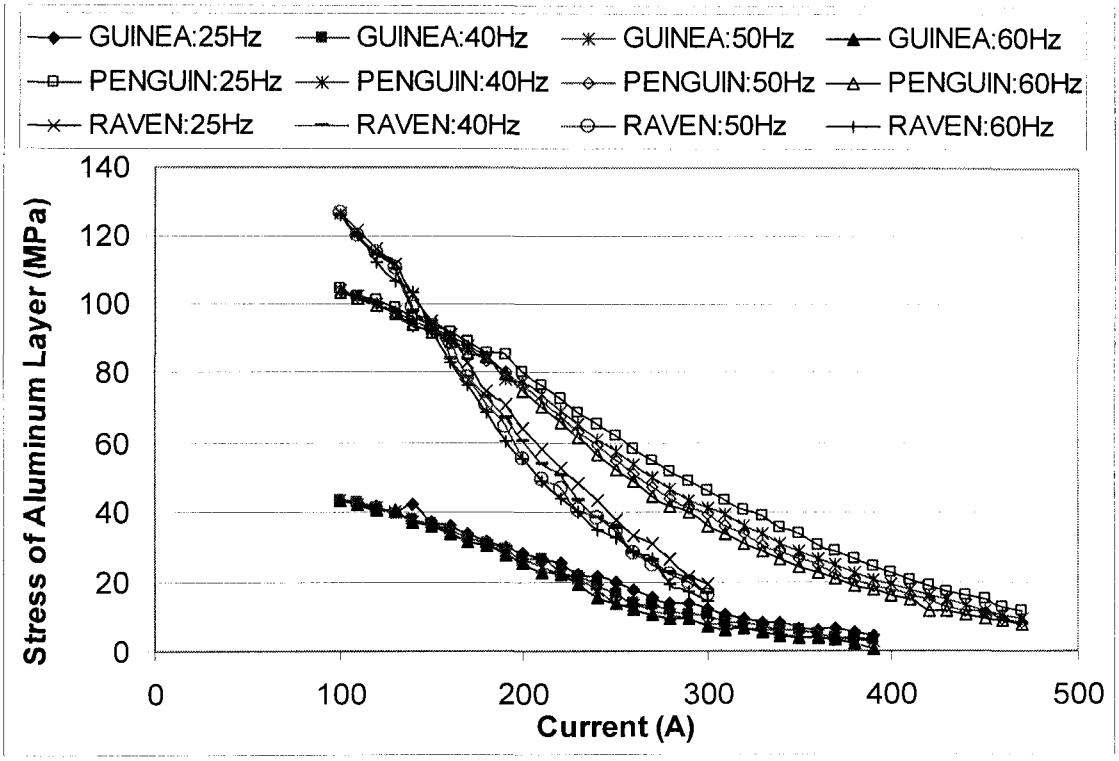

Figure 5.23 Variation of the aluminum stress with the current and frequency

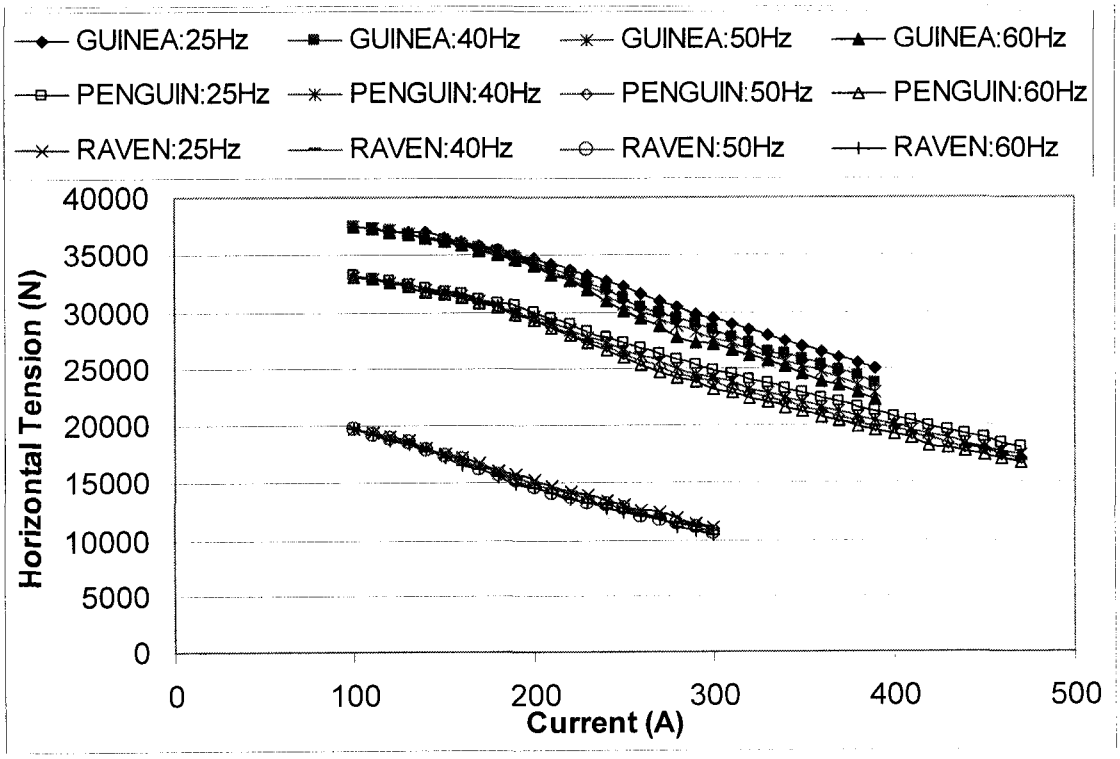

Figure 5.24 Variation of the horizontal tension with the current and frequency

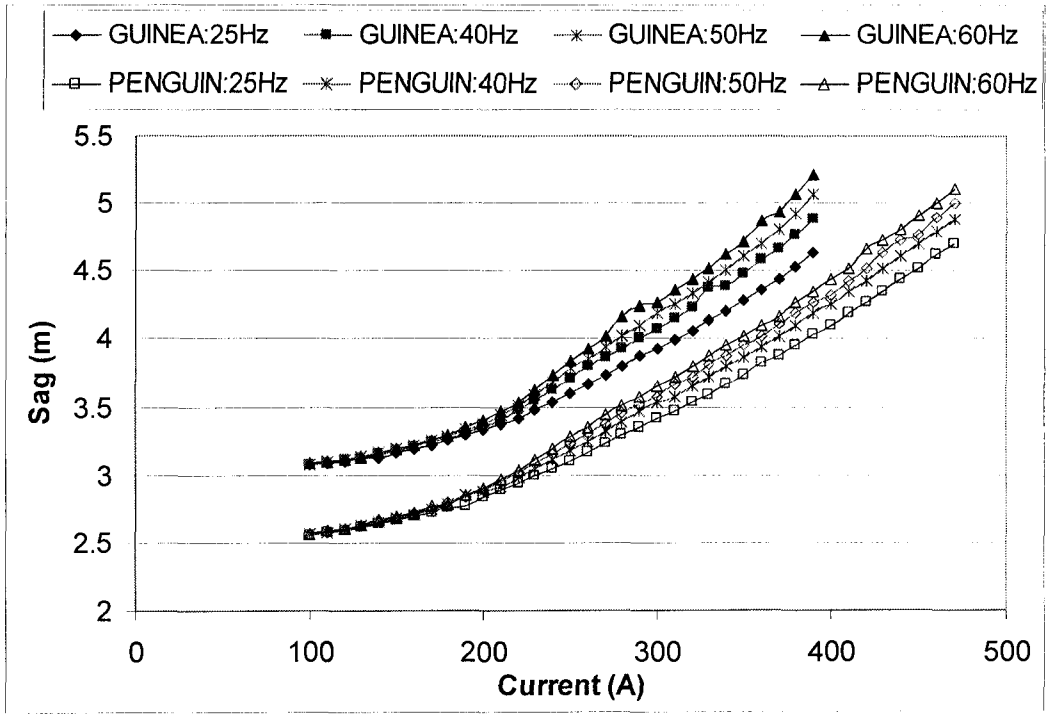

(a)

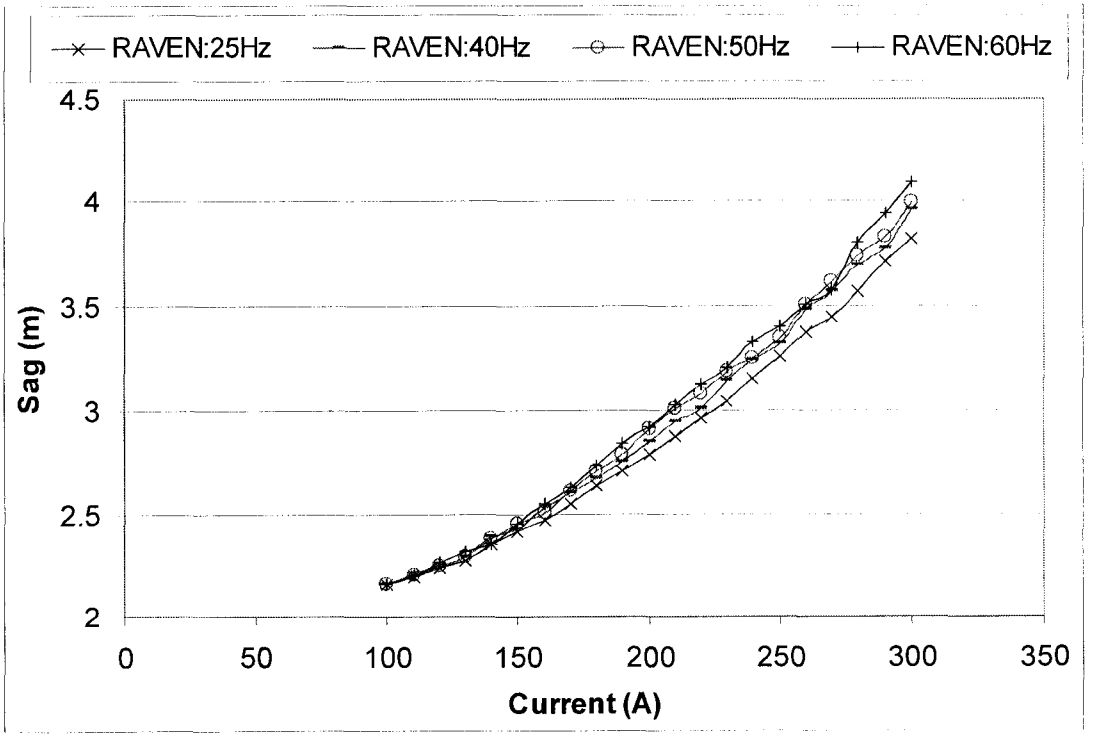

(b)

Figure 5.25 Variation of the sag with the current and frequency for (a) Guinea and Penguin, (b) Raven conductors, respectively

Figure 5.25 shows the variation of sag with current and frequency for Guinea, Penguin, and Raven conductors respectively. The sag increases with increases of the current and supply frequency. For Guinea conductor at 390 A, the sag is 4.6 m at 25 Hz and 5.2 m at 60 Hz.

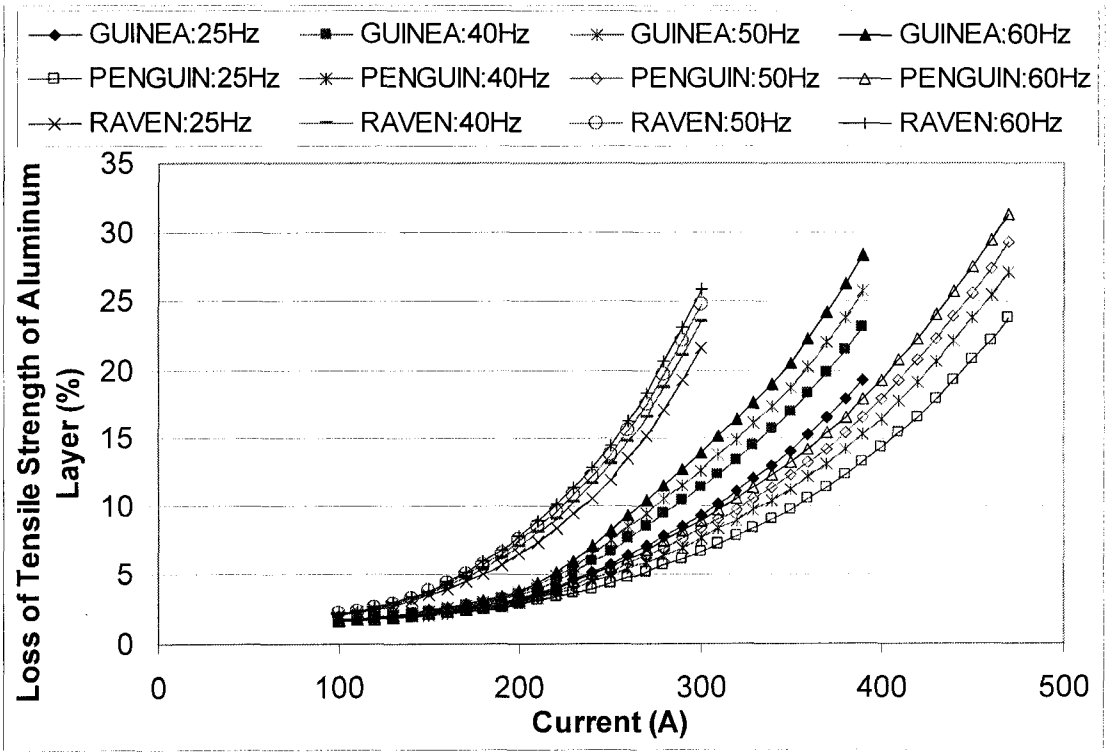

Figure 5.26 Variation of loss of aluminum tensile strength with the current and frequency

The effect of frequency on the loss of tensile strength of the aluminum layer is great, as can be seen from the curves in Figure 5.26. The accumulating loss of tensile strength of the aluminum layer increases with increasing current and supply frequency. For Guinea conductor at 390 A, the aluminum wires lose 19.3 % of their tensile strength at 25 Hz and 28.4 % at 60 Hz.

5.5 Time of Exposure

The algorithms including those that are deterministic and probabilistic are used in the Integrated Model. The probabilistic algorithm makes an analysis of time of exposure possible. For the total exposure time, 1 % is assumed with the additional load, and 99 % is the probability-based case. For comparison, the total exposure time is taken as 0.1 year, 1 year, 3 years, 10 years, and 30 years, with an ambient temperature of 10 °C and a supply frequency of 60 Hz.

- **Effect on AC Resistance and AC Reactance**

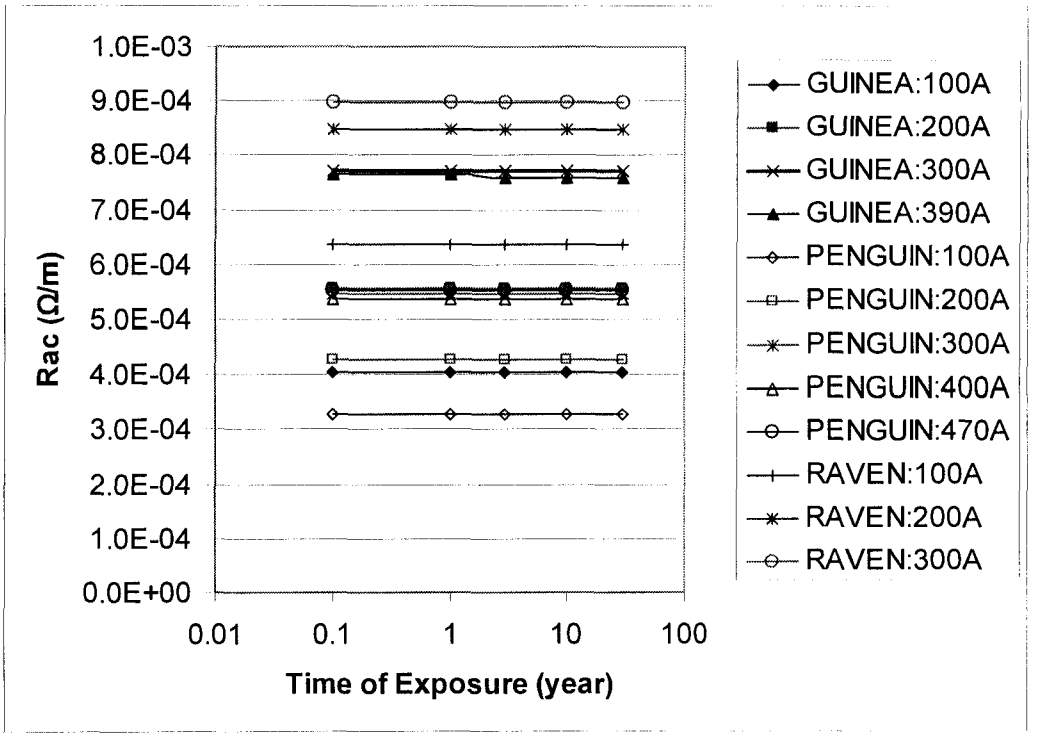

Figure 5.27 Variation of the ac resistance with the current and time of exposure

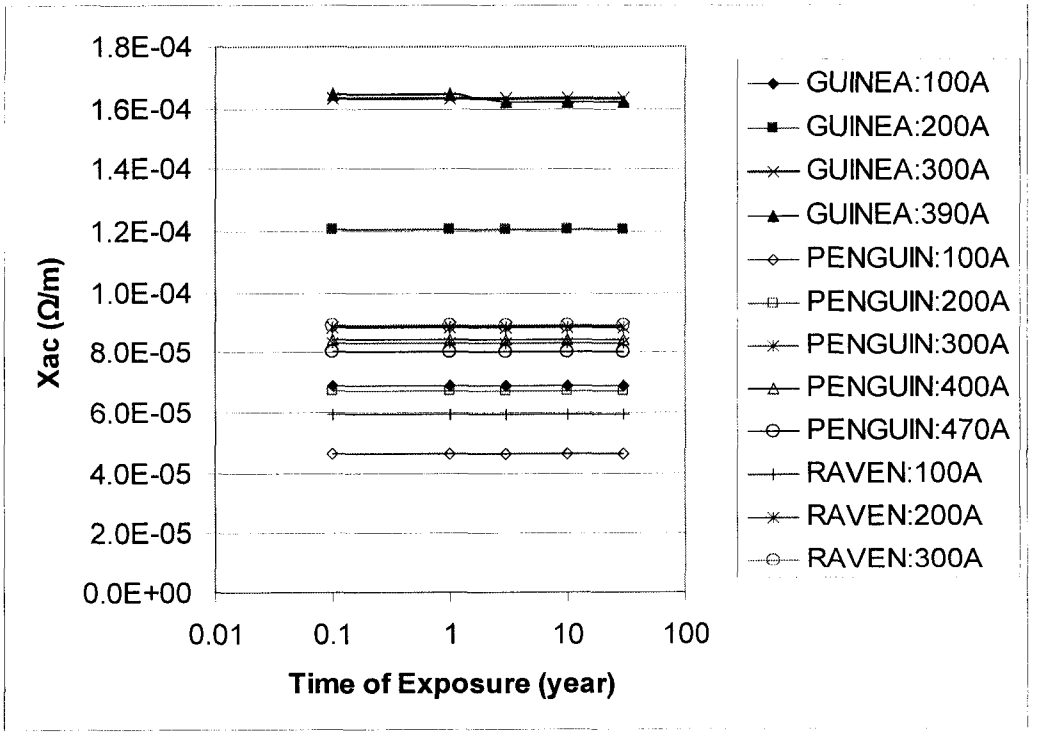

Figure 5.28 Variation of the ac reactance with the current and time of exposure

The variation of ac resistance and ac reactance with current and time of exposure is shown in Figures 5.27 and 5.28 respectively. AC resistance and ac reactance are relatively invariant with a variation of the exposure time, except Guinea near 390 A, where the variation is small. The heat gains and heat losses are also relatively invariant with a variation of exposure time. In other words, the electrical properties are almost constant with a variation of the exposure time.

- **Effect on Mechanical Properties**

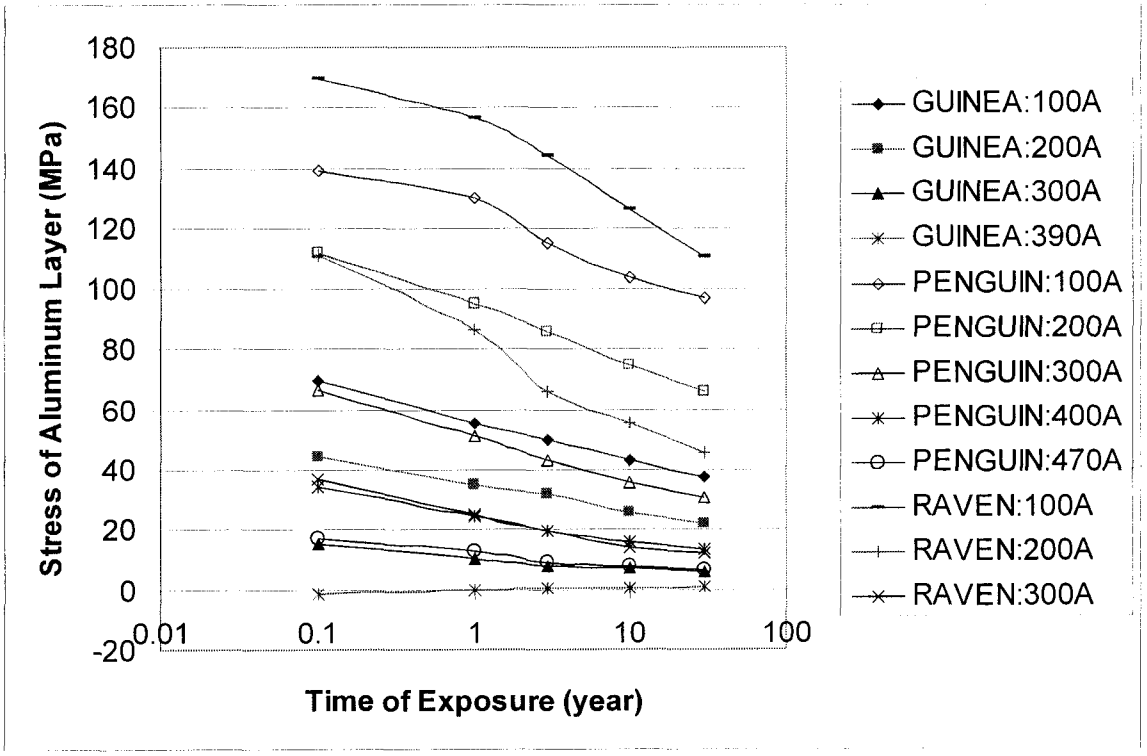

Figure 5.29 Variation of the aluminum stress with the current and time of exposure

Figure 5.29 shows the variation of the aluminum stress with the current and time of exposure. The aluminum stress decreases with increases of conductor current and time of exposure, and decreases quickest in the first year of exposure time. The amount of the decrease is larger at lower current. The aluminum stress is 112 MPa for Raven conductor at 200 A in 0.1 year, and 45 MPa in 30 years. The decrease of the aluminum stress is over 50%.

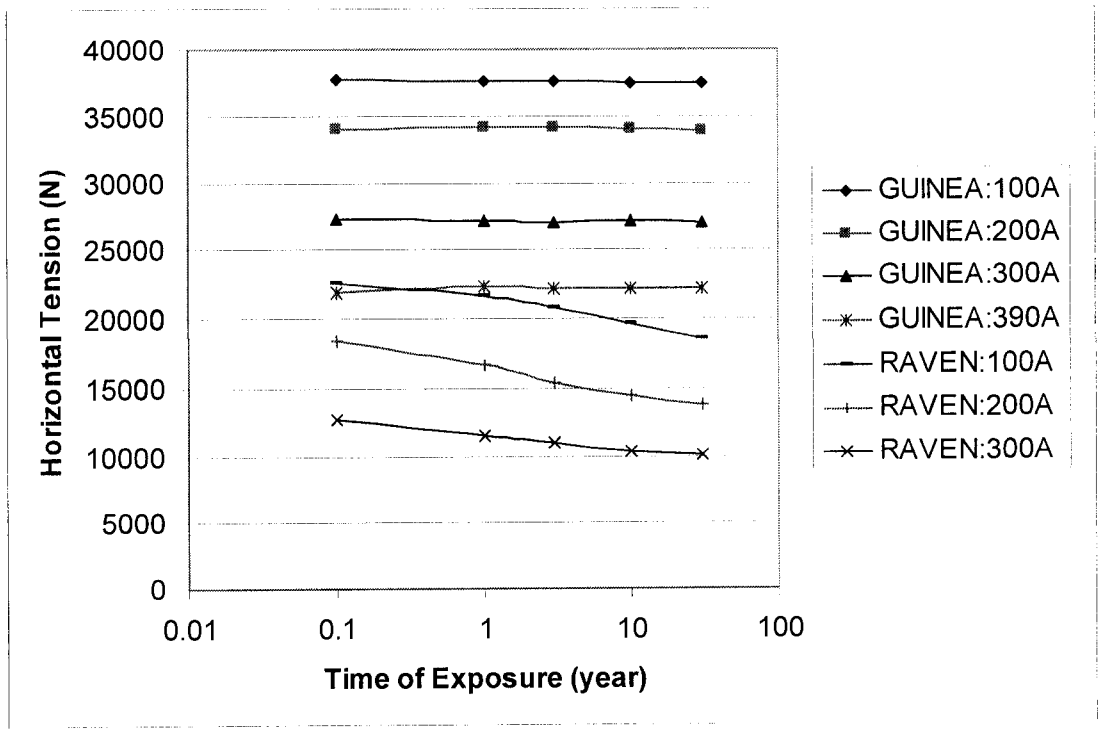

(a)

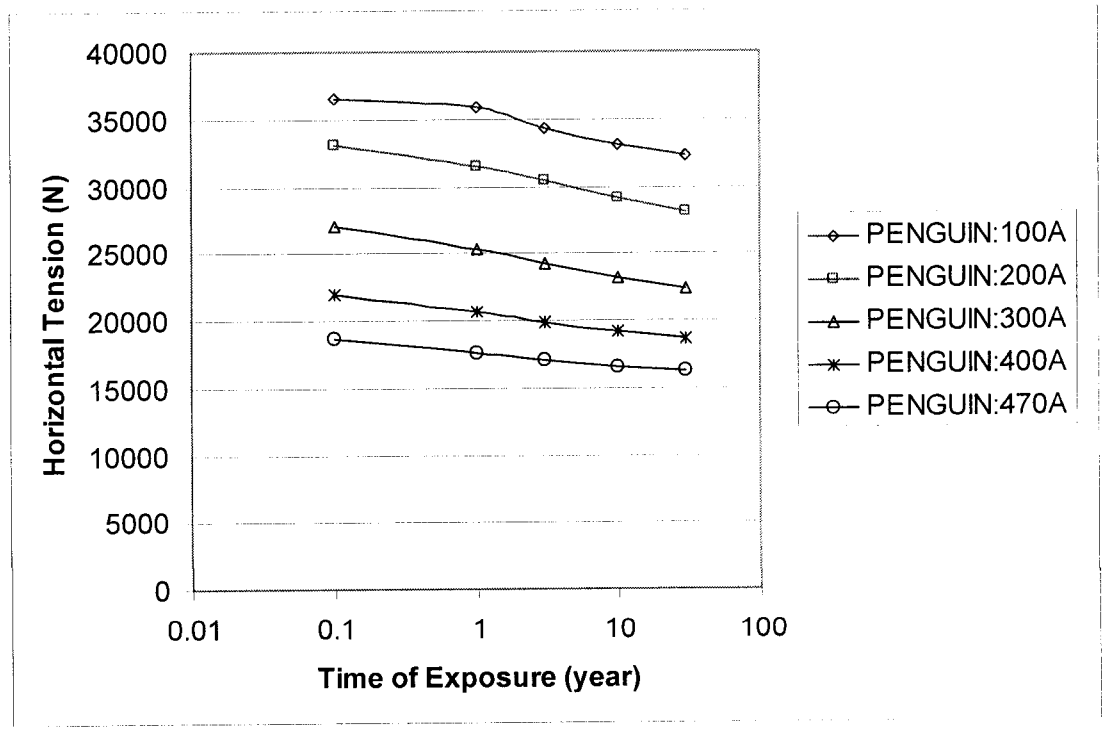

(b)

Figure 5.30 Variation of the horizontal tension with the current and time of exposure for (a) Guinea and Raven, (b) Penguin conductors, respectively

The variation of the horizontal tension with the current and time of exposure is shown in Figure 5.30 (a) for Guinea and Raven conductors, and in Figure 5.30 (b) for Penguin conductor. The horizontal tension decreases with increasing time of exposure and the current for Penguin and Raven conductors. Similarly to the aluminum stress, the big change occurs in the first year of exposure time. The variation of the horizontal tension for Guinea is not obvious, a result of the larger steel core. The more steel wires, the less the variation of the horizontal tension.

For Guinea conductor at 390 A, the horizontal tension is 21.9 kN after 0.1 year exposure duration, and it is 22.2 kN after 30 years. The difference of the horizontal tension is only 0.3 kN. For Penguin and Raven, with a king wire as steel core, the variation is evident. For Penguin conductor at 470 A, the horizontal tension is 18.6 kN after 0.1 year, and it is 16.2 kN after 30 years. The difference is as much as 2.4 kN. For Raven at 300 A, the difference is 2.7 kN from 12.7 kN after 0.1 year to 10.0 kN after 30 years.

Figure 5.31 shows the variation of the sag of the conductors with the time of exposure and the current. The sag increases with the increases of exposure time and the current. The variations of the sag for Penguin and Raven conductors are larger than that for Guinea conductor. The sag for Penguin conductor at 470 A increases from 4.56 m to 5.23 m when the exposure time increases from 0.1 year to 30 years. For Raven at 300 A, the sag increases from 3.3 m after 0.1 year duration to 4.2 m after 30 years duration.

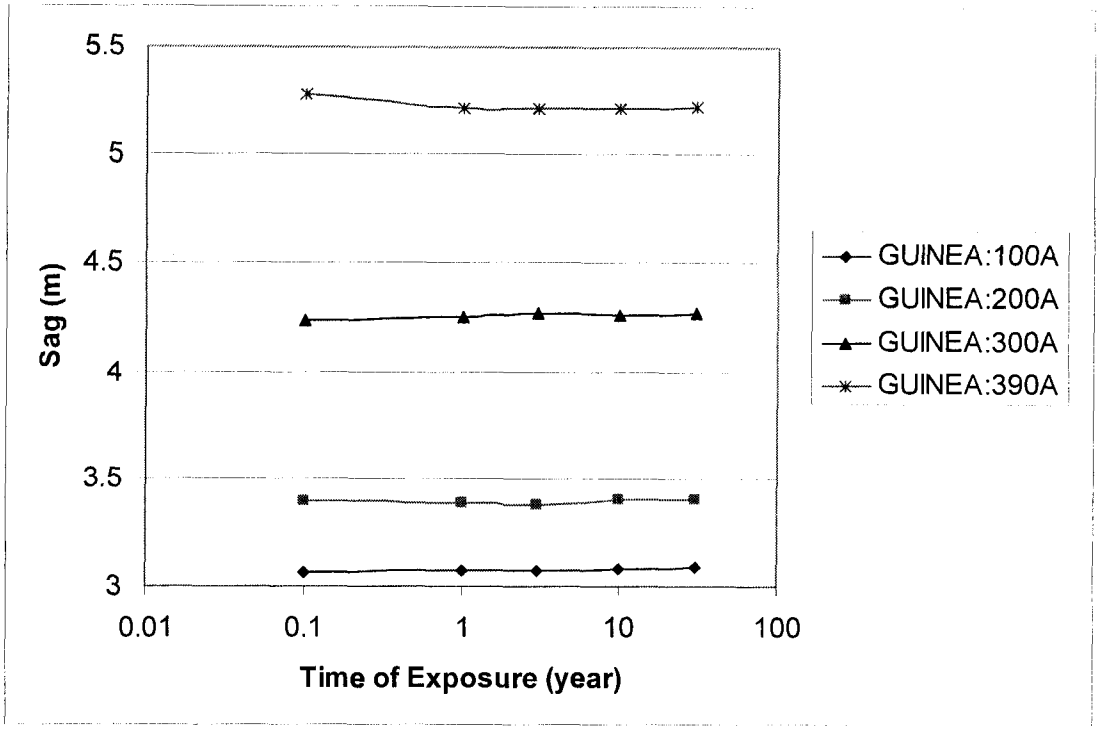

(a)

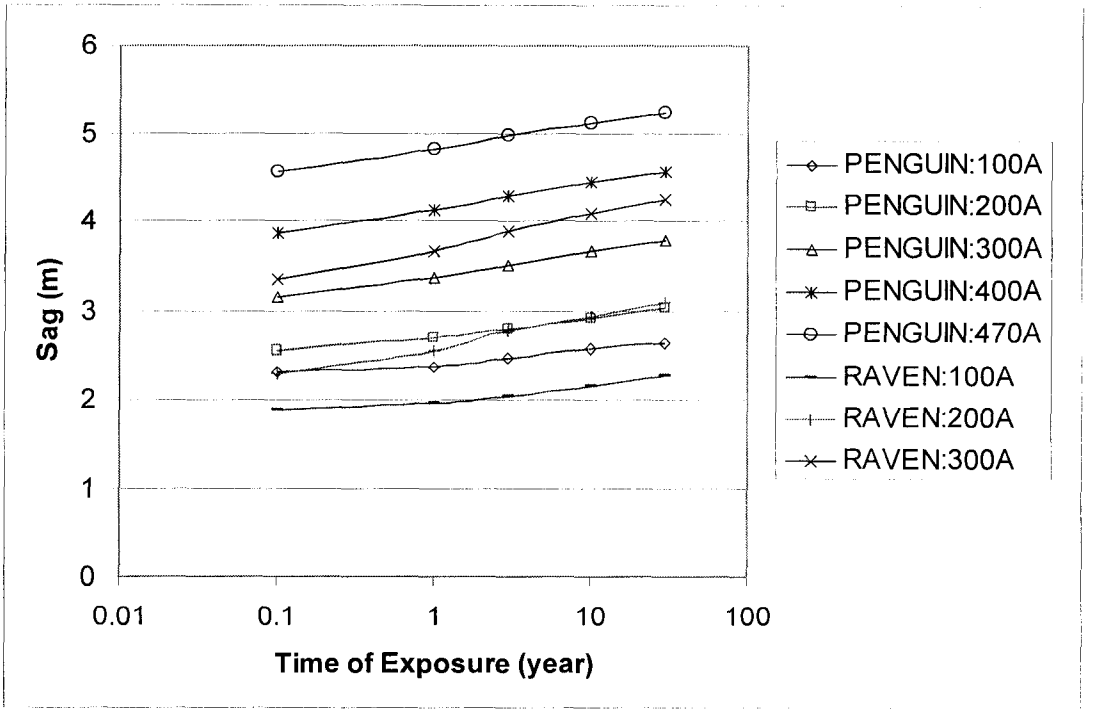

(b)

Figure 5.31 Variation of the sag with the current and the time of exposure for (a) Guinea (b) Penguin and Raven conductors, respectively

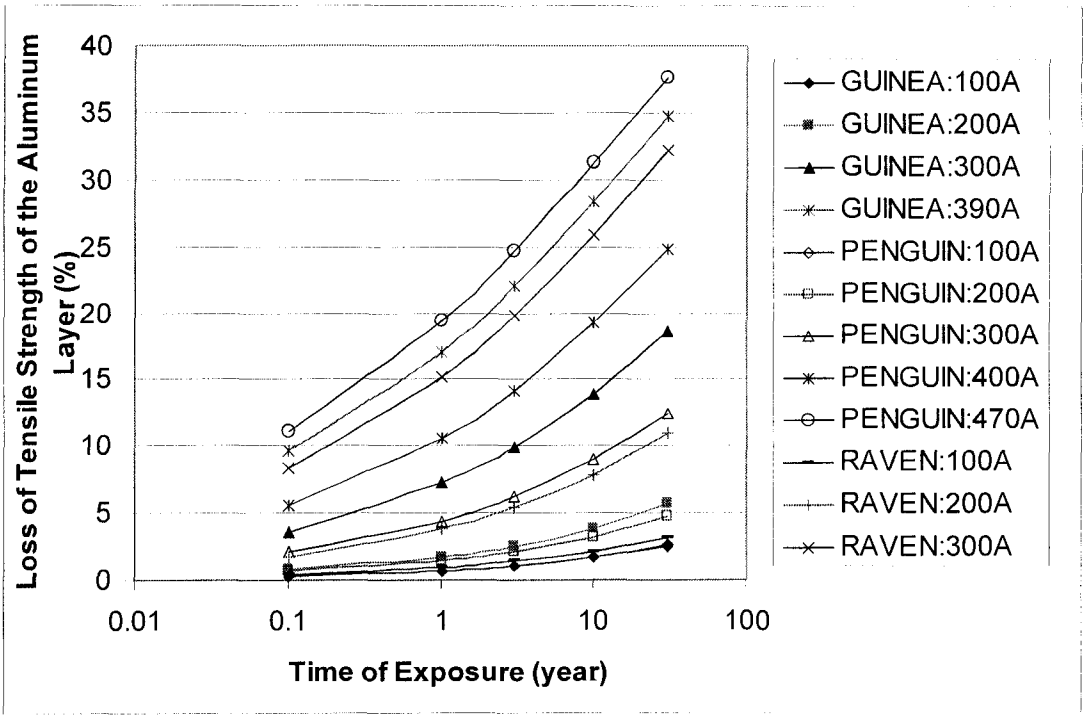

Figure 5.32 Variation of the loss of tensile strength of the aluminum layer with the current and the time of exposure

Figure 5.32 shows how the loss of tensile strength of the aluminum layer increases with increases of exposure time and conductor current. From Figure 5.32, we can see that the accumulating loss increases dramatically after one year of exposure. The higher the conductor current, the greater the tensile strength loses in the aluminum layer.

For Guinea conductor at 390 A and Raven conductor at 300 A, the accumulating tensile strength loss of the aluminum layer is less than 10 % after 0.1 year exposure, and it increases up to 35 % after 30 years exposure. For Penguin conductor at 470 A, the loss is 11 % after 0.1 year and 38 % after 30 years exposure.

5.6 Air Gap Thickness

During the drawing process of ACSR, the strands were spirally wounded and the very thin air gaps were formed at the contacts between strands in adjacent layers. The length of air gaps is affected by the pressure and tension of the conductor. The calculated effective gap at the contacts is 0.5 to 0.9 μm [34]. In this investigation, the thickness of the air gap is altered from 0.2 μm to 1.4 μm in steps of 0.2 μm.

- **Effect on AC Resistance and AC Reactance**

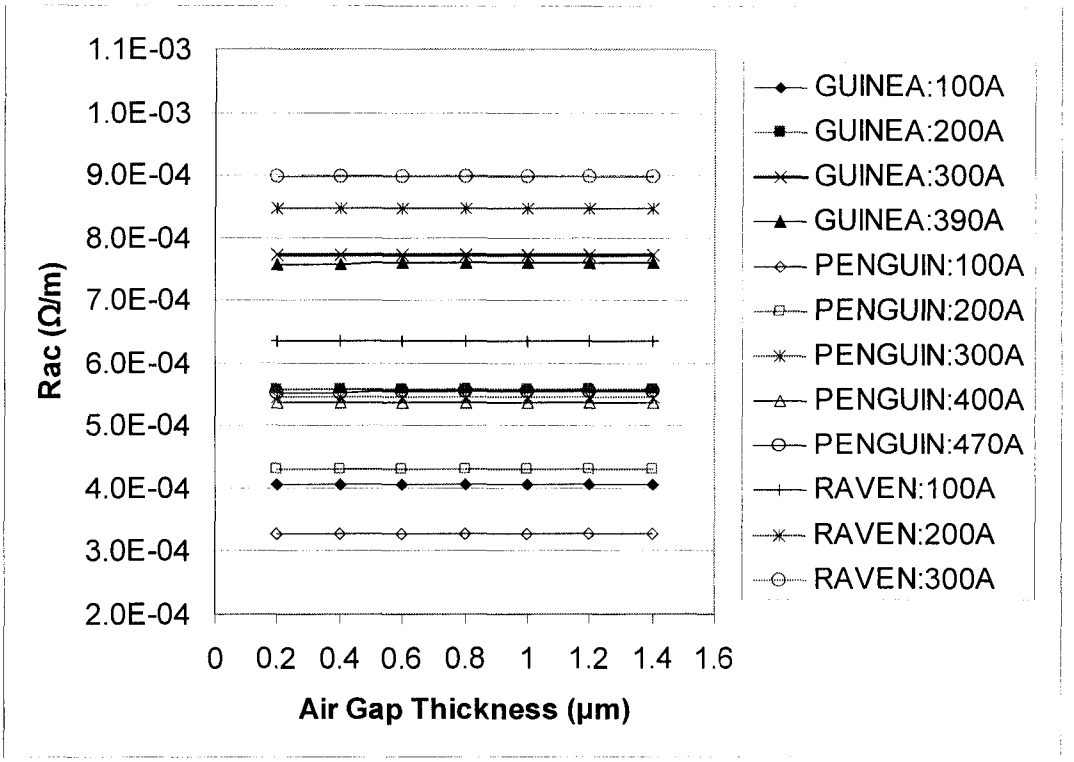

Figure 5.33 Variation of the ac resistance with the current and the air gap thickness

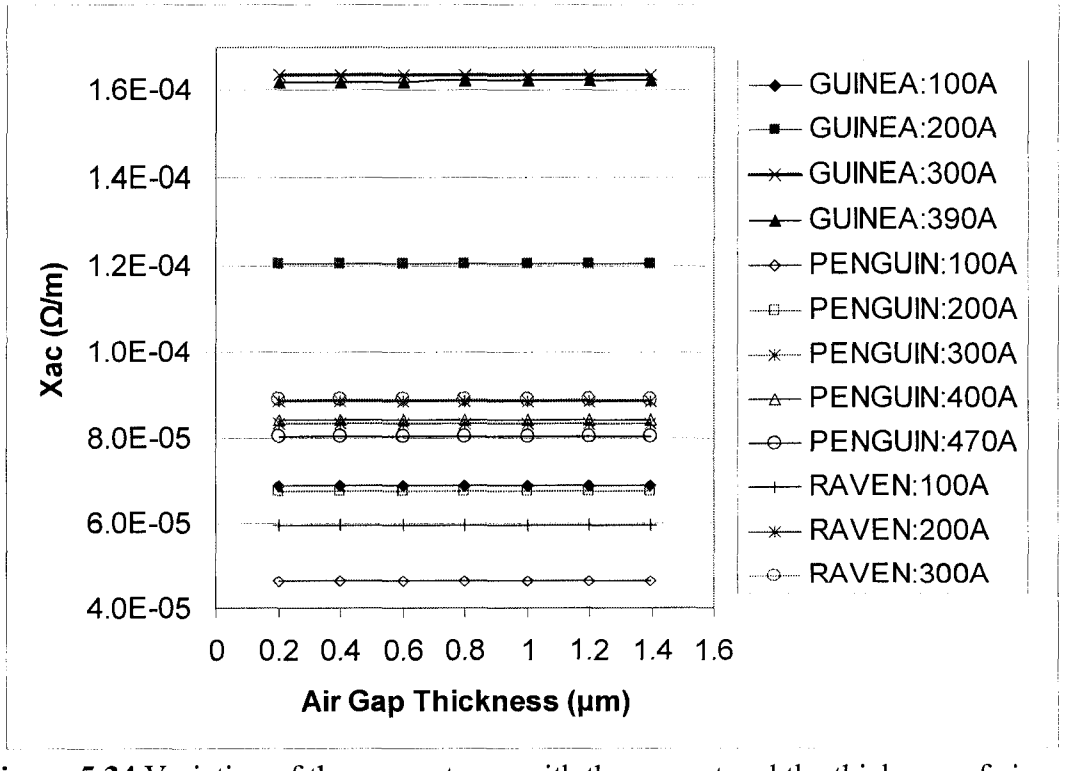

Figure 5.34 Variation of the ac reactance with the current and the thickness of air gap

Figure 5.33 shows the variation of ac resistance with air gap thickness and current. Figure 5.34 shows the variation of the ac reactance for Guinea, Penguin and Raven conductors, respectively. Resistance and reactance remain constant with the increase of the thickness of the air gap at certain current level. The resistive heating keeps constant as well with the variation of the air gap thickness at some fixed current.

- **Effect on Mechanical Properties**

The variation of the stress of the aluminum layer with current and thickness of the air gap is shown in Figure 5.35 for Guinea, Penguin, and Raven conductors, respectively. The aluminum stress for the three conductors remains almost constant with a variation of the air gap thickness. The only variation of aluminum stress occurs on Raven at 300 A from 14 MPa at 1.2 μm air gap thickness to 10 MPa at 1.4 μm.

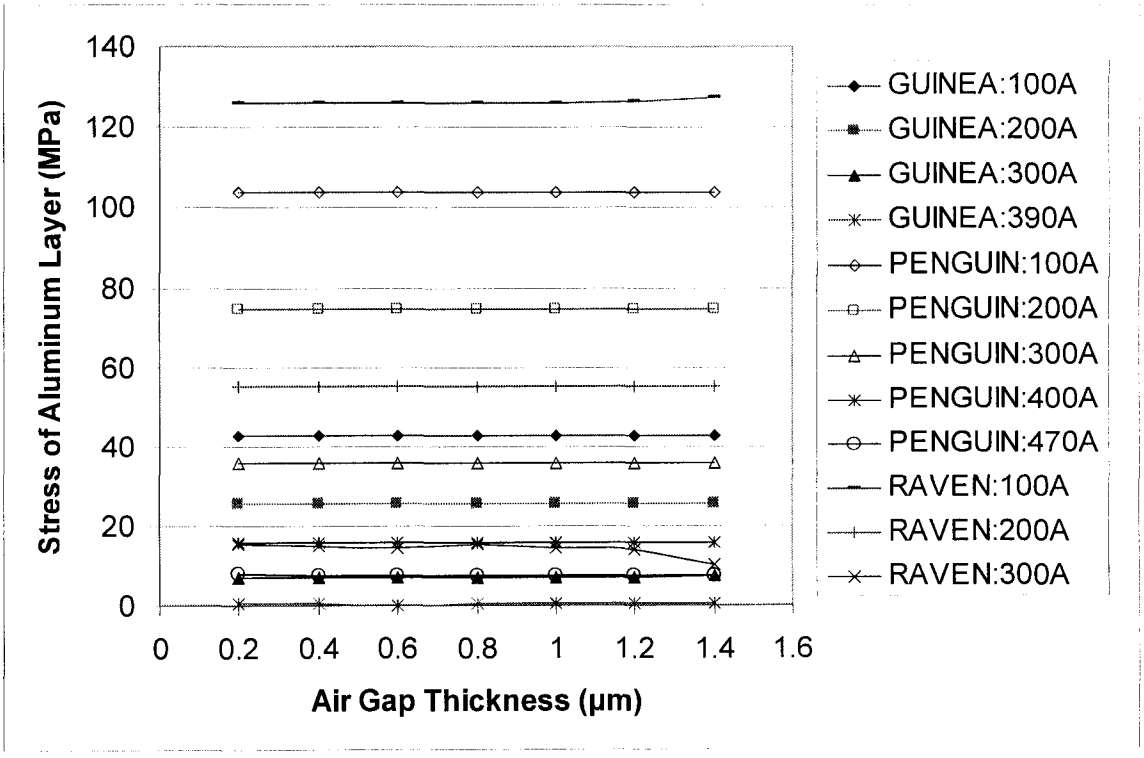

Figure 5.35 Variation of the stress of the aluminum layer with the current and the thickness of the air gap for Guinea, Penguin, and Raven conductors, respectively

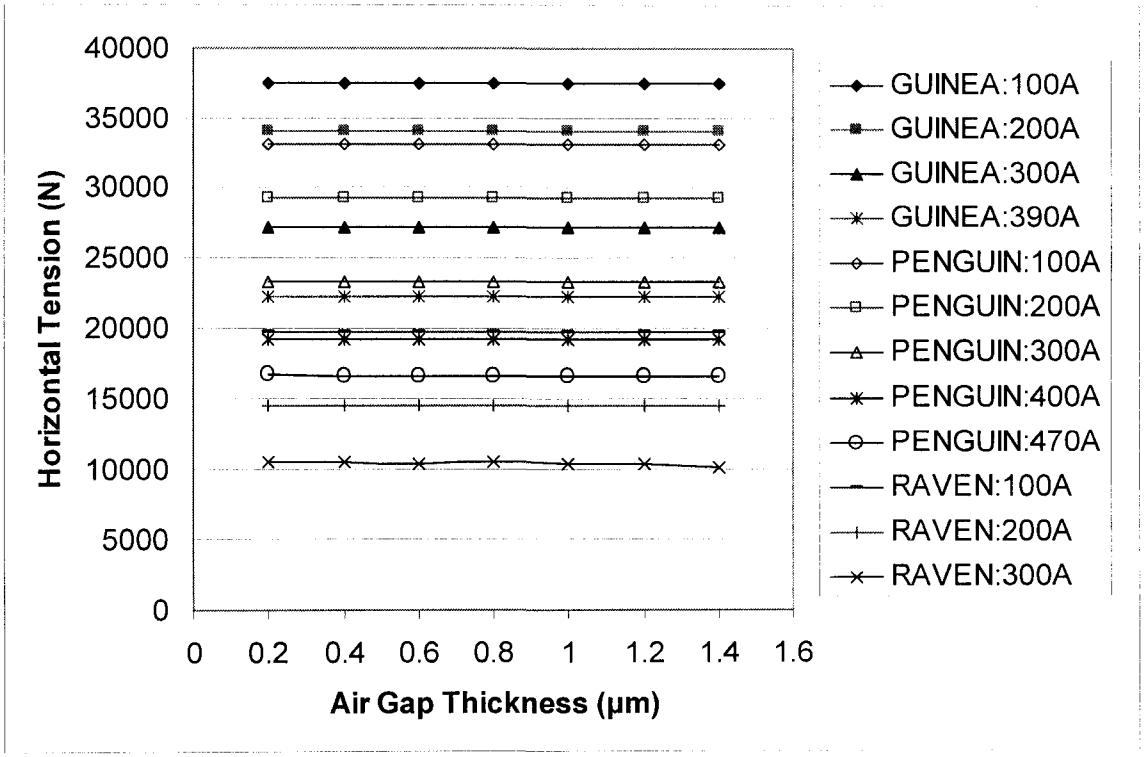

Figure 5.36 Variation of the horizontal tension with the current and the air gap thickness

From Figure 5.36 we can see that the horizontal tension remains constant with a variation of the thickness of the air gap except for Raven conductor at 300 A. The variation of the horizontal tension for Raven at 300 A with the increase of the air gap thickness is related to the variation of the aluminum stress with the air gap thickness.

The variation of the aluminum stress and the horizontal tension affects the variation of the sag with an increase of the thickness of the air gap. From Figure 5.37 we can see the sag remains constant at variant thickness of the air gap except for Raven conductor at 300 A. The sag increases 0.1 m for Raven conductor at 300 A when the thickness of the air gap increases from 1.2 μm to 1.4 μm.

The accumulating loss of tensile strength of the aluminum layer remains constant for the three single layer ACSR conductors with the variation of the air gap thickness are shown in Figure 5.38.

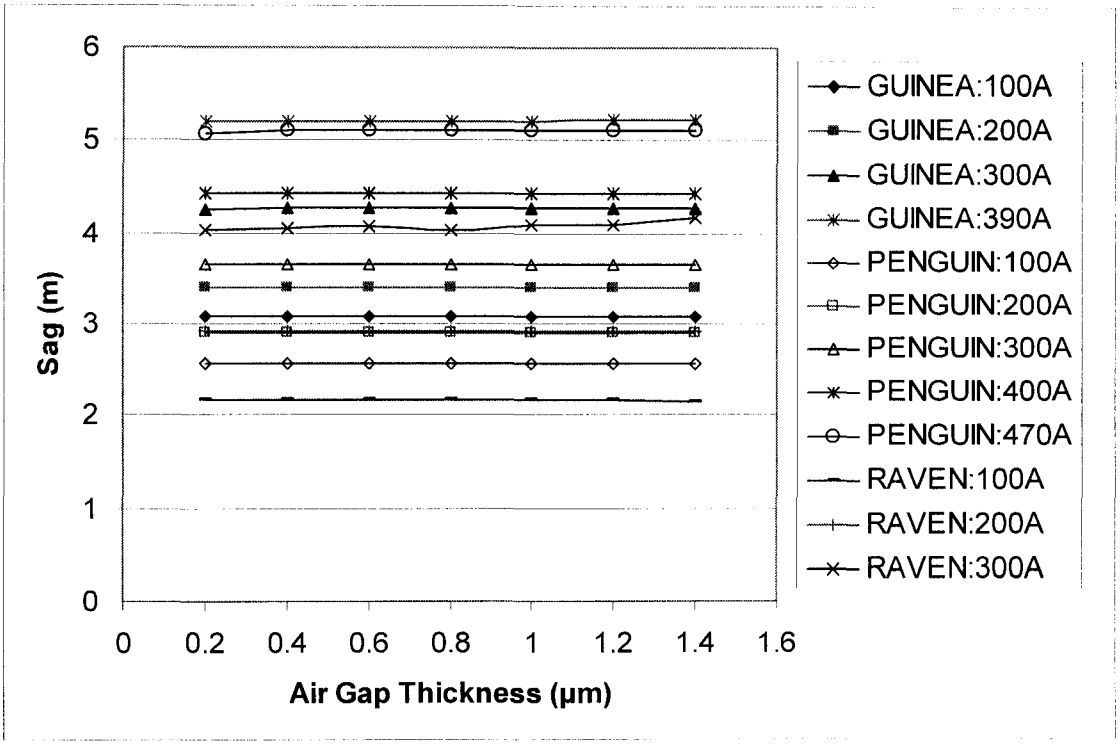

Figure 5.37 Variation of the sag with the current and the air gap thickness

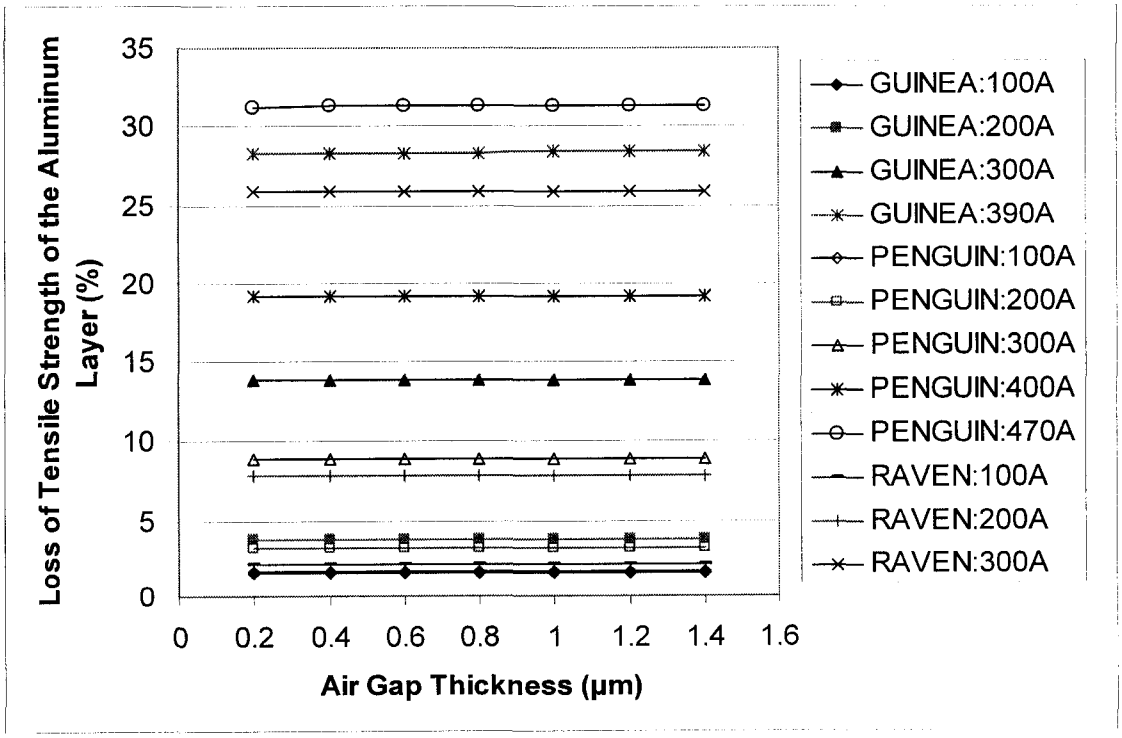

Figure 5.38 Variation of the loss of tensile strength of the aluminum layer with the current and the air gap thickness

5.7 Span

The span is changed from 200 m to 600 m in steps of 100 m. The span is assumed to be the distance between two tension towers. Spans from 400 ft (122 m) to 1600 ft (488 m) are suggested and studied in Aluminum Electrical Conductor Handbook [9].

- **Effect on AC Resistance and AC Reactance**

The variation of the ac resistance with the increases of span and current is shown in Figure 5.39. AC resistance remains constant at some fixed current ratings with the variant span lengths.

Figure 5.40 shows the variation of the ac reactance with the increases of span and current. The variation of the span does not alter the electrical characteristics of single layer ACSR conductors.

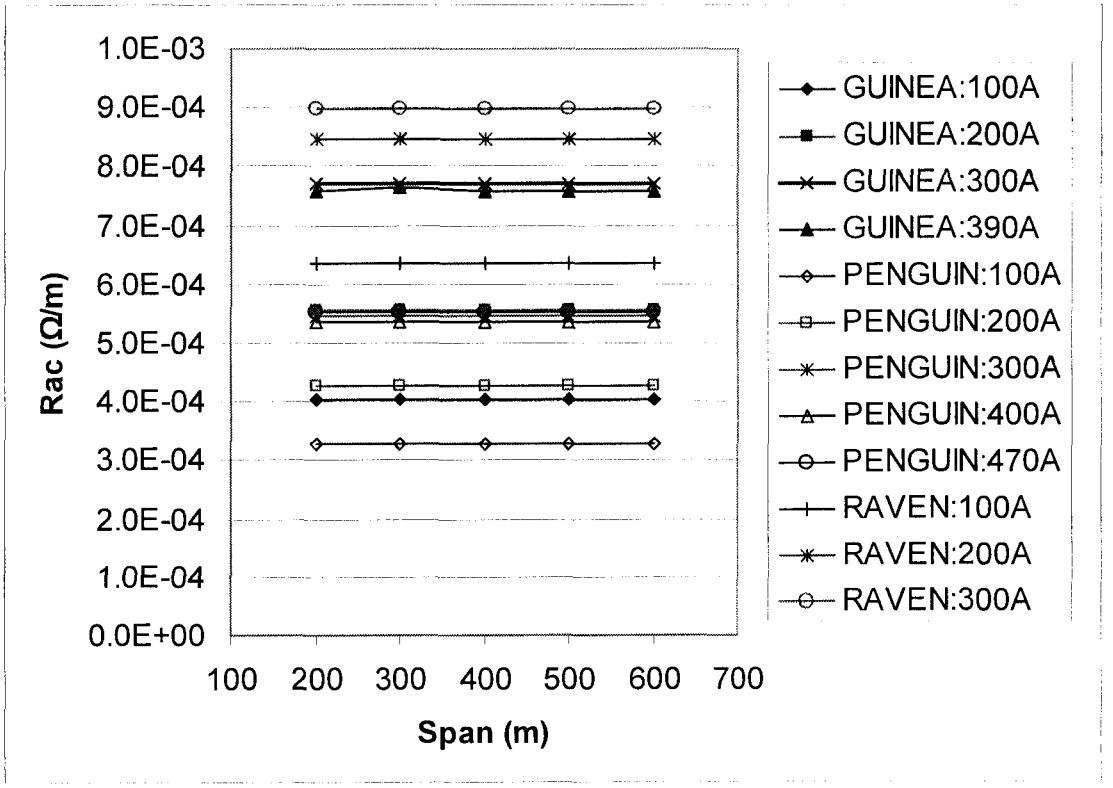

Figure 5.39 Variation of the ac resistance with the span and current

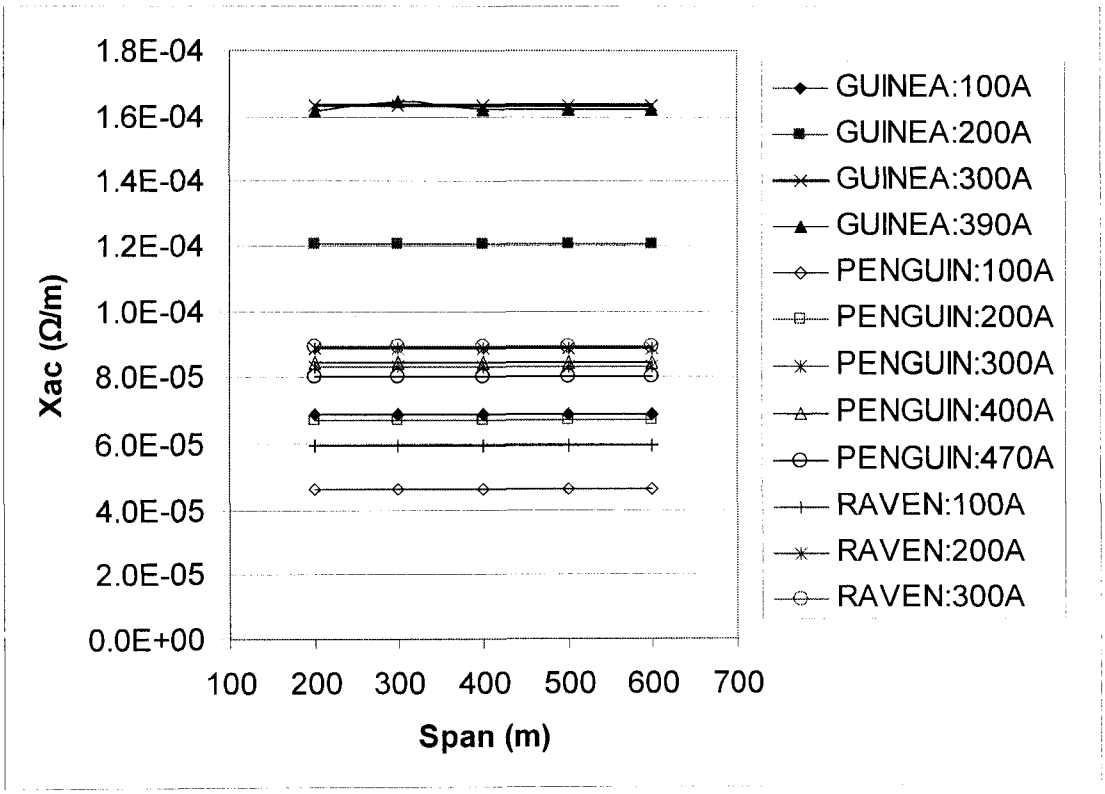

Figure 5.40 Variation of the ac reactance with the span and current

- **Effect on Mechanical Properties**

The variation of the aluminum stress with the span and current is shown in Figure 5.41 for Guinea, Penguin, and Raven conductors, respectively. Roughly speaking, the aluminum stress increases with an increase of the span, and decreases with an increase of the conductor current. The aluminum layer of Guinea conductor experiences a compressive load when the span is less than 420 m at 390 A.

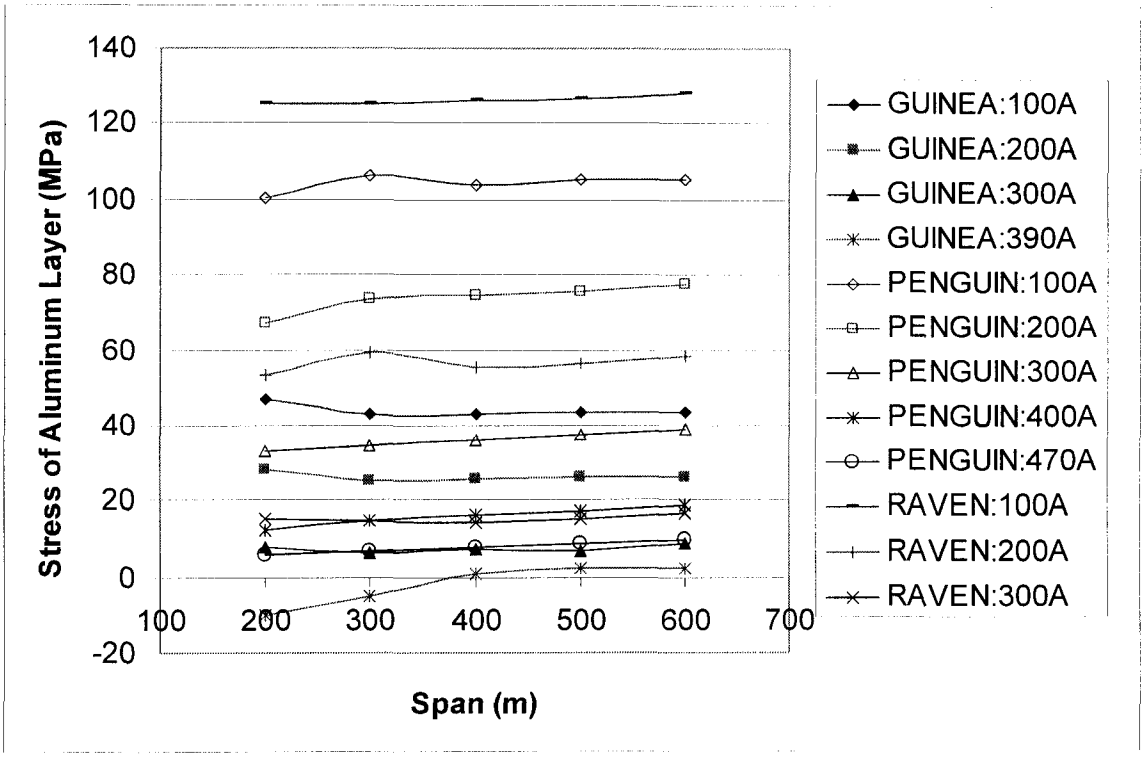

Figure 5.41 Variation of the aluminum stress with the span and current

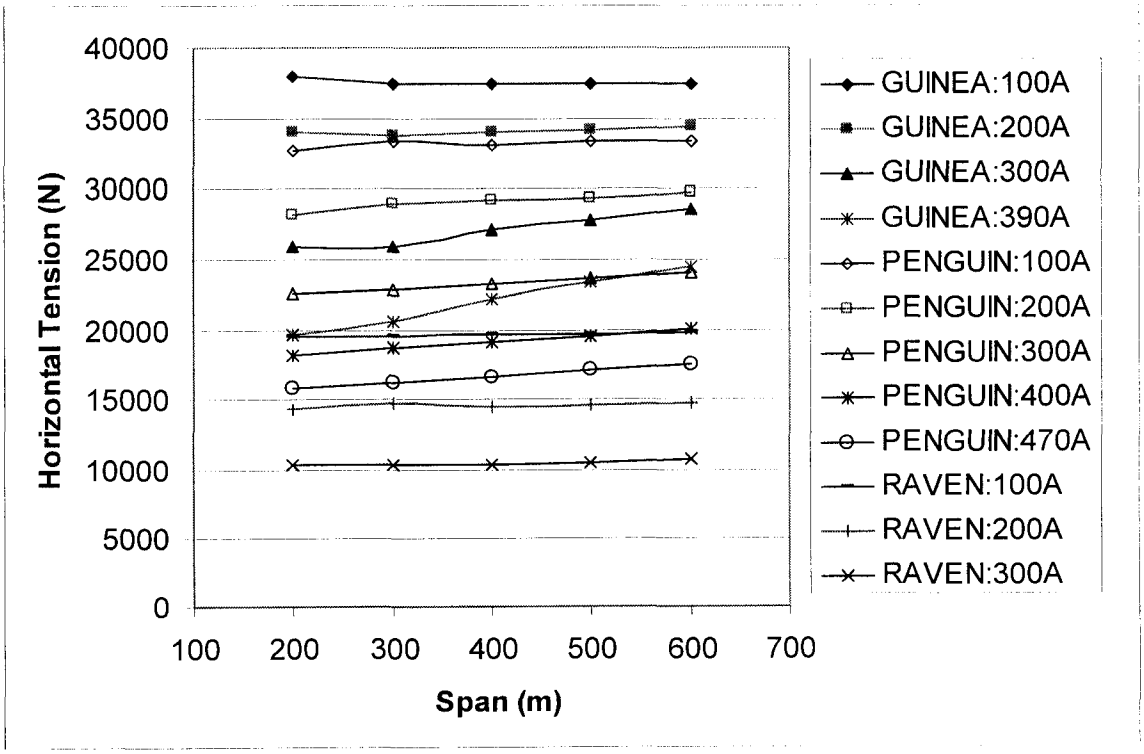

Figure 5.42 Variation of the horizontal tension with the span and current

Figure 5.42 shows how the horizontal tension varies with increases of span and current. The horizontal tension increases with an increase of the span, and decreases with the increase of the current.

The sag increases with increases of current and span, as shown in Figure 5.43 for the three conductors. The sag increases dramatically with an increase of the span. For Penguin conductor at 470 A, the sag increases from 1.3 m at 200 m span to 10.9 m at 600 m span, and the increase reaches 738 %. For Raven conductor, 1.0 m at 200 m span to 8.9 m at 600 m span, or 790 %.

The accumulating loss of tensile strength of the aluminum layer remains constant with the variation of the span length at a fixed current level as shown in Figure 5.44.

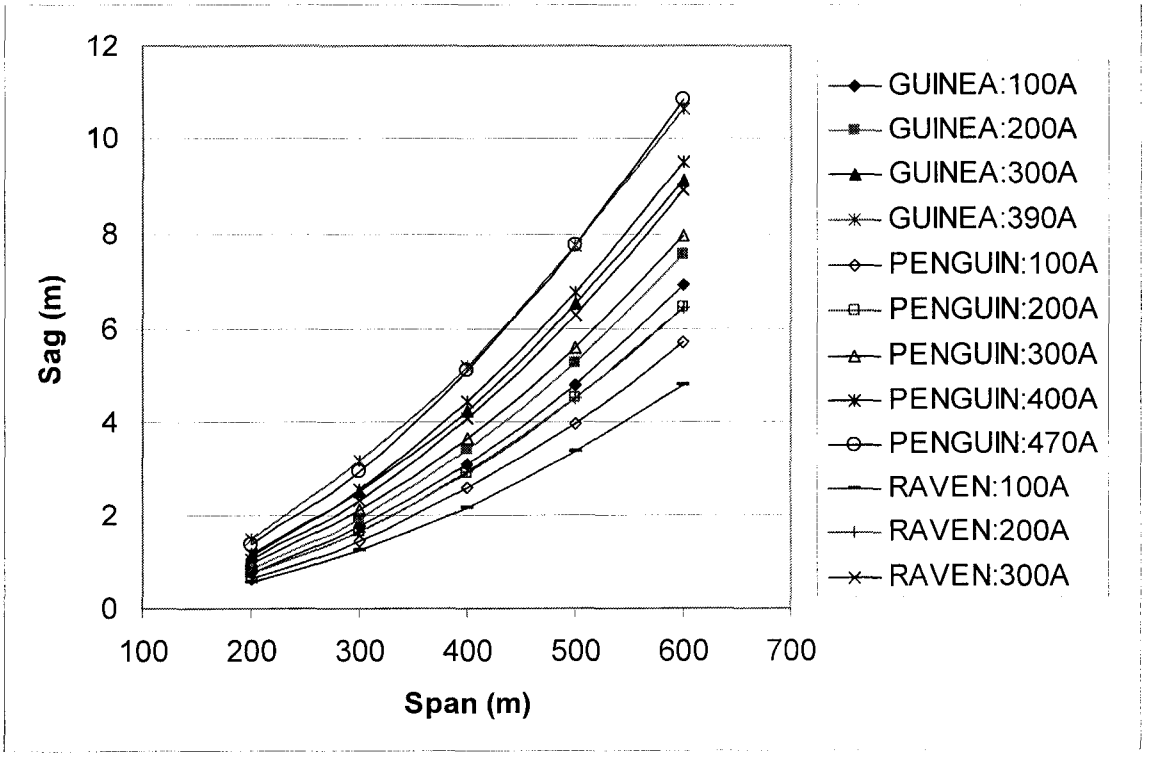

Figure 5.43 Variation of the sag with the span and current

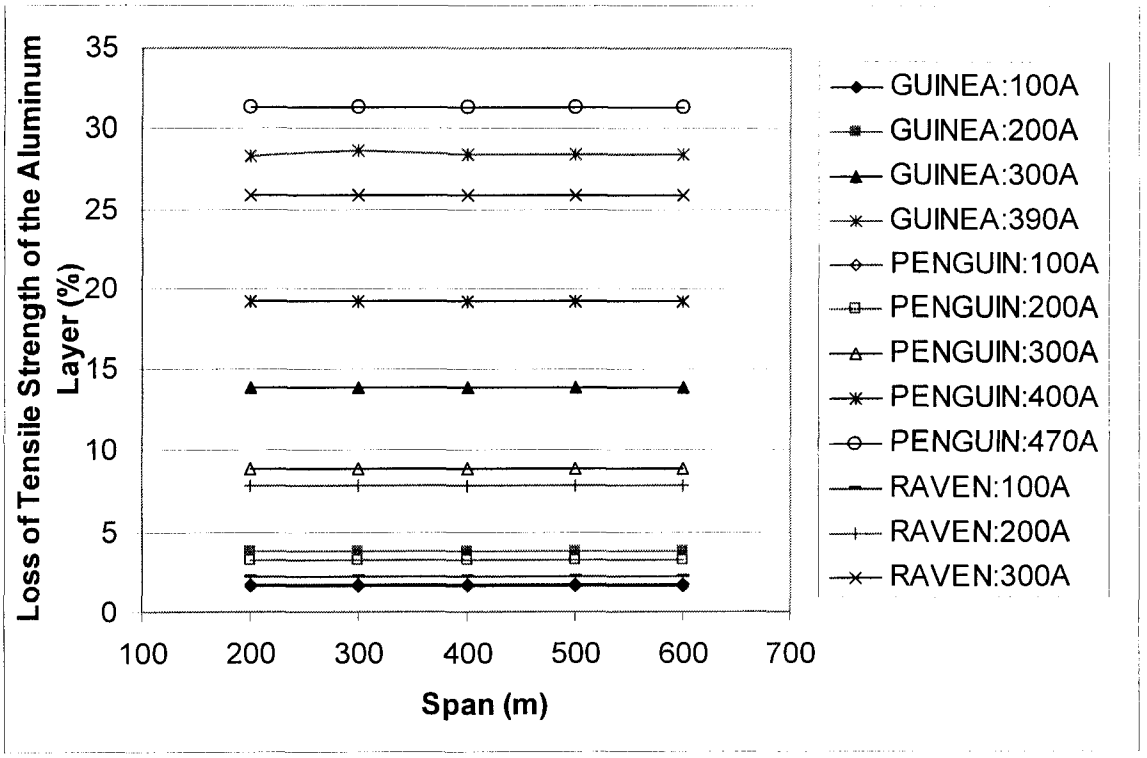

Figure 5.44 Variation of the loss of tensile strength of the aluminum layer with the span and current for Guinea, Penguin, and Raven conductors, respectively

CHAPTER 6
SENSITIVITY ANALYSIS OF THE INTEGRATED MODEL

6.1 Introduction

The Integrated Model, developed in this research, described in Chapter 2, validated in Chapter 4, and investigated in Chapter 5, has many input parameters from geometrical, environmental, and power supply, etc. The output of the Integrated Model involves electromagnetic, mechanical, and thermal characteristics of single layer ACSR conductors. This chapter examines some of the input parameters for their sensitivity in the Integrated Model.

The sensitivity analysis is a procedure to determine the outcomes of the model input parameters. If a small change in an input parameter results in relatively large changes in the outcomes, the outcomes are said to be sensitive to that parameter. The general procedure can be as follows: (1) to define a model output parameter that represents an important aspect of the model behavior; (2) to vary the value of a model input; (3) to examine the change of the output parameter. Large changes in the output parameter imply that the particular input parameter is important for model behaviors.

The sensitivity analysis in this chapter is not carried out for every parameter of the Integrated Model, but only for some parameters such as lay length of the aluminum layer (LAY), wire diameter of an aluminum strand (D), resistivity of aluminum (ρ_{al}), resistivity of steel (ρ_{st}), permeability (μ), frequency (f), and surface layer temperature (T). For each mentioned parameter varying with $\pm$ *5 %*, ac resistance, ac reactance, and heat losses are calculated and compared with their corresponding values without any other parameter variation. Since heat gains and heat losses constitute the fundamental equation of the Integrated Model, resistance (R_{ac}), reactance (X_{ac}), convection heat loss (P_{con}), and radiation heat loss (P_{rc}) are chosen as the output parameters in this sensitivity analysis. Solar heat gain has a fixed value if the distance and the relative position between the sun and the earth are relatively invariant. Resistive heat or Joule heat gain can be obtained from the ac resistance and the conductor current.

An example is given here to illustrate the performance: when the aluminum wire diameter D increases but *5 %*, we calculate the corresponding resistance, reactance, and heat losses with the wire diameter of *105 % D*. Similarly, we can obtain the resistance, reactance, and heat losses when the wire diameter D decreases to *95 %*.

6.2 Variation of Lay Length of the Aluminum Layer

Figure 6.1 shows the curves of ac resistance with the current and $\pm$ 5% variation of lay length for Guinea, Penguin, and Raven conductors, respectively. From Figure 6.1, we can find that the shorter the lay length, the larger the ac resistance is. This is consistent with the analyses of lay length effect in Chapter 5.

The curves of reactance with the current and the variation of lay length are shown in Figure 6.2. The reactance is more sensitive to the variation of lay length than the resistance.

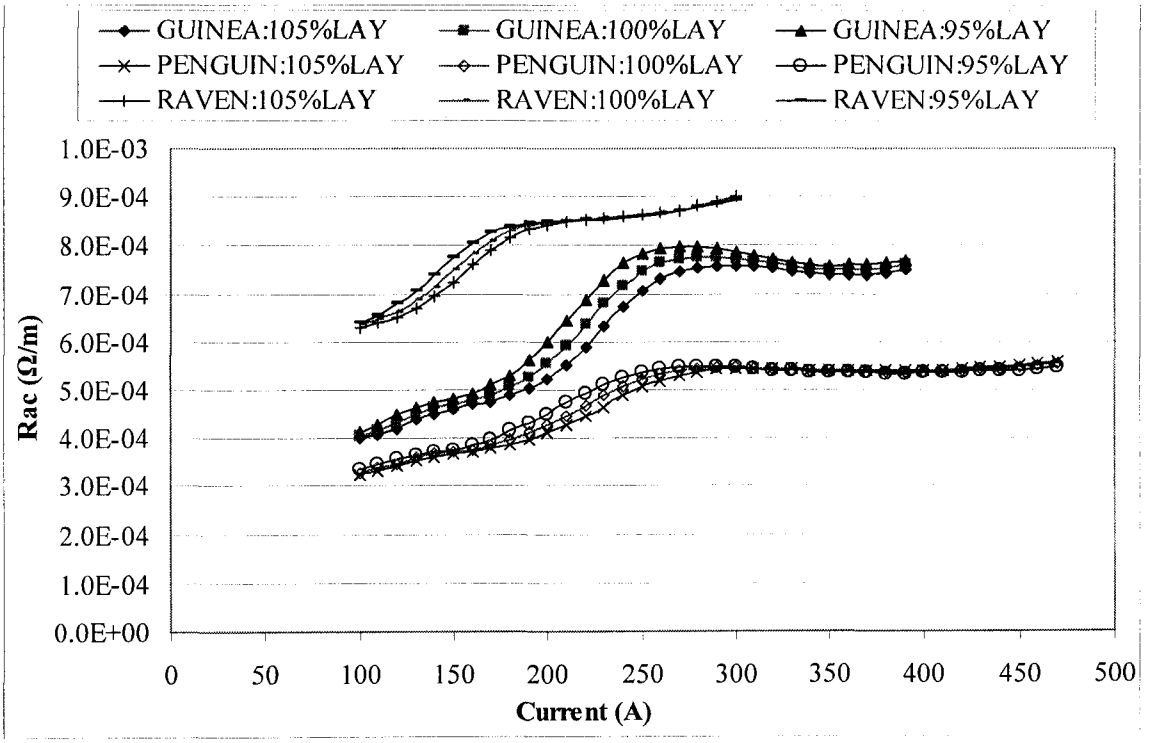

Figure 6.1 Variation of the ac resistance with the current and lay length

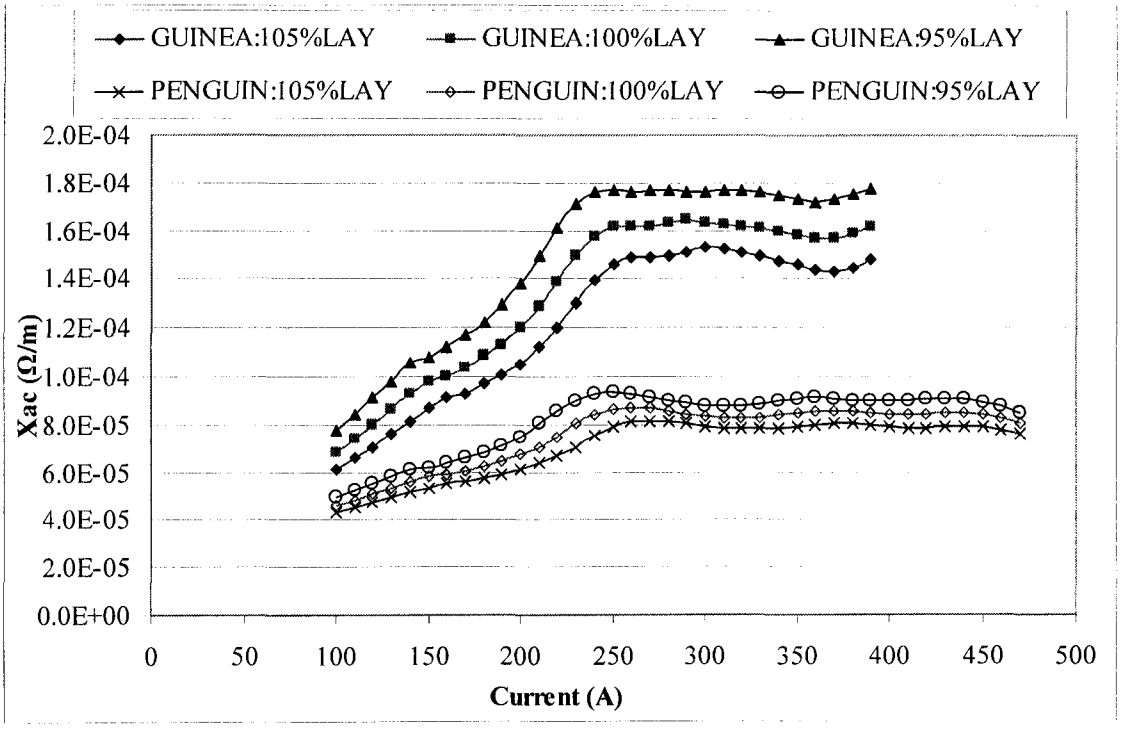

(a)

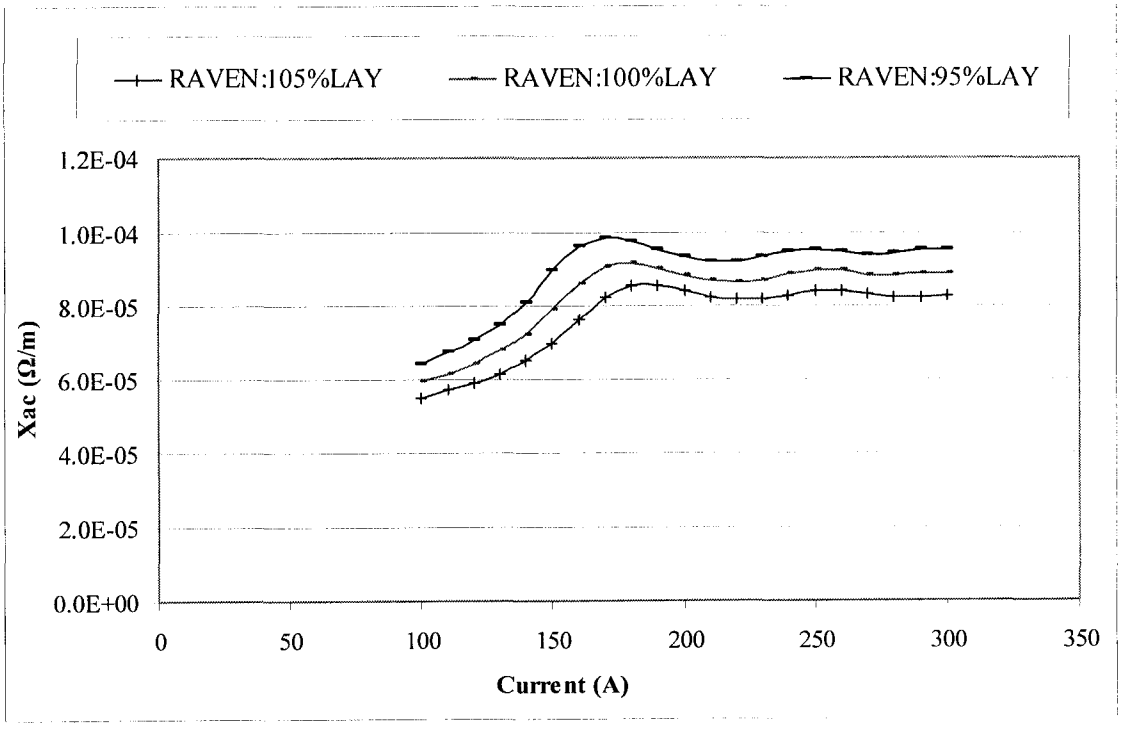

(b)

Figure 6.2 Variation of the ac reactance with the current and lay length for (a) Guinea and Penguin (b) Raven conductors, respectively

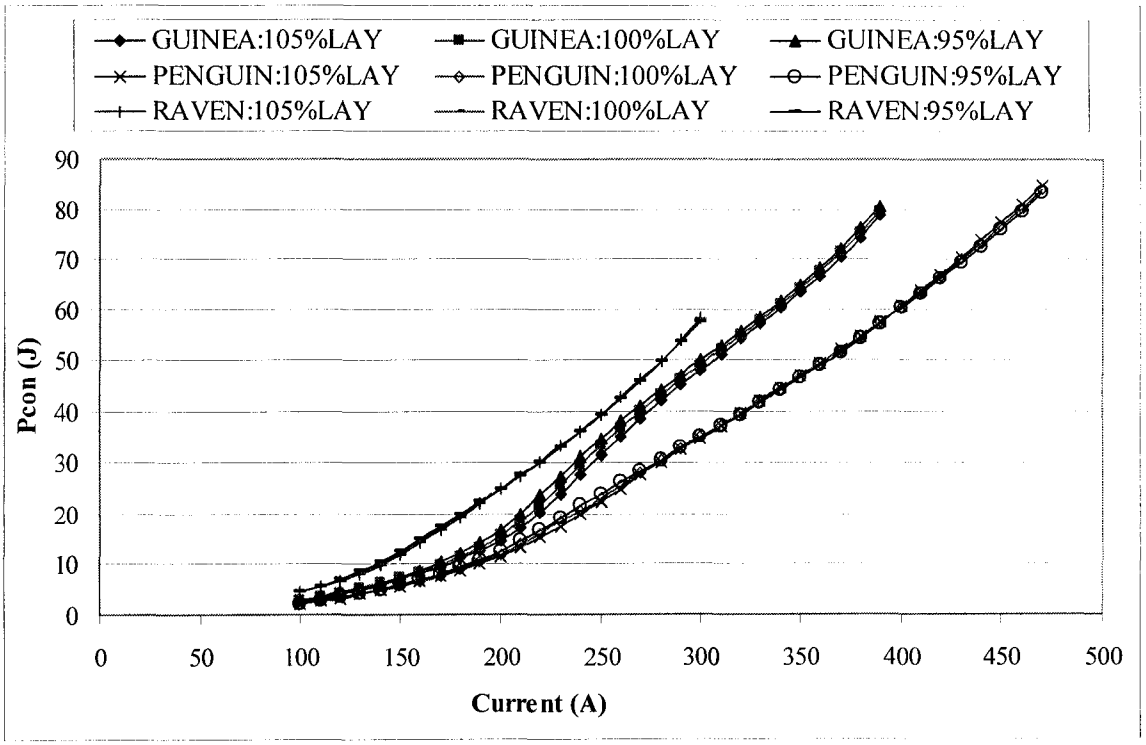

Figure 6.3 Variation of the convection heat with the current at various lay lengths

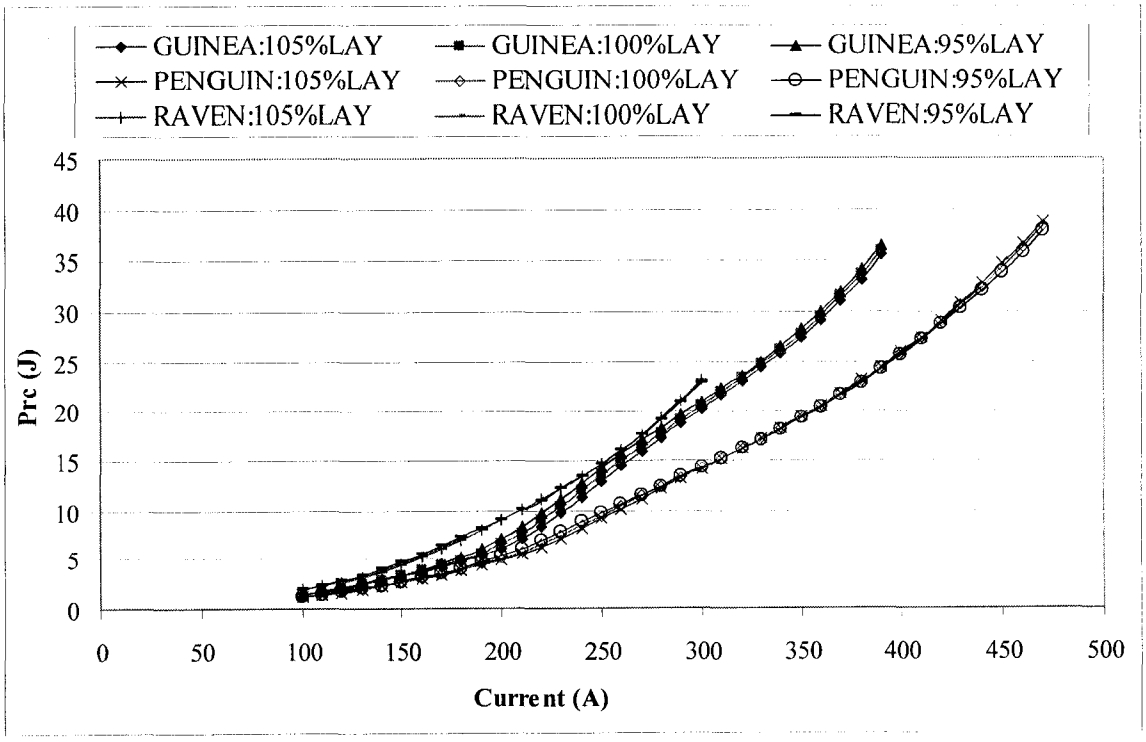

Figure 6.4 Variation of the radiation heat with the current and lay length

Figures 6.3 and 6.4 show the convection heat loss and the radiation heat loss with the current and the variation of lay length for three conductors, respectively. The convective and radiative heat losses are less with an increase of lay length because the resistive heat input per unit length decreases.

Tables 6.1 and 6.2 show quantitative results for resistance, reactance, heat losses at the interval of 50A in the sensitivity analyses for three conductors.

Table 6.1 Variation of resistance and reactance with the change of lay length

I(A)	ΔRac (%)						ΔXac (%)					
	Guinea		Penguin		Raven		Guinea		Penguin		Raven	
	105	95	105	95	105	95	105	95	105	95	105	95
100	-1.43	1.95	-1.09	1.44	-0.97	0.78	-10.6	13.0	-6.48	7.78	-7.89	7.72
150	-2.25	1.90	-1.60	1.08	-3.53	3.33	-11.0	10.7	-7.75	7.06	-11.8	13.6
200	-6.47	7.66	-3.96	5.03	-0.47	0.27	-12.7	15.0	-8.90	11.4	-4.87	5.66
250	-5.40	4.83	-3.24	2.96	0.18	-0.16	-9.79	9.35	-8.67	8.32	-6.12	6.35
300	-1.91	1.87	-0.41	0.08	0.36	-0.57	-6.47	7.69	-4.80	5.64	-6.64	7.09
350	-1.26	1.41	0.37	-0.38			-7.83	9.48	-6.37	6.96		
390	-1.17	1.29	0.29	-0.49			-8.66	9.65	-5.79	6.03		
440			0.67	-1.04					-6.61	6.97		
470			0.99	-0.96					-4.85	5.85		

Table 6.2 Variation of convection heat and radiation heat with the change of lay length

I(A)	ΔPcon (%)						ΔPrc (%)					
	Guinea		Penguin		Raven		Guinea		Penguin		Raven	
	105	95	105	95	105	95	105	95	105	95	105	95
100	-1.49	2.04	-1.14	1.51	-1.00	0.80	-1.26	1.72	-0.96	1.27	-0.87	0.69
150	-2.32	1.96	-1.66	1.12	-3.59	3.38	-2.05	1.73	-1.45	0.97	-3.35	3.17
200	-6.58	7.79	-4.05	5.15	-0.46	0.27	-6.14	7.29	-3.70	4.70	-0.47	0.28
250	-5.37	4.79	-3.26	2.97	0.26	-0.16	-5.44	4.91	-3.19	2.92	0.28	-0.18
300	-1.85	1.82	-0.41	0.08	0.40	-0.47	-2.02	2.00	-0.42	0.08	0.48	-0.57
350	-1.20	1.34	0.36	-0.37			-1.39	1.56	0.39	-0.40		
390	-1.09	1.21	0.28	-0.47			-1.33	1.48	0.32	-0.53		
440			0.63	-0.98					0.76	-1.17		
470			0.92	-0.89					1.14	-1.11		

From Figure 6.1 and Table 6.1, we can see that the resistance is sensitive to the variation of lay length, for Guinea and Penguin conductors, for a current range from 170 A to 300 A. For Raven, it is from 110 A to 190 A. When the current is outside of the sensitive current range, resistance is less sensitive. Take Guinea conductor as an example: the resistance variation is more than 8.5 % at 210 A while it is less than 1.3 % at 390 A.

From Tables 6.1 and 6.2, we can see that the reactance is more sensitive to the variation of the lay length than the other parameters such as resistance, heat gain, and heat losses. The variation of reactance can be as high as 27.7 % for Guinea at 200 A.

From Figures 6.1 and 6.2, Table 6.1, we also find that the resistance and reactance are more sensitive to the lay length decrease (95 %) than to the lay length increase (105 %). The output parameters of Guinea conductor are more sensitive to the variation of lay length than those of Penguin and Raven conductors.

Since the ac resistance decreases with an increase of the lay length, we can say that the power transmission efficiency can be improved by increasing the lay length of the aluminum layer, within mechanical constraints. The maximum allowable ratio of lay length to nominal outside diameter of aluminum layer for ACSR is 14.5 from ASTM standard [20], which is 116 % increase from the preferred lay length.

6.3 Variation of the Aluminum Wire Diameter

AC resistance and ac reactance with the variation of the current and the aluminum wire diameter are shown in Figures 6.5 and 6.6, respectively, for three types of single layer ACSR conductors. The ac resistance is more sensitive to the variation of wire diameter at high current rating than that at low current rating. From Figure 6.5, we can see that the change of ac resistance is more obvious when the current is larger than 320 A for Guinea, 350 A for Penguin, and 190 A for Raven.

However, the ac reactance is not sensitive to the variation of the aluminum wire diameter, especially at low conductor current ratings.

Figures 6.7 and 6.8 show the variation of the convection heat and the radiation heat with the wire diameter, respectively.

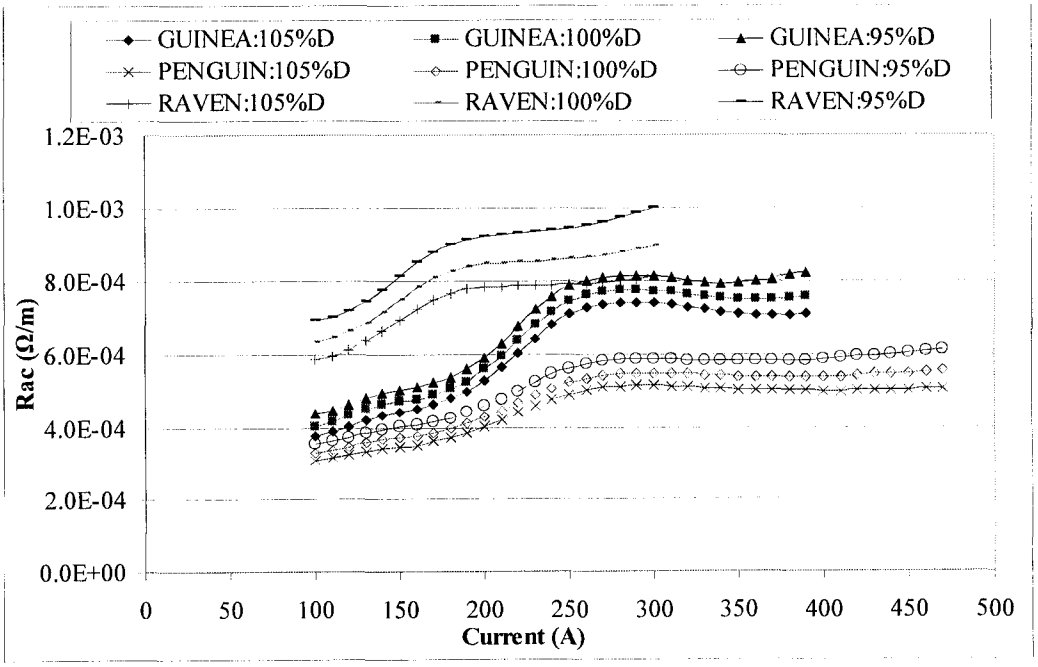

Figure 6.5 Variation of the ac resistance with the current and wire diameter

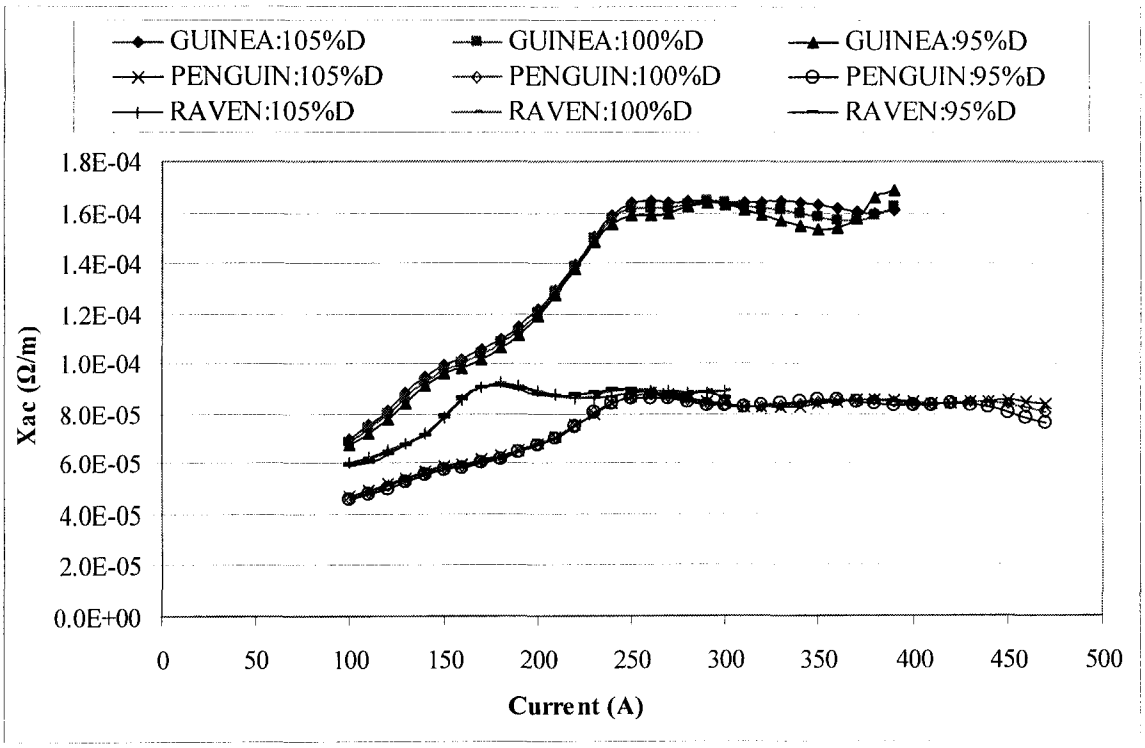

Figure 6.6 Variation of the ac reactance with the current and wire diameter

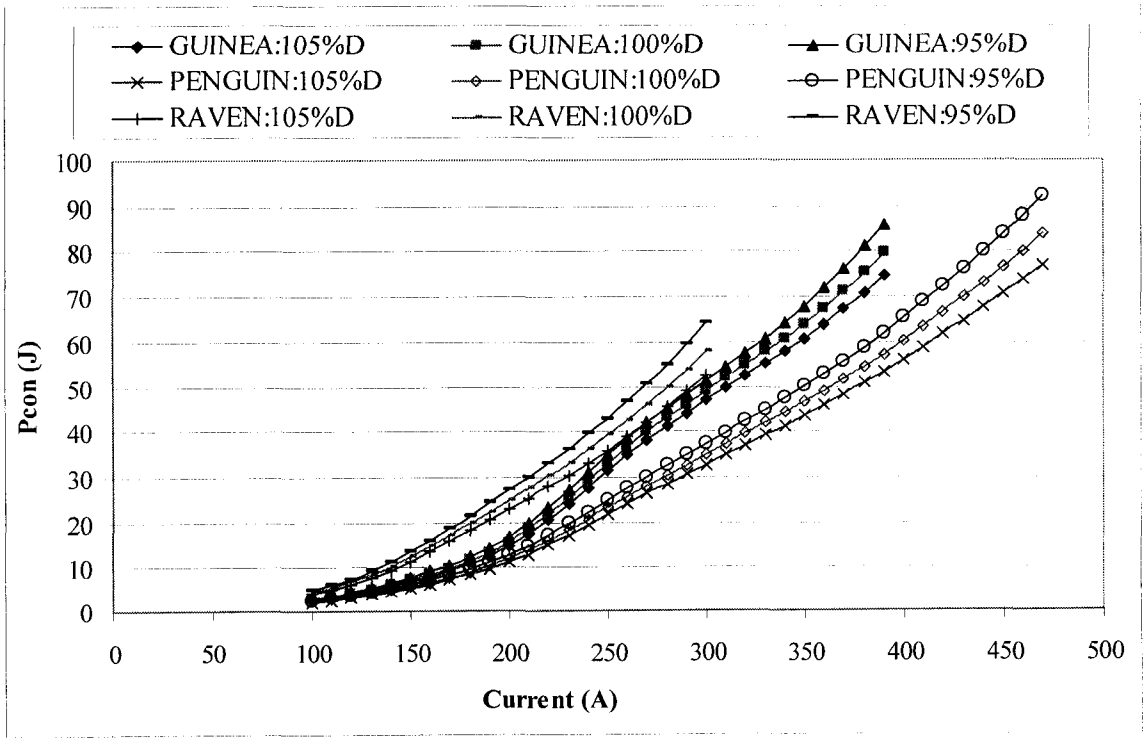

Figure 6.7 Variation of the convection heat with the current and wire diameter

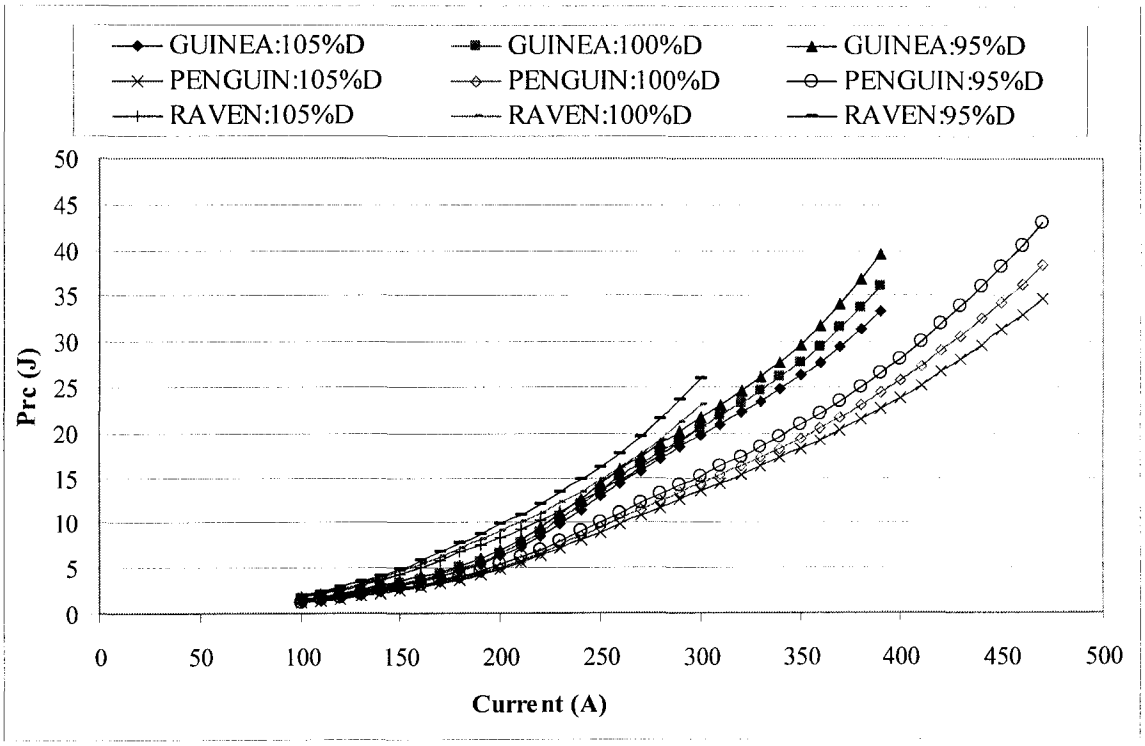

Figure 6.8 Variation of the radiation heat with the current and wire diameter

Table 6.3 Variation of ac resistance and reactance with the change of wire diameter

I(A)	ΔRac (%)						ΔXac (%)					
	Guinea		Penguin		Raven		Guinea		Penguin		Raven	
	105	95	105	95	105	95	105	95	105	95	105	95
100	-6.79	7.83	-7.04	8.18	-7.75	9.03	2.18	-2.33	1.30	-1.51	1.17	-1.01
150	-6.07	6.99	-6.58	7.64	-7.44	8.81	1.64	-1.84	1.03	-1.03	-0.13	0.13
200	-5.06	5.99	-5.95	6.97	-7.60	8.91	1.22	-1.30	0.59	-0.74	1.02	-0.79
250	-4.90	5.49	-6.05	7.11	-8.21	9.76	1.47	-1.74	0.23	-0.46	-1.45	-0.45
300	-4.41	5.06	-5.99	6.93	-9.35	11.7	0.17	-0.30	0.72	-0.36	0.00	-3.15
350	-5.11	6.23	-6.41	7.48			3.26	-3.00	-1.30	0.71		
390	-6.66	8.65	-6.84	8.32			-0.54	4.07	0.71	-1.54		
440			-7.79	9.73					0.24	-2.72		
470			-8.60	10.4					4.73	-4.98		

Table 6.4 Variation of convective heat and radiative heat with the change of wire diameter

I(A)	ΔPcon (%)						ΔPrc (%)					
	Guinea		Penguin		Raven		Guinea		Penguin		Raven	
	105	95	105	95	105	95	105	95	105	95	105	95
100	-7.37	8.51	-7.82	9.12	-8.38	9.78	-5.45	6.22	-5.26	6.05	-6.02	6.95
150	-6.52	7.51	-7.24	8.43	-7.87	9.31	-4.98	5.72	-5.02	5.80	-6.18	7.37
200	-5.37	6.33	-6.46	7.56	-7.82	9.12	-4.30	5.13	-4.68	5.51	-6.95	8.27
250	-5.02	5.61	-6.40	7.49	-8.21	9.58	-4.58	5.19	-5.16	6.14	-8.18	9.87
300	-4.41	5.03	-6.18	7.10	-8.99	11.2	-4.38	5.12	-5.51	6.48	-10.0	13.2
350	-4.98	6.01	-6.46	7.48			-5.39	6.73	-6.26	7.47		
390	-6.33	8.10	-6.77	8.13			-7.37	9.86	-6.99	8.75		
440			-7.51	9.21					-8.42	10.9		
470			-8.16	9.68					-9.56	12.0		

Table 6.3 shows ac resistance and ac reactance with the variation of the aluminum wire diameter at some fixed current ratings. The change of resistance is larger than the change of reactance with ±5 % variation of the aluminum wire diameter. The highest variation of resistance for Raven at 300 A is 12 % to -9 % for 105 % to 95 %, respectively. And most of the variations are larger than 5 %. All the variation of reactance is less than 5 % and most of them are less than 2 %.

The variations of the heat losses with the current and the wire diameter are shown in Table 6.4. These variations may be as high as 13 %.

Similarly to the effect of the lay length, almost all parameters are more sensitive to the wire diameter decrease (95 %) than to its increase (105 %).

Since ac resistance and resistive heat gain decrease with the increase of the aluminum wire diameter, reasonably increasing wire diameter can decrease the power loss during transmission and distribution.

6.4 Variation of the Aluminum Resistivity

The variation of resistance with the current and aluminum resistivity is shown in Figure 6.9. AC resistance increases or decreases with the increase or decrease of the aluminum resistivity. Comparing with Guinea and Penguin, Raven conductor shows more obvious change in resistance with the variation of the aluminum resistivity.

Figure 6.10 shows the variation of ac reactance curves with the current and resistivity. Reactance is not sensitive to the variation of aluminum resistivity.

The variation of the convection heat loss and the radiation heat loss with the current and the aluminum resistivity is shown in Figures 6.11 and 6.12, respectively. The curves show that the change of heat losses is more obvious with high current than with low current.

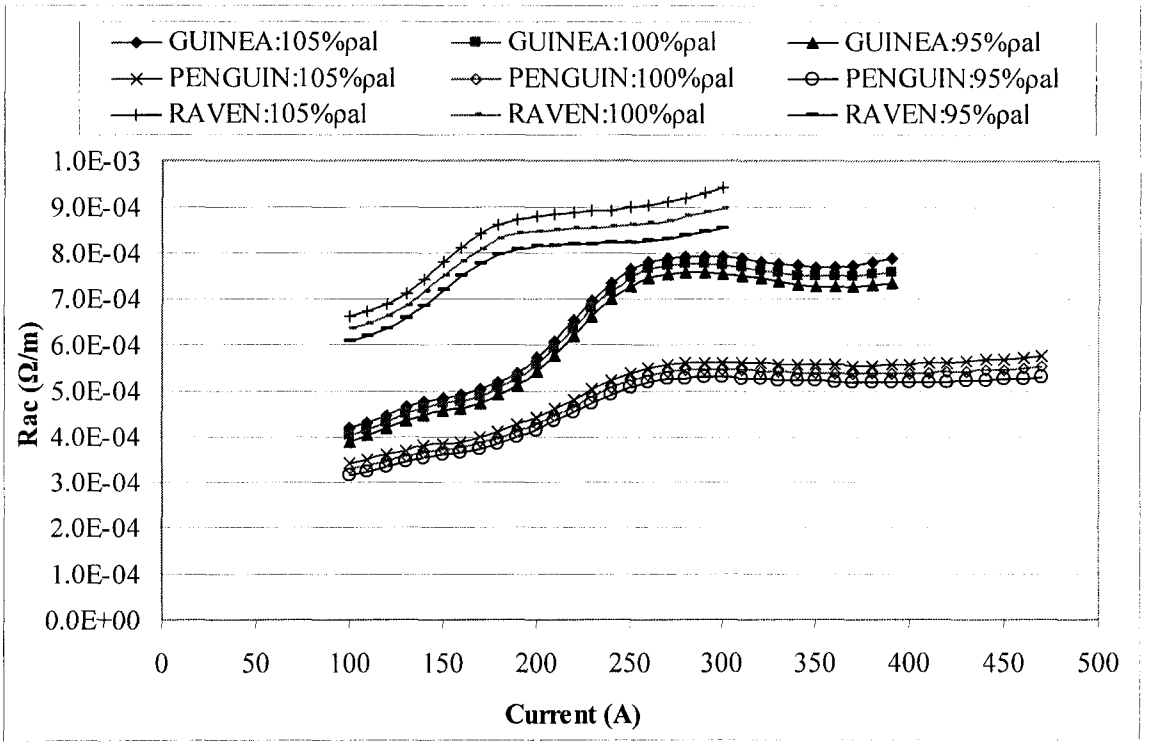

Figure 6.9 Variation of the ac resistance with the current and aluminum resistivity

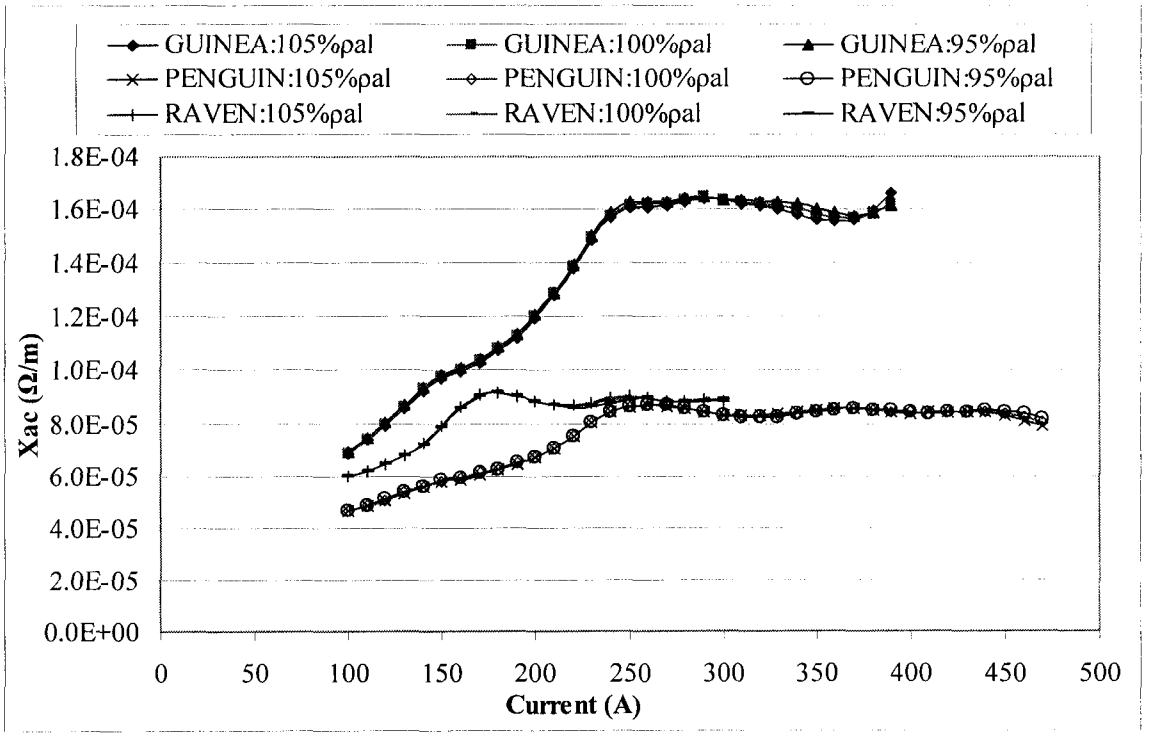

Figure 6.10 Variation of the ac reactance with the current and aluminum resistivity

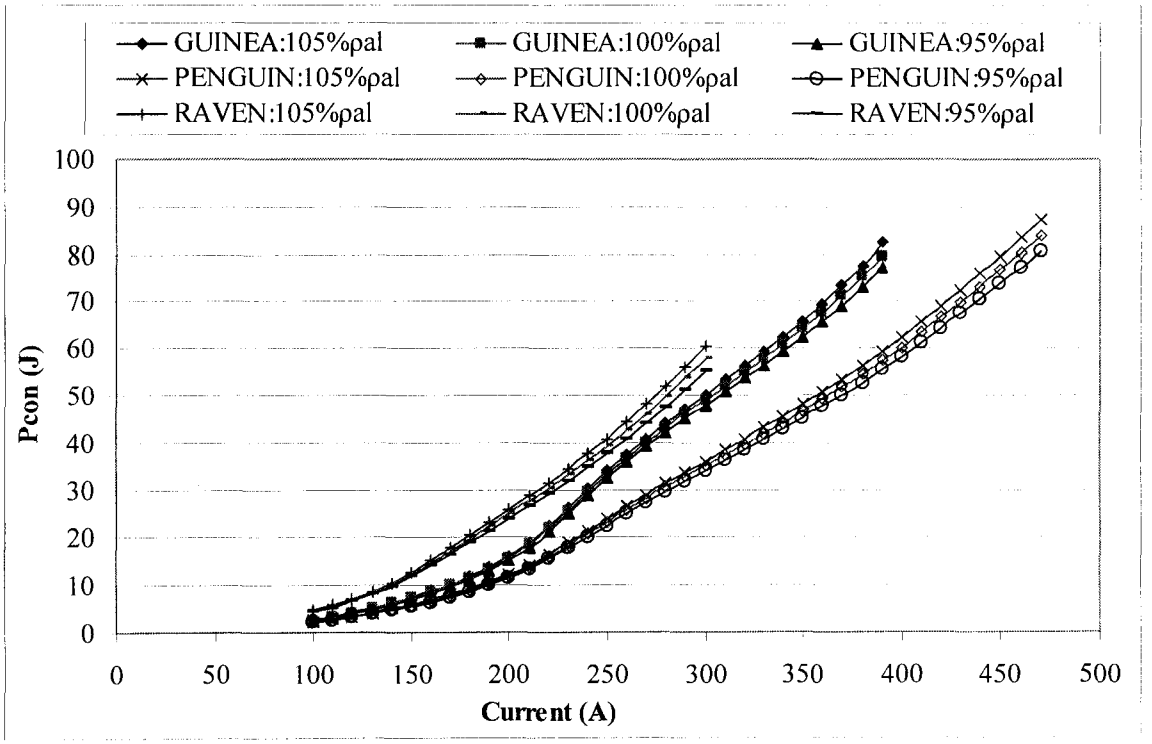

Figure 6.11 Variation of the convection heat with the current and aluminum resistivity

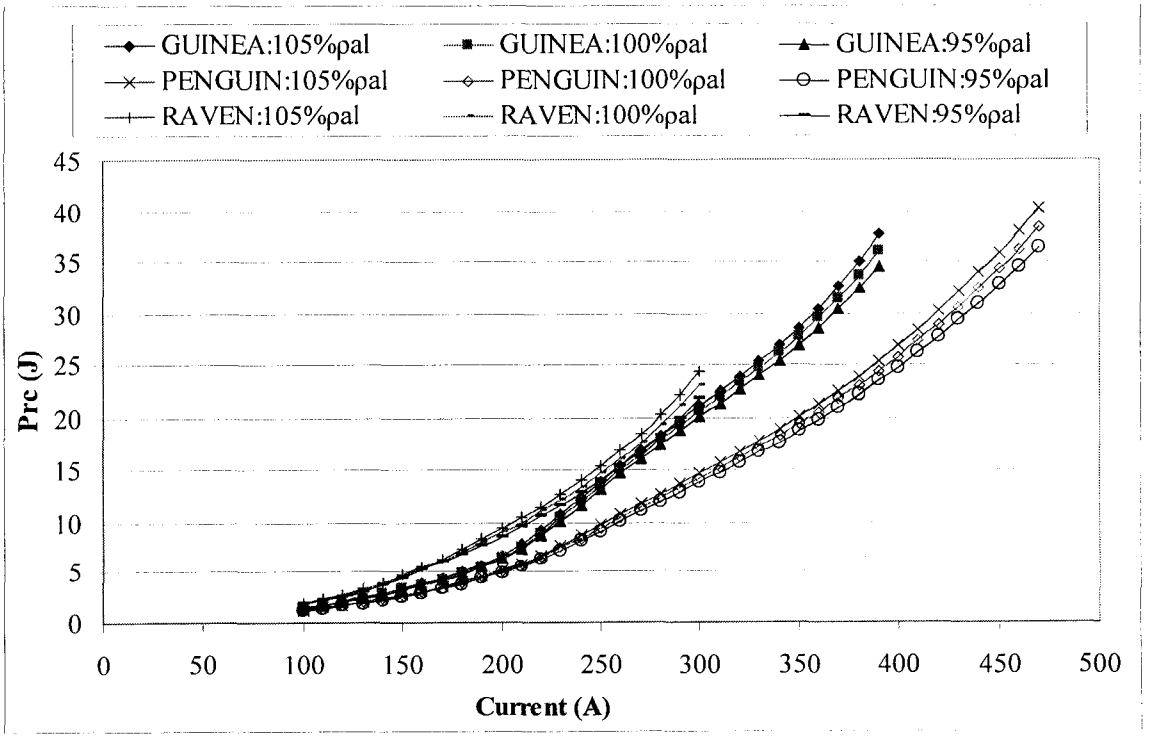

Figure 6.12 Variation of the radiation heat with the current and aluminum resistivity

Tables 6.5 and 6.6 show that ac resistance, convection heat loss, and radiation heat loss varies less than ± 5 % with a 5 % change of aluminum resistivity. AC reactance varies less than 1 % with 5 % change of aluminum resistivity.

Table 6.5 Variation of resistance and reactance with the change of aluminum resistivity

I(A)	ΔRac (%)						ΔXac (%)					
	Guinea		Penguin		Raven		Guinea		Penguin		Raven	
	105	95	105	95	105	95	105	95	105	95	105	95
100	3.63	-3.65	3.79	-3.79	4.15	-4.15	-0.73	0.73	-0.22	0.00	0.00	0.17
150	3.23	-3.24	3.51	-3.51	3.93	-3.91	-0.61	0.61	0.00	0.00	0.25	-0.25
200	2.69	-2.68	3.15	-3.15	3.94	-3.93	-0.51	0.52	0.00	0.00	-0.11	0.23
250	2.42	-2.44	3.06	-3.05	4.29	-4.25	-0.63	0.62	0.00	0.00	0.33	-0.67
300	2.32	-2.33	3.04	-3.04	4.94	-4.80	-0.08	0.06	0.00	0.00	-0.67	0.11
350	2.74	-2.71	3.28	-3.26			-1.22	1.33	0.59	-0.59		
390	4.04	-3.38	3.54	-3.50			2.44	-0.43	-0.24	0.24		
440			4.02	-3.93					-0.47	0.12		
470			4.36	-4.29					-1.74	1.74		

Table 6.6 Variation of convection and radiation heat losses with the change of aluminum resistivity

I(A)	ΔPcon (%)						ΔPrc (%)					
	Guinea		Penguin		Raven		Guinea		Penguin		Raven	
	105	95	105	95	105	95	105	95	105	95	105	95
100	3.79	-3.80	3.95	-3.94	4.28	-4.28	3.20	-3.23	3.32	-3.33	3.73	-3.74
150	3.33	-3.35	3.64	-3.64	3.99	-3.97	2.94	-2.95	3.16	-3.17	3.73	-3.71
200	2.73	-2.73	3.23	-3.22	3.91	-3.90	2.56	-2.55	2.95	-2.94	4.01	-3.98
250	2.40	-2.43	3.07	-3.07	4.15	-4.13	2.46	-2.47	3.01	-3.00	4.63	-4.56
300	2.25	-2.27	3.01	-3.01	4.71	-4.49	2.48	-2.47	3.11	-3.09	5.75	-5.37
350	2.61	-2.59	3.19	-3.18			3.04	-2.98	3.48	-3.45		
390	3.76	-3.17	3.40	-3.36			4.64	-3.84	3.88	-3.80		
440			3.77	-3.71					4.57	-4.42		
470			4.03	-3.99					5.06	-4.92		

AC resistance changes with the variation of resistivity, so the resistive heat gain changes as well. According to energy conservation and heat balance equation, the convection and radiation heat losses vary correspondingly.

6.5 Variation of the Steel Resistivity

The variations of ac resistance and ac reactance with the current and steel resistivity are shown in Figures 6.13 and 6.14, respectively. From these two figures, we can find that resistance and reactance are not very sensitive to the variation of steel resistivity.

Figures 6.15 and 6.16 show the variation of the convection heat loss and the radiation heat loss with the current and steel resistivity, respectively. Similar to resistance and reactance, they are not very sensitive to the variation of steel resistivity.

So, the Integrated Model is not sensitive to the variation of steel resistivity from the respective of resistance, reactance, convection heat loss, and radiation heat loss.

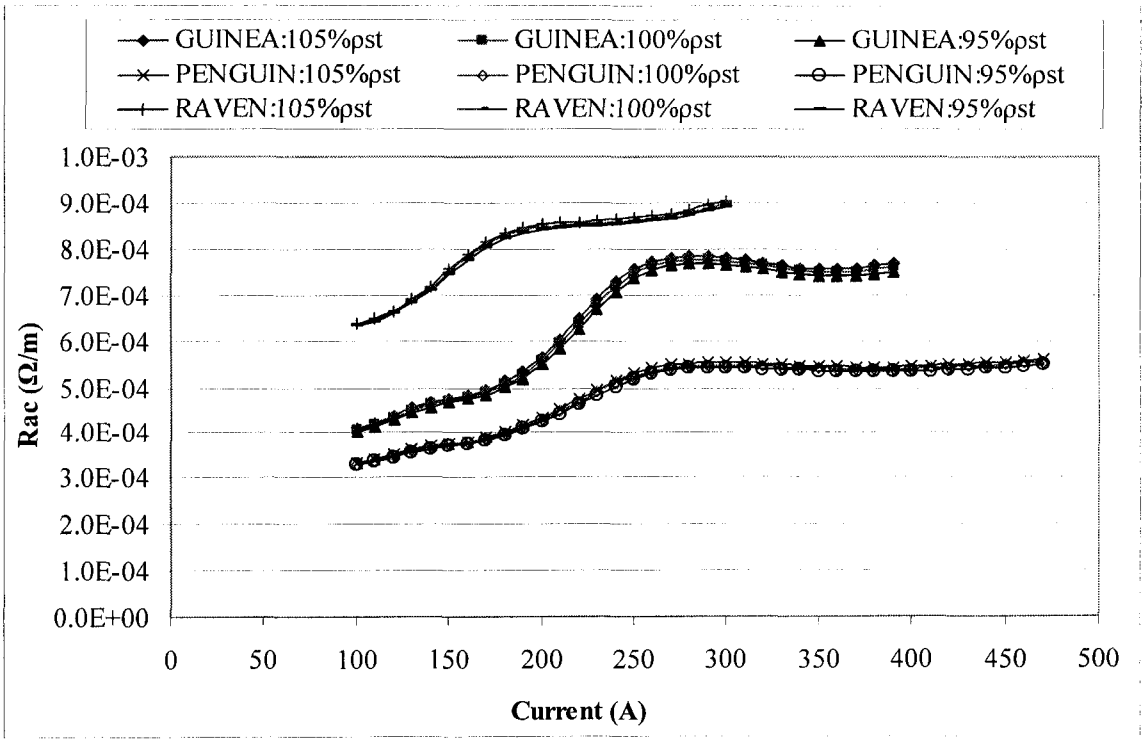

Figure 6.13 Variation of the ac resistance with the current and steel resistivity

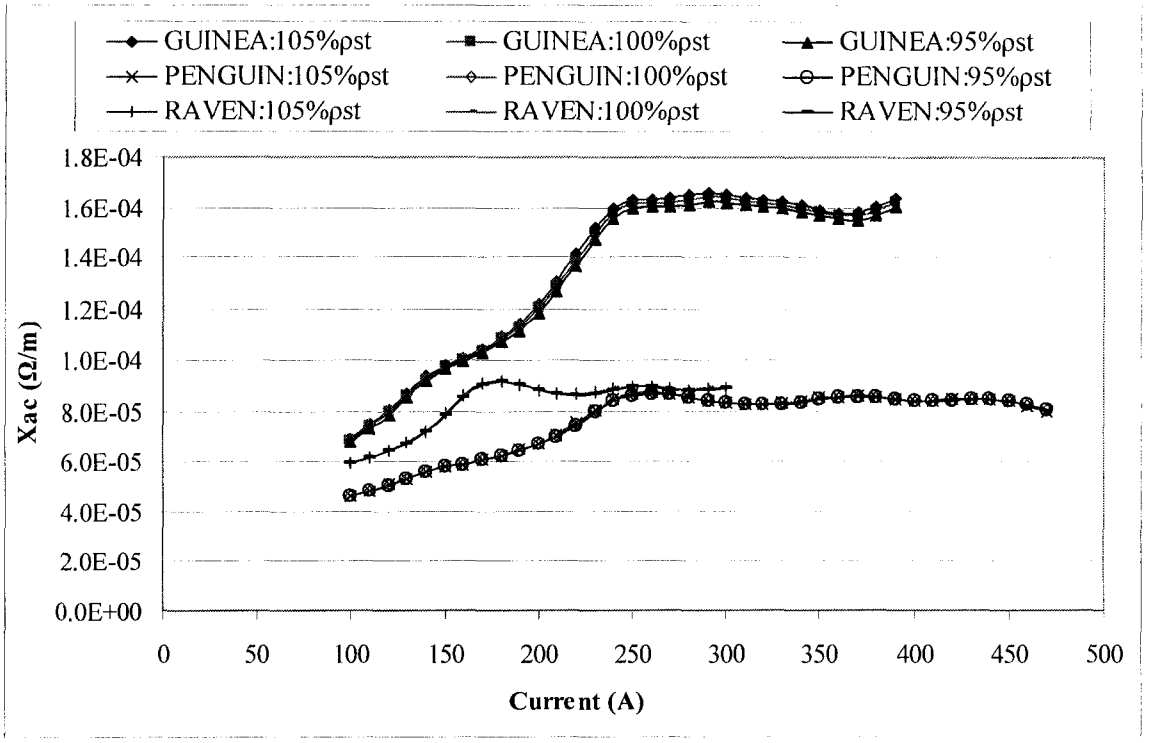

Figure 6.14 Variation of the ac reactance with the current and steel resistivity

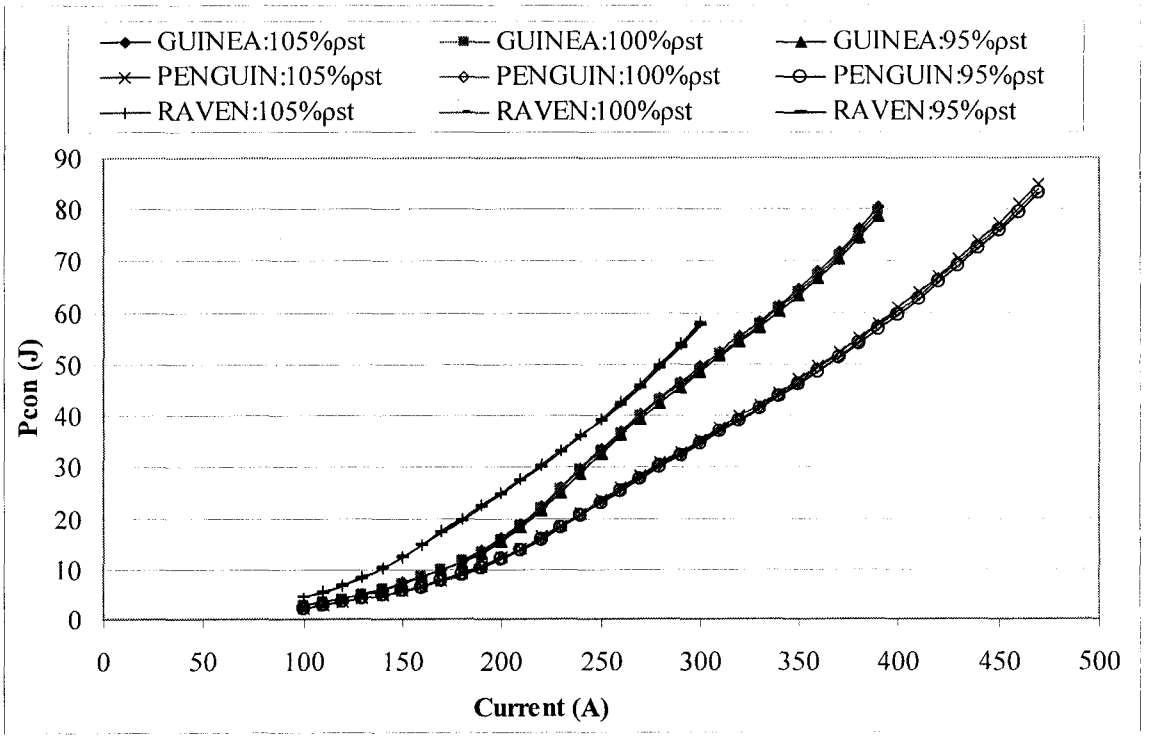

Figure 6.15 Variation of the convection heat with the current and aluminum resistivity

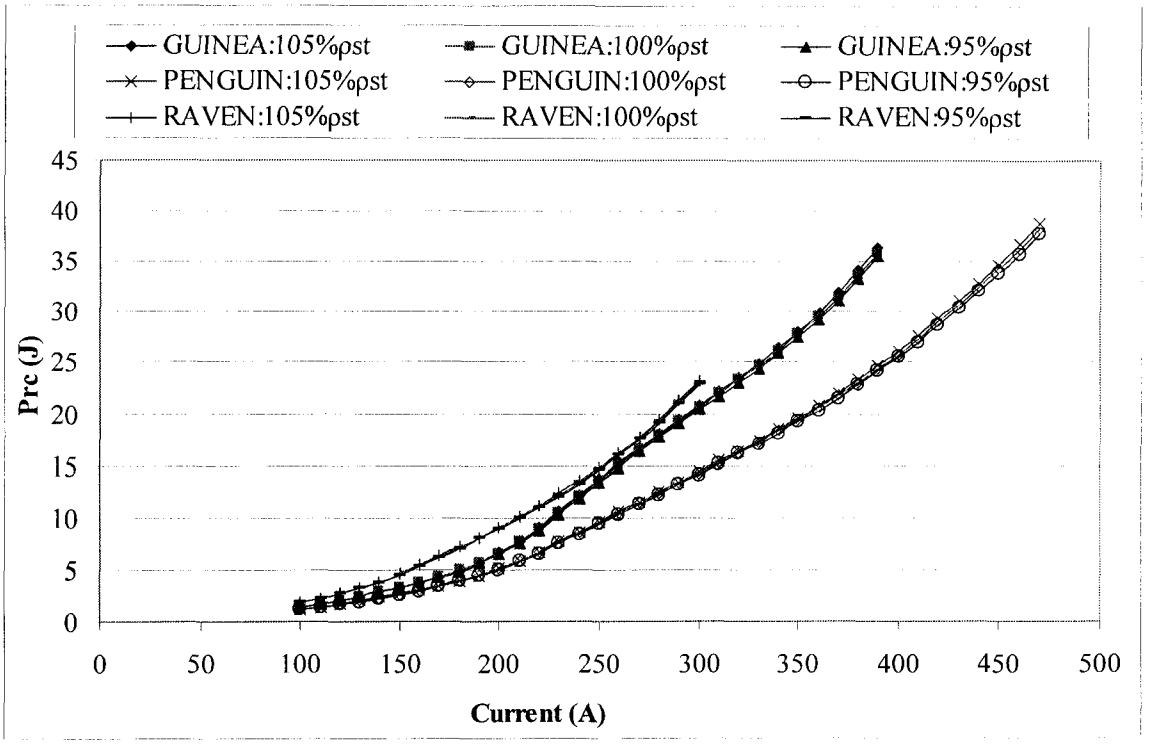

Figure 6.16 Variation of the radiation heat with the current and steel resistivity

Tables 6.7 and 6.8 give a quantitative variation of the parameters with the variation of steel resistivity in some current ratings. The variation is around or less than 1 % with ± 5 % change of steel resistivity. The output parameters are not related directly to the steel resistivity, so they are not very sensitive to its variation.

Table 6.7 Variation of resistance and reactance with the change of steel resistivity

I(A)	ΔRac (%)						ΔXac (%)					
	Guinea		Penguin		Raven		Guinea		Penguin		Raven	
	105	95	105	95	105	95	105	95	105	95	105	95
100	0.85	-0.90	0.66	-0.69	0.49	-0.51	0.87	-0.87	0.00	-0.22	0.17	0.00
150	0.94	-0.98	0.76	-0.79	0.68	-0.71	0.82	-0.92	0.17	-0.17	0.25	-0.38
200	1.43	-1.49	0.95	-0.98	0.67	-0.69	1.30	-1.38	0.15	-0.30	0.11	-0.11
250	1.40	-1.50	1.09	-1.13	0.64	-0.66	1.07	-1.19	0.35	-0.23	0.22	-0.22
300	0.95	-1.01	0.97	-1.00	0.66	-0.67	0.84	-0.92	0.12	-0.12	0.11	-0.11
350	0.93	-0.97	0.94	-0.97			0.70	-0.76	0.35	-0.35		
390	1.08	-1.13	0.96	-0.98			1.20	-1.30	0.12	0.00		
440			1.01	-1.04					0.00	-0.12		
470			1.04	-1.07					-0.37	0.25		

Table 6.8 Variation of convection and radiation heat losses with the change of steel resistivity

I(A)	ΔPcon (%)						ΔPrc (%)					
	Guinea		Penguin		Raven		Guinea		Penguin		Raven	
	105	95	105	95	105	95	105	95	105	95	105	95
100	0.89	-0.94	0.69	-0.71	0.51	-0.53	0.75	-0.80	0.59	-0.60	0.44	-0.46
150	0.97	-1.02	0.79	-0.82	0.70	-0.72	0.85	-0.90	0.69	-0.72	0.65	-0.67
200	1.46	-1.52	0.97	-1.00	0.66	-0.69	1.36	-1.42	0.88	-0.92	0.68	-0.70
250	1.39	-1.49	1.10	-1.14	0.62	-0.64	1.43	-1.52	1.08	-1.11	0.69	-0.71
300	0.92	-0.98	0.96	-0.99	0.62	-0.57	1.01	-1.07	0.99	-1.02	0.76	-0.69
350	0.89	-0.92	0.92	-0.94			1.03	-1.07	1.00	-1.03		
390	1.01	-1.05	0.92	-0.95			1.23	-1.29	1.05	-1.07		
440			0.94	-1.02					1.14	-1.22		
470			0.97	-1.00					1.21	-1.24		

6.6 Variation of Permeability

The curves of ac resistance and ac reactance with the current and the variation of permeability are shown in Figures 6.17 and 6.18 for three types of single layer conductors, respectively. Figures 6.19 and 6.20 show the variation of convection heat loss and radiation heat loss.

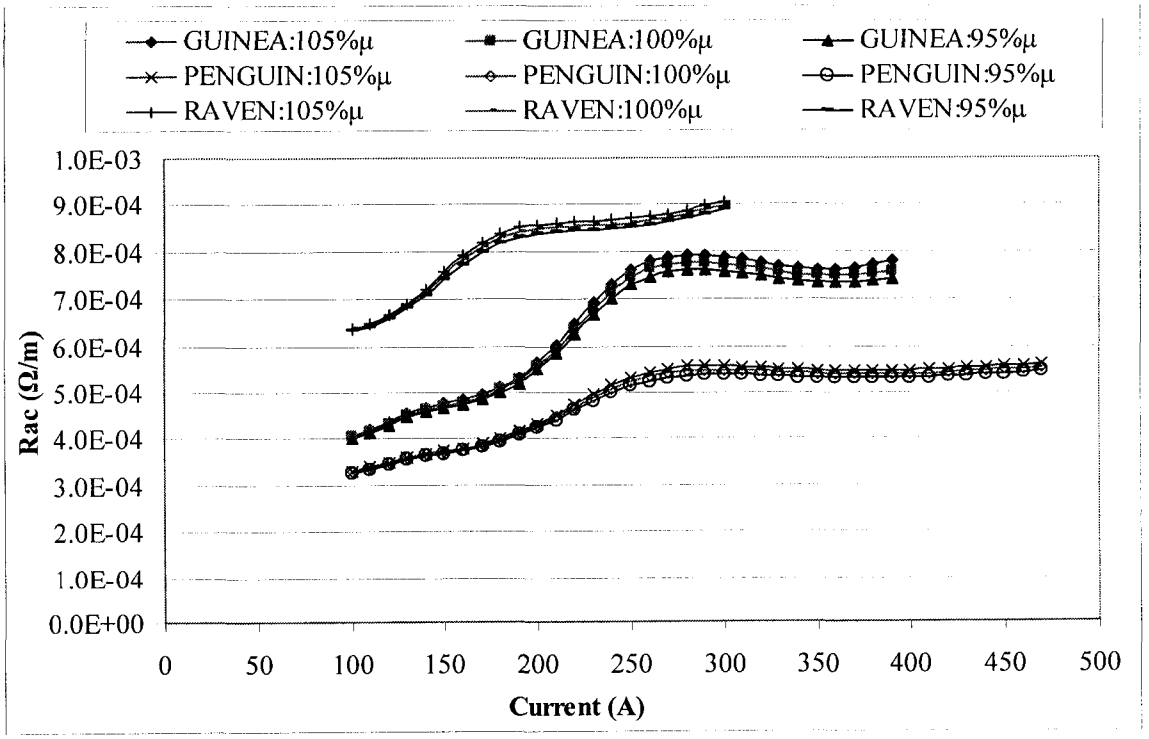

Figure 6.17 Variation of the ac resistance with the current and permeability

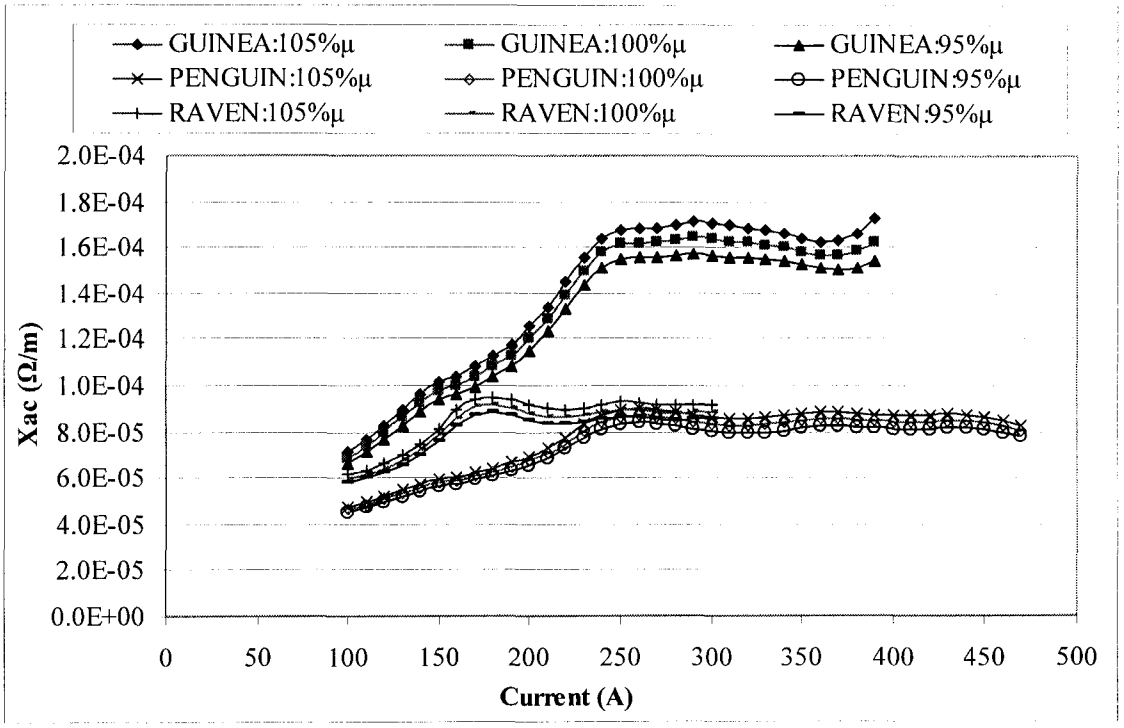

Figure 6.18 Variation of the ac reactance with the current and permeability

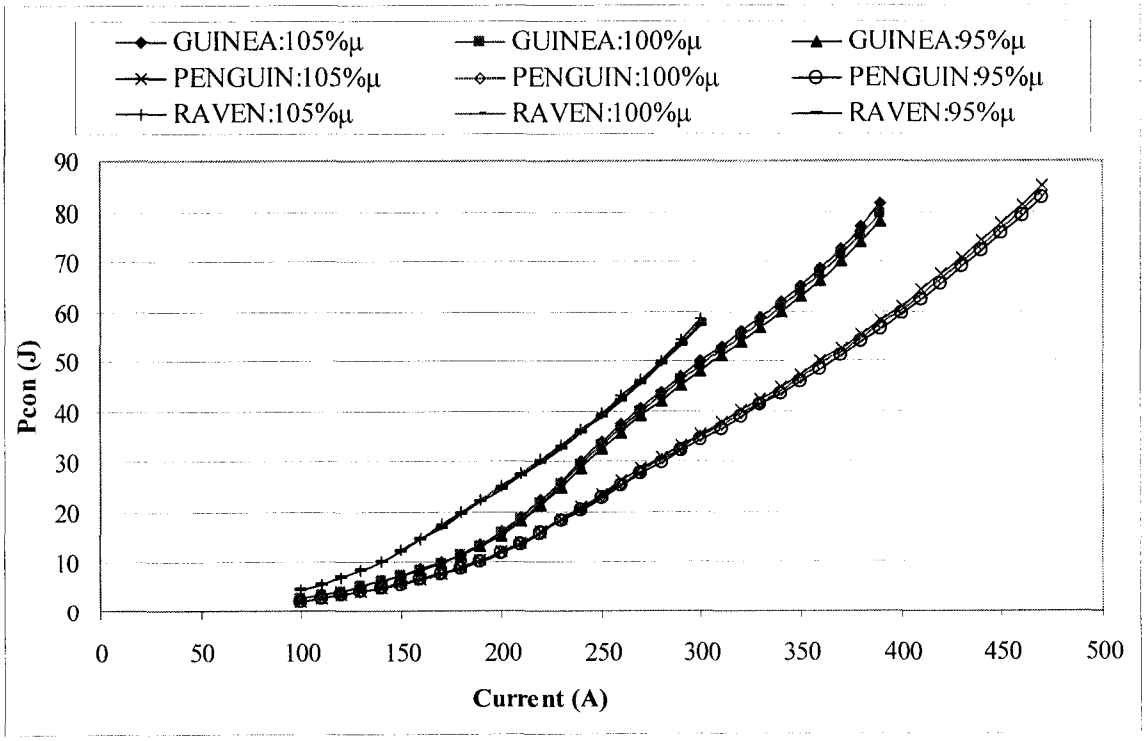

Figure 6.19 Variation of the convection heat with the current and permeability

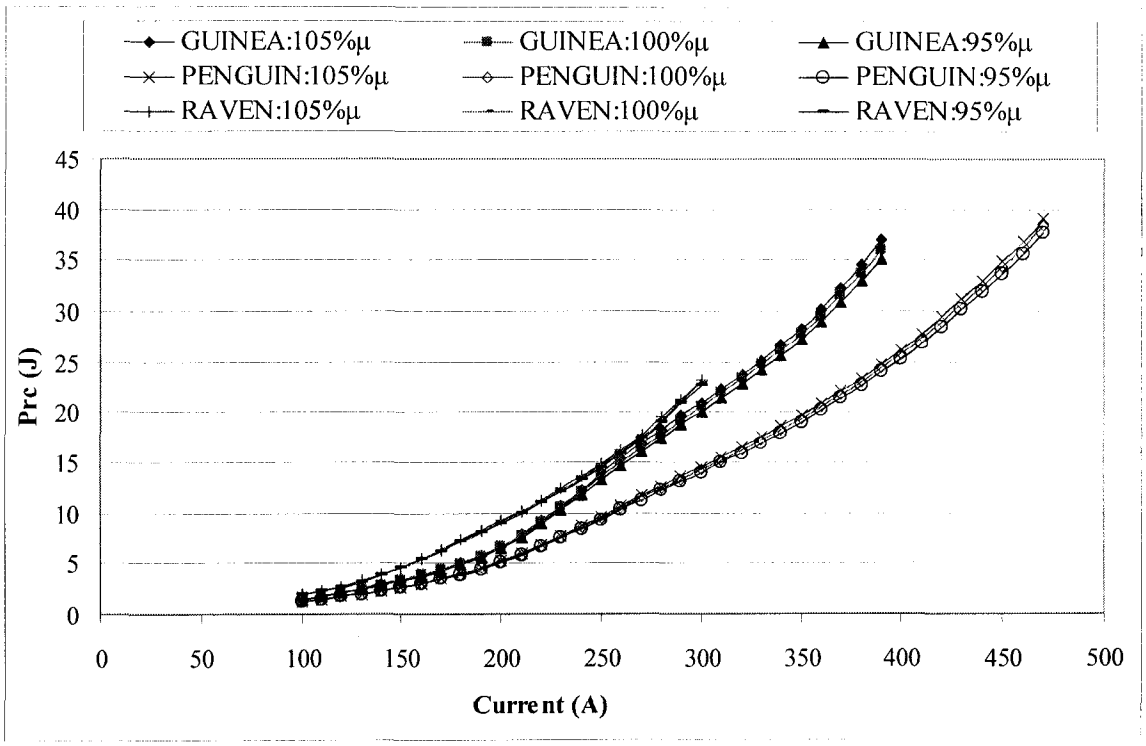

Figure 6.20 Variation of the radiation heat with the current and permeability

Table 6.9 Variation of resistance and reactance with the change of permeability

I(A)	ΔRac (%)						ΔXac (%)					
	Guinea		Penguin		Raven		Guinea		Penguin		Raven	
	105	95	105	95	105	95	105	95	105	95	105	95
100	0.58	-0.59	0.61	-0.62	0.53	-0.54	3.78	-3.78	2.16	-2.38	2.85	-2.85
150	1.00	-1.01	0.90	-0.92	0.94	-0.95	4.51	-4.10	2.75	-2.75	3.42	-3.55
200	1.33	-1.35	1.19	-1.21	1.16	-1.17	4.13	-4.15	3.12	-3.12	3.51	-3.51
250	2.18	-2.20	1.75	-1.76	0.99	-1.00	3.94	-4.00	3.58	-3.58	3.67	-3.67
300	1.94	-1.97	1.71	-1.73	0.94	-0.94	4.47	-4.49	3.48	-3.48	3.49	-3.49
350	1.83	-1.84	1.56	-1.58			3.65	-3.67	3.77	-3.77		
390	2.68	-2.06	1.48	-1.49			6.70	-4.82	3.43	-3.31		
440			1.48	-1.49					3.31	-3.42		
470			1.53	-1.53					2.74	-2.86		

Table 6.10 Variation of convection and radiation heat losses with the change of permeability

I(A)	ΔPcon (%)						ΔPrc (%)					
	Guinea		Penguin		Raven		Guinea		Penguin		Raven	
	105	95	105	95	105	95	105	95	105	95	105	95
100	0.60	-0.61	0.64	-0.65	0.55	-0.56	0.51	-0.52	0.54	-0.55	0.48	-0.49
150	1.03	-1.05	0.94	-0.96	0.95	-0.96	0.91	-0.92	0.82	-0.83	0.89	-0.90
200	1.35	-1.37	1.22	-1.24	1.15	-1.16	1.26	-1.28	1.11	-1.13	1.18	-1.19
250	2.16	-2.19	1.75	-1.77	0.96	-0.97	2.21	-2.23	1.72	-1.73	1.06	-1.08
300	1.88	-1.92	1.69	-1.71	0.95	-0.96	2.07	-2.09	1.75	-1.77	1.15	-1.15
350	1.74	-1.76	1.51	-1.54			2.03	-2.03	1.65	-1.67		
390	2.44	-1.93	1.42	-1.43			2.99	-2.35	1.62	-1.62		
440			1.39	-1.40					1.69	-1.68		
470			1.42	-1.42					1.77	-1.76		

Figures 6.17, 6.18, and Table 6.9 show that reactance is more sensitive to the variation of permeability than resistance. Reactance varies larger than 3 % with the 5 % variation of permeability while resistance varies less than 2 % which shows that the contribution of imaginary part of complex permeability varies less than 2 %.

The Integrated Model is not very sensitive to the variation of permeability from the respective of resistance, resistive heat, and heat losses. Most of the variation is less than 2 %.

Among the three conductors, Guinea is the most sensitive one to the variation of permeability.

6.7 Variation of the Supply Frequency

The curves of resistance and reactance with the current and the variation of supply frequency are shown in Figures 6.21 and 6.22, respectively. Reactance is more sensitive to a change of frequency than resistance because reactance is proportional to frequency.

Figures 6.23 and 6.24 show the variation of convection heat loss and radiation heat loss with the supply frequency for three types of conductors.

Comparing with the sensitivity of reactance, the Integrated Model is not very sensitive to the variation of the supply frequency for the output parameters of resistance, resistive heat, convection heat loss, and radiation heat loss. The variation is less than 2 % as shown in Tables 6.11 and 6.12. Also from Table 6.11, ac reactance is sensitive to the variation of frequency and the variation is larger than 4 %.

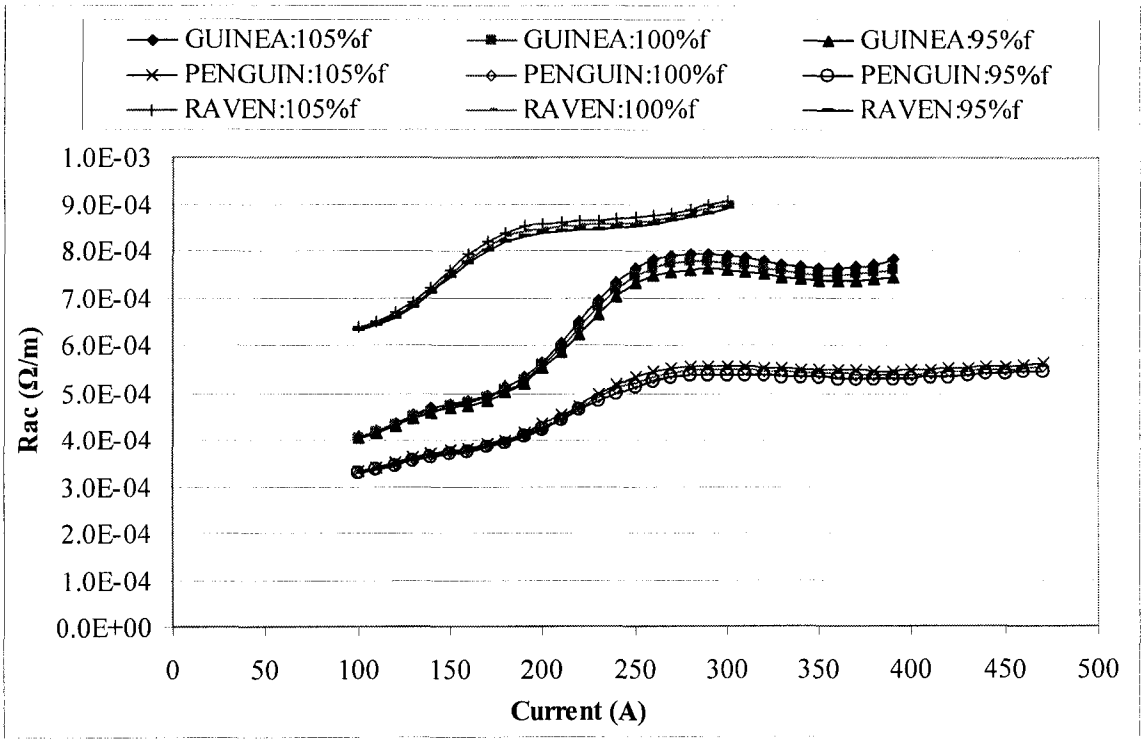

Figure 6.21 Variation of the ac resistance with the current and supply frequency

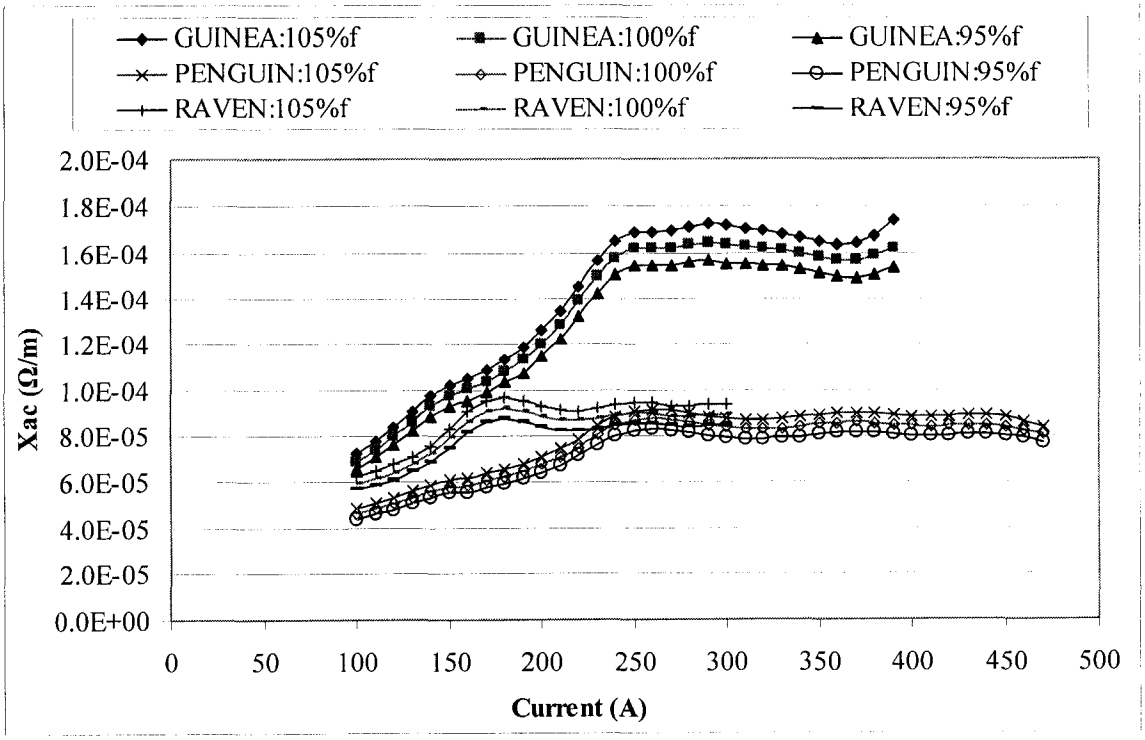

Figure 6.22 Variation of the ac reactance with the current and supply frequency

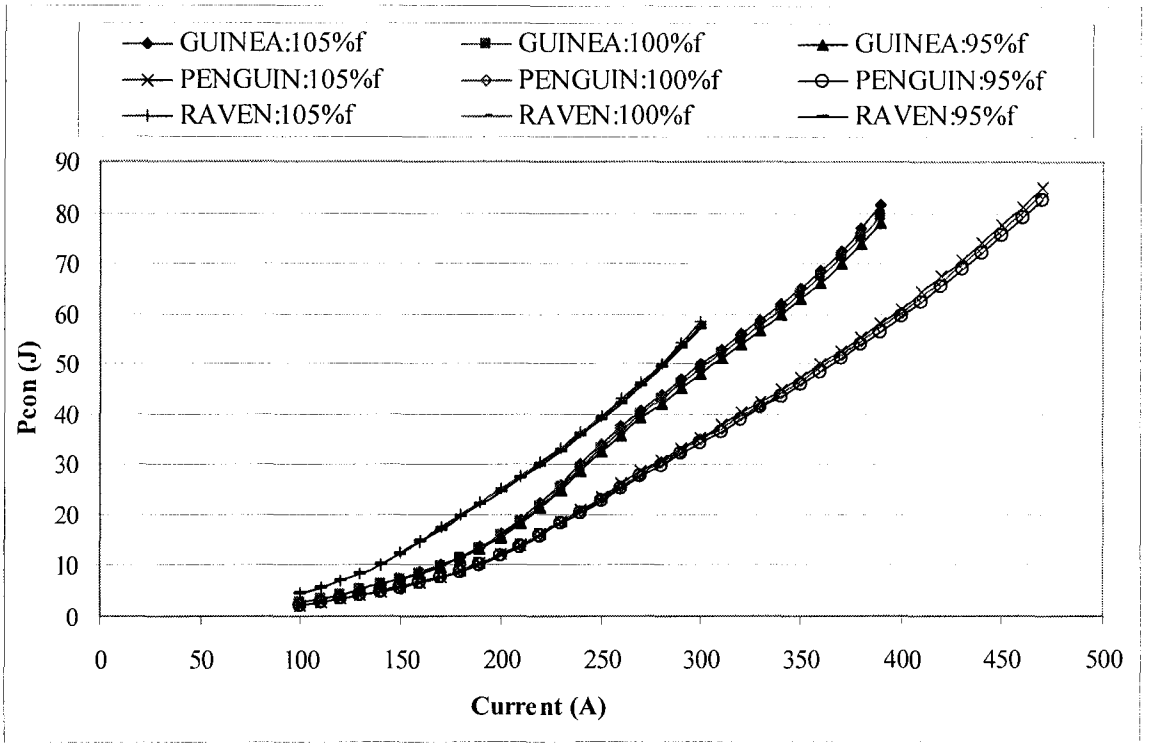

Figure 6.23 Variation of the convection heat with the current and supply frequency

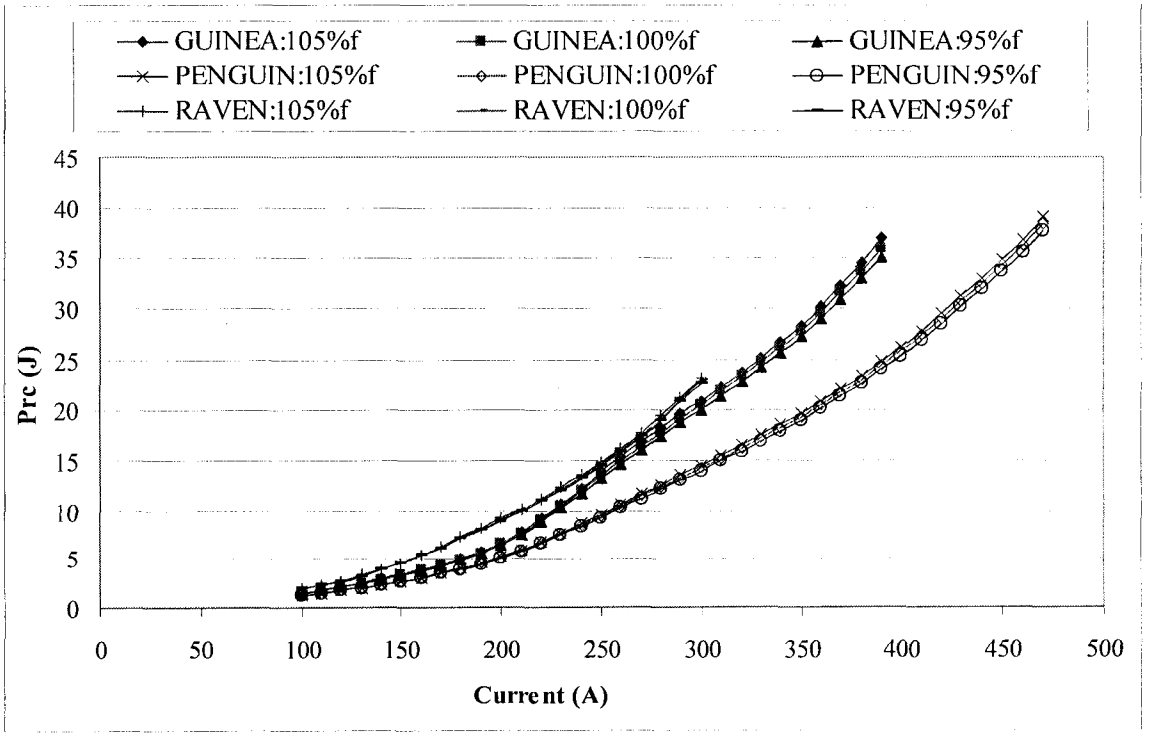

Figure 6.24 Variation of the radiation heat with the current and supply frequency

Table 6.11 Variation of resistance and reactance with the change of supply frequency

I(A)	ΔRac (%)						ΔXac (%)					
	Guinea		Penguin		Raven		Guinea		Penguin		Raven	
	105	95	105	95	105	95	105	95	105	95	105	95
100	0.58	-0.59	0.61	-0.62	0.53	-0.54	4.80	-4.80	4.97	-5.18	5.03	-4.87
150	1.00	-1.01	0.90	-0.92	0.94	-0.95	4.51	-4.82	4.99	-4.99	5.07	-5.07
200	1.33	-1.34	1.19	-1.21	1.16	-1.17	4.75	-4.78	4.90	-5.04	4.98	-4.98
250	2.17	-2.20	1.75	-1.76	0.98	-1.00	4.42	-4.47	5.09	-4.97	5.12	-5.12
300	1.93	-1.97	1.71	-1.73	0.94	-0.94	4.94	-4.95	5.04	-5.04	4.95	-4.95
350	1.83	-1.84	1.55	-1.58			4.13	-4.15	5.31	-5.19		
390	2.68	-2.06	1.48	-1.49			7.16	-5.28	4.96	-4.85		
440			1.48	-1.49					4.84	-4.96		
470			1.53	-1.53					4.35	-4.35		

Table 6.12 Variation of convection and radiation heat losses with the change of supply frequency

I(A)	ΔPcon (%)						ΔPrc (%)					
	Guinea		Penguin		Raven		Guinea		Penguin		Raven	
	105	95	105	95	105	95	105	95	105	95	105	95
100	0.60	-0.61	0.64	-0.65	0.55	-0.56	0.51	-0.52	0.54	-0.55	0.48	-0.49
150	1.03	-1.05	0.94	-0.96	0.95	-0.96	0.91	-0.92	0.82	-0.83	0.89	-0.90
200	1.35	-1.37	1.22	-1.24	1.15	-1.16	1.26	-1.28	1.11	-1.13	1.18	-1.19
250	2.16	-2.19	1.75	-1.77	0.96	-0.97	2.21	-2.22	1.72	-1.73	1.06	-1.08
300	1.88	-1.92	1.69	-1.71	0.95	-0.96	2.07	-2.09	1.75	-1.77	1.15	-1.15
350	1.74	-1.75	1.51	-1.54			2.03	-2.03	1.65	-1.67		
390	2.44	-1.93	1.42	-1.43			2.99	-2.35	1.62	-1.62		
440			1.39	-1.40					1.68	-1.68		
470			1.42	-1.42					1.77	-1.76		

6.8 Variation of the Surface Layer Temperature

The curves in Figures 6.25 and 6.26 show ac resistance and ac reactance with the current and the variation of surface layer temperature. The variations of the convection heat loss and the radiation heat loss are given in Figures 6.27 and 6.28, respectively.

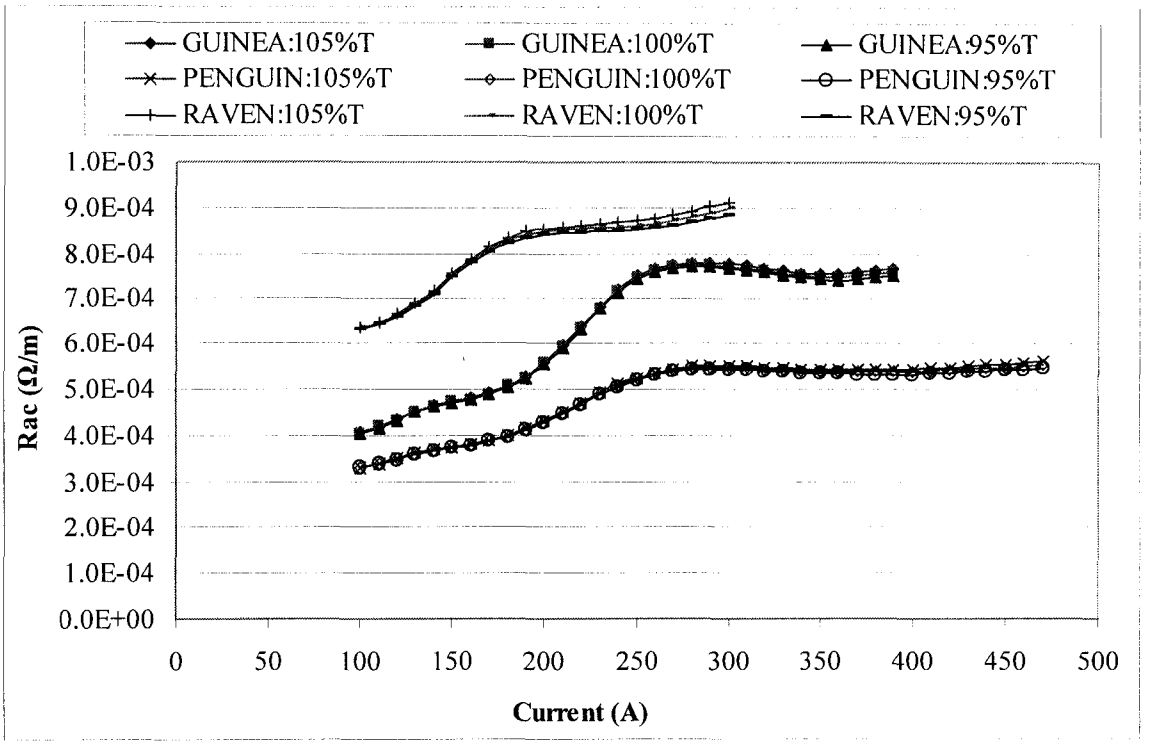

Figure 6.25 Variation of the ac resistance with the current and surface temperature

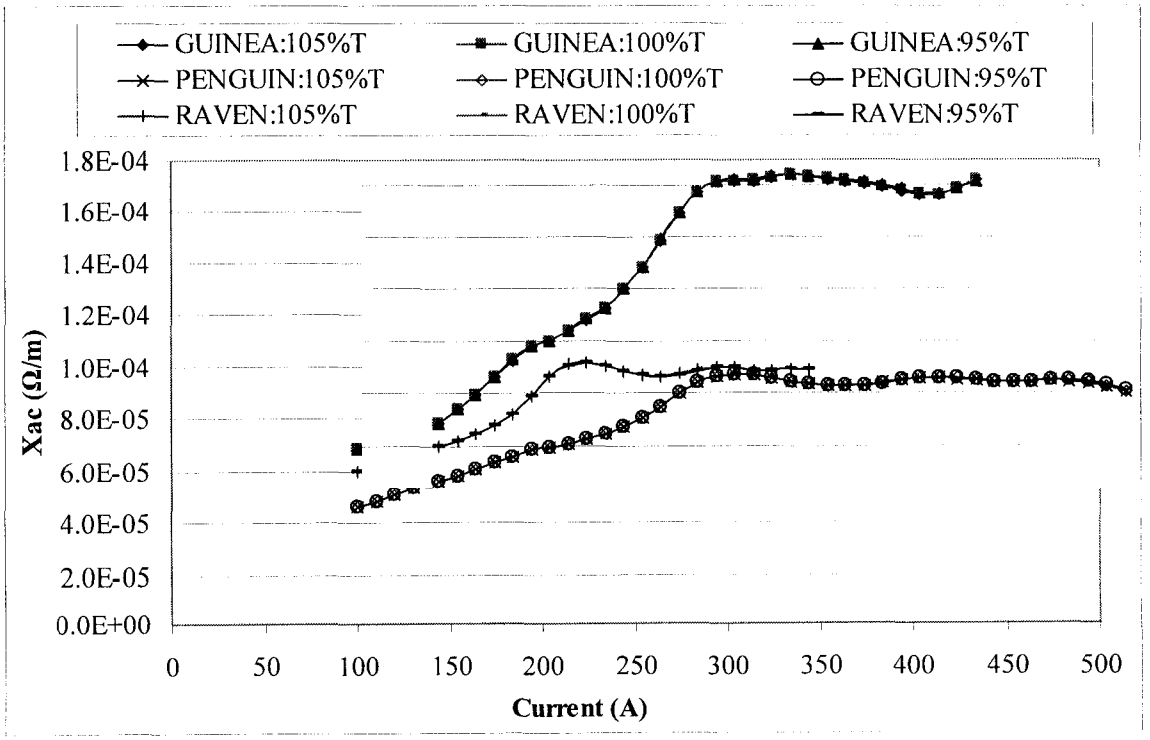

Figure 6.26 Variation of the ac reactance with the current and surface temperature

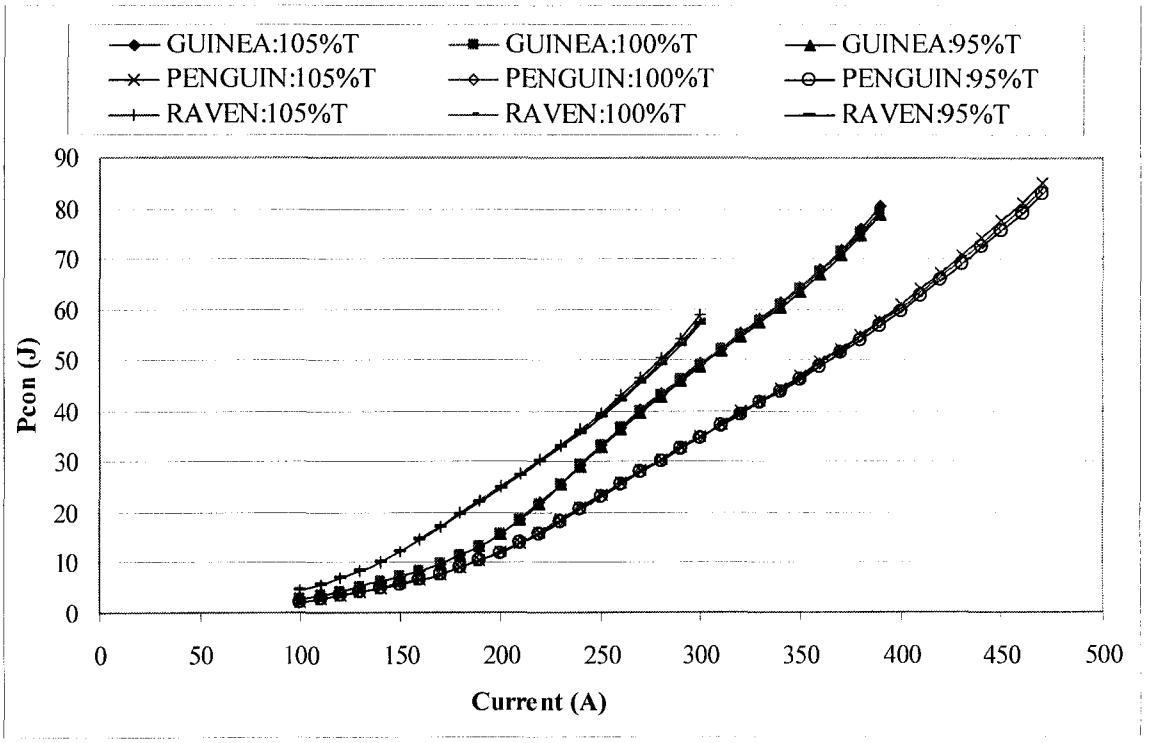

Figure 6.27 Variation of the convection heat with the current and surface temperature

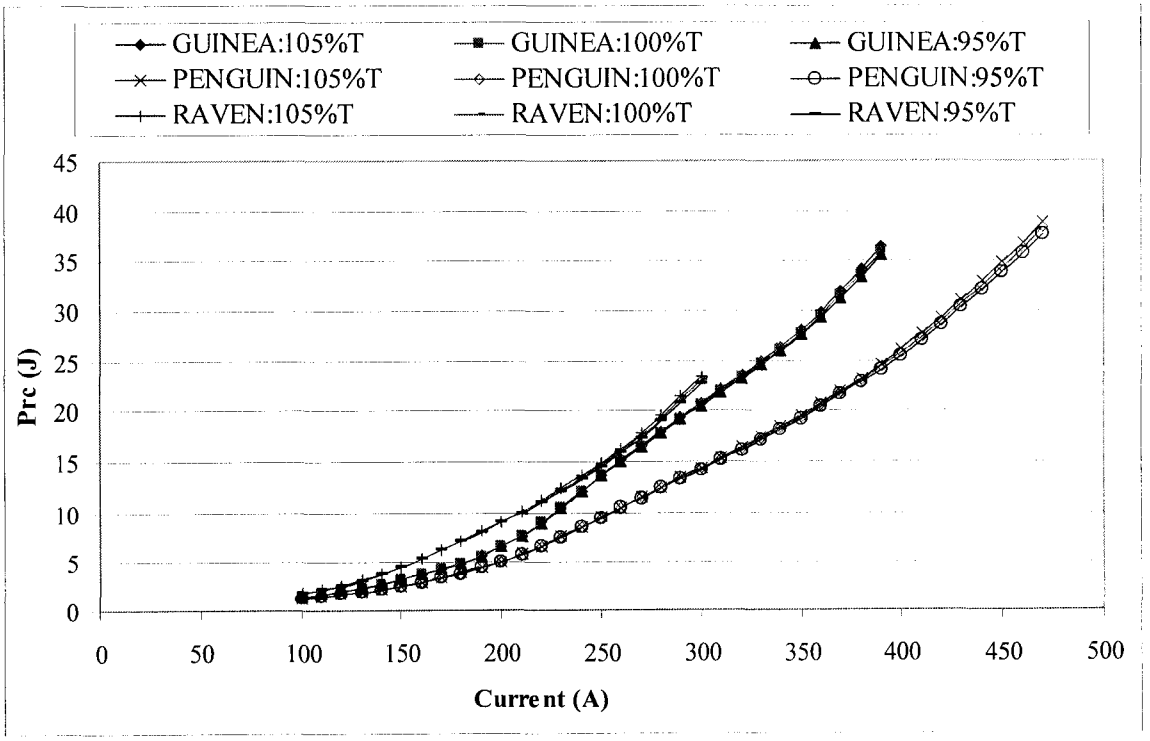

Figure 6.28 Variation of the radiation heat with the current and surface temperature

From Figures 6.25, 6.26, 6.27, and 6.28, we can find that the selected output parameters of the Integrated Model are not sensitive to the variation of surface layer temperature.

Table 6.13 Variation of resistance and reactance with the surface layer temperature

I(A)	ΔRac (%)						ΔXac (%)					
	Guinea		Penguin		Raven		Guinea		Penguin		Raven	
	105	95	105	95	105	95	105	95	105	95	105	95
100	0.24	-0.24	0.24	-0.23	0.36	-0.35	0.00	0.00	-0.22	0.00	0.00	0.17
150	0.31	-0.31	0.30	-0.30	0.53	-0.53	-0.10	0.00	0.00	0.00	0.00	-0.13
200	0.36	-0.36	0.38	-0.38	0.78	-0.77	-0.07	0.07	0.00	0.00	0.00	0.11
250	0.49	-0.49	0.51	-0.51	1.09	-1.07	-0.13	0.12	0.00	0.00	0.11	-0.11
300	0.58	-0.58	0.64	-0.63	1.54	-1.50	-0.02	0.02	0.00	0.00	-0.11	0.11
350	0.78	-0.78	0.80	-0.79			-0.36	0.37	0.24	-0.12		
390	1.10	-1.08	0.97	-0.95			0.19	-0.17	0.00	0.12		
440			1.24	-1.22					-0.12	0.00		
470			1.45	-1.43					-0.62	0.62		

Table 6.14 Variation of convective and radiative heat with the surface layer temperature

I(A)	ΔPcon (%)						ΔPrc (%)					
	Guinea		Penguin		Raven		Guinea		Penguin		Raven	
	105	95	105	95	105	95	105	95	105	95	105	95
100	0.25	-0.25	0.25	-0.24	0.37	-0.37	0.21	-0.21	0.21	-0.21	0.32	-0.32
150	0.32	-0.32	0.31	-0.31	0.54	-0.53	0.28	-0.28	0.27	-0.27	0.51	-0.50
200	0.37	-0.37	0.39	-0.38	0.78	-0.77	0.35	-0.34	0.35	-0.35	0.79	-0.78
250	0.49	-0.49	0.51	-0.51	1.05	-1.04	0.50	-0.49	0.50	-0.50	1.16	-1.16
300	0.56	-0.56	0.63	-0.63	1.51	-1.41	0.62	-0.61	0.65	-0.64	1.84	-1.70
350	0.75	-0.74	0.78	-0.78			0.87	-0.86	0.85	-0.85		
390	1.03	-1.01	0.93	-0.92			1.25	-1.24	1.06	-1.04		
440			1.17	-1.15					1.41	-1.38		
470			1.35	-1.32					1.68	-1.64		

Tables 6.13 and 6.14 show a quantitative comparison of properties with the surface layer temperature from which, we can determine that the Integrated Model is not very sensitive to the variation of surface layer temperature. When the temperature of the aluminum layer increases or decreases 5 %, most of the variation about the parameters are less than 1 %. Reactance is less sensitive than resistance. Resistance, heat gain, and heat losses have the same sensitivity level for the surface layer temperature.

The results are as expected since the resistance, reactance, and heat losses are functions of temperature. When the temperature varies, the parameters vary correspondingly. Strictly speaking, the surface layer temperature is not an input parameter of the Integrated Model. It is just a middle parameter resulting from the input

conductor current. It is chosen because it plays important role in the analyses of ACSR conductors.

6.9 Summary

To sum up, the sensitivity analysis of the Integrated Model for different parameters can be concluded in Table 6.15:

Table 6.15 Sensitivity level of the Integrated Model

Parameter	Most Sensitive			.....		Least Sensitive
Resistance (Resistive heat)	D	ρ_{al}	LAY	f; μ	ρ_{st}	T
Reactance	LAY	$f>\mu$	D	ρ_{st}	ρ_{al}	T
Convection heat loss	D	ρ_{al}	LAY	f; μ	ρ_{st}	T
Radiation heat loss	D	ρ_{al}	LAY	f; μ	ρ_{st}	T

Where D: wire diameter of the aluminum layer;
LAY: lay length of the aluminum layer;
ρ_{al}: aluminum resistivity;
ρ_{st}: steel resistivity;
μ: permeability;
f: supply frequency;
T: surface layer temperature.

Table 6.15 shows relative sensitivities for the various parameters.

From the perspective of ac resistance, convection heat loss, and radiation heat loss, the most sensitive factor is the aluminum wire diameter; the second most sensitive factor is aluminum resistivity; the third one is lay length or lay factor. The fourth to the sixth sensitive factors are frequency and permeability, steel resistivity, and surface layer temperature. Among them, the sensitivity level of permeability and supply frequency is almost the same.

From a reactance perspective, lay factor is the most sensitive factor and frequency is the second. From the third to the seventh are permeability, aluminum wire diameter, steel resistivity, aluminum resistivity, and surface layer temperature.

Sensitivity analysis shows that aluminum wire diameter, aluminum resistivity, and lay factor are the most important design factors for single layer ACSR conductors. Their variation greatly affects the operational behaviors of conductors. This provides a possible way for the others in optimization design to re-construct conductors to achieve some optimum.

CHAPTER 7
ARTIFICIAL NEURAL NETWORK MODEL AND LOAD FORECASTING

7.1 Introduction

This chapter introduces the development of an artificial neural network model trained by Levenberg-Marquardt optimization algorithm [45]. System identification and statistical techniques have been discussed and exploited in this chapter to build and validate this model. Hourly load demands in Ontario have been successfully forecasted through an implementation of this artificial neural network model. Many modeling techniques are involved in this chapter, such as pre-processing and post-processing of the dataset; division of training, testing, and forecasting sub-datasets; improvement of the convergence rate and weight updating; neural network topology selection; adaptive parameters optimization.

Efficient system management requires accurate and reliable prediction of load demands. Inaccurate prediction can have serious disruptive effects on operations. For the current state of energy management, power companies continuously monitor the variation of the load. Load records are usually kept on an hourly basis. The load from one hour to the next is assumed to vary linearly, with the maximum load occurring in the early evening or late afternoon, and the minimum load at night.

Generally speaking, there are two different ways to build a model: in terms of physical laws or by experimental or empirical results. The Integrated Model was built from the knowledge of its physical subsystems and their interactions. Information such as voltage, current, force, tension, stress, etc. and the knowledge of physical laws are used to formulate this Integrated Model for single layer ACSR. In some other cases, it is very difficult to make a model from physical knowledge when the system is dynamic, and a complete knowledge of all of the interacting subsystems is not available. An artificial neural network is an adaptive system that learns to perform a mathematical function as an input/output map from data. After the training and testing phases, the neural network model can be used for the purpose of forecasting.

7.2 Artificial Neural Network Modeling

This section includes the modeling procedure, the modeling structure, and the modeling algorithm. The validation of model is a main point in the modeling procedure and the residual analysis is involved. A three layer feed-forward neural network is selected in this research and trained by the Levenberg-Marquardt optimization algorithm.

7.2.1 Modeling Procedure

The purpose of the neural network is to build a relationship between the input and the measured observations as output. The input/output training data are fundamental in

neural network technology, because they convey the necessary information to "discover" the optimal operating point. Ontario hourly demands prediction works as an implementation of this neural network model, so the input/output should be the hourly load variation. Hourly load is a time series, i.e., a collection of observations generated sequentially through time per hour. The special features of a time series are that the data are ordered with respect to time, and the successive observations are usually expected to be dependent. This dependency from one time period to another makes reliable prediction possible.

The hourly load demands can be forecasted with the built neural network model, which should pass the validation and testing phase. The following model validation methods are used in this research:

- Visual comparison of the plots of the observations, i.e., the actual output, and predictions, i.e., the model output.
- Evaluation of the whiteness of residuals. Whiteness comes from the white noise which is a zero-mean random vector, with uncorrelated elements.

The residuals represent misfit or mismatch between the observed data and the prediction of the model, and the presence of any information remaining in the residuals is a clue that the model might be insufficiently complex or otherwise inappropriate. If the model is correct and the method prerequisites are satisfied, then the residuals should be uncorrelated.

A simple check is to plot the residual versus the fitted values. Another valuable diagram is the histogram of the residual amplitudes, which reveals distributions that differ from normal distributions, and is a valuable complement to analysis of variance.

Both visual comparison and statistical techniques such as residual analyses are necessary to validate the neural network model as we performed in this research. Only with visual comparison, it is not easy to determine how good or how bad the model is. Only with statistical test, there is possibility to accept an incorrect model because it is impossible to qualify the risk of accepting it.

Residual analysis comprises:

- Residuals constitute a white-noise process with mean zero
- Residuals are normally distributed
- Residuals are symmetrically distributed (zero crossings of the residual sequence)
- Residuals are independent (autocorrelation functions)

- **Calculation of Autocorrelations and Standard Errors**

The mathematical expectation of a random variable $\tilde{x}$, and denoted as $E(\tilde{x})$, is the mean of the probability distribution of $\tilde{x}$. If a random variable $\tilde{x}$ can take on the discrete values $x = x_1, x_2, \cdots x_n$, and if each value has an associated probability $f(x_i) = \text{Prob}(\tilde{x} = x_i)$, then the mathematical expectation is defined as

$$E(\tilde{x}) = x_1 f(x_1) + x_2 f(x_2) + \cdots + x_n f(x_n) \tag{7.1}$$

The mean is defined as

$$\mu = \frac{1}{n}\sum_{i=1}^{n} x_i \tag{7.2}$$

The variance of a random variable $\tilde{x}$ is defined as

$$\sigma_x^2 = E\left\{[\tilde{x} - E(\tilde{x})]^2\right\} = \frac{1}{n}\sum_{i=1}^{n}(x_i - \mu)^2 \tag{7.3}$$

The autocovariance γ_k is defined as

$$\gamma_k = Cov(\tilde{x}_i, \tilde{x}_{i+k}) = E[(\tilde{x}_i - \mu)(\tilde{x}_{i+k} - \mu)] \qquad k = 0,1,2,\ldots,K \tag{7.4}$$

for some number K.

The autocorrelation at lag k is

$$\rho_k = \frac{E[(\tilde{x}_i - \mu)(\tilde{x}_{i+k} - \mu)]}{\sigma_x^2} = \frac{\gamma_k}{\gamma_o} \tag{7.5}$$

For a stationary process $\sigma_x^2 = \gamma_0$, then $\rho_0 = 1$.

The estimate of the kth lag autocorrelation ρ_k is

$$r_k = \frac{c_k}{c_0} \tag{7.6}$$

where

$$c_k = \frac{1}{n}\sum_{i=1}^{n-k}(x_i - \mu)(x_{i+k} - \mu) \tag{7.7}$$

is the estimate of the autocovariance γ_k and $c_0 = \gamma_0 = \sigma_x^2$, the variance of variable $\tilde{x}$.

To provide a guide to whether theoretical autocorrelations are essentially zero beyond a particular lag, we can compute Standard Errors (S.E.) for larger lags from the simplified Bartlett's formula [46]:

$$S.E.[r_k] = \frac{1}{\sqrt{n}}\sqrt{1 + 2\sum_{i=1}^{q} r_i^2} \qquad k > q \tag{7.8}$$

- **Residual Analysis**

The residual is defined as the difference between the prediction from the model and the actual observation. The autocorrelations of the residuals yield valuable information about possible model inadequacies. If the residuals are truly white noise, then their autocorrelation function should have no spikes, and the sample autocorrelations should all be small. Based on Bartlett's formula [46], the estimate of the approximate large sample standard error for individual autocorrelations under the assumption that the errors follow a white noise process is $1/\sqrt{n}$. Thus, residual correlations, which lie outside the range $\pm 1.96/\sqrt{n}$ (that is, outside the approximate 95 % confidence limits), are significantly different from zero [46].

- **Residual Analysis of White Noise Series**

White noise series are assumed to be normally and independently distributed with mean zero, constant variance, and uncorrelated over time. Figure 7.1 shows the white noise series produced by Matlab code written by the author with n = 300 observations. Calculations of autocorrelation functions and the standard errors are done using the equations mentioned previously in this section. From the autocorrelation coefficients which are within the standard error range in Figure 7.1 we can see that the white noise is uncorrelated and within 95 % confidence limit range.

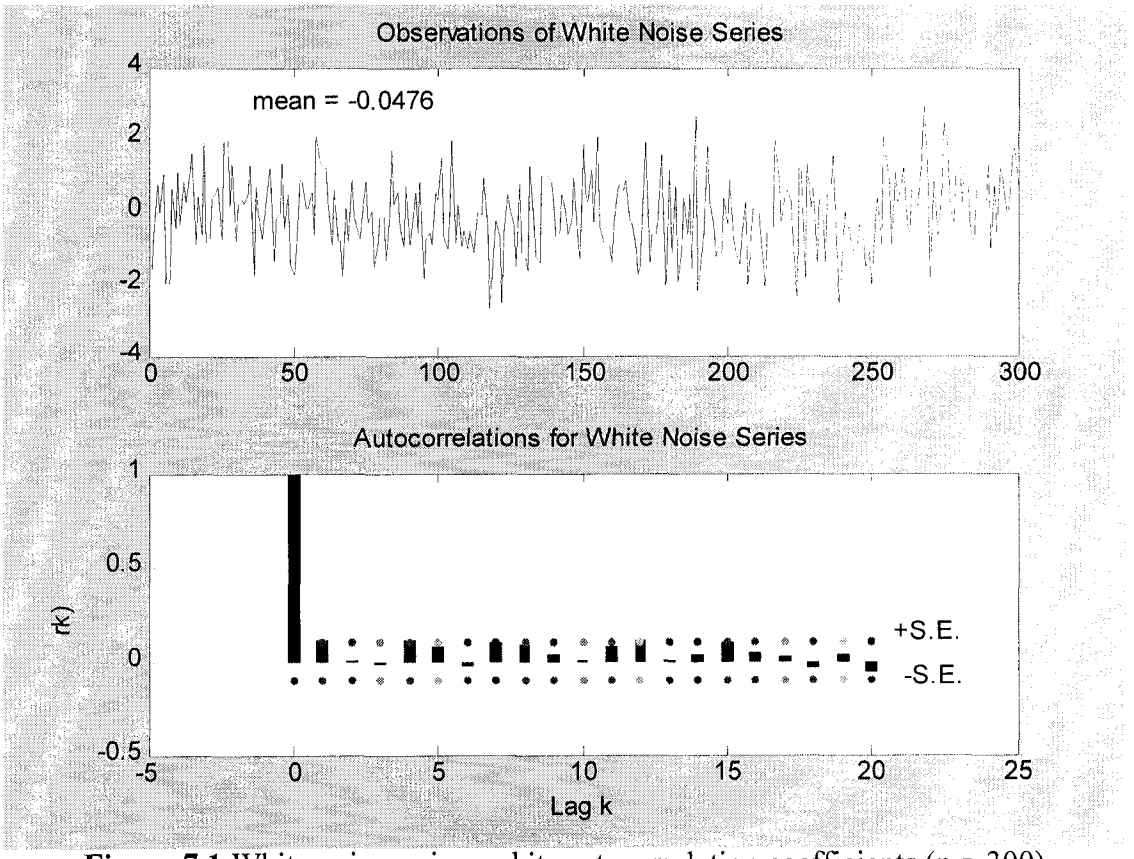

Figure 7.1 White noise series and its autocorrelation coefficients (n = 300)

The model can be used to forecast further realizations after whiteness analyses of the residuals. In summary, we can use the system identification analysis to forecast the behavior of the series in the future based upon the knowledge of the past.

7.2.2 Structure of the Artificial Neural Network

Artificial neural networks are an attempt to import human brain functionality into a computational tool. To reach this goal many disciplines are involved: psychology, neurobiology, physics, statistics, parallel processing, optics, computer science, adaptive

systems, most of the engineering disciplines, and even business and management systems.

From an engineering design point of view, the designer chooses the network topology, the performance function, the learning rule, and the criteria to stop the training phase, but the system automatically adjusts the parameters. It is difficult to bring a priori information into the design, and when the system does not work properly it is also hard to incrementally refine the solution. But neural-network-based solutions are extremely efficient in terms of development time and resources, and in many difficult problems neural networks provide performance that is difficult to match with other technologies. Denker [47] said that "Artificial neural networks are the second best way to implement a solution motivated by the simplicity of their design and because of their universality, only shadowed by the traditional design obtained by studying the physics of the problem."

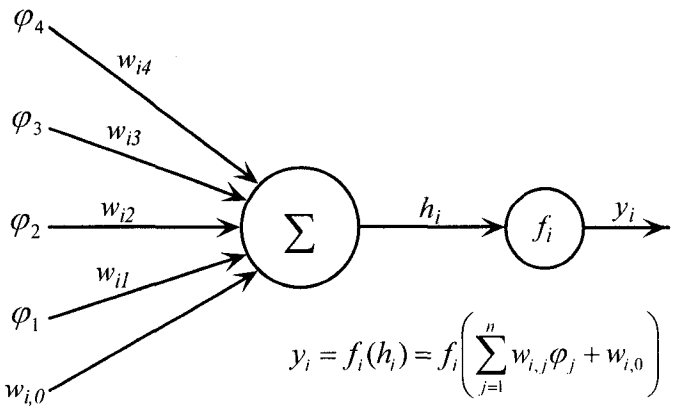

Figure 7.2 A neuron [45]

A human brain is built of very simple basic computational units called "neurons". A neuron is a biological cell that receives information from a number of sources and produces a response that is independent of the information received. The capabilities of a human brain arise from the collective behavior of a very large number of these simple units: the neurons. Such a densely connected system is fault tolerant since any lost connection can be covered by many other existing connections. In neural network processing, the neuron or node or unit is a processing element that takes a number of inputs, weights them, sums them up, and uses the result as the argument for a singular values function, the activation function. A neuron model is shown in Figure 7.2.

The activation function f_i can take any form but most often it is monotonic. It is desirable to have the activation function range from -1 to +1, in which case the activation function assumes an anti-symmetric form with respect to the origin; that is, the activation function is an odd function of the induced local field [48]. The hyperbolic tangent function can be chosen as the corresponding form function and used in this research. Allowing an activation function to assume negative values as prescribed by the hyperbolic tangent function has analytic benefits. In reality, the hyperbolic tangent function is just the logistic function rescaled and biased.

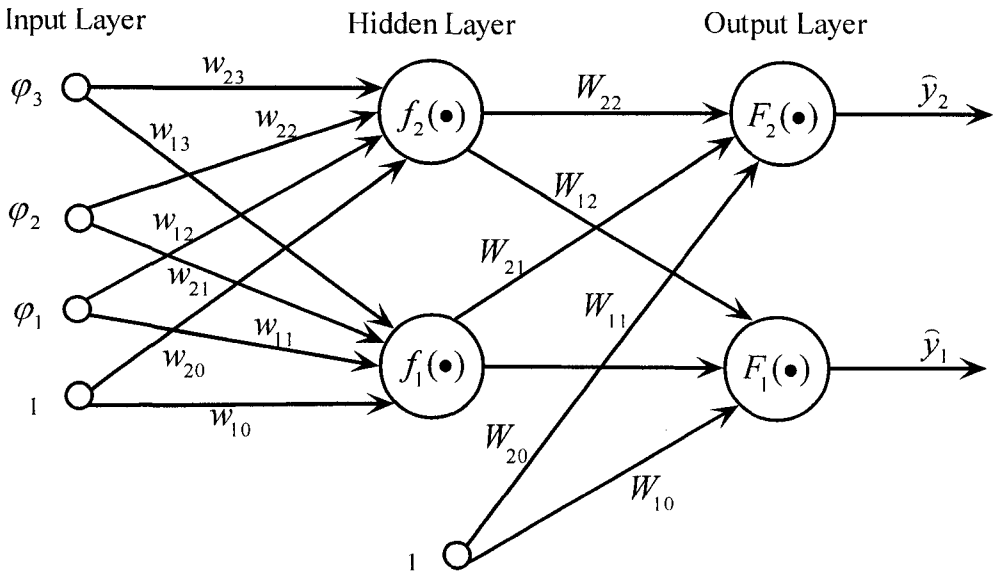

Figure 7.3 A fully connected three layer feed-forward neural network [45]

How the inter-neuron connections are arranged and the nature of the connections determines the structure of a neural network. Figure 7.3 shows a multiple layer feed-forward network with three layers: the input layer, the output layer, and the hidden layer. Its corresponding mathematical formula takes the form:

$$\hat{y}_i = g_i[\varphi,\theta] = F_i[\sum_{j=1}^{n_h} W_{i,j} f_j(\sum_{l=1}^{n_\varphi} w_{j,l}\varphi_l + w_{j,0}) + W_{i,0}] \tag{7.9}$$

Where θ specifies the parameter vector, which contains all the adjustable parameters of the network, i.e., the weights and biases $\{W_{i,j}, w_{j,l}\}$. Since the bias can be interpreted as weight acting on an input clamped to 1, the joint description weight will most often be applied covering both weights and biases.

To determine the weight values, a set of data should be exploited to build a relationship between the outputs and the inputs. The task of determining the weights from these examples is called training or learning, and it is basically a conventional estimation problem. The weights are estimated from the examples in such a way that the neural network models the true relationship as accurately as possible.

7.2.3 Levenberg-Marquardt Algorithm

To minimize the prediction error:

$$V_N(\theta, Z^N) = \frac{1}{2N}\sum_{t=1}^{N}[d(t) - y(t \mid \theta)]^2 = \frac{1}{2N}\sum_{t=1}^{N}\varepsilon^2(t,\theta) \tag{7.10}$$

where θ contains all adjustable weights of the neural network; Z^N is a set of data with observations $d(t)$ and predictions $y(t)$.

So the objective of a neural network model is to determine its weights to meet the criterion:

$$\hat{\theta} = \arg\min V_N(\theta, Z^N) \tag{7.11}$$

The Levenberg-Marquardt (L-M) method is adopted to train the neural network and search for an optimal point due to its fast and robust convergence. With an initial guess and in an iterative manner, L-M method generally takes the form: [45]

$$\theta^{(i+1)} = \theta^{(i)} + f^{(i)} \tag{7.12}$$

$$[R(\theta^{(i)}) + \lambda^{(i)} I] f^{(i)} = -G(\theta^{(i)}) \tag{7.13}$$

where $\theta^{(i)}$ specifies the i^{th} iterate; $f^{(i)}$ is the search direction; $\lambda^{(i)}$ is the adjustable parameter; $G(\theta^{(i)})$ is the gradient; $R(\theta^{(i)})$ is the Hessian matrix.

With the notation $\psi(t,\theta) = -\dfrac{dy(t,\theta)}{d\theta}$, we have

$$G(\theta^{(i)}) = \frac{1}{N}\sum_{t=1}^{N} \psi(t,\theta^{(i)})[d(t) - y(t \mid \theta^{(i)}] \tag{7.14}$$

$$R(\theta^{(i)}) = \frac{1}{N}\sum_{t=1}^{N} \psi(t,\theta^{(i)})\psi^{T}(t,\theta^{(i)}) \tag{7.15}$$

The following ratio is used to measure the accuracy of the approximation and search direction:

$$r^{(i)} = \frac{V_N(\theta^{(i)}, Z^N) - V_N(\theta^{(i)} + f^{(i)}, Z^N)}{V_N(\theta^{(i)}, Z^N) - L^{(i)}(\theta^{(i)} + f^{(i)})} \tag{7.16}$$

where

$$L^{(i)}(\theta^{(i)} + f^{(i)}) = V_N(\theta^{(i)}, Z^N) + f^{(i)T} G(\theta^{(i)}) + \frac{1}{2} f^{(i)T} R(\theta^{(i)}) f^{(i)} \tag{7.17}$$

The procedure of L-M method is outlined as follows: [45]

Step 1: Set initial guess $\theta^{(0)}$ and an initial value $\lambda^{(0)}$

Step 2: Determine the search direction from $[R(\theta^{(i)}) + \lambda^{(i)} I] f^{(i)} = -G(\theta^{(i)})$

Step 3: $r^{(i)} > 0.75 \Rightarrow \lambda^{(i)} = \lambda^{(i)}/2$

Step 4: $r^{(i)} < 0.25 \Rightarrow \lambda^{(i)} = 2\lambda^{(i)}$

Step5: If $V_N(\theta^{(i)} + f^{(i)}, Z^N) < V_N(\theta^{(i)}, Z^N)$, then accept $\theta^{(i+1)} = \theta^{(i)} + f^{(i)}$ as a new iterate, and let $\lambda^{(i+1)} = \lambda^{(i)}$

Step6: If the stopping criterion is not satisfied, go to *Step 2.*

The iteration continues until $\theta^{(i)}$ is believed to sufficiently close to the minimum. By adjusting λ, the search direction of L-M method interpolates between the gradient direction ($\lambda \to \infty$) and the Gauss-Newton direction ($\lambda = 0$). [45]

7.3 Ontario Hourly Demands Forecasting

Ontario hourly demands forecasting is illustrated in this section as an implementation of the neural network modeling. The objective is to forecast hourly load variation in Ontario so the input/output set for neural network should be the hourly demands.

7.3.1 Preliminary Work for the Raw Time Series Dataset

The first step in any time series analysis should be to plot the available observations against time to check the stationarity [46]. This is valuable because qualitative features such as trend, seasonality, discontinuities, and outlines will usually be visible if present in the data. The violations of stationarity should be removed before the dataset is modeled.

Ontario hourly demands in the year 2004 are selected as the dataset in this chapter. Raw data shown in Figure 7.4 (a) comes from Independent Electricity System Operator (IESO) [49]. There are 8784 observations in 2004 on an hourly basis. Figure 7.4 (a) also shows non-zero mean value and seasonality which are not suitable for neural network modeling due to the properties of training algorithms.

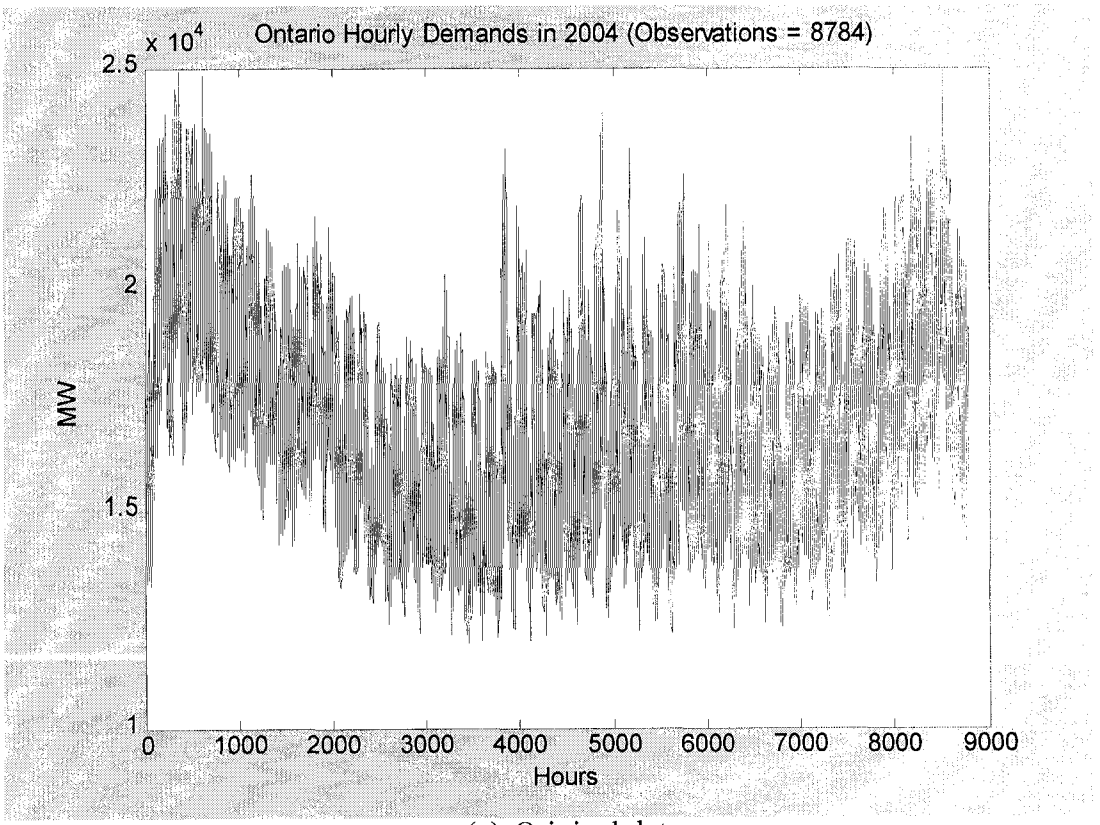

(a) Original data

Figure 7.4 Ontario hourly load demands in 2004 (a)

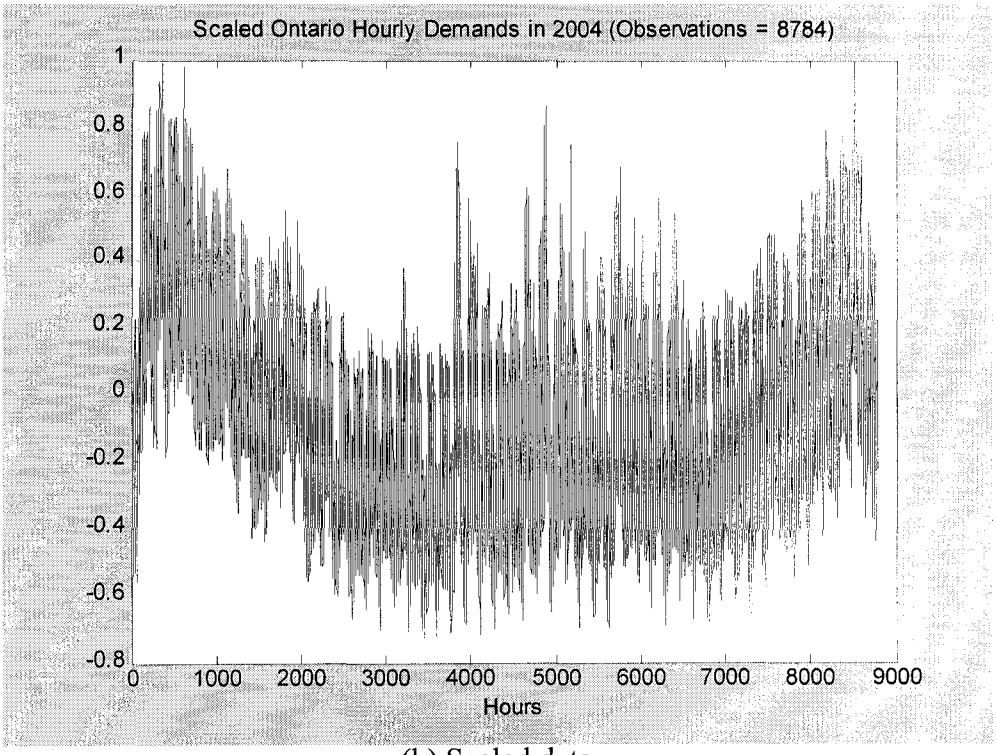

(b) Scaled data

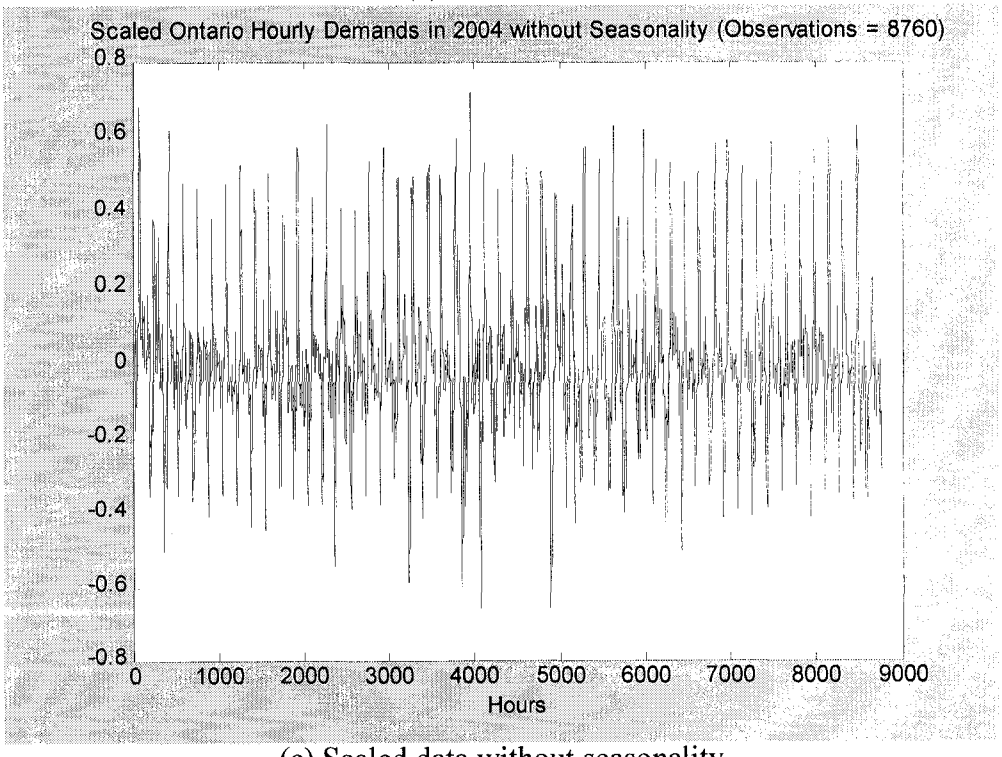

(c) Scaled data without seasonality

Figure 7.4 Ontario hourly load demands in 2004

Removing the mean of the input data can greatly improve the convergence of weight updating. Scaling is also helpful. In this research, the observations are scaled between -1 and 1 as shown in Figure 7.4 (b). The dataset does not change its shape after mean removing and scaling. The seasonal pattern is still in Figure 7.4 (b). Differencing at 24-hour intervals is used to eliminate the seasonality [46] and the dataset is shown in Figure 7.4 (c). This constitutes pre-processing of the raw data. Correspondingly, post-processing of the output of the neural network needs to be done to convert the output to the required form.

7.3.2 Division of the Observations

Dataset is fundamental and it is unwise to use all the available examples in the training set to estimate the neural network parameters. As shown in Figure 7.5, a dataset of observations is divided into three sub-data sets: training set, testing set, and forecasting set. The testing and forecasting dataset are not used during the neural network training procedure.

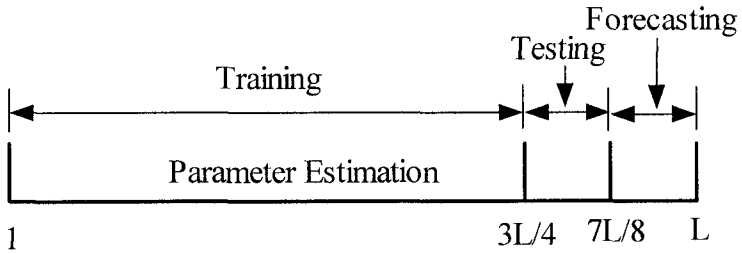

Figure 7.5 Division of dataset into three parts (L is the number of observations)

The size of the training dataset is very important for good performance because the neural network obtains information from the training set. If the training dataset does not cover the full range of operating conditions, the model may perform badly when deployed. Under no circumstances should the training set be less than the number of weights in the neural network. A good size of the training dataset is ten times the number of weights in the network, with the lower limit being set around three times the number of weights. [48]

The size of the neural network topology should also be carefully selected. If the number of layers or the size of each layer is too small, the network does not have enough degrees of freedom to classify the data to approximate the function, and the performance suffers. Vice versa, if the size of the network is too large, performance may also suffer.

The generalization error can be decomposed into the sum of the bias squared plus the variance [50]. A model which is too simple, or too inflexible, will have a large bias or under-fitting, while one which has too much flexibility in relation to the particular dataset will have large variance or over-fitting. The best generalization is obtained when we have the best compromise between the conflicting requirements of small bias and small variance.

The purpose of neural networks is to make good predictions for new inputs, not to learn an exact representation of the training data itself. So estimating prediction error is necessary. There are two widely used methods for estimating prediction error. One is by means of a testing set and the other by cross-validation. Bishop [51] comments "no matter how one fine tunes cross-validation, it will not do as well as having a test set of the same size as the learning set". This also highlights the need to optimize the complexity of the model in order to achieve the best generalization. In this research, changing the number of adaptive parameters in the neural network is exploited to obtain the optimal complexity.

7.3.3 Computer Experiment

Ontario hourly demands in 2004 are used as the experimental dataset to train this feed-forward neural network shown in Figure 7.2 with L-M algorithm. The division of the dataset is shown in Figure 7.5. The results of training, testing, and forecasting of whole year load show the generality and validation of this neural network model.

Figure 7.6 shows the prediction errors and the visual comparison of observations and predictions from the neural network model. Autocorrelation functions of the prediction error are shown in Figure 7.7. Lags are selected from 0 to 20. Autocorrelation coefficients from lag 1 to lag 20 are almost within the standard error range (dashed red line ± S.E.). The first several lags are significant important. Histograms over the prediction errors are also shown in Figure 7.7. Most of the errors are within ± 0.05, and almost 80 % of the errors are within ± 0.025. Figure 7.7 means that the errors are uncorrelated, Gaussian distributed, and within a 95 % confidence limit range.

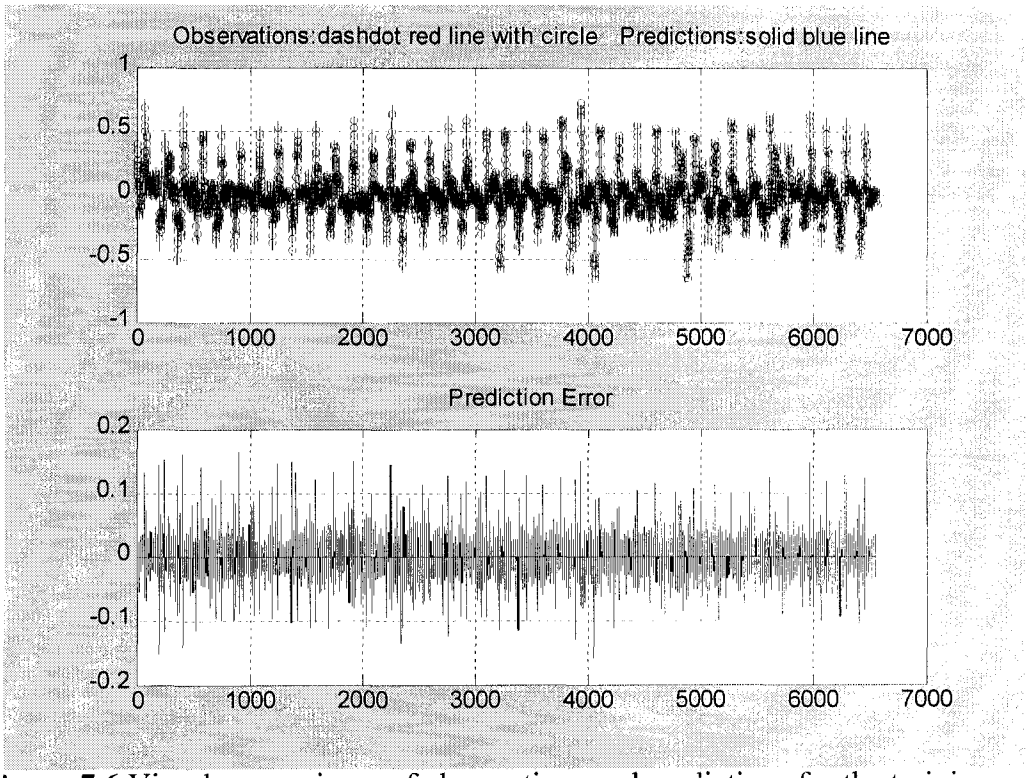

Figure 7.6 Visual comparisons of observations and predictions for the training part

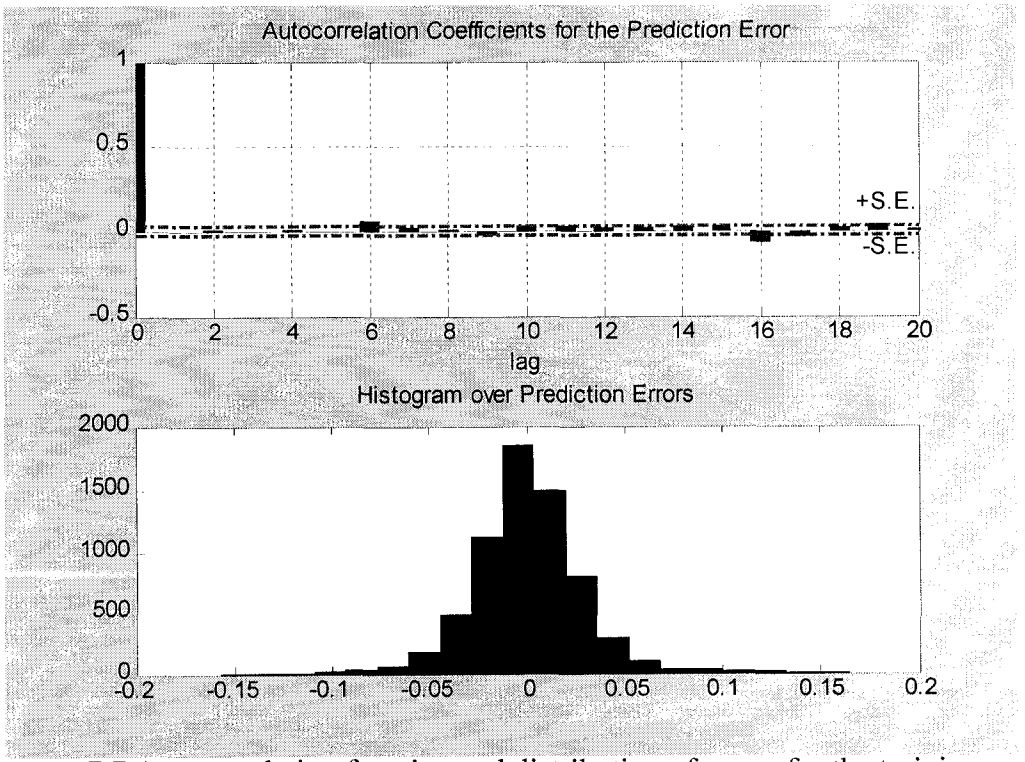

Figure 7.7 Autocorrelation function and distribution of errors for the training part

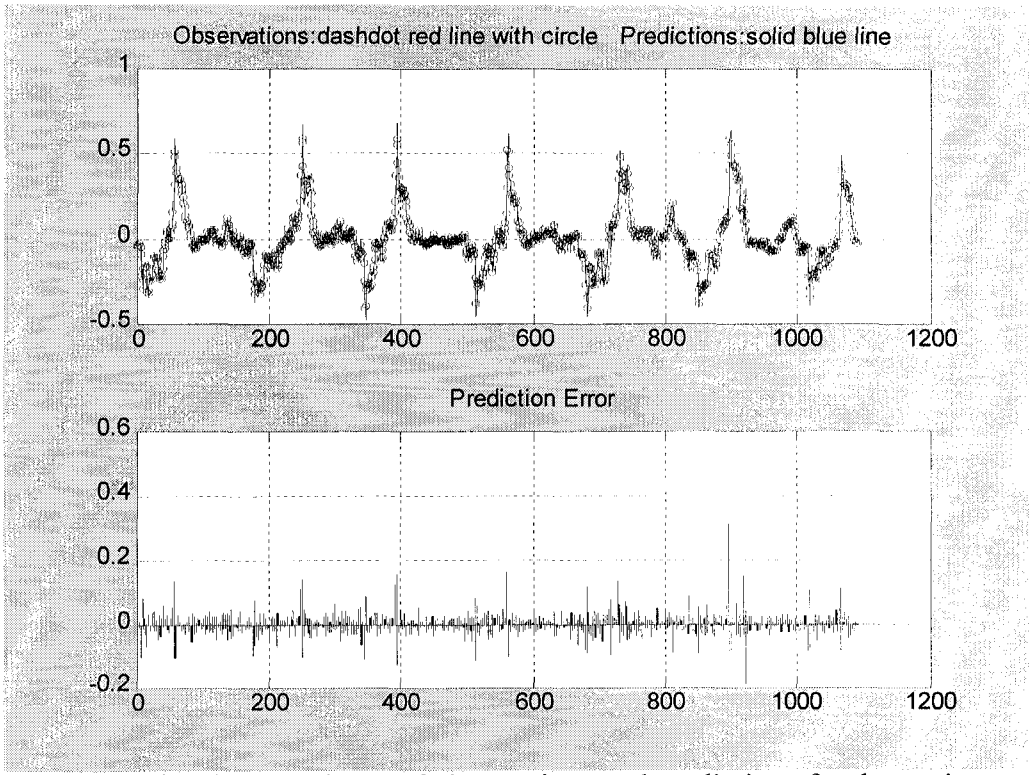

Figure 7.8 Visual comparisons of observations and predictions for the testing part

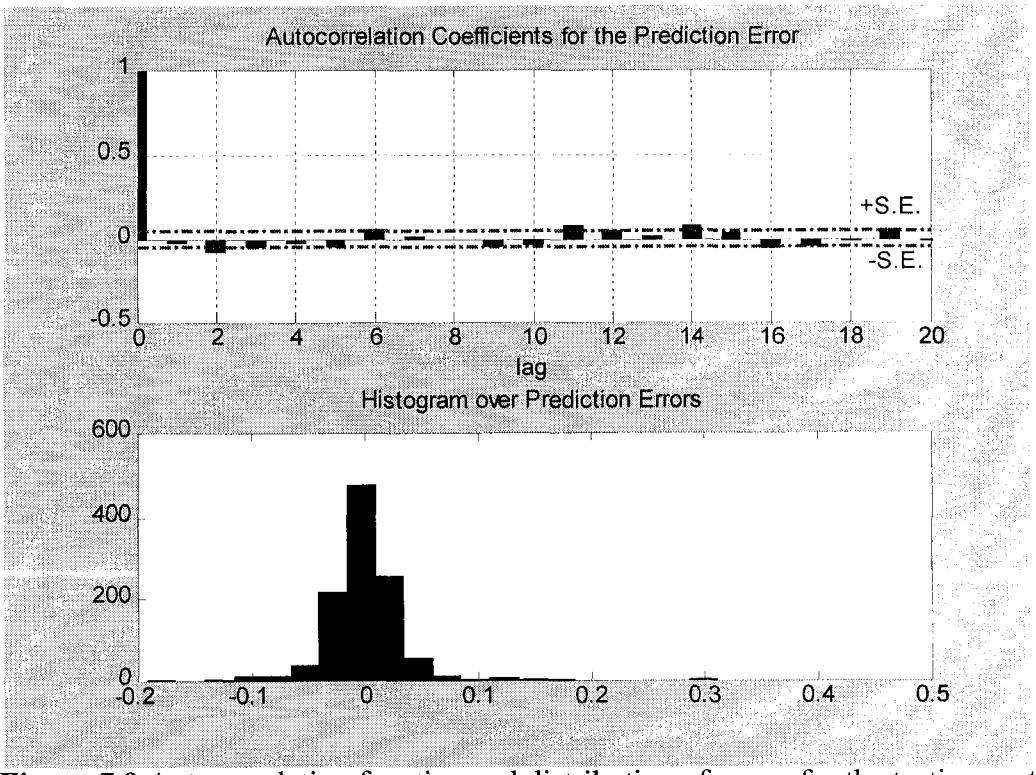

Figure 7.9 Autocorrelation function and distribution of errors for the testing part

The visual comparison of observations and predictions of the testing part and the prediction errors are shown in Figure 7.8. Figure 7.9 shows the autocorrelation coefficients and the histogram of the prediction error. Autocorrelation coefficients from lag 1 to lag 20 are almost within the standard error range. From the histograms over the prediction error we can see most of the errors are within ± 0.05.

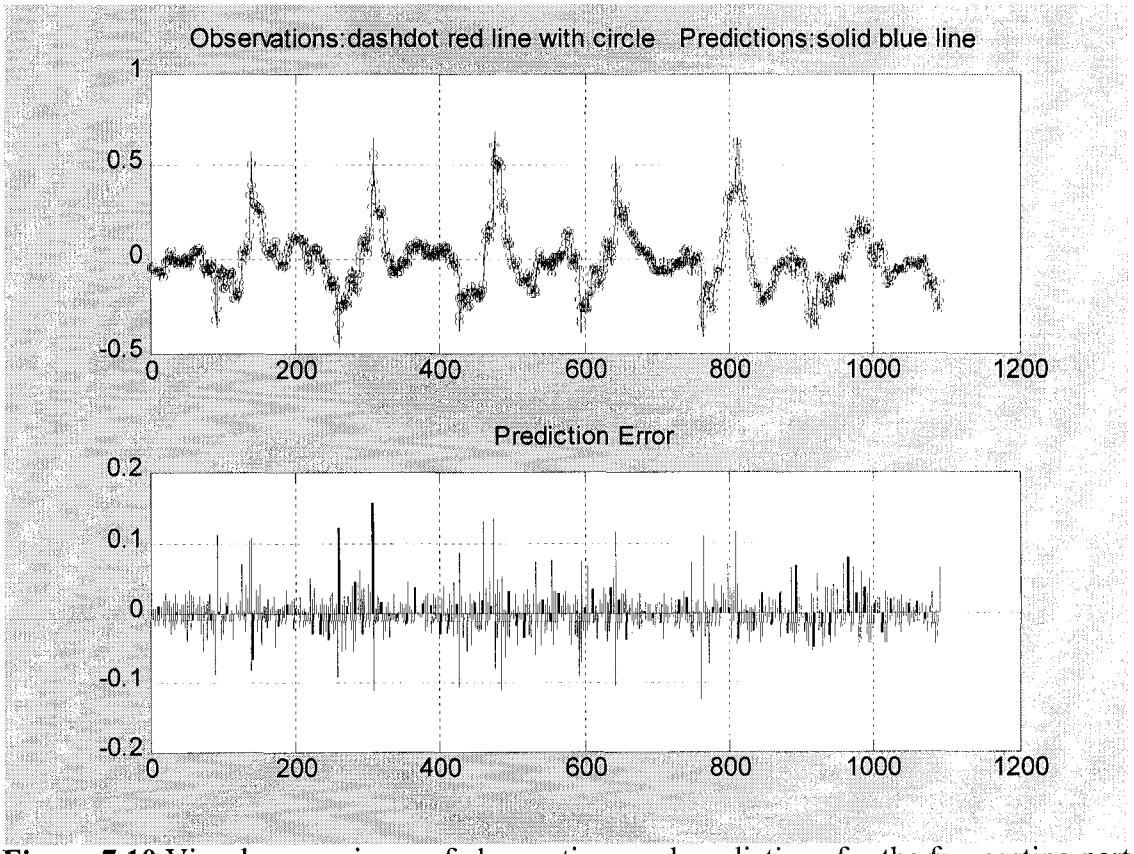

Figure 7.10 Visual comparisons of observations and predictions for the forecasting part

The visual comparison of observations and predictions of the forecasting part and the prediction errors are shown in Figure 7.10. The prediction comes from the fixed-weight neural network in the testing as well as in the forecasting.

Figure 7.11 shows the autocorrelation coefficients and the histogram of the prediction error for the forecasting data subset. Autocorrelation coefficients from lag 1 to lag 20 are almost within the standard error range. Most of the prediction errors are within ± 0.025. From the comparison and statistical analysis we can see the forecasting is practically acceptable.

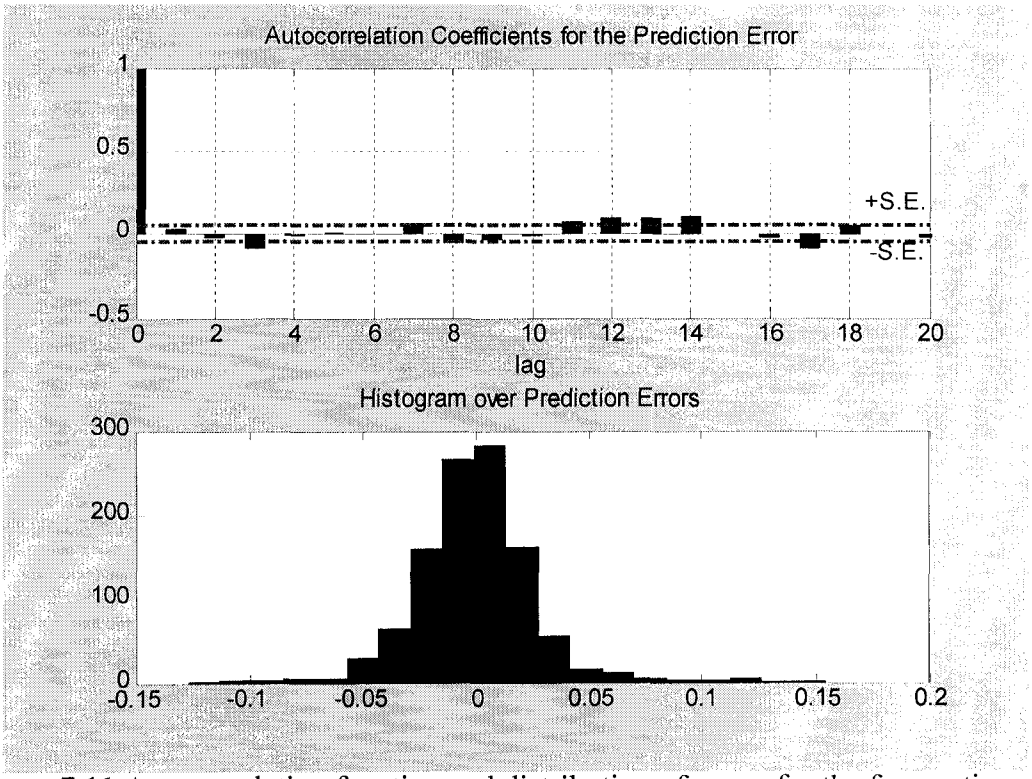

Figure 7.11 Autocorrelation function and distribution of errors for the forecasting part

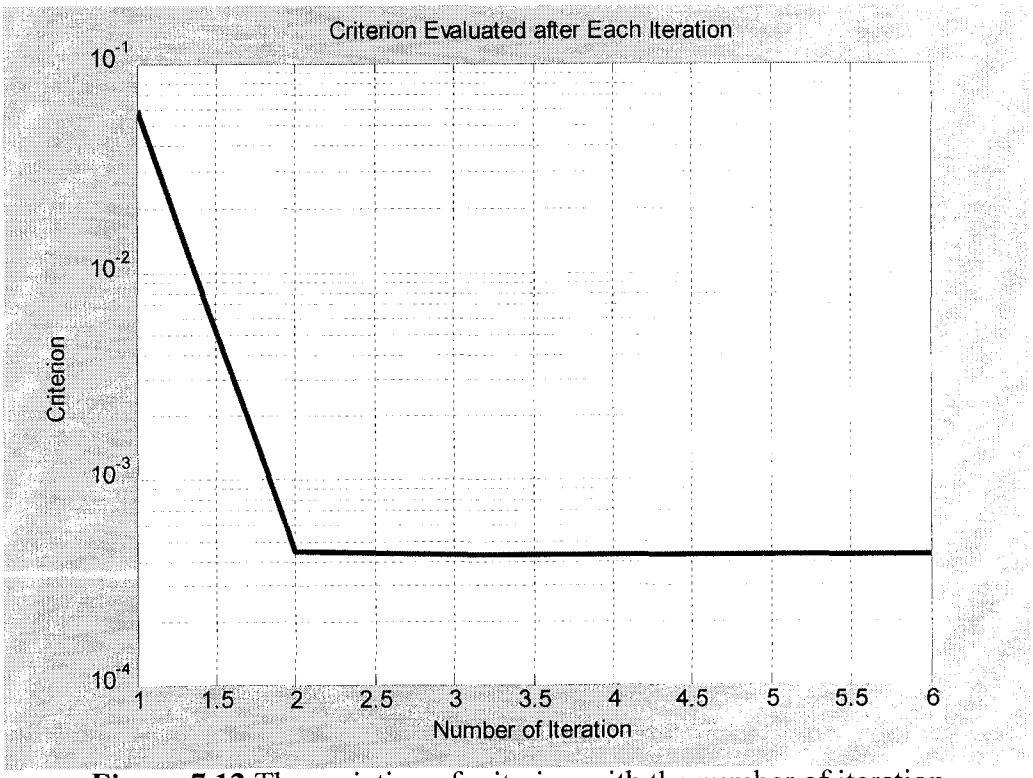

Figure 7.12 The variation of criterion with the number of iteration

Figure 7.12 shows the variation of criterion with each number of iteration. L-M is an effective optimization algorithm. It converges only after 2 iterations.

Accurate and reliable load forecasting is necessary to ameliorate energy management. The prediction of hourly load variations and hourly load demands in Ontario can be achieved through the neural network modeling as shown in this chapter.

CHAPTER 8
DISCUSSION AND PREDICTION OF MECHANICAL PROPERTIES OF SINGLE LAYER ACSR CONDUCTORS

8.1 Introduction

This research is concerned with the operational behaviors of single layer ACSR conductors. Chapter 2 mentioned that the mechanical properties of ACSR have been studied from practical and theoretical aspects for over fifty years. This chapter deals with some discussion and prediction of mechanical properties of single layer ACSR, using the Integrated Model and the neural network model.

Some ACSR used in Ontario, Canada was installed around 1950s. Most of these conductors have exceeded their 50-year design life. The decreased reliability of aged lines reduces system operability, maintainability, supply reliability, and public safety. This chapter seeks to answer the question as to the long time reliability of these conductors. The variation of mechanical properties with daily load demands is also been discussed and predicted.

8.2 Discussion of Mechanical Properties of Guinea Conductor

The mechanical properties are studied on a 400 m span length of 159 kcmil ACSR 19/7 Guinea under typical conditions, such as at 20 °C ambient temperature, 60 Hz supply frequency, 1 μm air gap thickness, 50 % rated tensile strength stringing force, etc. The mechanical properties include strain, stress, horizontal tension, sag, loss of strength of aluminum layer due to annealing, etc.

The total strain is comprised of the thermal strain, the elastic strain, the settling strain, and the creep strain [14]. The thermal strain is a function of the conductor temperature. The stress-strain curves of the conductor vary with the increasing load and duration time. The elastic moduli of the steel and aluminum are obtained from the "final" curves of stress-strain curves for each conductor and the elastic strain is obtained by the axial stress over the modulus of the material. The settling strain is a temperature-independent permanent strain, complete after one hour of loading at a stress level which has not previously been exceeded. The creep strain is the plastic deformation of the wire materials under a given stress and the creep strain consists of the permanent strain of the material, aluminum and steel, itself. The creep strain increases gradually in time but at a decreasing rate, which depends on stress, temperature, and the amount of prior creep strain. Besides the settling hysteresis, the fact that the creep rate depends on prior creep strain also accounts for loading hysteresis [16, 17].

Stress-strain curves are the usual curves expressed in publication. It is also popular for the strains to be expressed as a function of duration time with hours. In this chapter the strains are functions of the current with the load variation, the average service

time, and the environmental conditions for a specific conductor. Strain-hardening has been taken into consideration.

8.2.1 Variation of Mechanical Properties with the Current

The interaction among mechanical properties including strain, stress, horizontal tension, sag, loss of tensile strength of the aluminum layer due to annealing, etc., is calculated with iterations. The probabilistic algorithm makes it possible to ensure that the creep strain depends on the prior creep strain and the loading history as part of the iteration procedure.

Figure 8.1 shows the variation of the creep strain, the settling strain, the thermal strain, the elastic strain, and the total strain with the current for Guinea conductor. "St" means steel and "Al" means aluminum material. The creep strain decreases with an increase of the current. The decreasing rate is different at various current ratings. The decreasing rate of aluminum is higher than that of steel. The settling strain remains constant for aluminum and decreases a little for steel with an increase of the current. The thermal strain is a function of the temperature and increases with the increase of the current. We note from Figure 8.1 that the increasing rate of aluminum is higher than that of steel. The elastic strain decreases with an increase of the current. The decreasing rate of steel is larger than that of aluminum. The total strain is the summation of the four strains, and it is the same for aluminum and for steel as described in Chapter 2. Some quantitative values are listed in Table 8.1.

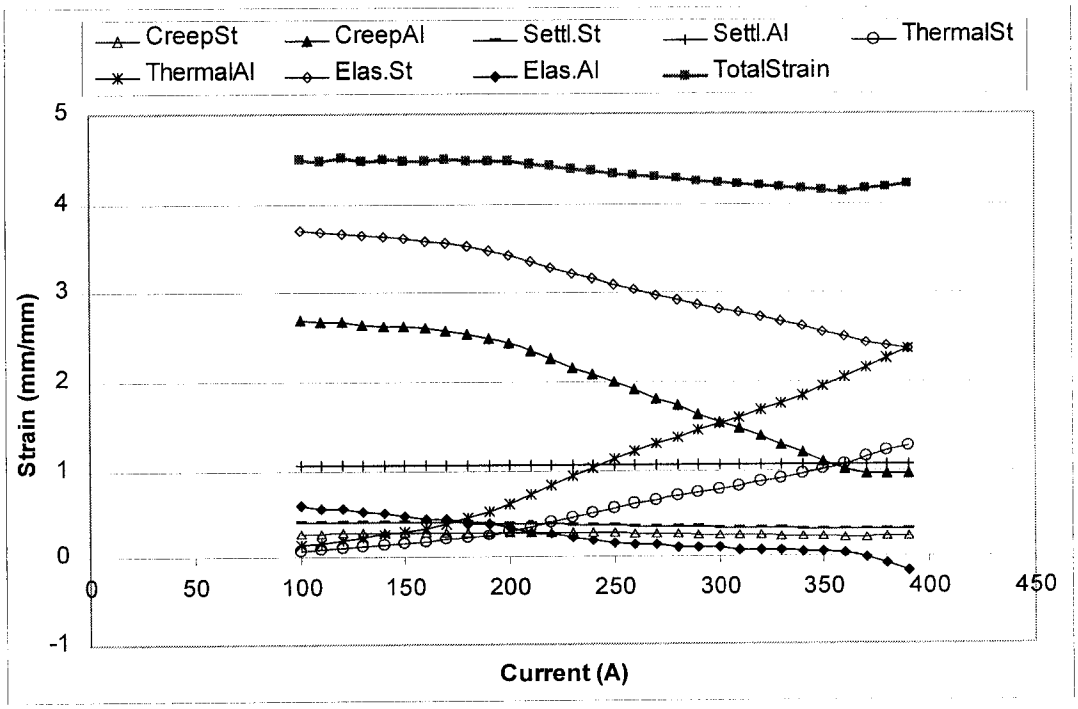

Figure 8.1 Variation of the strains with the current of Guinea

Table 8.1 Variation of strains at various current ratings

I (A)	CreepSt	CreepAl	Settl.St	Settl.Al	ThermalSt	ThermalAl	Elas.St	Elas.Al	Total
100	0.290	2.69	0.426	1.06	0.071	0.14	3.70	0.607	4.49
150	0.299	2.62	0.420	1.06	0.161	0.319	3.60	0.486	4.48
200	0.304	2.43	0.408	1.06	0.319	0.628	3.42	0.364	4.48
250	0.293	1.99	0.381	1.06	0.578	1.13	3.09	0.166	4.34
300	0.270	1.55	0.358	1.06	0.788	1.53	2.82	0.102	4.24
350	0.244	1.10	0.336	1.06	1.00	1.94	2.56	0.0561	4.15
390	0.252	0.956	0.329	1.06	1.27	2.37	2.36	-0.163	4.22

The variation of the stress of the aluminum layer with the current is shown in Figure 4.17. When the current is larger than 350 A (temperature higher than 192°C), the negative value of the aluminum stress in Figure 4.17 means that the aluminum layer experiences a compressive load which is opposite to the elongation direction.

Figure 8.2 shows the variation of stress in the steel core with the current. The rate of stress decreases to 180 A, 156°C is nearly half as large as it is for current larger than 180 A. Comparing with the curve for Guinea in Figure 4.17, the smoothness of the steel stress curve is better than that of aluminum stress. The rate of aluminum stress decreases to 270 A, 176 °C is almost twice as high as it is for temperature above 176 °C.

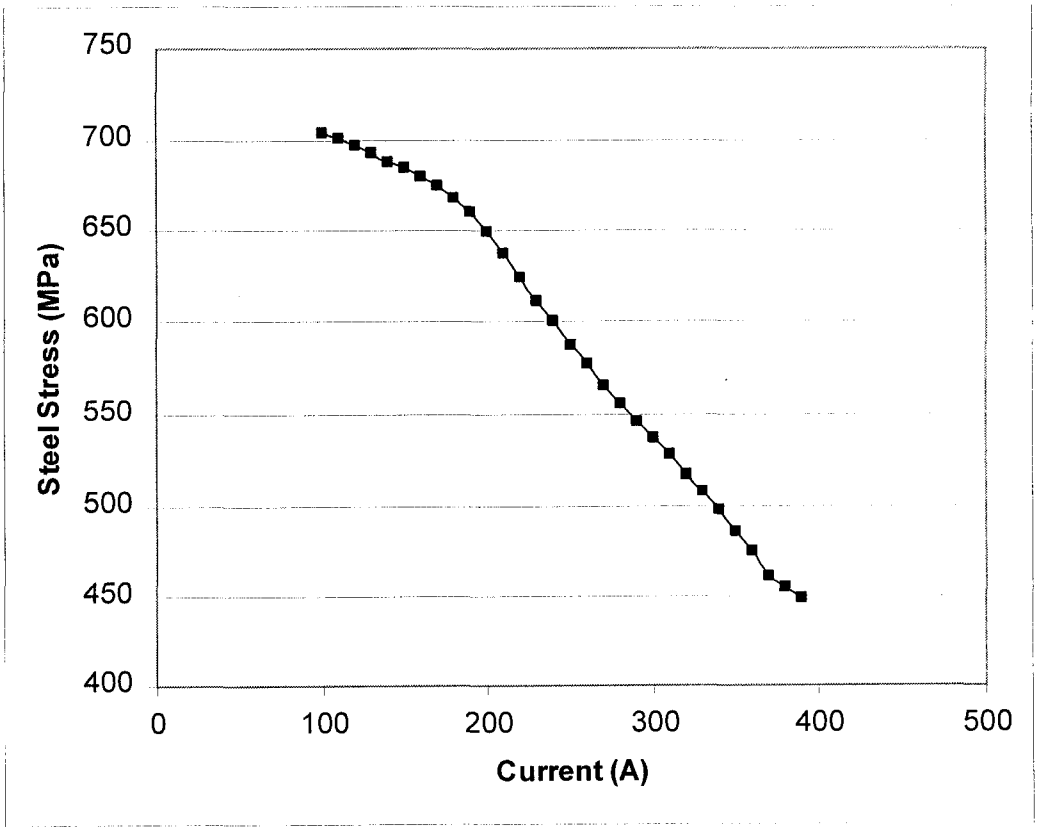

Figure 8.2 Variation of the stress in the steel core with the current

The other properties, horizontal tension, sag, and loss of tensile strength of aluminum with the variation of the conductor current are shown in Figures 4.18, 4,19, and 4.20, respectively. The variation of the horizontal tension for Guinea in Figure 4.18 is similar as that of the steel stress in Figure 8.2. The sag increases dramatically with the compressive load shown in Figure 4.19 for Guinea conductor. From Figure 4.20, we can see that the loss of tensile strength of Guinea reaches near 35 % at 390 A with 20 °C ambient temperature, which is a lot comparing with 20 % loss of Grackle aluminum at 1400 A.

8.2.2 Mechanical Properties of Conductor with 50 Years Duration

Initially ACSR was designed for 50 years service life. What are the mechanical properties during the 50 years? A case study is performed on Guinea at 350 A loading with 20 °C ambient temperature from 1 year to 50 years duration in this section.

The variation of the strains with the duration time from 1 year to 50 years is shown in Figure 8.3. Since the failure of ACSR conductors is related to the stress or strain of the aluminum wires, only aluminum strains are shown here. The creep strain increases from 1.02 mm/mm in year 1 to 1.18 mm/mm in year 50. The settling strain remains invariant. So does the thermal strain because of the 350 A load assumption. The elastic strain decreases from 0.06 mm/mm in year 1 to 0.03 mm/mm in the duration year of 50. The variation of the total strain during the conductor service life is mainly caused by the cumulative creep strain.

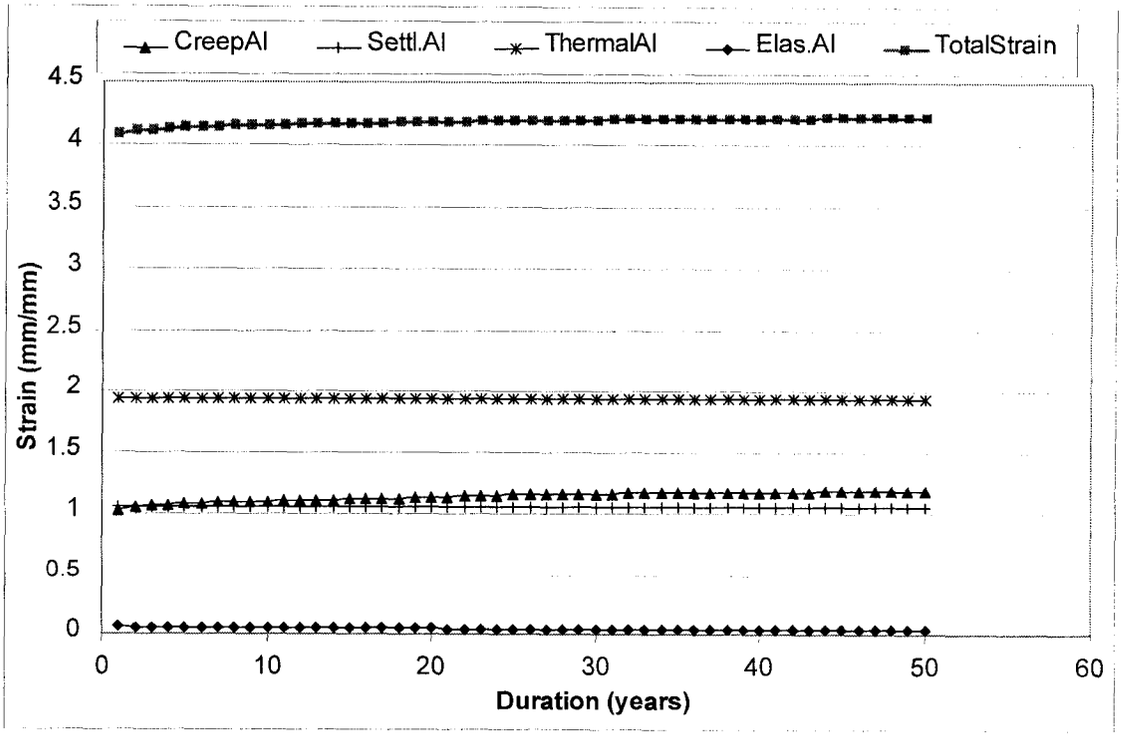

Figure 8.3 Variation of the strains with the time of duration

At a fixed current rating, the sag of the conductor increases with an increase of time of duration. From Figure 8.4 we can see the sag increases greatly in the first 4 years. The increasing rate decreases in the following 16 years. It is noteworthy to find that after 20 years service the conductor sag has a relatively big jump. After that, the increasing rate of sag becomes smaller comparing with that in the previous 16 years.

The big jump (3.2 mm) in Figure 8.4 causes discontinuity in the simulation. The Integrated Model has ability to predict birdcaging phenomenon which contributes to discontinuity. For some reason, the elongation of aluminum is longer than that of steel and the aluminum wires radially move away from the steel core to accommodate the compressive stress since aluminum and steel are clapped together in ACSR conductors. Even though the Integrated Model can predict the birdcaging instantly, it takes years of time to observe the birdcaging phenomenon occurring in field conductors.

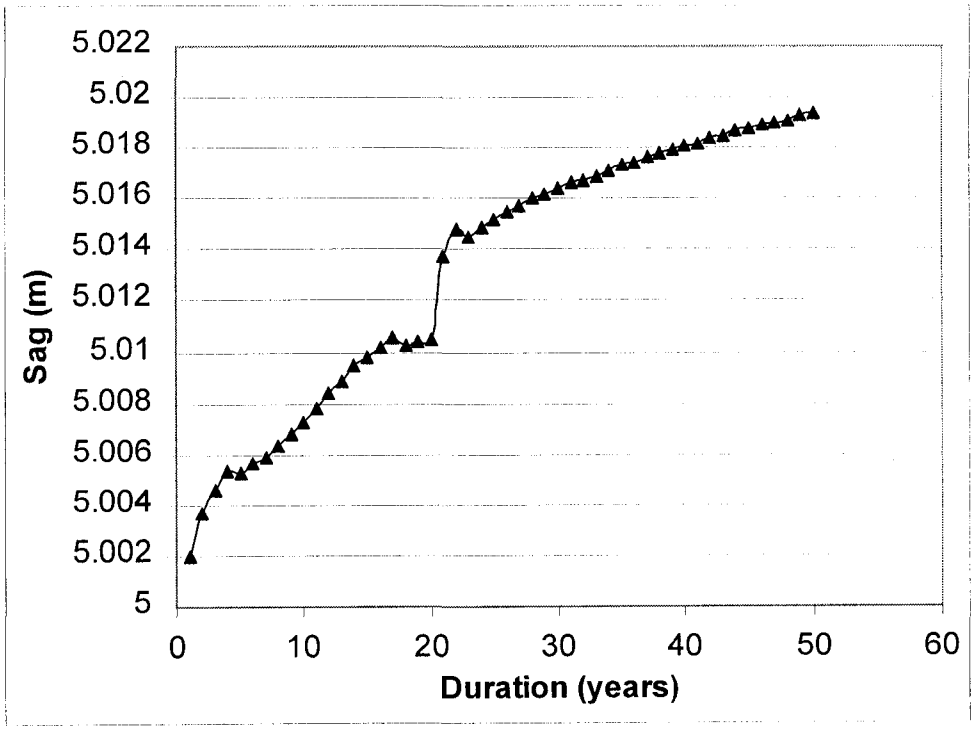

Figure 8.4 Variation of the sag with the duration time

Figures 8.5 and 8.6 show the variation of the aluminum stress and the horizontal tension with the duration time from year 1 to year 50, respectively. After 20 years service, there is a sudden decrease in stress in the aluminum layer, caused in part by the horizontal tension.

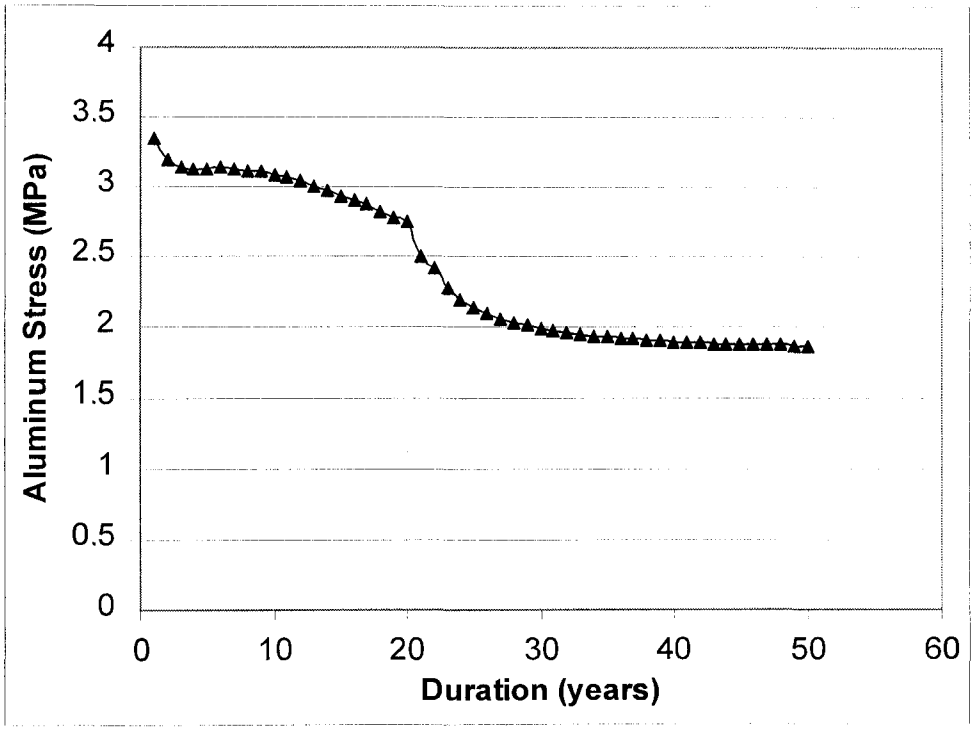

Figure 8.5 Variation of the stress in the aluminum layer with the duration time

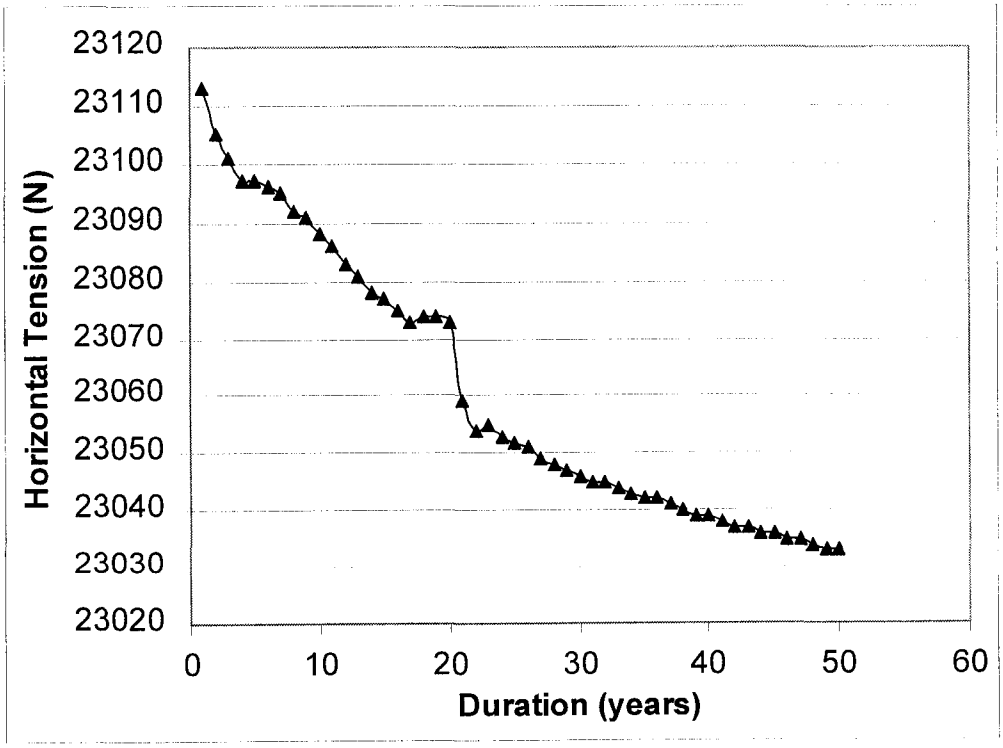

Figure 8.6 Variation of the horizontal tension with the duration time

The loss of tensile strength of the aluminum layer varies with the duration time as shown in Figure 8.7. As expected, the biggest loss of strength due to annealing happens in the first year. The loss of strength increases 10 % in the first 10 years and increases another 10 % in the remaining 40 years.

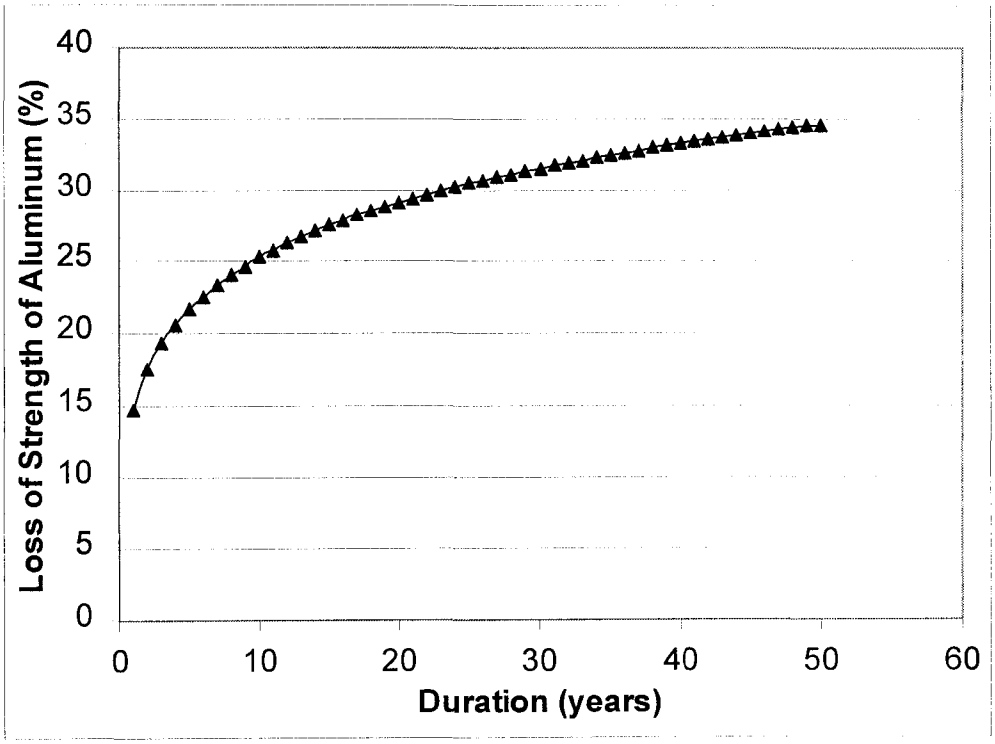

Figure 8.7 Variation of the strength loss of aluminum with the duration time

8.2.3 Mechanical Properties with Daily Load Variation after 55 Years Service

We would like to establish the mechanical properties of aged single layer ACSR conductors varying with daily load over the lifetime of existing conductors (which is taken as 55 years for some conductors in service in Ontario). The variation is investigated on Guinea, which is a single layer conductor. Ontario hourly demands shown in Figure 8.8 come from the IESO website [49]. There are 720 observations, and that would be 30 groups of daily loads (720/24 = 30). Among them, hourly loads in April 18 - 30, 2005 are selected as the actual daily load input to calculate the variation of mechanical properties of Guinea. These selected daily loads can be predicted from the neural network model. We will see the prediction in the next section.

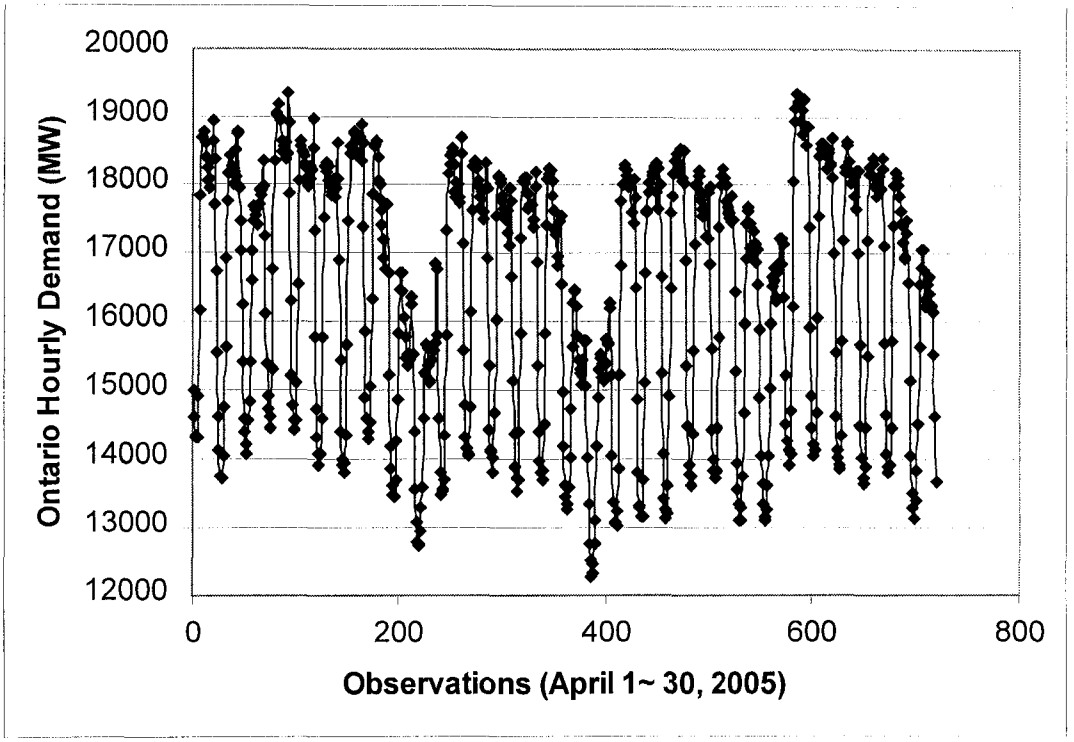

Figure 8.8 Ontario hourly demands in April 2005

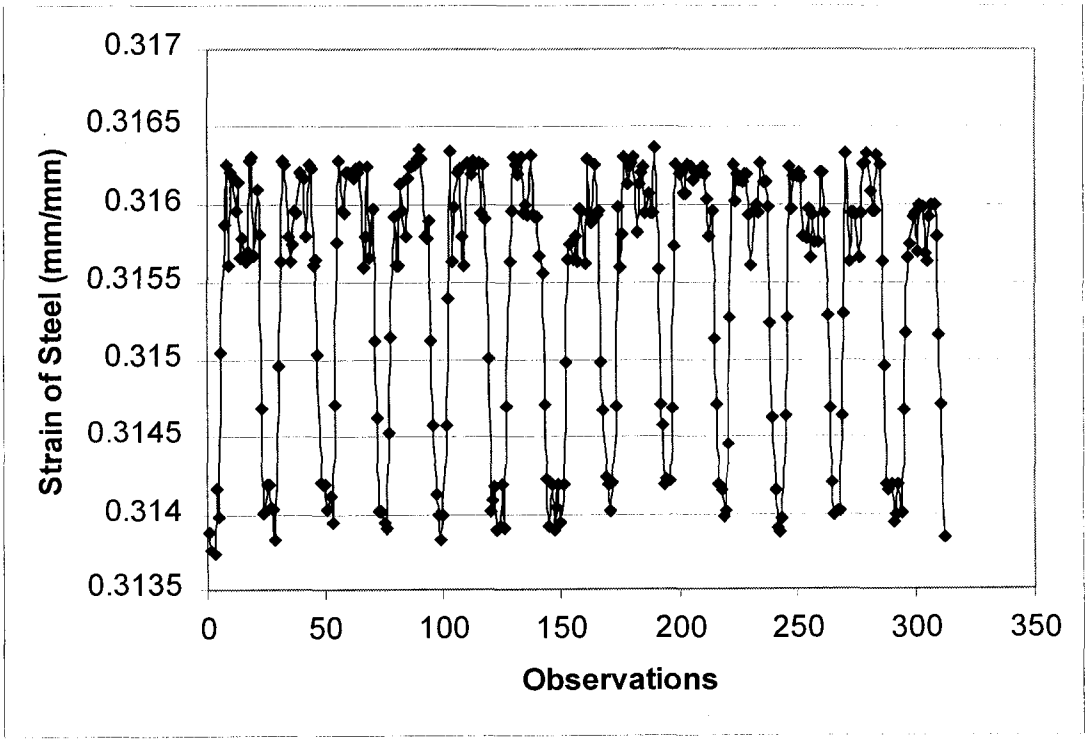

Figure 8.9 Variation of the steel strain with the daily load demand

Figures 8.9 and 8.10 show the variation of strains for steel and aluminum of Guinea conductor after the average of 55 years service life. The conductor strain varies greatly with the variation of daily load.

The variation of thermal strain and elastic strain of aluminum with the daily load is shown in Figures 8.11 and 8.12, respectively. Figure 8.13 shows the variation of the sag with the daily load after conductor 55 years duration.

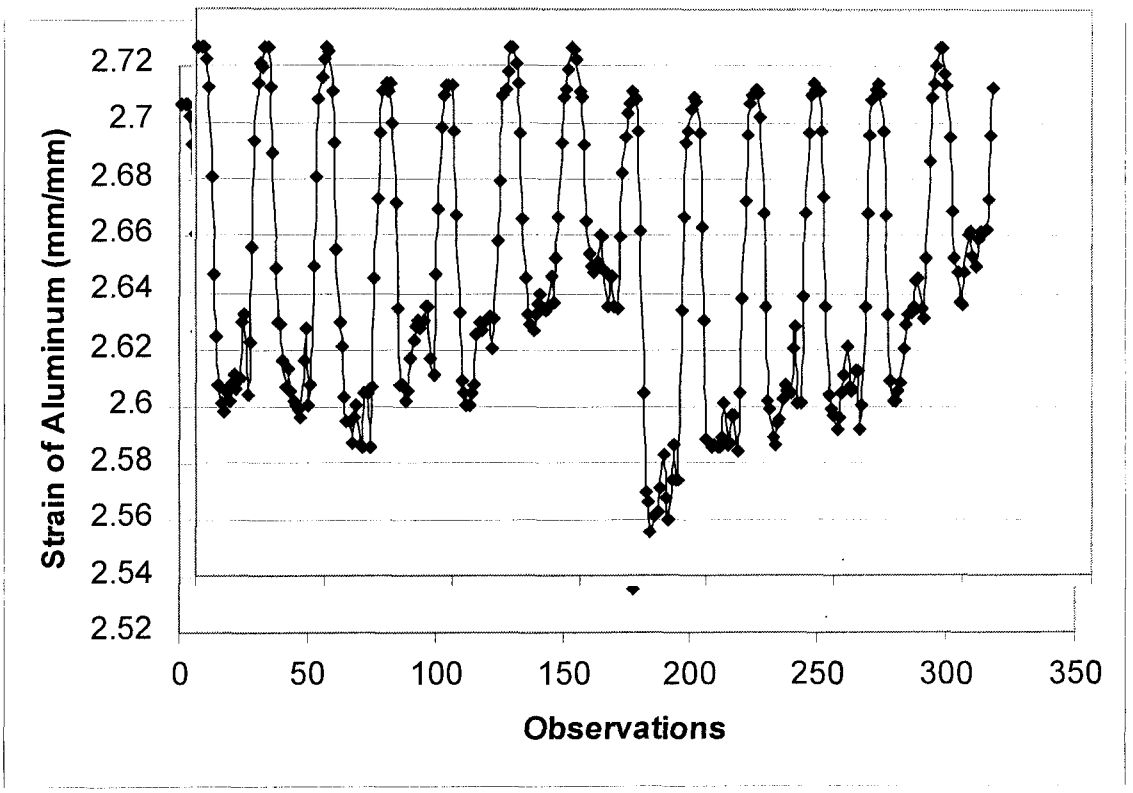

Figure 8.10 Variation of the aluminum strain with the daily load

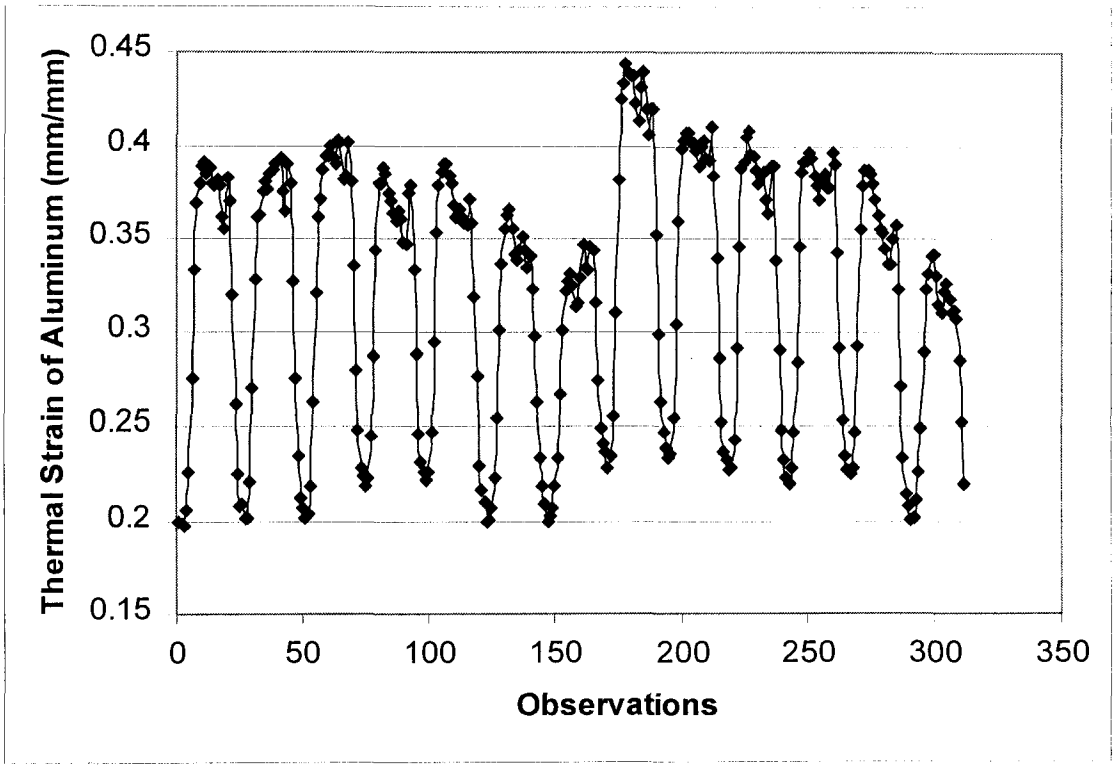

Figure 8.11 Variation of the thermal strain with the daily load

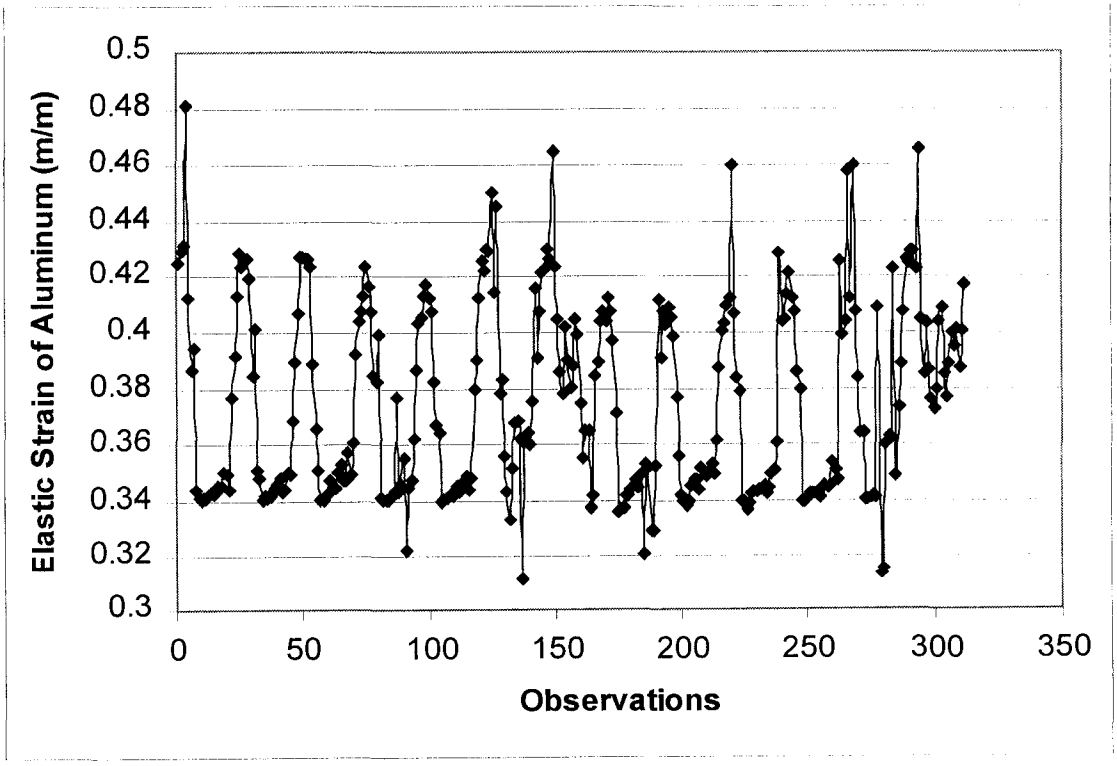

Figure 8.12 Variation of the elastic strain with the daily load

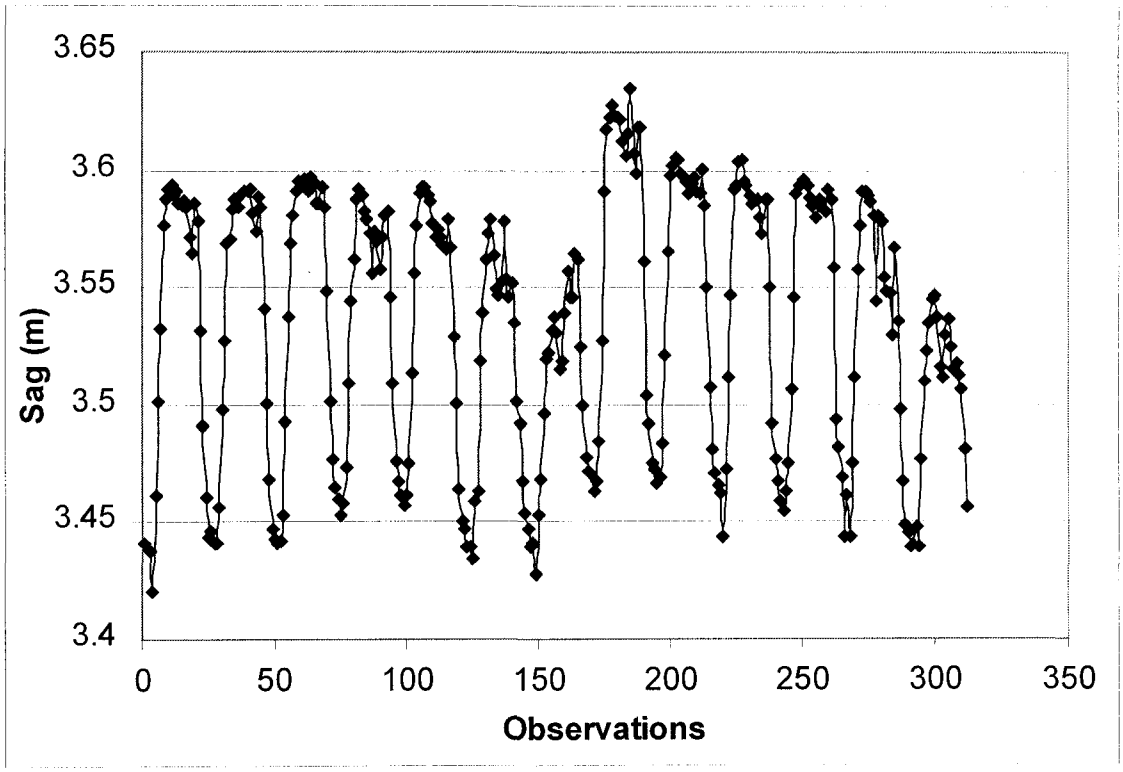

Figure 8.13 Variation of the sag with the daily load

8.3 Prediction of Mechanical Properties of Guinea Conductor

The prediction is performed with the neural network model developed in the previous chapter. All the observations in this section are divided into two parts: the training part and the prediction part. Visual comparisons and statistical criteria are given to check the validation of prediction.

8.3.1 Prediction of Ontario Daily Load as Input to Obtain Mechanical Properties

Ontario hourly loads in April 2005 shown in Figure 8.8 are selected as the experimental dataset in this section. As we did for load forecasting in Chapter 7, pre-processing of the raw data is performed to remove the means, eliminate the seasonality, and scale the observations between 1 and - 1. Correspondingly, the post-processing of the prediction from the neural network is also performed to convert the data to the required form as input to the Integrated Model.

For the input of the neural network, the first 17 groups data (April 1 ~ 17) are used as the training set and the rest 13 groups (April 18 ~ 30) are used as the testing. There are three neurons in the hidden layer and the activation function is the sum of the input.

Figure 8.14 shows the visual comparison of observations and predictions from the neural network model and the prediction errors for the training data set.

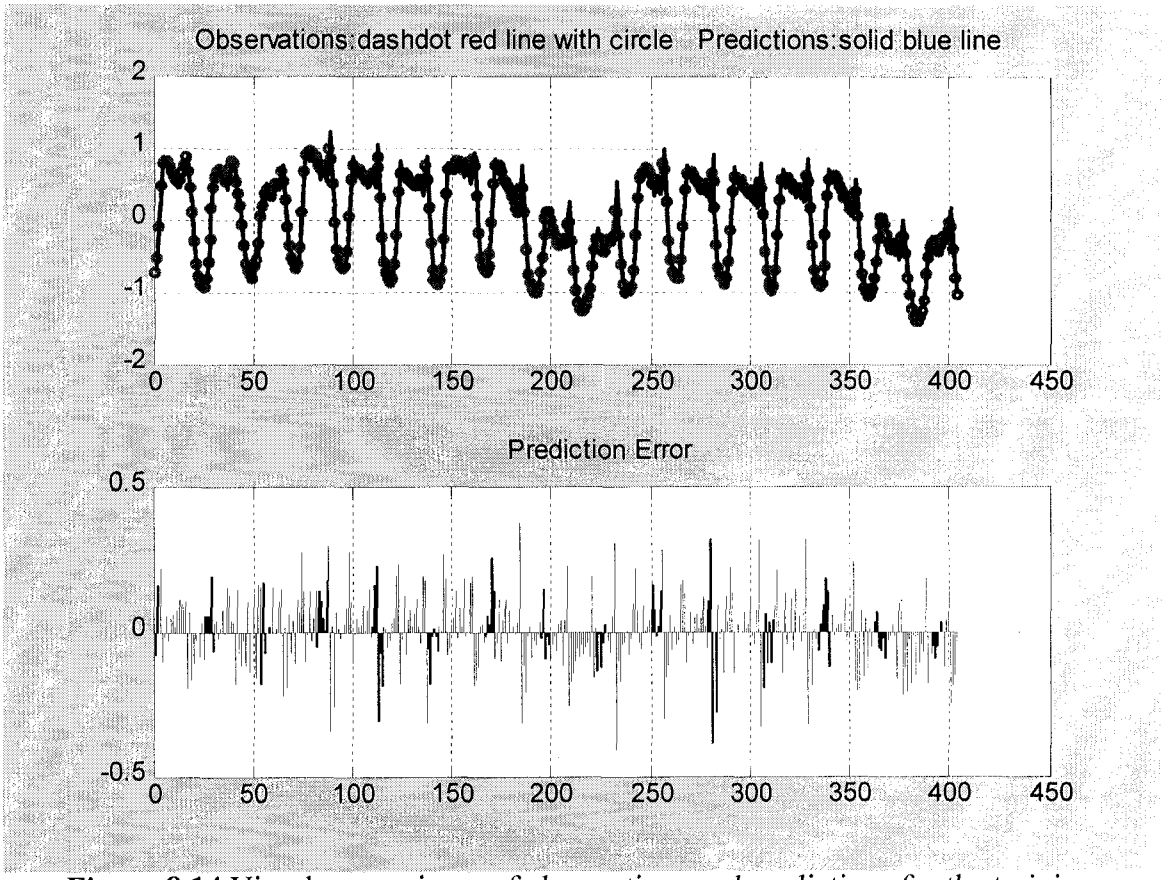

Figure 8.14 Visual comparisons of observations and predictions for the training

The autocorrelation function of the prediction error analysis is shown in Figure 8.15. Lags are selected from 0 to 20. Autocorrelation coefficients from lag 1 to lag 20 are almost within the standard error range, especially the first six lags. That means the errors are uncorrelated and the prediction is within the 95 % confidence limit range. Histograms over the prediction errors are also shown in Figure 8.15. Most of the errors are within ± 0.1 and the distribution is Gaussian.

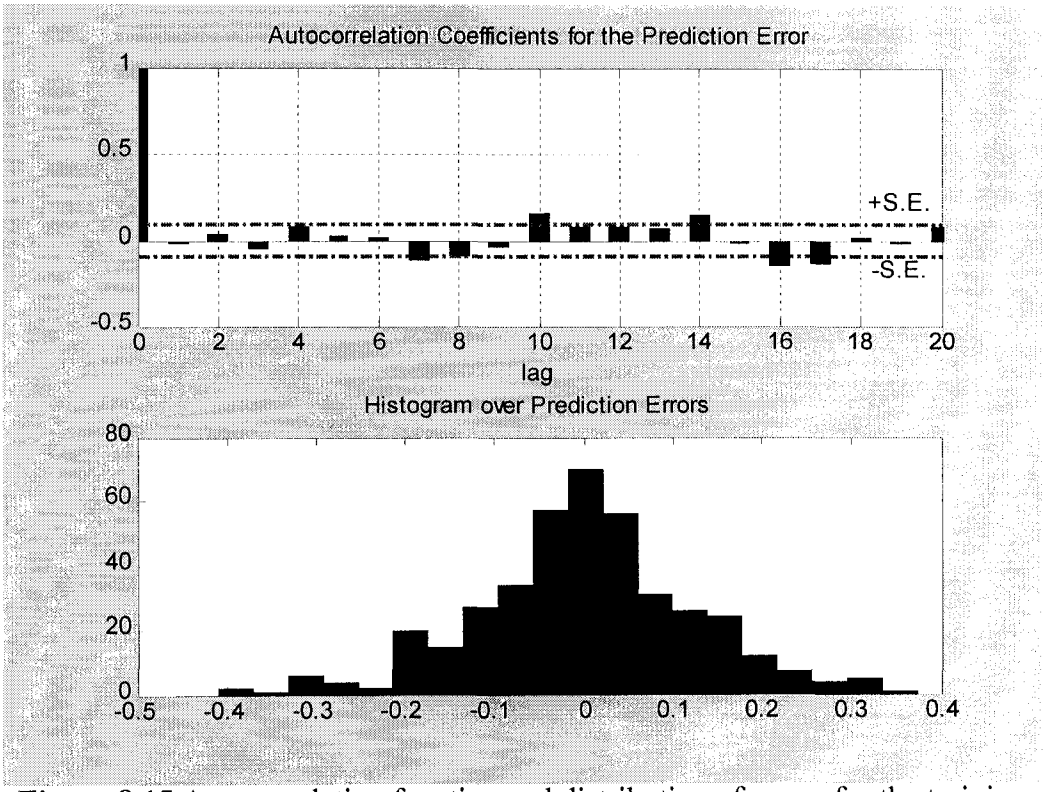

Figure 8.15 Autocorrelation function and distribution of errors for the training

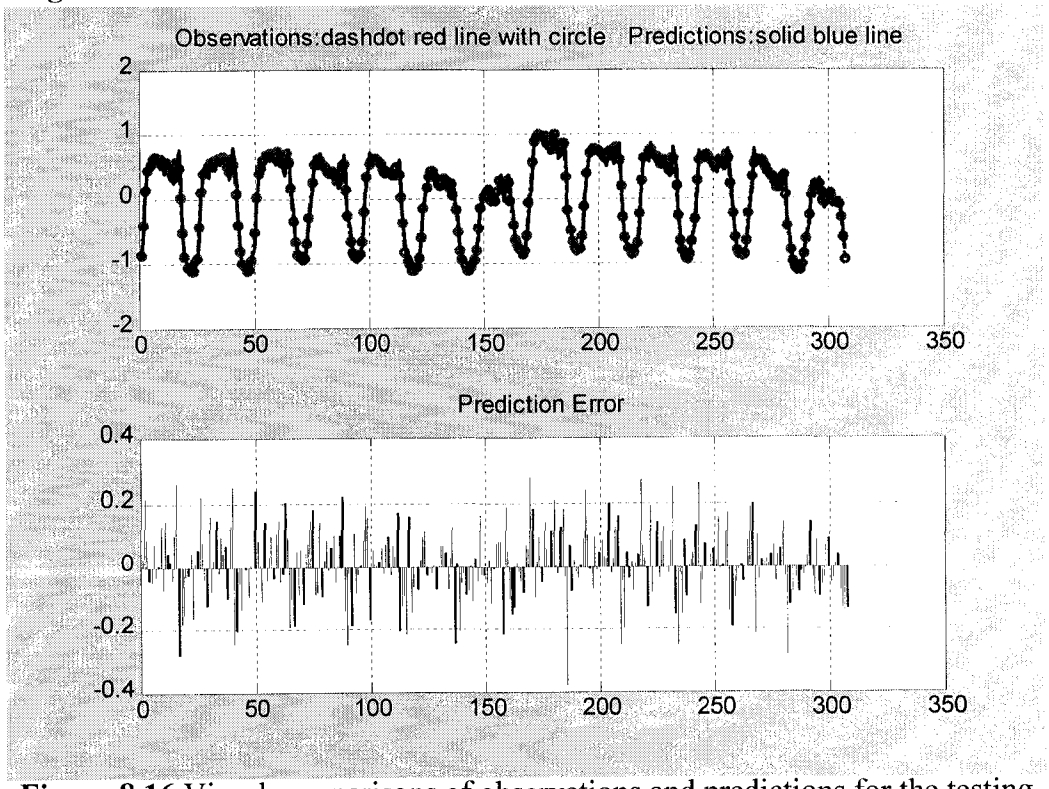

Figure 8.16 Visual comparisons of observations and predictions for the testing

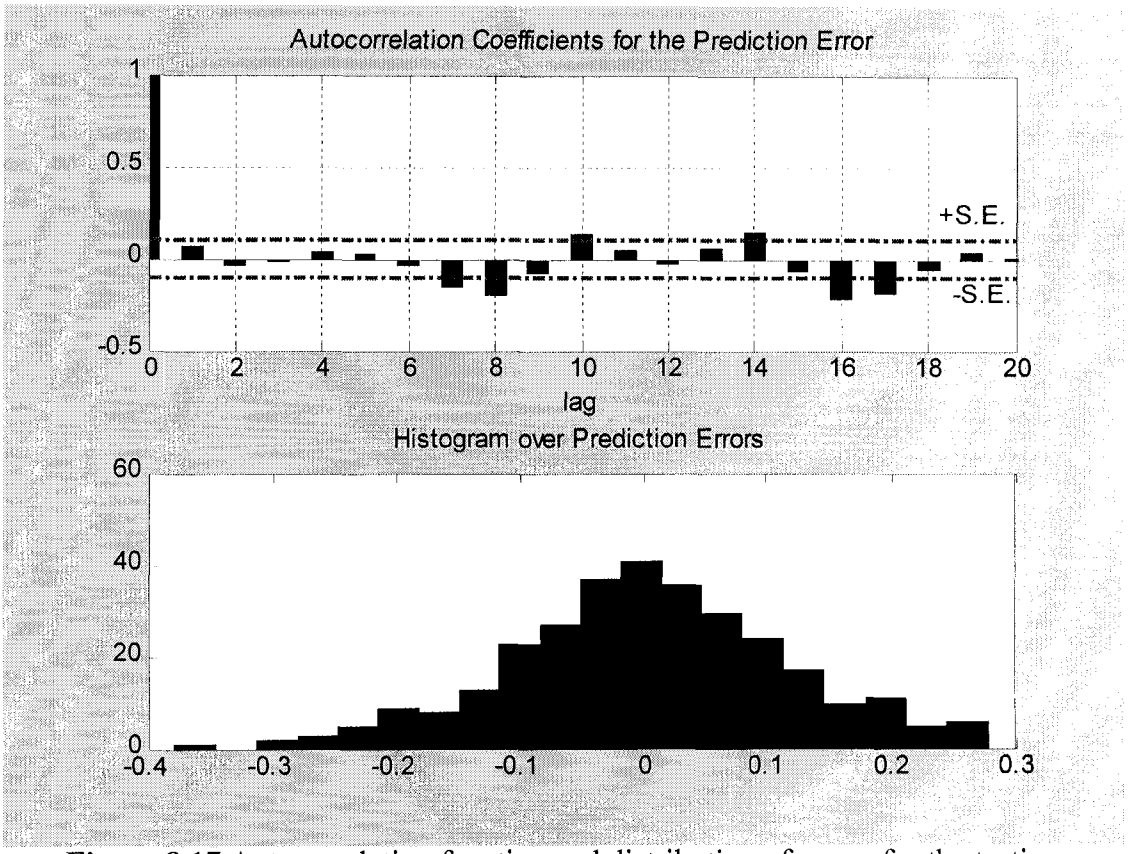

Figure 8.17 Autocorrelation function and distribution of errors for the testing

The visual comparison of observations and predictions of the testing part and the prediction errors are shown in Figure 8.16. The prediction is the output of the weight-fixed neural network. The observations in Figure 8.16 are intended for the comparison and error analyses.

Figure 8.17 shows the autocorrelation coefficients and the histogram of the prediction error. Autocorrelation coefficients from lag 1 to lag 20 are within the standard error range. From the histograms over the prediction error we can see most of the errors are within ± 0.1.

Figure 8.18 shows the variation of the criterion with each number of the iteration. The Levenberg-Marquardt algorithm is an effective optimization method. The algorithm converges after only 2 iterations seen from Figure 8.18.

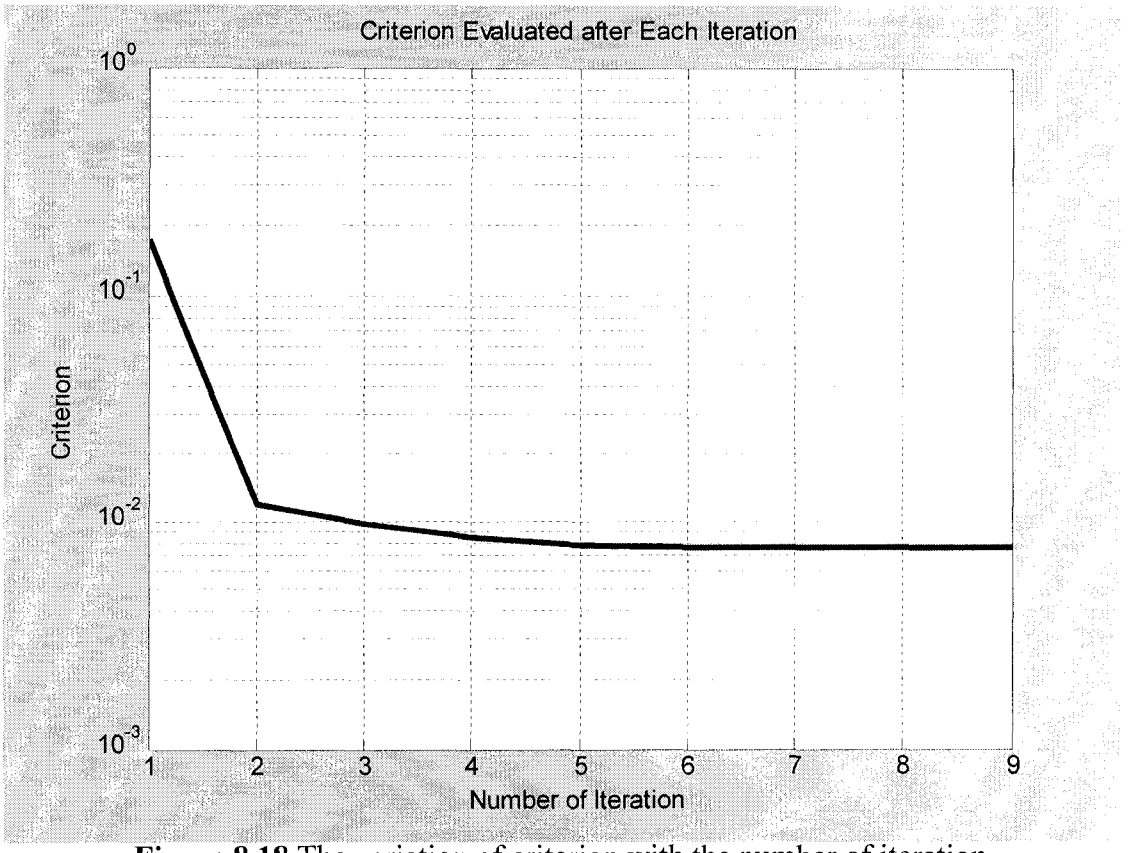

Figure 8.18 The variation of criterion with the number of iteration

8.3.2 Prediction of the Strain

From Figure 8.3 we know that the strain is the main effect to result in sag increasing during the conductor long time service.

The aim of this section is to predict the variation of strain with hourly load demands for Guinea after 55 years service life. The experimental dataset of strain from the Integrated Model is in Figures 8.9 and 8.10 for steel and aluminum, respectively. There are 312 observations in each Figure 8.9 or 8.10, and they can be divided into 13 groups with daily data. One group serves to test the concept, and the rest of the 12 groups work as the training part.

To predict the strain of aluminum, 29 hidden neurons are used and the activation function is a hyperbolic tangent. This is a typical non-linear neural network model. The visual comparisons for the training and for the testing are shown in Figures 8.19 and 8.21, respectively. Figures 8.20 and 8.22 show the prediction errors and their distribution. Autocorrelation coefficients for the training and for the testing are all within the standard error range. From the visual comparison and statistical analysis, the prediction of the aluminum strain with daily load variation is acceptable.

Figure 8.23 shows the variation of criterion with each number of the iteration. The algorithm converges after 15 iterations.

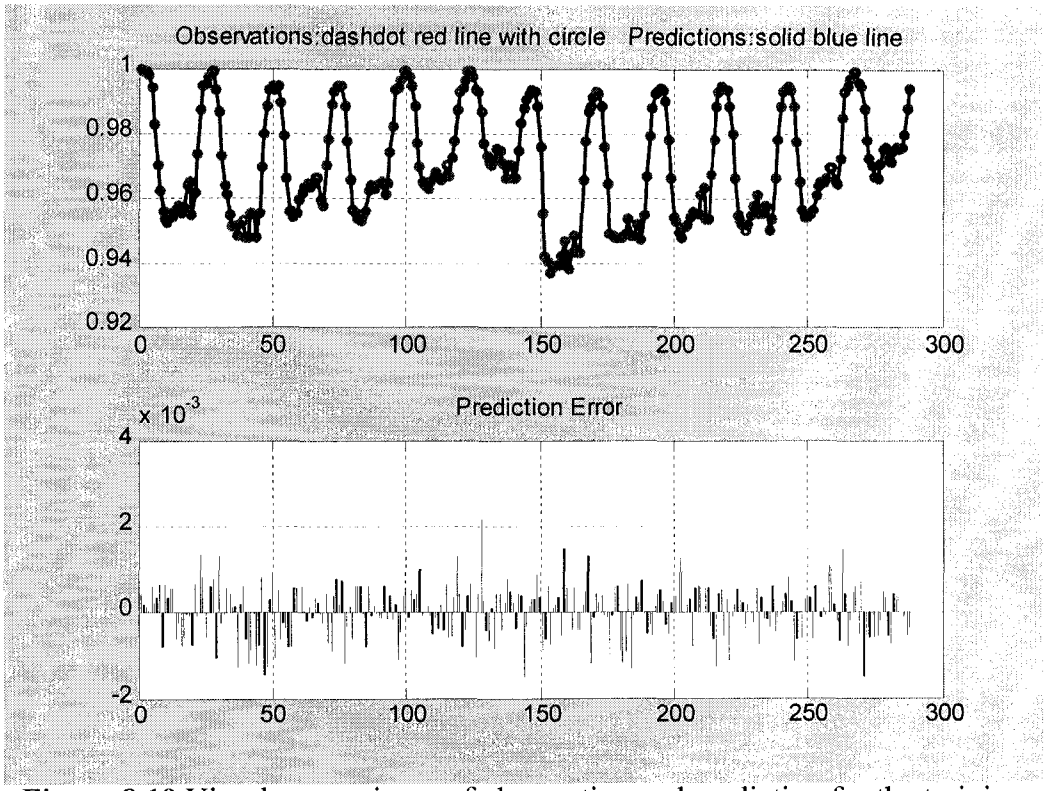

Figure 8.19 Visual comparisons of observation and prediction for the training

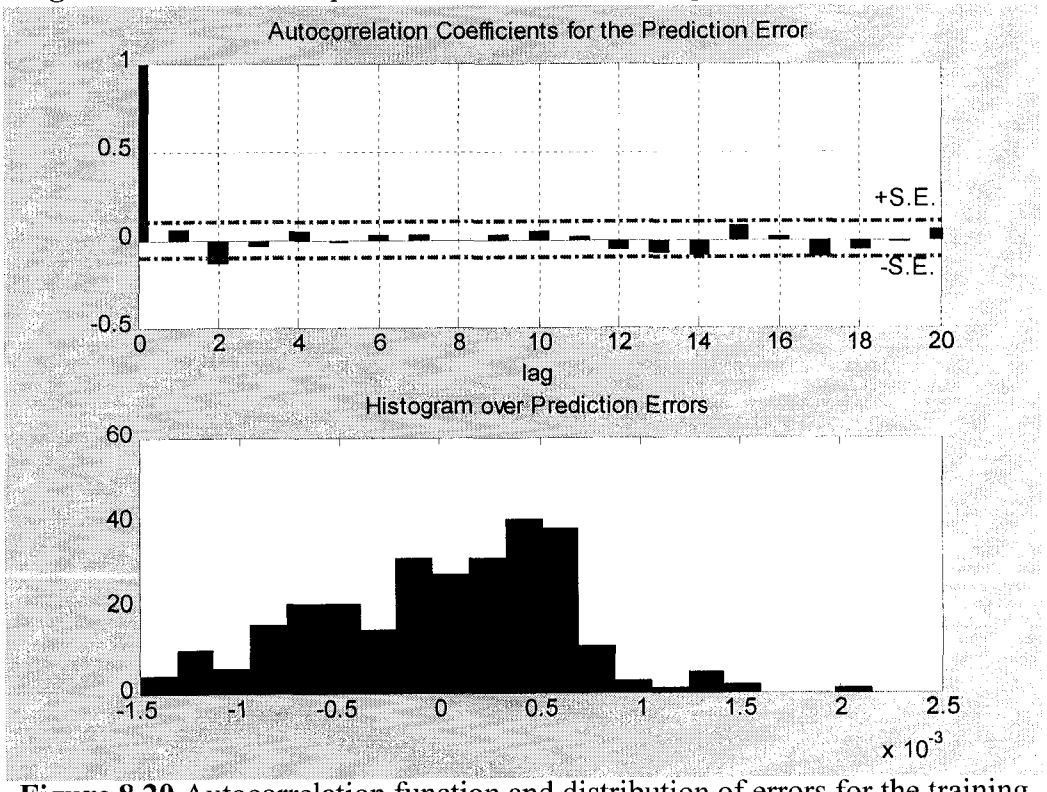

Figure 8.20 Autocorrelation function and distribution of errors for the training

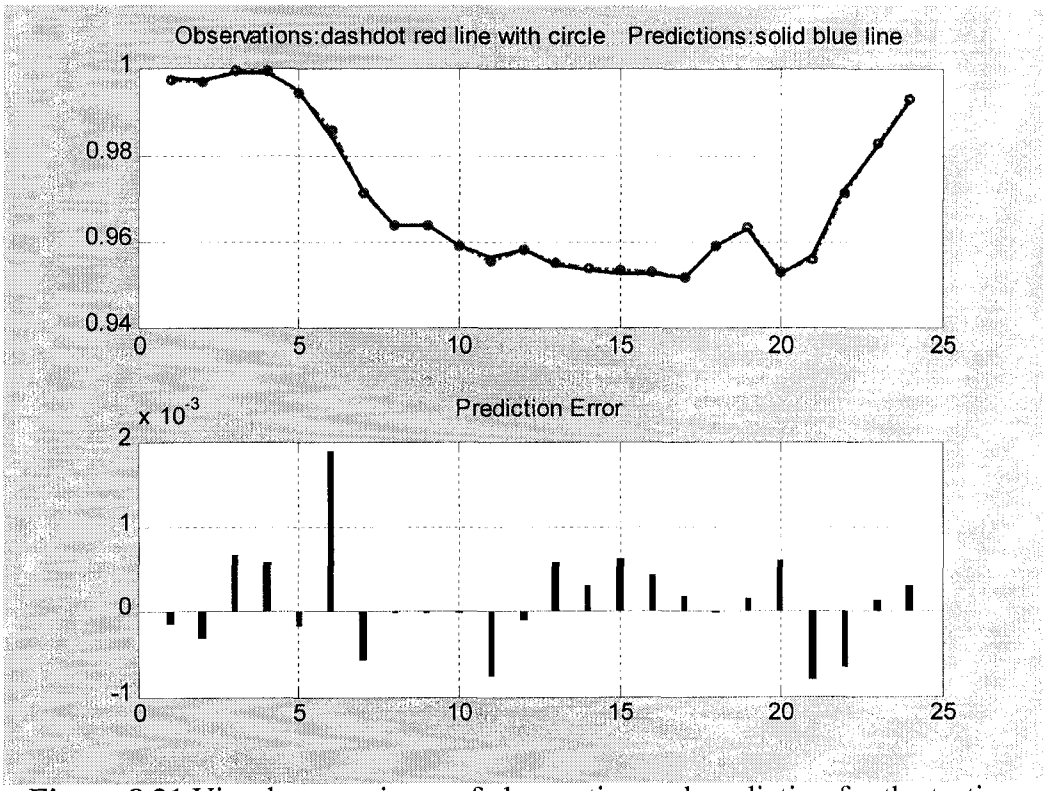

Figure 8.21 Visual comparisons of observation and prediction for the testing

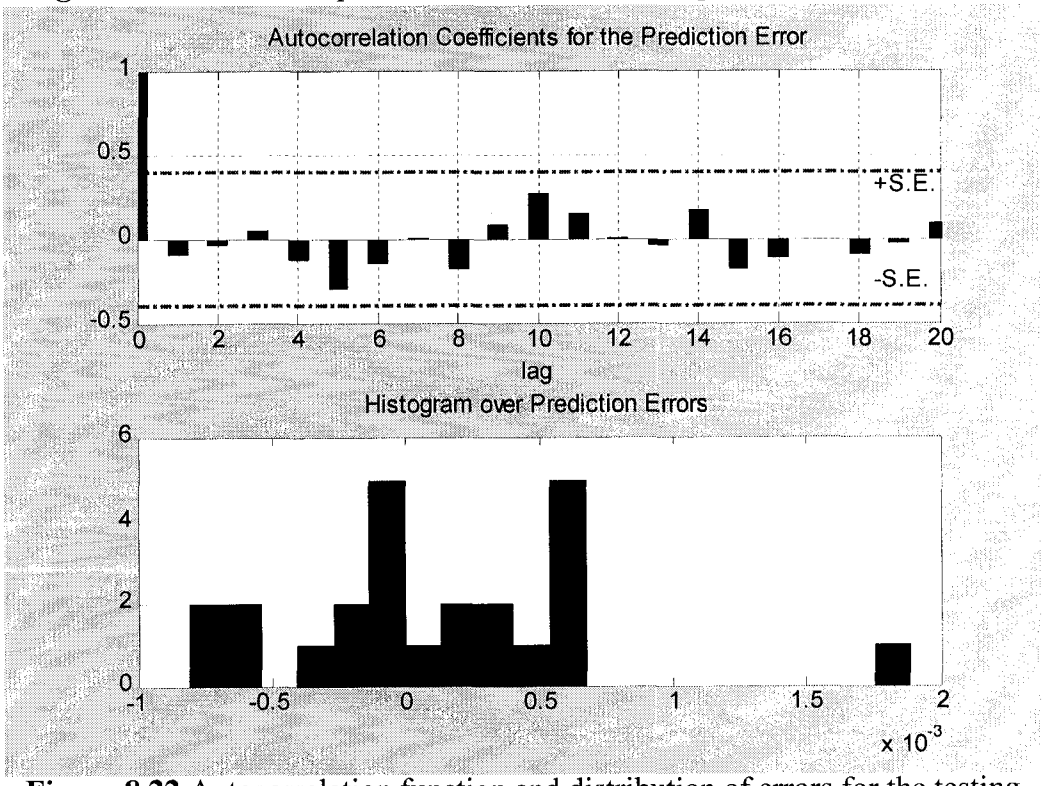

Figure 8.22 Autocorrelation function and distribution of errors for the testing

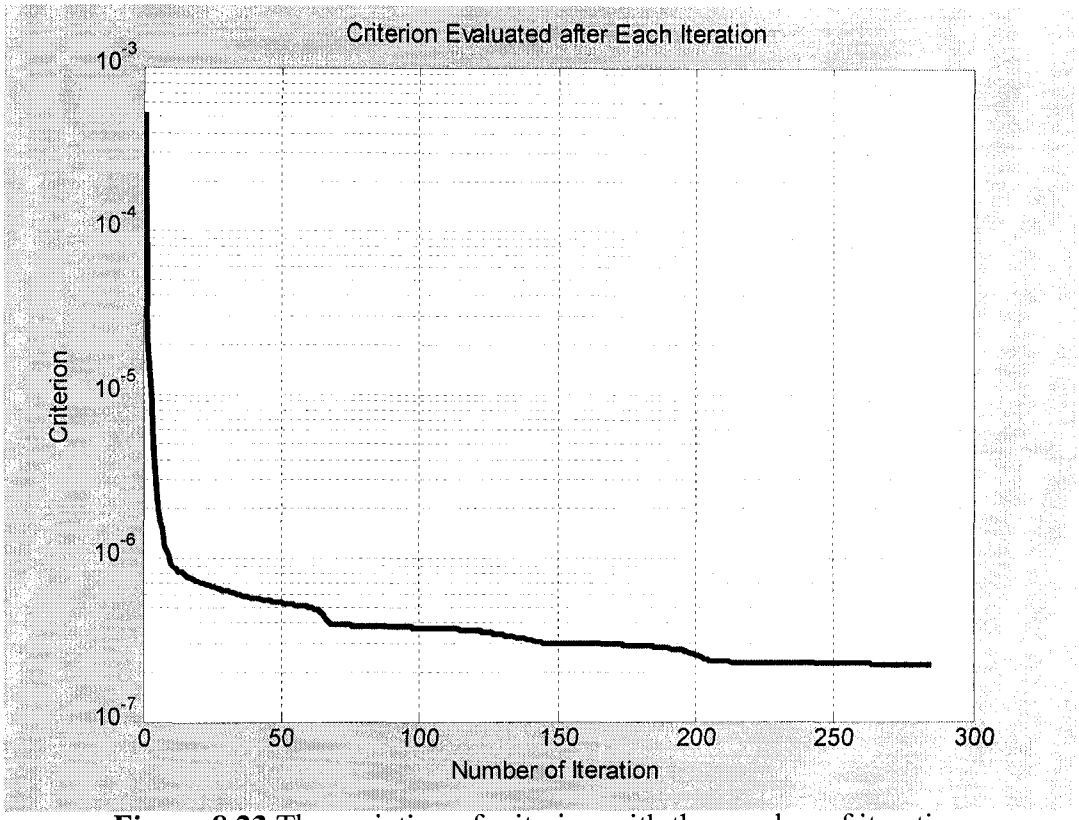

Figure 8.23 The variation of criterion with the number of iteration

A different neural network structure is used to train and predict the steel strain. There are 5 neurons in the hidden layer and the activation function is a hyperbolic tangent. This is still a nonlinear neural network model.

Figures 8.24 and 8.26 show the visual comparisons for the training and for the testing, respectively. Figures 8.25 and 8.27 show the prediction errors and their distribution. Similarly, from the visual comparison and statistical analysis, the prediction of the steel strain with load variation is acceptable.

Figure 8.28 shows the variation of criterion with each iteration number. The algorithm to predict the steel strain converges after 7 iterations, faster than that to predict the aluminum strain. The prediction for steel is not as good as that for aluminum due to high nonlinearity of the steel strain variations.

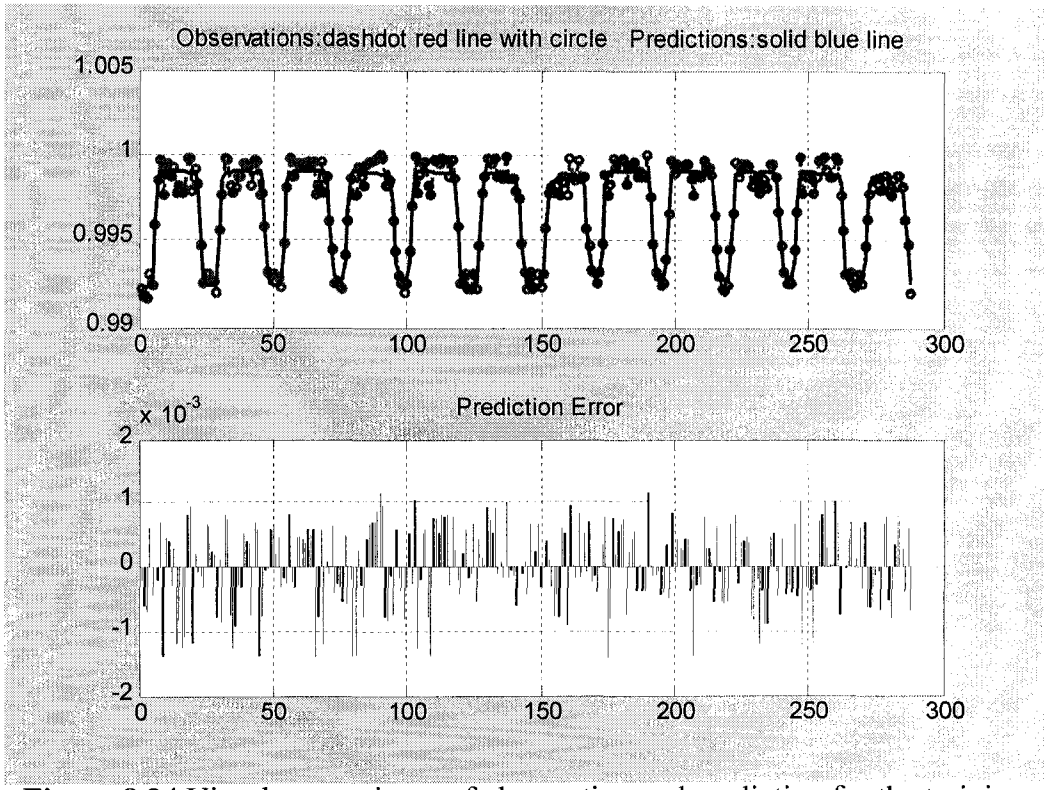

Figure 8.24 Visual comparisons of observation and prediction for the training

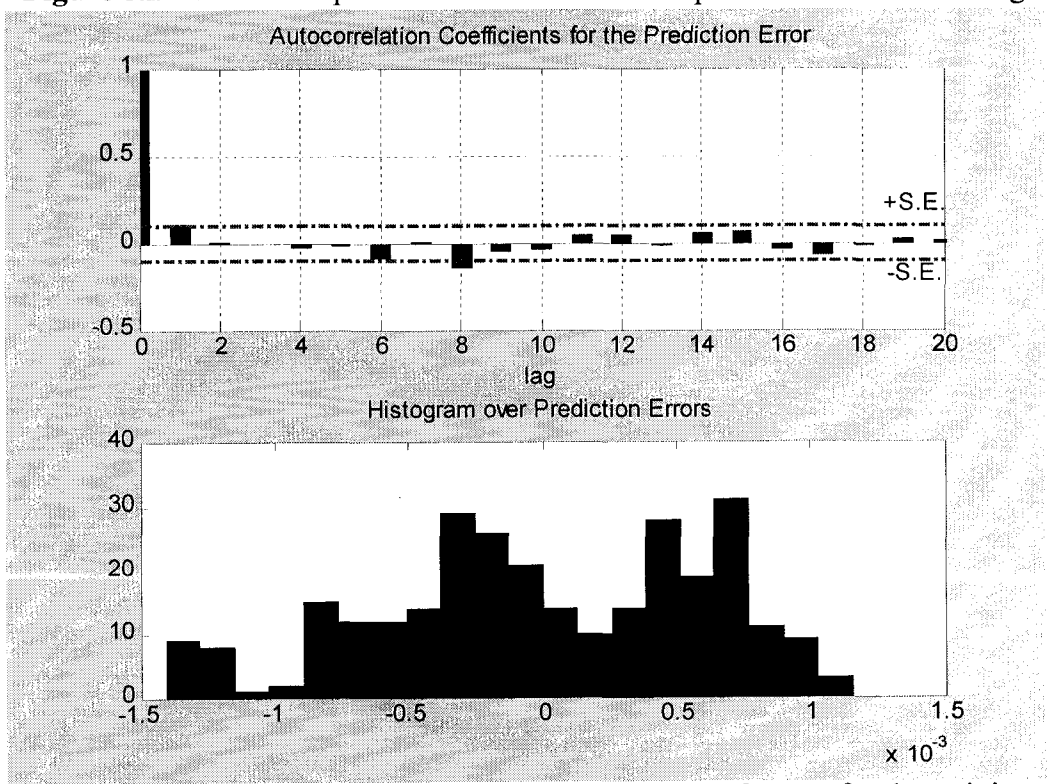

Figure 8.25 Autocorrelation function and distribution of errors for the training

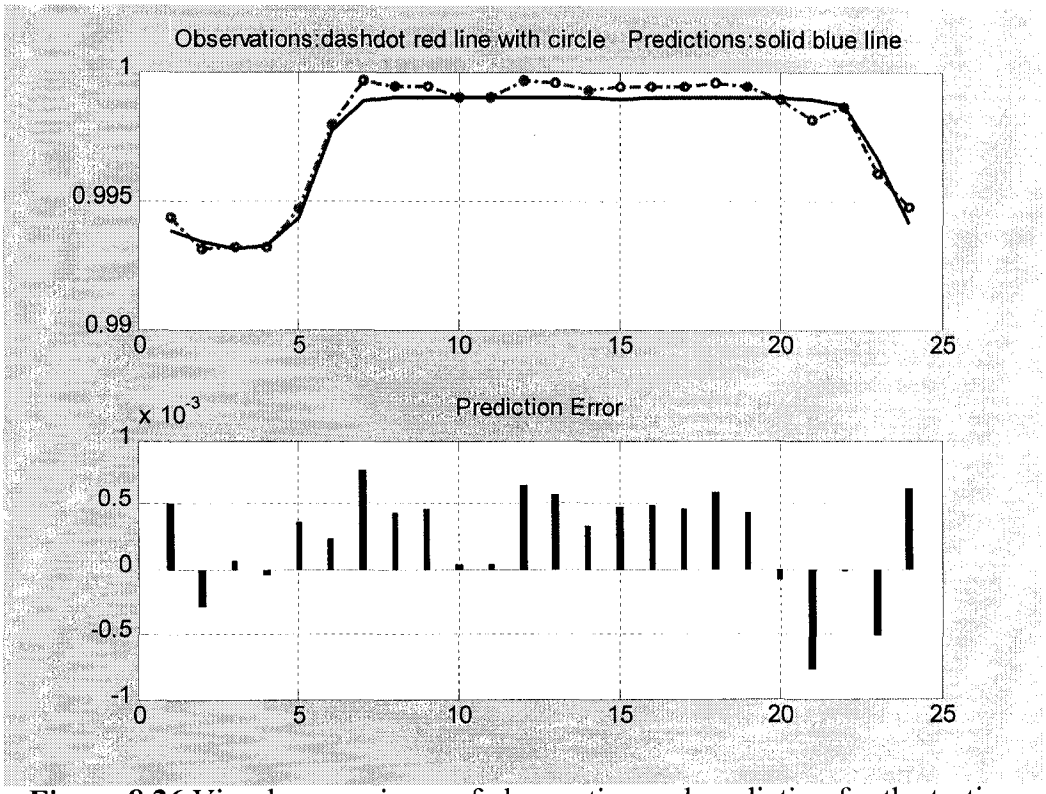

Figure 8.26 Visual comparisons of observation and prediction for the testing

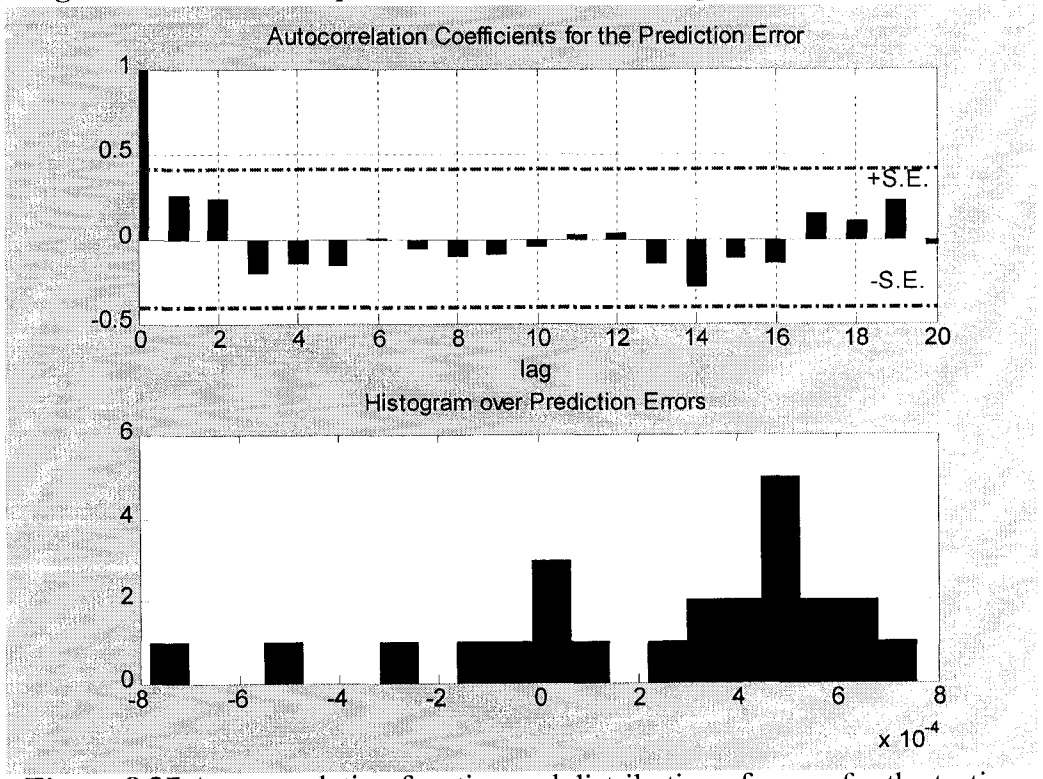

Figure 8.27 Autocorrelation function and distribution of errors for the testing

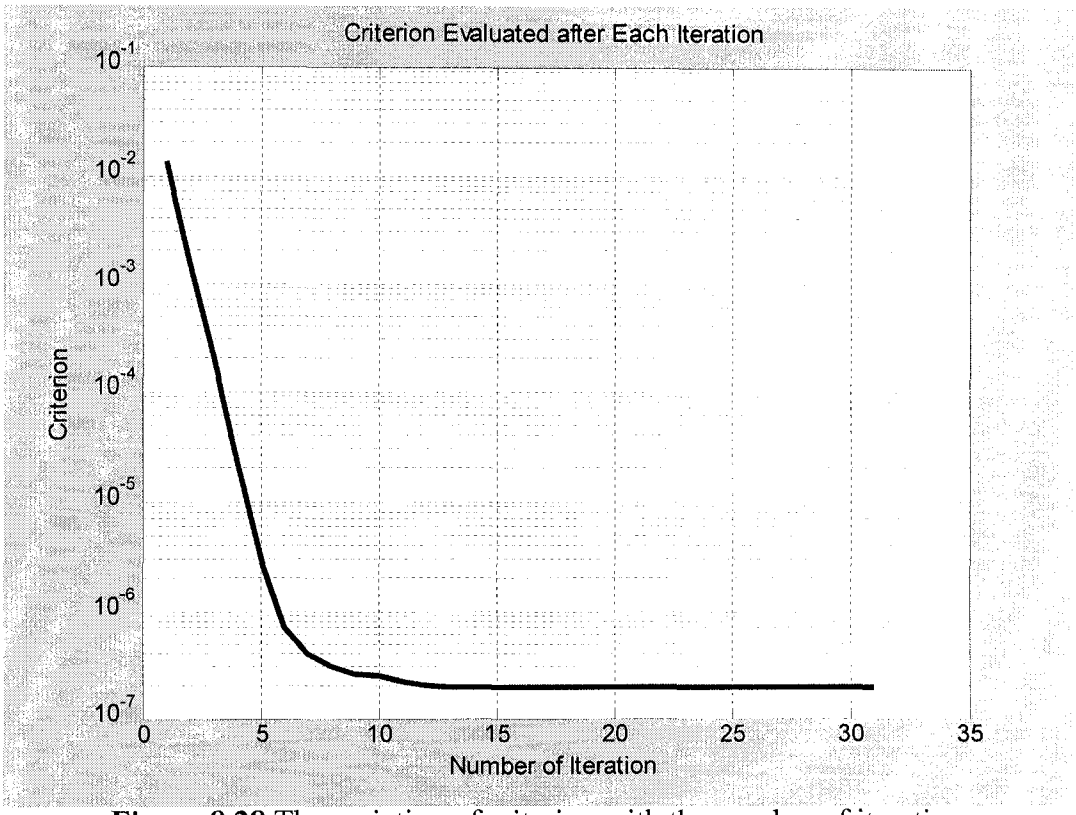

Figure 8.28 The variation of criterion with the number of iteration

8.3.3 Prediction of the Sag

Accurate sag calculation, which involves analyzing the strain or elongation, has been attracting attention for several decades. According to the sag data in Figure 8.13, we can predict the sag directly with the neural network model. The prediction of sag is performed in this part with actual or predicted hourly load input after conductor 55 years exposure time.

There are 13 groups of data in Figure 8.13. 12 of them work as the training dataset and 1 group works as the testing part. With 3 hidden neurons and the hyperbolic tangent activation function, the prediction and visual comparison of the training set is shown in Figure 8.29. The error analysis and distribution is shown in Figure 8.30. The prediction and error analysis for the testing are shown in Figures 8.31 and 8.32, respectively. From the figures we can see the prediction of sag is practically acceptable. Figure 8.33 shows the variation of criterion with each number of iteration. After 10 iterations, the algorithm converges.

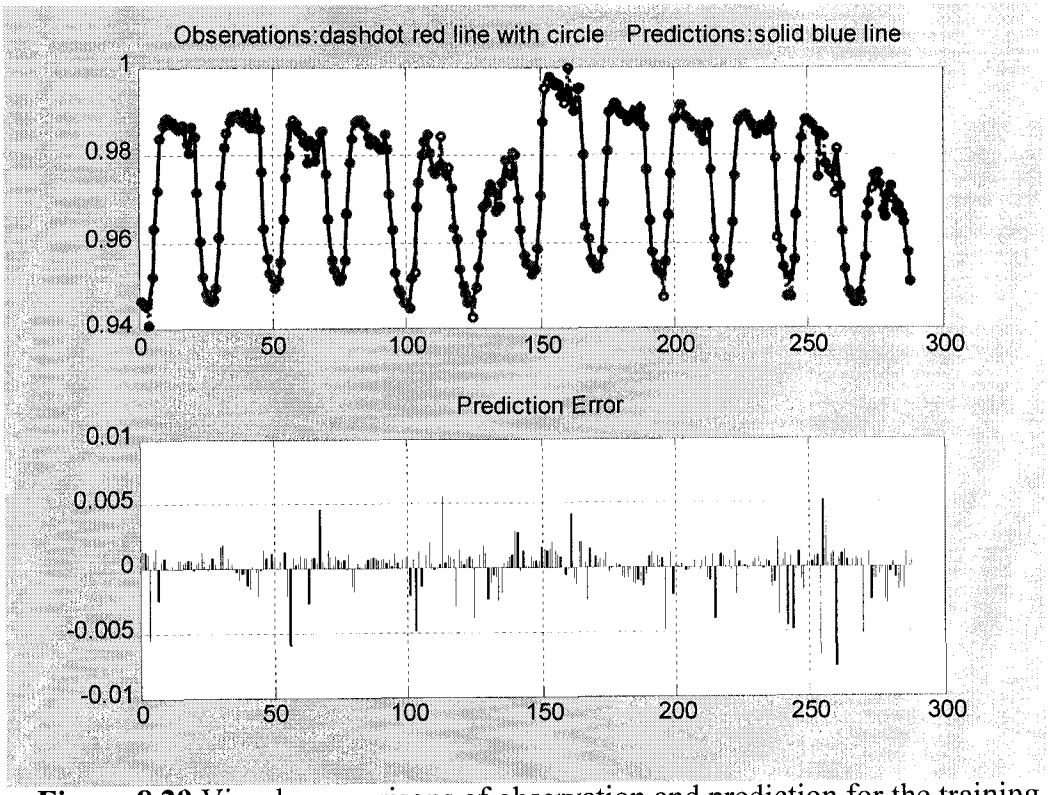

Figure 8.29 Visual comparisons of observation and prediction for the training

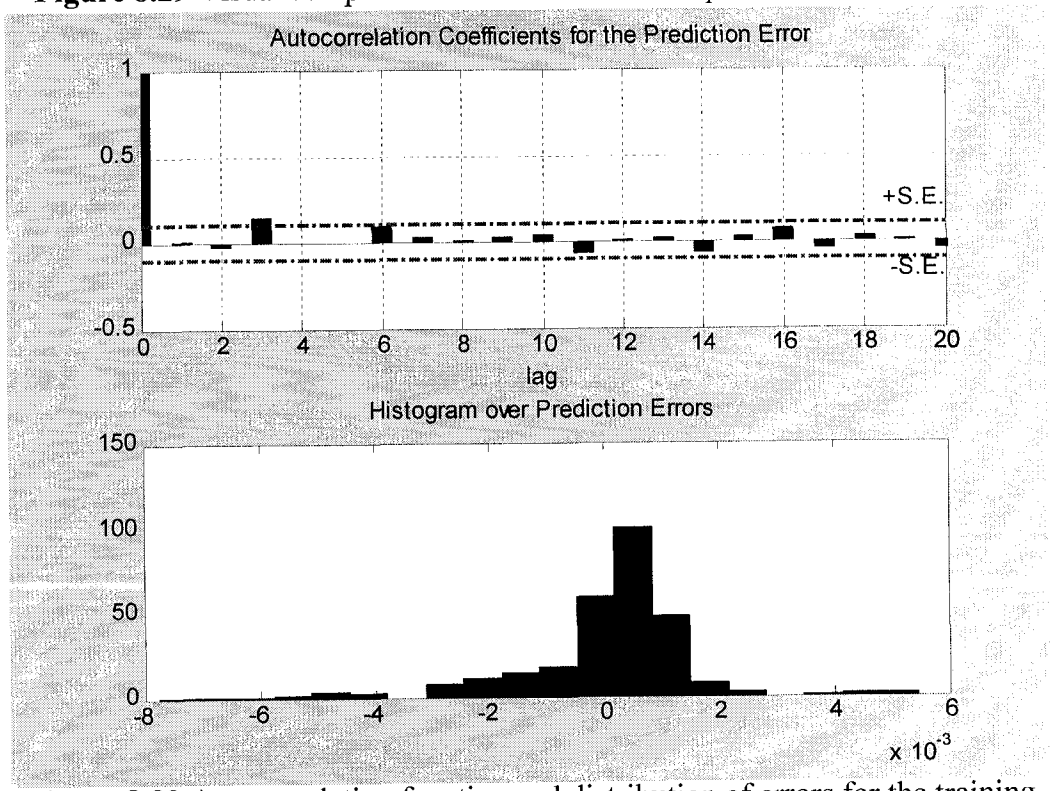

Figure 8.30 Autocorrelation function and distribution of errors for the training

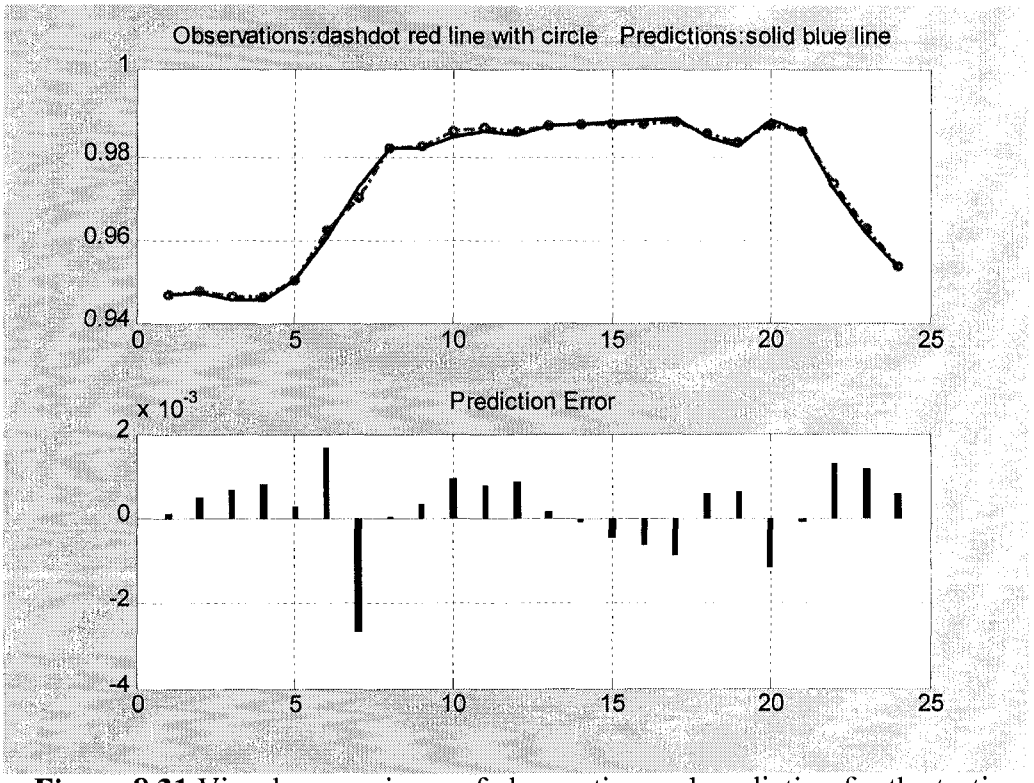

Figure 8.31 Visual comparisons of observation and prediction for the testing

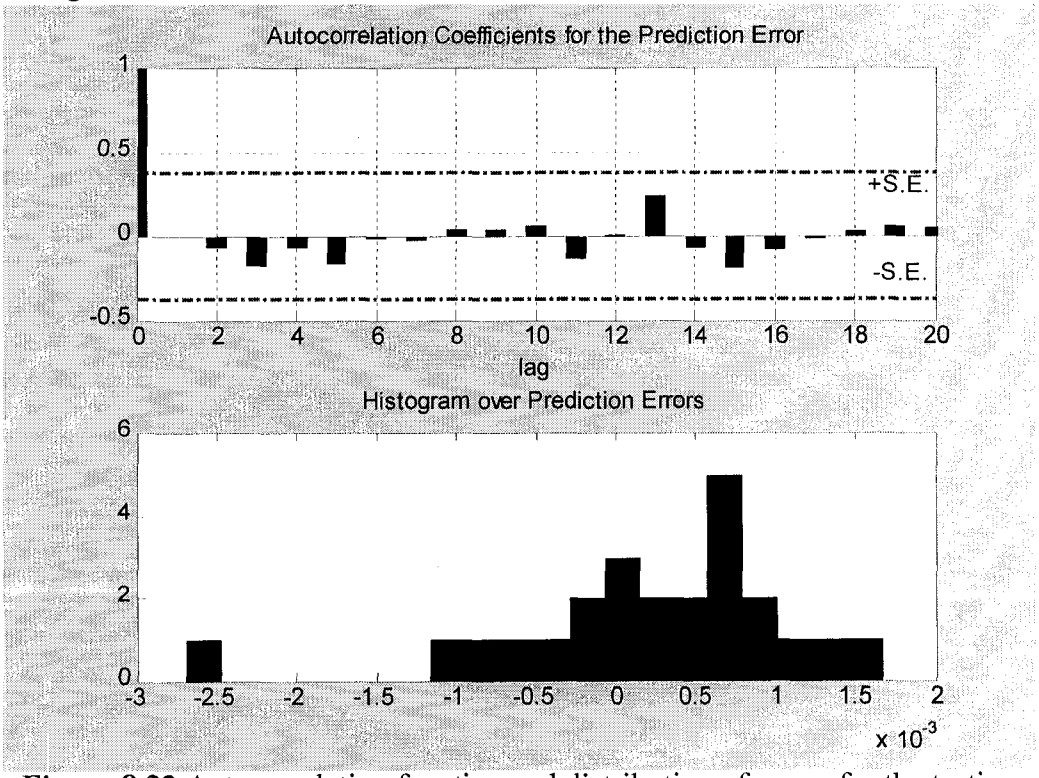

Figure 8.32 Autocorrelation function and distribution of errors for the testing

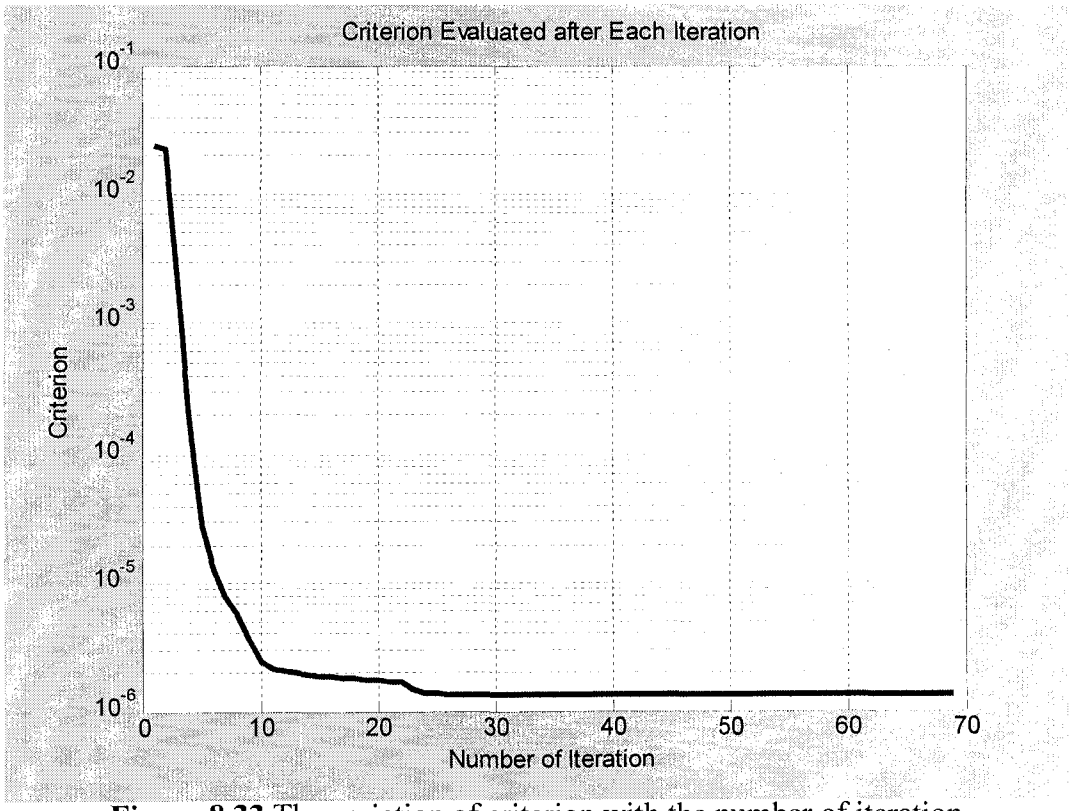

Figure 8.33 The variation of criterion with the number of iteration

CHAPTER 9
CONCLUSIONS

This research has developed and verified the Integrated Model, the physical experimental model, and the artificial neural network model to study and predict the operational behaviors of single layer ACSR conductors.

The Integrated Model is an original work to enable the simultaneous prediction of all aspects of the behavior of single layer overhead ACSR conductors at various conditions. Electromagnetic, mechanical, thermal, and radial conduction models are greatly modified and improved to adapt to the single layer ACSR conductors in the Integrated Model.

The comprehensive physical experimental model has been designed and performed on three different types of single layer ACSR conductors coded as Guinea, Penguin, and Raven to verify the Integrated Model in this research. Electromagnetic properties of aluminum and steel were measured, so was the experimental resistivity of an aluminum wire removed from Penguin. In the physical experiments, as many as possible technical skills were used to ensure that the experimental results were valid.

The good agreement of the results from the Integrated Model and from the experiment shows the effectiveness of the Integrated Model to model single layer ACSR conductors. This Integrated Model can be applied to other single layer ACSR conductors with the similar configurations of Guinea, Penguin, and Raven conductors, for example, Cochin, Dorking, Dotterel, Leghorn, Minorca, Petrel, Pigeon, Quail, Robin, Sparrow, Swan, and Turkey. Their mechanical, thermal, and electromagnetic properties can be obtained in the Integrated Model as a reference for the designer and the manufacturer.

The artificial neural network model has been developed and tested in this research. System identification and statistical techniques are used to build and validate this model. The Levenberg-Marquardt optimization algorithm is used to train the neural network by minimizing the sum-of-squares error. Ontario daily load variation has been successfully forecasted through an implementation of the neural network model.

Discussion and prediction of mechanical properties of single layer ACSR conductors are performed in this research using the Integrated Model and the neural network model. The relationship among mechanical properties including strain, stress, horizontal tension, sag, loss of tensile strength of the aluminum layer due to annealing, etc., is calculated and analyzed. The variation of mechanical properties with the time of duration from year 1 to year 50 and with Ontario daily demands after conductor 55 years service life is also obtained from the Integrated Model. The prediction of mechanical properties involves daily load demands, the creep strain of aluminum, the creep strain of steel, and the sag with daily load variation after conductor 55 years duration time.

The Integrated Model should be a very powerful tool to design new single layer conductors and to improve existing conductors for the reduction of losses, optimization of electrical and mechanical characteristics. This Integrated Model will also be very useful in operations to improve the safety through accurate evaluation of the sag and annealing to decrease power losses and to determine maximum transmissible power.

The discussion and prediction of mechanical properties will help to determine the appropriate operating conditions of existing conductors, and to optimally design new conductors through intensive understanding of conductor mechanical properties. The significance to predict the creep strain of ACSR conductors lies in power system safety because power failure might be avoided with limitation of the creep strain, especially in stormy weather. The design tension expressed from experience as a percentage of rated tension strength is not a very good criterion for new conductors or conductors under different conditions. From a design perspective, aluminum strain would be a better design criterion than tension of the complete conductor since the failure of ACSR conductors is related to the stress or strain of the aluminum wires.

9.1 Conclusions for the Physical Experimental Model

The physical experiment results in the following:

1. Carefully selected probes, especially current density probe, were successfully implemented in the aluminum layer of single layer ACSR conductors. The good agreement of values from the experiment and from the Integrated Model shows the usefulness and validation for both the experimental and the modeling techniques.
2. The saturation current range of single layer ACSR conductors depends on the conductor temperature, the number of steel wires, and the diameter of each wire.
3. The relative complex permeability of the steel core measured in single layer ACSR conductors has the same characteristics as that in three layer ACSR conductors measured by Zhang [8]. The relative complex permeability of the steel core is a function of conductor temperature, tensile stress, and magnetic field strength. It is more sensitive to the variation of the temperature than to the variation of the tensile stress.
4. Measurement of the aluminum resistivity on a test conductor is great asset in modeling to both experiment and the Integrated Model.

9.2 Conclusions for the Integrated Model

The Integrated Model can be used for various conditions. The following can be drawn in simulating the behavior of conductors:

5. To simulate the convection loss for indoor single layer ACSR conductors, both the natural convection and the buoyancy effects are taken into consideration in the Integrated Model. This loss was successfully found as a result.
6. Surface roughness caused by the conductor helical strands is also considered for convective cooling.
7. The lay angle of wires for single layer ACSR conductors is incorporated in the analysis of the ACSR convection heat loss.

- **Conclusions for Electromagnetic Properties**

Some conclusions can be obtained through the implementation of the Integrated Model on Guinea, Penguin, and Raven conductors. Electromagnetic, mechanical, and

steady state thermal characteristics of single layer ACSR conductors are summarized individually as follows:

Steel core losses are necessary to be added in the aluminum layer to predict the electromagnetic performance of single layer ACSR conductors. The loss caused by the eddy current in the steel core is a dominant factor to predict electromagnetic properties of single layer conductors with strong internal electromagnetic field. The analyses show:

8. Spiraling effect, skin effect, and transformer effect are necessary to predict the ac resistance for stranded single layer ACSR conductors.
9. To predict the ac resistance for single layer ACSR conductors, the core losses caused by hysteresis and eddy currents are found in the aluminum layer and used to calculate the longitudinal flux in the steel core.
10. The more steel wires, the higher the ac/dc resistance ratio is. The larger the steel wire diameter, the higher the ac/dc resistance is. The ac/dc resistance ratio for Guinea conductor reaches as high as 1.99 which means that the power losses in this type of single layer ASCR is appreciable and cannot be neglected in engineering practice.
11. Single layer ACSR conductors reach saturation within its thermal ratings, so modeling techniques for single layer ACSR conductors should consider the saturation. Three layer ACSR conductors do not reach saturation within their maximum current ratings [1, 4].
12. The geometrical parameters affect the distribution of the total current in the single layer ACSR conductors. For Guinea at 390 A, 87 % of the total current injects into the aluminum layer while 13 % of the total current leaks through the steel core. For Penguin at 470 A, and Raven at 300 A, 96 % of the total current goes through the aluminum layer and 4 % leakage in the steel core.

- **Conclusions for Mechanical Properties**

The mechanical properties are affected by the geometrical structure of the conductor. Comparing the mechanical properties among Guinea, Penguin, and Raven, we have:

13. The thinner the wire diameter, the greater the aluminum stress decreases. The stress of the aluminum layer for Raven conductor changes fastest during the conductor current ratings among the three kinds of single layer ACSR conductors.
14. The steel core is supposed to carry most tension for the complete ACSR conductor. This is the case for three-layer ACSR whose aluminum layer carries tension less than 20 MPa. For single layer ACSR, the aluminum layer carries higher tension than that for three-layer ACSR. The stress experienced by the aluminum layer for Guinea conductor is 33 MPa at 100 A, for Penguin, 85 MPa at 100 A, and for Raven, 101 MPa at 100 A.
15. The heavier the conductor, the higher the horizontal tension is. The horizontal tension of Guinea conductor is the largest among the three because it has the heaviest weight among the three.
16. The accumulating loss of tensile strength of the aluminum layer is affected significantly by the conductor temperature. For a fixed current rating, Raven

conductor has the largest loss of tensile strength in its aluminum layer because it has the highest conductor operating temperature among the three types of single layer conductors tested.

17. The loss of tensile strength of single layer ACSR conductors reaches over 30 % under 20 °C ambient temperature at their maximum current ratings. The loss of tensile strength of three layer ACSR conductor Grackle is only 20 % at its maximum current rating under 20 °C ambient temperature [4].

- **Conclusions for Thermal Properties**

The steady state heat transfer model and the radial conduction model are affected significantly by the geometrical and environmental parameters. We can obtain some thermal properties for single layer ACSR conductors from the Integrated Model:

18. The solar heat gain depends on the diameter of the conductor, position of the area, and specific time of the year.
19. The resistive or Joule heating is a function of ac resistance and the current. The larger the current, the higher the conductor temperature, the larger the resistive heating is.
20. The convective heat cooling is a function of the conductor temperature and the ambient temperature, so is the radiative cooling. The radiative cooling is around one third of the total cooling for single layer ACSR conductors.

- **Conclusions for the Investigations with Variant Parameters**

The investigation of the Integrated Model shows the influences on electrical, thermal, and mechanical properties of single layer conductors with parameters as the lay length, ambient temperature, power supply frequency, time of exposure, air gap thickness, and span length in this research.

(1) Conclusions for the Influence of Variant Lay Lengths

The properties of single layer ACSR conductors are greatly affected by the lay length of the aluminum layer. Observations regarding the influence of the variant lay lengths can be summarized as follows:

21. The longer the lay length, the smaller the ac resistance and the ac reactance. The ac/dc resistance ratio decreases with the increase of the lay length. Increasing lay length is a reasonable way to improve energy transmission efficiency and to reduce distribution or transmission losses for overhead bare single layer ACSR conductors.
22. A longer lay length results in lower conductor temperature. Also, saturation of the steel strand occurs at relatively larger conductor currents.
23. A longer lay length results in lower convective heat cooling and lower radiative cooling.
24. Loss of tensile strength decreases as well as the increase of the lay length with lower conductor surface temperature.

25. The mechanical properties of Penguin and Raven conductors are not affected as much as those of Guinea conductor by the variation of the lay length. For Penguin and Raven, the variation of the stress of the aluminum layer at various lay lengths is more obvious than the variation of other mechanical properties.
26. The variation of the mechanical properties is affected by the number of steel strands of the conductor at various lay lengths.

(2) Conclusions for the Effects of the Ambient Temperature

The effects of the ambient temperature are as follows for single layer ACSR conductors:

27. AC resistance and ac reactance increase when the ambient temperature increases.
28. The convective heat cooling is not very sensitive to the variation of the ambient temperature, but the radiative cooling is.
29. The mechanical properties of single layer ACSR conductors are greatly affected by the variation of the ambient temperature. The aluminum stress and the horizontal tension decrease with the increases of the current and the ambient temperature. The sag increases with the increase of the ambient temperature.
30. The accumulated loss of the aluminum layer due to annealing increases dramatically at the maximum current rating when the ambient temperature reaches 30°C. The determination of the maximum current rating in some areas with high ambient temperature should be paid much attention to.

(3) Conclusions for the Influence of Supply Frequency

The operational behaviors of single layer ACSR conductors are greatly affected by the supply frequency:

31. AC resistance and ac reactance are affected by the variation of supply frequencies. When the supply frequency increases, the additional resistance caused by core losses and the current redistribution increases and it results in higher resistive heating in the conductor.
32. The higher the frequency, the larger the ac to dc resistance ratio.
33. The convective heat cooling and the radiative cooling increase with the increase of the frequency at a fixed current rating.
34. The mechanical properties are also affected by change in frequency. The stress of the aluminum layer and the horizontal tension decrease with an increase of the frequency. The sag increases with an increase of the frequency. The aluminum layer loses tensile strength with an increase of the frequency.

(4) Conclusions for the Influence of the Time of Exposure

Electromagnetic properties remain invariant with an increase of exposure time. Observations regarding the influence of the time of exposure are as follows:

35. The stress of the aluminum layer and the horizontal tension decrease with an increase of the time of exposure, fastest during the first year of the exposure time.
36. The sag increases with an increase of the time of exposure.
37. The loss of tensile strength of the aluminum layer increases with an increase of the exposure time. The accumulating loss increases largely after one year exposure.

(5) Conclusions for the Influence of the Air Gap

Resistance and reactance remain constant with various thicknesses of the air gap. Other observations regarding the influence of the thickness of the air gap are as follows:

38. The stress of the aluminum layer and the horizontal tension remain constant with the variation of the thickness of the air gap except for Raven conductor at 300 A.
39. The sag remains constant with the variation of the air gap thickness except for Raven conductor at 300 A.
40. The accumulating loss of tensile strength of the aluminum layer remains constant for three types of single layer ACSR conductors with the variation of the air gap thickness.

(6) Conclusions for the Influence of the Span Length

The variation of the span length does not alter the electrical characteristics of single layer ACSR conductors. Observations regarding the influence of the span length are as follows:

41. Generally speaking, the stress of the aluminum layer and the horizontal tension increase with an increase of the span.
42. The sag increases dramatically with an increase of the span.
43. The accumulated loss of tensile strength of the aluminum layer remains constant with the variation of the span at a fixed current rating.

- **Conclusions for the Sensitivity Analysis**

The sensitivity analysis of the Integrated Model shows:

44. The Integrated Model is most sensitive to a variation of diameter and of lay length of the aluminum layer, and least sensitive to a variation of surface layer temperature.
45. From the point view of resistance, resistive heat, convection heat loss, and radiation heat loss, the most to least sensitive factors are aluminum wire diameter, aluminum resistivity, lay length, frequency and permeability, steel resistivity, surface layer temperature. Among them, the sensitivity level of permeability and supply frequency is almost the same.
46. From the point view of reactance, the most to least sensitive factors are lay length, the supply frequency, permeability, aluminum wire diameter, steel resistivity, aluminum resistivity, and surface layer temperature.

9.3 Conclusions for the Artificial Neural Network Model

The following can be drawn from the neural network modeling:

47. Trade-off between bias and variance components in the generalization error of the neural network was tested in this research and the neural network topology selection helps to avoid overfitting or underfitting in implementations.
48. Both visual comparisons and statistical techniques such as residual analyses are necessary to validate the neural network model. Only with visual comparisons, it is not easy to determine how good or how bad the model is. Only with statistical tests, there is possibility to accept an incorrect model because it is impossible to qualify the risk of accepting it.

9.4 Conclusions for the Prediction of the Daily Load Variation in Ontario

In the implementation of the neural network model to predict daily load variation in Ontario, pre-processing of the input variables is necessary as required by the majority of neural network applications. Correspondingly, post-processing of the output of the neural network needs to be done to convert to the required form.

49. The mean and seasonality should be removed from the time-series input variables before they are trained by the neural network structure as performed in this research.
50. The daily load prediction is practically acceptable based on validation techniques. It can be used in optimal and efficient energy management.

9.5 Conclusions for Discussion and Prediction of Mechanical Properties

Discussion and prediction of mechanical properties of single layer ACSR results in the following:

51. The elongation of ACSR is caused by creep, cold work during stranding, conductor temperature, and the material itself. The stress decreases and sag increases with an increase of current resulting from the variation of elongation.
52. The analysis of mechanical properties with long time of exposure shows that the cumulative creep strain is the determinate factor to cause the elongation. The loss of tensile strength of the aluminum layer is greatest in the first ten years.
53. The prediction of mechanical properties such as the strain and sag with actual daily load demands after 55 years duration has been achieved through applications of the neural network model.

9.6 Future Work

Further development and improvement of the Integrated Model should include the verification and comparison of the results from simulations and from experiments in mechanical properties and thermal properties for single layer ACSR conductors.

Kim and Morcos [52] state that "presently, a large number of ACSR conductors have exceeded their forecasted useful life". The conductors used on Ontario Hydro's

lines built before 1950 are mainly ACSR conductors. Most of them have exceeded their 50-year design life [53]. The average service life of ACSR conductor predicted by Havard et al. [54] varies between about 67 and 77 years depending on the local contamination level. The remaining life prediction of ACSR conductors will be of great use in practical determination of service life. The prediction can be completed when the experimental data is available from Ontario's Hydro One.

Most of the original lines built in Central Iowa, the United States, in the 1940's and 1950's, have 3/0 ACSR, 6/1 conductors [55]. Central Iowa Power (CIPCO)'s service territory has a rich history of damaging ice and wind storms, and since 1987, CIPCO has been rebuilding and upgrading approximately 30 miles of 34.5 kV lines each year [55]. For example, 266.8 ACSR 26/7 (Partridge) and 397.5 ACSR 26/7 (Ibis) are being replaced by 1/0 ACSR 6/1 (Raven) and 4/0 ACSR 6/1 (Penguin) [55].

To satisfy the increasing need of energy demand in industrialized countries, traditional ACSR conductors are modified or improved with the gap-type aluminum conductor steel reinforced (GTACSR) [56] or with trapezoidal O'-tempered aluminum wires helically wound around a hybrid glass/carbon composite core produced by pultrusion (ACCC/TW) [57]. To analyze those newly developed conductors, the linked electromagnetic, thermal and mechanical properties proposed and developed in this research are still useful.

APPENDIX A

MEASURING INSTRUMENTS

A.1 Thermocouple

The thermocouple we selected is type T: copper (+) versus constantan (-). The limits of error for the common letter designated thermocouple types are taken from ASTM E 230 [58]. Most manufacturers supply thermocouples and thermocouple wire to these limits of errors or better. From the product description of OMEGA Company, we know that the maximum temperature useful range of T-type thermocouple is from - 200 °C to 370 °C, and the limit of error is 1.0 °C or 0.75 % above 0 °C.

These T-type thermocouples are resistant to corrosion in moist atmospheres and are suitable for subzero temperature measurements. Their use in air or in oxidizing environments is restricted to 370 °C (700 °F) due to oxidation of the copper thermo-element. They can be used in a vacuum and in oxidizing, reducing or inert atmospheres over the temperature range of - 200 to 370 °C (- 330 to 700 °F). This is the only thermocouple type for which limits of error are established in the subzero temperature range. [59]

The type T temperature-emf relationship and tables presented in ASTM E230 [58] are the results of empirical data developed by National Bureau of Standards (NBS) from experimental data on real type T thermocouples from several sources and including several sizes of wire. These documents present statistical information believed to represent the typical type T thermocouple. ASTM E220 [60] provides calibration methods to reduce the uncertainty which can be realized, especially at low temperatures. We assumed the thermocouples that we bought from OMEGA Engineering Incorporation meet the requirements stated in the ASTM standard.

A.2 Fluke 2240C Data Logger

The Fluke 2240C data logger was used to record the temperature through thermocouples. The thermocouple itself is very cheap and simple in construction. The indicating instruments are usually quite elaborate. Fluke 2240C data logger is compatible with IEEE Standard 488-1978, including Fluke DVM's, counters, calibrators, synthesizers, printers, and a 1720A controller. In the temperature range of -130°C to 400°C and for thermocouple type "T", the system precision of 2240C data logger is ±0.5°C. It can be operated in conjunction with other instruments compatible with the same standard. Fluke 2240C meets requirements of MIL-T-28800 for the shock and vibration. Fluke 2240C needs one hour to warm up, and one hour later it reaches its full accuracy and accuracy reduced by 0.02 % of range on initial turn-on. In this physical experiment, the actual measurement was performed one hour later after Fluke 2240C was turned on.

A.3 HP 3575A Gain-Phase Meter

The Hewlett-Packard Model 3575A gain-phase meter is used to record the phase difference between the probe voltage and the conductor current. An accurate phase meter is of little value unless the precision can be maintained in the presence of noise and distortion. Unlike conventional phase meters, the 3575A uses two phase detectors rather than a single phase detector. This, in conjunction with a highly effective error correction scheme, greatly reduces the effects of noise and distortion on phase readings.

When phase display is selected, the 3575A measures the phase difference between two input signals. The phase measurement range is from -180 degrees to 180 degrees with 12 degrees overrange and 0.1 degree display resolution. Due to the wide dynamic range of the instrument, phase difference can be measured between two signals that differ in amplitude by as much as 100 dB.

When phase measurement is performed:
Error introduced by noise: < 2 degrees for a 1 V rms 10 KHz sine wave.
Error introduced by distortion:

Even harmonics: cancelled, no error

Odd, in-phase harmonics: no error

Odd, out-of-phase harmonics: < 0.6 degrees when total odd harmonic distortion is more than 40 dB below the fundamental.

A.4 Digital Multimeters and Ruler

The BBC M2110 multimeter was made in West Germany. For dc voltage measurement within 300 mV, the precision reaches $\pm(0.05\% + 2Dig.)$. When dc voltage is from 3 V to 1000 V, the precision is within $\pm(0.05\% + 1Dig.)$. For ac voltage measurement, the precision is $\pm(0.25\% + 20Dig.)$. If this multimeter is used to measure ac current, the precision is $\pm(0.5\% + 20Dig.)$. The precision is $\pm(0.35\% + 2Dig.)$ when measuring dc current.

The BBC M2110 multimeter has 4.5 digits precision. HP 3435A multimeter has 3.5 digits precision. Generally speaking, the more digits, the more accurate the multimeter is. The less accurate HP 3435A is used in our experimental error analysis. The HP Model 3435A is a 3.5 digit, five functions, autoranging multimeter. When it works as ac voltmeter and "200 mV" range is selected, the maximum display is 199.9 mV. The maximum error is 0.5 mV.

The ammeter made by Conway Electronic Enterprises was chosen to measure current in this physical experiment. The ammeter shows "0, 5" class for alternating current measurement. "0, 5" class means 5 % error of the full scale. We chose 5 A scale in the experiment, and the maximum error is 5*5% = 0.25 A. The ratio used in our experiment is 100, so the maximum error for current should be 0.25*100 = 25 A.

The length of probe was measured by a scaled ruler. The minimum scale of the ruler is 0.159 cm (1/16 inch).

A.5 Measuring Instruments with DC Source

The following instruments were involved:

- PFA Telfon insulated T-type 24 AWG thermocouple: limit of error is 1.0 °C above 0 °C
- Fluke 2240C data logger: system precision is ± 0.5 °C
- BBC M2110 Multimeter: 300 mV dc range, ± (0.05 % + 2 Dig.)
- BBC M2110 Multimeter: 20 A dc range, ± (0.35 % + 2 Dig.)
- Ruler: scale accuracy in 1 mm
- Caliper: scale accuracy in 0.01 mm

REFERENCES

[1] W. A. Lewis and P. D. Tuttle, "The Resistance and Reactance of Aluminum Conductors, Steel Reinforced", Trans. A.I.E.E, Vol. 77, part III, Feb. 1959, pp. 1189 - 1215.

[2] L. W. Matsch and W. A. Lewis, "The Magnetic Properties of ACSR Core Wire", AIEE Transactions, Vol. 77, part III, 1958, pp.1178-1189.

[3] D. A. Douglass, L. A. Kirkpatrick, and L. S. Rathbun, "AC Resistance of ACSR - Magnetic and Temperature Effects", Task Force of the IEEE Working Group on Calculation of Bare Overhead Conductor Temperature, (B.S. Howington, Chairman), IEEE Trans. on Power Apparatus and Systems, Vol. PAS-104, No. 6, June 1985, pp. 1578-1584.

[4] Visnja Filipovic-Gledja, "A Probability Based Unified Model for Predicting Electrical, Mechanical and Thermal Characteristics of Stranded Overhead-line Conductors", Ph.D. Thesis, McMaster University, 1997

[5] V. Filipovic-Gledja; V. T. Morgan and R. D. Findlay, "A Probability Based Unified Model for Predicting the Electrical Mechanical and Thermal Characteristics of Stranded Overhead-Line Conductors", Proceedings of the 1994 Canadian Conference on the Electrical and Computer Engineering, Vol. 1, September 1994, pp. 182-185.

[6] J. S. Barrett, O. Nigol, C. J. Fehervari and R. D. Findlay, "A New Model of AC Resistance in ACSR Conductors", IEEE Trans. on Power Systems, Vol.PWRD-1, No.2, April 1986, pp. 198- 208.

[7] R. D. Findlay and D. T. Jones, "Modeling Techniques for Single-Layer Conductors with Steel Reinforcing", IEEE PES Summer Meeting, Portland, OR, July 18-23, 1976, A76 434-1.

[8] B. Zhang, "A Study of the Magnetic Properties of ACSR Core Wire with the Objective of Reducing Transmission Losses". Master Thesis, McMaster University, 1996.

[9] "Aluminum Electrical Conductor Handbook", the Aluminum Association, Second Edition, 1982.

[10] L. Rong, "A Study of the Electrical and Magnetic Properties of Single Aluminum ACSR Guinea". Master Thesis, McMaster University, 2001

[11] L. Xue, "An Improved Unified Model of ACSR". Master Thesis, McMaster University, 1998.

[12] D. Brocilo, "Modifications of COOLTEMP Program: An Analysis and Prediction Program for Aluminum Conductor, Steel Reinforced (ACSR)". Master Thesis, McMaster University, 1999

[13] CIGRE WG 22-05, "Predictor Equations for Creep of Conductors", Electra, No. 75, 1981, pp. 63-98.

[14] J. S. Barrett, S. Dutta and O. Nigol, "A New Computer Model of ACSR Conductors", IEEE Trans. on Power Apparatus and Systems, Vol. PAS-102, 1983, pp. 614-621.

[15] J. S. Barrett, "Optimization of Conductor Design", IEEE Transaction on Power Delivery, Vol.4, No.1, 1989, pp. 453-463.

[16] O. Nigol and J. S. Barrett, "Characteristics of ACSR Conductors at High Temperatures and Stresses", IEEE Trans. on Power Apparatus and Systems, Vol. PAS-100, No. 2, 1981, pp. 485-493.

[17] O. Nigol and J. S. Barrett, "Development for an Accurate Model of ACSR Conductors for Calculating Sags at High Temperatures – Part I", Report for the Canadian Electrical Association, Hydro One, Nov. 1980.

[18] M. J. Sinnott, "The Solid State for Engineers", John Wiley & Sons. Ltd, 1958

[19] V. T. Morgan, "Effect of Elevated Temperature Operation on the Tensile Strength of Overhead Conductors", IEEE Trans. on Power Delivery, Vol. 11, No.1, January, 1996

[20] ASTM Designation: B 232M-97 "Standard Specification for Concentric-Lay-Stranded Aluminum Conductors, Coated Steel-Reinforced (ACSR)" Annual Book of ASTM Standard, Vol.02.03

[21] V. T. Morgan, "Electrical Characteristics of Steel-cored Aluminum Conductors". PROC. IEE, Vol. 112, No. 2, 1965

[22] V. T. Morgan, "Thermal Behaviour of Electrical Conductors, Steady, Dynamic and Fault Current Ratings" Research Studies Press, John Wiley & Sons, 1991.

[23] R. D. Findlay, "Electromagnetic and Thermal Field Distributions in an Induction Heating System." Ph.D. Thesis - University of Toronto, 1968.

[24] V. T. Morgan and C. F. Price, "Magnetic Properties in Axial 50 Hz Fields of Steel Core Wire for Overhead-Line Conductors", Proc. IEE (London), Vol. 116, No. 10, October 1969, pp. 1681 – 1694.

[25] V. T. Morgan, B. Zhang and R. D. Findlay, "Effects of Temperature and Tensile Stress on the Magnetic Properties of a Steel Core from an ACSR Conductor", IEEE Transactions on Power Delivery, Vol. 11, No. 4, 1996, pp. 1907-1913.

[26] IEEE Std 738-1993 "IEEE Standard for Calculating the Current-Temperature relationship of Bare Overhead Conductors", ISBN 1-55937-338-5.

[27] V. T. Morgan, "The Thermal Rating of Overhead-line Conductors. Part I, The Steady-State Thermal Model", Elec. Power Sys. Res., Vol. 5, 1982, pp. 119-139.

[28] S. Goldstein, "Modern Developments in Fluid Dynamics". Vol. 1, Clarendon, Oxford, 1938

[29] S. C. R. Dennis and G. Z. Chang, "Numerical Solutions for Steady Flow Past a Circular Cylinder at Reynolds Numbers up to 100". J. Fluid Mech. 42. pp. 471-489, 1970.

[30] http://www2.icfd.co.jp/examples/karman/kr3.htm

[31] P. H. Oosthuizen and S. Madan, "The Effect of Flow Direction on Combined Convective Heat Transfer from Cylinder to Air", ASME J. Heat Transfer 93, pages 240-242, 1971.

[32] A. P. Hatton, D. D. James and H. W. Swire, "Combined Forced and Natural Convection with Low-speed Air Flow over Horizontal Cylinders", J. Fluid Mech. 42, pages 17-31, 1970.

[33] V. T. Morgan and R. D. Findlay, "Effects of Axial Tension and Reduced Air Pressure on the Radial Thermal Conductivity of Stranded Conductors", IEEE Trans. on Power Delivery, Vol. PWRD-8, 1993, pp. 553-558.

[34] R. D. Findlay and H. Riaz, "An Analysis of the Jervis Crossing AACSR Conductor", IEEE Winter Power Meeting, January 1972, Paper No. C72 191.

[35] E. H. Salter, "Problems in the Measurement of AC Resistance and Reactance of Large Conductors," AIEE Trans., Vol. 67, 1948, pp. 1390-1397.

[36] P. E. Burke and R. T. H. Alden, "Current Density Probes", IEEE Trans. on Power Apparatus and Systems, Vol. PAS-88, No. 2, February 1969, pp. 181-185.

[37] E. R. Quant and E. W. Fink, "Experimental and Theoretical Analysis of the Transient Response of Surface Bonded Thermocouples", Bettis Technical Review, WAPD-BT-19, Reactor Technology, June 1960.

[38] S. J. Green and T. W. Hunt, "Accuracy and Response of Thermocouples for Surface and Fluid Temperature Measurements", Temperature, Its Measurement and Control in Science and Industry. Vol. 3, Part 2, Reinhold, New York, p. 695.

[39] F. J. White, "Accuracy of Thermocouples in Radiant Heat Testing", Experimental Mechanics, Vol. 2, July 1962.

[40] H. D. Baker, E. A. Ryder and N. H. Baker, "Temperature Measurement in Engineering", John Wiley & Sons, Inc., 1975.

[41] K. W. Garrett and H. M. Rosenberg, "The Thermal Conductivity of Epoxy-Resin Powder Composite Materials", J. Phys. D: Appl. Phys., Vol. 7, 1974.

[42] F. T. de Araujo and H. M. Rosenberg, "The Thermal Conductivity of Epoxy - Resin/Metal - Powder Composite Materials from 1.7 to 300 K", J. Phys. D: Appl. Phys., Vol. 9, 1976.

[43] John R. Taylor, "An Introduction to Error Analysis", University Science Books, 1982.

[44] V. T. Morgan and R. D. Findlay, "The Effect of Frequency on the Resistance and Internal Inductance of Bare ACSR Conductors", IEEE Transactions on Power Delivery, Vol. 6, No. 3, 1991, pp. 1319-1326.

[45] M. Nørgaard, O. Ravn, N. K. Poulsen and L. K. Hansen, "Neural Networks for Modeling and Control of Dynamic Systems", Springer, 1999.

[46] Walter Vandaele, "Applied Time Series and Box-Jenkins Models", Academic Press, Inc., 1983

[47] Richard C. Dorf (Edit-in-Chief) *et al.,* "The Electrical Engineering Handbook", CRC Press LLC, 2000.

[48] Simon Haykin, "Neural Networks: A Comprehensive Foundation" Prentice-Hall, 1999

[49] Website: http://www.ieso.ca/imoweb/marketdata/marketSummary.asp

[50] C. M. Bishop, "Neural Networks for Pattern Recognition", New York: Oxford University Press, 1995

[51] Christopher M. Bishop, "Neural Networks and Machine Learning", Springer-Verlag Berlin Heidelberg New York, 1998.

[52] S. D. Kim and M. M. Morcos, "Diagnosis of Useful Life for ACSR Conductors Using a Fuzzy Inference System", IEEE Power Engineering Review, May 2002, pp. 61-64.

[53] D. G. Havard, G. Bellamy, P. G. Buchan, H. A. Ewing, D. J. Horrocks, S. G. Krishnasamy, J. Motlis, and K. S. Yoshiki-Gravelsins, "Aged ACSR Conductors Part I – Testing Procedures for Conductors and Line Items", IEEE Trans. on Power Delivery, Vol. 7, No. 2, April 1992, pp. 581-587.

[54] D. G. Havard, M. K. Bissada, C. G. Fajardo, D. J. Horrocks, J. R. Meale, J. Motlis, M. Tabatabai, and K. S. Yoshiki-Gravelsins, "Aged ACSR Conductors Part II – Prediction of Remaining Life", IEEE Trans. on Power Delivery, Vol. 7, No. 2, April 1992, pp. 588-595.

[55] M. W. Vogt, "T2 ACSR Conductors: Lessons Learned", Rural Electric Power Conference, April 20-22, 1997.

[56] A. J. Mazon, I. Zamora, P. Eguia, E. Torres, S. Miguelez, R. Medina, and J. R. Saenz, "Analysis of Traditional Suspension Strings with GTACSR Conductors", IEEE Trans. on Power Delivery, Vol. 19, No. 3, July 2004, pp. 1198-1203.

[57] A. Alawar, E. J. Bosze, and S. R. Nutt, "A Composite Core Conductor for Low Sag at High Temperatures", IEEE Trans. on Power Delivery, Vol. 20, No. 3, July 2005, pp. 2193-2199.

[58] ASTM Designation: E230 - 98
"Standard Specification and Temperature-Electromotive Force (EMF) Tables for Standardized Thermocouples" Annual Book of ASTM Standard, Vol. 14.03

[59] "Manual on the Use of Thermocouples in Temperature Measurement", ASTM Publication Code Number (PCN) 04-470020-40.

[60] ASTM Designation: E220 - 86
"Standard Test Method for Calibration of Thermocouples by Comparison Techniques" Annual Book of ASTM Standard, Vol. 14.03